Tectonic and climatic influence on the evolution of the Bhutan Himalaya

by

Byron A. Adams

A Dissertation Presented in Partial Fulfillment
of the Requirements for the Degree
Doctor of Philosophy

Approved April 2014 by the
Graduate Supervisory Committee:

Kelin X. Whipple (Co-chair)
Kip V. Hodges (Co-chair)
Arjun M. Heimsath
J. Ramón Arrowsmith
Jose M. Hurtado, Jr.

ARIZONA STATE UNIVERSITY

May 2014

ABSTRACT

The Himalaya are the archetypal example of a continental collision belt, formed by the ongoing convergence between India and Eurasia. Boasting some of the highest and most rugged topography on Earth, there is currently no consensus on how climatic and tectonic processes have combined to shape its topographic evolution. The Kingdom of Bhutan in the eastern Himalaya provides a unique opportunity to study the interconnections among Himalayan climate, topography, erosion, and tectonics.

The eastern Himalaya are remarkably different from the rest of the orogen, most strikingly due to the presence of the Shillong Plateau to the south of the Himalayan rangefront. The tectonic structures associated with the Shillong Plateau have accommodated convergence between India and Eurasia and created a natural experiment to test the possible response of the Himalaya to a reduction in local shortening. In addition, the position and orientation of the plateau topography has intercepted moisture once bound for the Himalaya and created a natural experiment to test the possible response of the range to a reduction in rainfall. I focused this study around the gently rolling landscapes found in the middle of the otherwise extremely rugged Bhutan Himalaya, with the understanding that these landscapes likely record a recent change in the evolution of the range.

I have used geochronometric, thermochronometric, and cosmogenic nuclide techniques, combined with thermal-kinematic and landscape evolution models to draw three primary conclusions.

1) The cooling histories of bedrock samples from the hinterland of the Bhutan Himalaya show a protracted decrease in erosion rate from the Middle Miocene toward the Pliocene. I have attributed this change to a reduction in shortening rates across the Himalayan mountain belt, due to increased accommodation of shortening across the Shillong Plateau.

2) The low-relief landscapes of Bhutan were likely created by backtilting and surface uplift produced by an active, blind, hinterland duplex. These landscapes were formed during surface uplift, which initiated ca. 1.5 Ma and has totaled 800 m.

3) Millennial-scale erosion rates are coupled with modern rainfall rates. Non-linear relationships between topographic metrics and erosion rates, suggest a fundamental difference in the mode of river incision within the drier interior of Bhutan and the wetter foothills.

DEDICATION

This dissertation is a mere stepping stone on a path I set upon when someone convinced me that I could live my life deliberately.

Some awards come with titles and promotions, and some are a dingy penny. But they mean what you think they mean.

To Lyndon Wall.

ACKNOWLEDGMENTS

Someone once suggested that the most “Byron” thing to do here would be to list the people that helped me during my Ph.D. career in alphabetical order, and to move on. While that idea is compelling, as one acquires a great deal of people to thank over the course of seven years, I should probably make a few notes.

Kip Hodges taught me a lot about what I didn’t know about thermochronology, and more to the point, how to quantify it using a Monte Carlo simulation. I had a lot of fun with Kip in the field and in deciphering Bhutan. One of the nicest, things anyone has said to me was that I reminded them of a young Kelin Whipple. While I discovered it was mostly because of my stature, I was quite pleased with myself for 30 seconds. I thank you both for sharing your time and knowledge, and giving me the time to have failures and successes.

I would be remiss to not mention my “third advisor” Arjun Heimsath. I will remember Arjun as one of my biggest supporters. I would also like to thank my other committee members: Ramon Arrowsmith and Jose Hurtado. Despite Ramon’s insane schedule and Jose living in El Paso, TX, these two men found time to advise and support me. For that I am eternally grateful. Todd Ehlers was a very influential part of this dissertation. He helped me understand thermal models and the process of using models in general.

There were a lot of other people around me that helped do a lot of the heavy lifting (large magnets and acid mostly, sometimes dense syntax) including Matthijs van Soest, Jo Ann Wartho, Brian Monteleone, Alka Tripathy, Roman DiBiase, Matthew Rossi, Matthew Jungers, and my boys of WorD. I likely still owe you all a

drink. Thank you also to the other members of all my groups who tolerated my crazy ideas and rants and gave me feedback: Wendy Bohon, Nathaniel Borneman, Kelsey Young, Scott Robinson, Marina Bravo, and Andy Darling.

I have been fortunate to have consistent funding for my Ph.D. career. The Geomorphology and Land Use Dynamics and Tectonics programs of the National Science Foundation (NSF) provided the bulk of funding for this work via two awards (EAR-0708714 to Kip Hodges, and EAR-1049888 to Kelin Whipple and Arjun Heimsath).

Another person once told me that sometimes lists are in alphabetical order and sometimes you save the best for last. On to my family - Ron, Jennifer, Emily, Kimberly and Nathan, thank you for supporting me, especially the times when none of this made any sense. My dad calls Frances and I the “Coopas” and that is fine by me. She was my motivation when I struggled near the end of this process.

TABLE OF CONTENTS

Page

APPENDIX

LIST OF TABLES

LIST OF FIGURES

PREFACE

There are certain queer times and occasions in this strange mixed affair we call life when a man takes this whole universe for a vast practical joke, though the wit thereof he but dimly discerns, and more than suspects that the joke is at nobody's expense but his own. However, nothing dispirits, and nothing seems worthwhile disputing. He bolts down all events, all creeds, and beliefs, and persuasions, all hard things visible and invisible, never mind how knobby; as an ostrich of potent digestion gobbles down bullets and gun flints. And as for small difficulties and worryings, prospects of sudden disaster, peril of life and limb; all these, and death itself, seem to him only sly, good-natured hits, and jolly punches in the side bestowed by the unseen and unaccountable old joker. That odd sort of wayward mood I am speaking of, comes over a man only in some time of extreme tribulation; it comes in the very midst of his earnestness, so that what just before might have seemed to him a thing most momentous, now seems but a part of the general joke. There is nothing like the perils of whaling to breed this free and easy sort of genial, desperado philosophy; and with it I now regarded this whole voyage of the Pequod, and the great White Whale its object.

- Herman Melville, *The Whale* (1851)

CHAPTER 1

INTRODUCTION

MOTIVATION

In the early 1930s, a time when much of the Himalaya were inaccessible to foreigners, legendary Swiss geologists Albert Heim and Augusto Gansser were exploring regions of India, Nepal and Tibet. Their findings from these pioneering explorations have shaped the study of the Himalaya to this day. As a means of classification Heim and Gansser (1939) divided the mountain range into regions based on physiography and underlying geology. Though geomorphology was still a fledgling science, Heim and Gansser (1939) saw the importance of the topographic provinces within the range and coined the terms *Lower Himalaya*, in reference to the more subdued foothills that rise from the plains of the Ganges River, and *High Himalaya*, in reference to the higher and more rugged peaks nearer the crest of the range.

The exact definition and distribution of physiographic provinces, and associated transitions, were subsequently better described and evaluated (e.g. Hodges et al., 2001; Wobus et al., 2003; Hodges and Adams, 2013), and causal mechanisms of these topographies were hypothesized. Whereas some investigators concluded that the dichotomy in topographic state was due to a ramp in the basal décollement (Lyon-Caen and Molnar, 1983; Lyon-Caen and Molnar, 1985; Cattin et al., 2001; Lave and Avouac, 2001), the growth of a blind duplex (Robinson et al., 2003; Bollinger et al., 2004; 2006; Pearson and DeCelles, 2005), or an out-of-sequence south-vergent thrust fault (Wobus et al., 2003; 2005; 2006; Hodges et al.,

2004), all of these hypotheses imply that the rock uplift rates are positively correlated with mean elevation (i.e. the Lower Himalaya were experiencing lower rock uplift rates that the High Himalaya). Moreover, some of these researchers also proposed that the erosion and uplift pattern in the central Himalaya were coupled with a similar gradient in orographic precipitation (Wobus et al., 2003; Hodges et al., 2004; Huntington et al., 2006).

The topography of the eastern Himalaya is remarkably different than the central Himalaya, especially in the Kingdom of Bhutan. Steep terrains, similar to the High Himalaya, climb rapidly from the foreland plains, and are also found near the crest of the range. However, subdued terrains similar to the Lower Himalaya are found in the middle latitudes, forming a low-relief bench in the middle of an otherwise extremely rugged landscape. Two previous publications have focused on the generation of these low-relief landscapes in the Bhutan Himalaya. Baillie and Norbu (2004) concluded that these landscapes where formed via tectonic processes - most likely large throw on a thrust fault downstream. Conversely, Grujic et al. (2006) proposed that the Shillong Plateau rain shadow (Figure 1.1) decreased erosion rates in Bhutan, which led to the uplift of the low-relief landscapes due to higher, unchanging rock uplift rates. To further complicate the tectonic and geomorphic history of the Bhutan Himalaya, Clark and Bilham (2008) asserted that the activity on the bounding structures of the Shillong Plateau decreased the slip and rock uplift of structures in the eastern Himalaya (Figure 1.1). They went on to predict that the continued activity and growth of the Shillong Plateau would lead to the demise of the eastern Himalaya.

Unfortunately, the formation mechanism, timing, and magnitude of proposed effects within the Bhutan Himalaya have made it difficult to know which techniques would be most fruitful for disentangling the possible influences of climate versus tectonics. Because of this, I have used many techniques within this dissertation ranging from: analysis of modern topography, modeling of erosion rates on million-year timescales using thermochronometric data; measurement of millennial-scale erosion rates using cosmogenic radionuclides; and testing the plausibility of hypotheses using landscape evolution models. This combination of techniques yielded robust constraints the evolution of the Bhutan Himalaya at a reasonably high temporal and spatial resolution.

A summary of the chapters is provided below. Chapters 2 – 5 were prepared individually for publication as independent journal articles, so there is a necessary overlap in background material within the chapters.

CHAPTER OUTLINE

Chapter 2 quantitatively described and located the low-relief surfaces in the central and eastern regions of the Bhutan Himalaya using analyses of digital topography data, which introduced and developed the ideas and metrics used throughout this dissertation. In this paper, we focused on a physiographic transition in Bhutan thought to have formed by an active, south-vergent thrust fault, similar to the central Himalaya. However, using a combination of fieldwork, satellite imagery, apatite (U-Th)/He and zircon (U-Th)/He thermochronometry, and hematite (U-Th)/He geochronometry, we discovered and described a previously unmapped

normal fault in the hinterland of the range, the Lhuentse fault. We also were able to constrain its activity to Quaternary to Pleistocene times, and suggested it was related to an active blind duplex to the south of the fault.

Chapter 3 aimed to elucidate the long-term thermal evolution and erosion rate history of the Bhutan Himalaya. We described the results of 1D thermal-kinematic modeling of thermochronometric data throughout the hinterland. For this analysis, we used $^{40}Ar/^{39}Ar$ muscovite, apatite (U-Th)/He, and zircon (U-Th)/He data to extend our erosion histories from the Middle Miocene to the Pliocene. Our results showed a protracted decrease in erosion rates across Bhutan. We suggested this decrease was caused by an extended period of lower fault slip rates and rock uplift rates in the eastern Himalaya due to activity of Shillong Plateau structures. Furthermore, the reduction in erosion rates throughout Bhutan suggests that this portion of the range has responded in unison, and therefore, possible transfer structures from the Shillong Plateau must intersect the Himalayan range west of Bhutan (Figure 1.1). Our data analysis suggests that the low-relief landscapes are younger than the range of all of our thermochronometric closure ages, and are therefore, likely Plio-Pleistocene features rather than older, uplifted surfaces.

Chapter 4 explored a new hypothesis for the creation of low-relief landscapes that have undergone significant surface uplift in Bhutan. This new hypothesis was based on geomorphic observations and spatial patterns in millennial-scale basin averaged cosmogenic radionuclide erosion rates. The erosion rates and observations suggested that a hinterland antiformal uplift rate pattern, associated with the growth of a blind duplex, may have caused the backtilting and uplift of low-

relief landscapes. The erosion rate data also confirmed that the low-relief landscapes are transient features that are being erased as major slope-break knickpoints move headward. To test the plausibility of this hypothesis, we utilized a landscape evolution model and impose an antiformal uplift rate pattern on a steady-state landscape. Low-relief landscapes above migrating knickpoints formed readily upstream of the hinge of the antiform. Our findings show that these landscapes were formed during surface uplift, and were not once part of a subdued foreland terrain. In the final steps, we calculated the surface uplift magnitude of low-relief landscapes by reconstructing non-glaciated river reaches that have not been deformed or aggraded during surface uplift, and we calculate the timing of surface uplift initiation using the basin-averaged erosion rate data. We concluded that the low-relief landscapes have been uplifted ca. 800 m in the past ca. 1.5 Ma.

Chapter 5 tested the hypothesis that erosion rates are coupled with mean annual rainfall in the Bhutan Himalaya, and that this coupling could have an effect on the topography. We presented a large suite of basin-averaged cosmogenic radionuclide erosion rates from basins receiving between 0.4 to 4.5 m of rainfall per year (Figure 1.1) and having a wide range of topographic form. The data from drier interior regions of Bhutan (rainfall < 0.65 m $y.^{-1}$) exhibited a non-linear relationship between channel steepness and erosion rate similar to that shown by data from the eastern margin of the Tibetan Plateau (Ouimet et al., 2009), which receives similar amounts of rainfall. Similarly, data from the wetter portions of Bhutan (rainfall > 1.5 m $y.^{-1}$) showed a similar non-linear relationship as data from the central Nepal Himalaya (Godard et al., 2014). This relationship suggests that there is coupling

between topographic form, erosion rate, and climate in Bhutan and that regions receiving more rainfall have higher erosivity values. However, these data also suggest that it is unlikely that the climate change proposed by Grujic et al. (2006) created the surface uplift of the low-relief landscapes in Bhutan.

Chapter 6 is a synthesis of the preceding chapters and suggests further avenues of research.

Chapter 2 has been published in a journal, it should be cited as indicated below:

Chapter 2: Adams, B.A., K.V. Hodges, M.C. van Soest, and K.X. Whipple (2013), Evidence of Pliocene-Quaternary normal faulting in the hinterland of the Bhutan Himalaya, *Lithosphere*, 5(4), 438-449.

FIGURE CAPTIONS

Figure 1.1. Spatial variation in convergence and rainfall created by the Shillong Plateau. Rainfall data derived from Tropical Rainfall Measuring Mission satellite data (Bookhagen, in review). Political boundaries shown as grey and white lines. Primary contractional structures are shown as black lines. Note that the Shillong Plateau intercepts a great deal of the moisture coming from the south and may also accommodate some of the convergence between the Indian and Eurasian plates.

REFERENCES

Adams, B. A., Hodges, K. V., van Soest, M. C., & Whipple, K. X. (2013). Evidence for Pliocene-Quaternary normal faulting in the hinterland of the Bhutan

Himalaya. *Lithosphere, 5*(4), 438-449. doi: 10.1130/l277.1

Baillie, I. C., & Norbu, C. (2004). Climate and other factors in the development of river and interfluve profiles in Bhutan, Eastern Himalayas. *Journal of Asian Earth Sciences, 22*(5), 539-553. doi: 10.1016/s1367-9120(03)00092-0

Bollinger, L., Avouac, J. P., Beyssac, O., Catlos, E. J., Harrison, T. M., Grove, M., Goffé, B., & Sapkota, S. (2004). Thermal structure and exhumation history of the Lesser Himalaya in central Nepal. *Tectonics, 23*(5), TC5015.

Bollinger, L., Henry, P., & Avouac, J. P. (2006). Mountain building in the Nepal Himalaya: Thermal and kinematic model. *Earth and Planetary Science Letters, 244*(1), 58-71.

Bookhagen, B., in review, High resolution spatiotemporal distribution of rainfall seasonality and extreme events based on a 12-year TRMM time series.

Cattin, R., Martelet, G., Henry, P., Avouac, J. P., Diament, M., & Shakya, T. R. (2001). Gravity anomalies, crustal structure and thermo-mechanical support of the Himalaya of central Nepal. *Geophysical Journal International, 147*(2), 381-392.

Clark, M. K., & Bilham, R. (2008). Miocene rise of the Shillong Plateau and the beginning of the end for the Eastern Himalaya. *Earth and Planetary Science Letters, 269*(3), 337-351.

Godard, V., Bourlès, D. L., Spinabella, F., Burbank, D. W., Bookhagen, B., Fisher, G. B., Moulin, A., & Léanni, L. (2014). Dominance of tectonics over climate in Himalayan denudation. *Geology*, G35342. 35341.

Grujic, D., Coutand, I., Bookhagen, B., Bonnet, S., Blythe, A., & Duncan, C. (2006).

Climatic forcing of erosion, landscape, and tectonics in the Bhutan Himalayas. *Geology, 34*(10), 801-804. doi: 10.1130/g22648.1

Heim, A., & Gansser, A. (1939). *Central Himalaya: Geological Observations of the Swiss Expedition 1936* (Vol. 73). Zurich: Mémoires de la Société Helvétique des Sciences Naturelles.

Hodges, K. V., & Adams, B. A. (2013). The influence of middle and lower crustal flow on the landscape evolution of orogenic plateaus: Insights from the Himalaya and Tibet. In L. Owen (Ed.), *Treatise on Geomorphology* (Vol. 5). San Diego: Academic Press.

Hodges, K. V., Hurtado, J. M., & Whipple, K. X. (2001). Southward extrusion of Tibetan crust and its effect on Himalayan tectonics. *Tectonics, 20*(6), 799-809.

Hodges, K. V., Wobus, C., Ruhl, K., Schildgen, T., & Whipple, K. (2004). Quaternary deformation, river steepening, and heavy precipitation at the front of the Higher Himalayan ranges. *Earth and Planetary Science Letters, 220*(3), 379-389.

Huntington, K. W., Blythe, A. E., & Hodges, K. V. (2006). Climate change and Late Pliocene acceleration of erosion in the Himalaya. *Earth and Planetary Science Letters, 252*(1-2), 107-118. doi: 10.1016/j.epsl.2006.09.031

Lave, J., & Avouac, J. P. (2001). Fluvial incision and tectonic uplift across the Himalayas of central Nepal. *Journal of Geophysical Research-Solid Earth, 106*(B11), 26561-26591. doi: 10.1029/2001jb000359

Lyon-Caen, H., & Molnar, P. (1983). Constraints on the structure of the Himalaya from an analysis of gravity anomalies and a flexural model of the lithosphere.

Journal of Geophysical Research, 88(B10), 8171-8191.

Lyon-Caen, H., & Molnar, P. (1985). Gravity anomalies, flexure of the Indian plate, and the structure, support and evolution of the Himalaya and Ganga basin. *Tectonics, 4*(6), 513-538.

Ouimet, W. B., Whipple, K. X., & Granger, D. E. (2009). Beyond threshold hillslopes: Channel adjustment to base-level fall in tectonically active mountain ranges. *Geology, 37*(7), 579-582.

Pearson, O. N., & DeCelles, P. G. (2005). Structural geology and regional tectonic significance of the Ramgarh thrust, Himalayan fold-thrust belt of Nepal. *Tectonics, 24*(4), TC4008.

Robinson, D. M., DeCelles, P. G., Garzione, C. N., Pearson, O. N., Harrison, T. M., & Catlos, E. J. (2003). Kinematic model for the Main Central thrust in Nepal. *Geology, 31*(4), 359-362.

Wobus, C., Heimsath, A., Whipple, K., & Hodges, K. (2005). Active out-of-sequence thrust faulting in the central Nepalese Himalaya. *Nature, 434*(7036), 1008-1011.

Wobus, C. W., Hodges, K. V., & Whipple, K. X. (2003). Has focused denudation sustained active thrusting at the Himalayan topographic front? *Geology, 31*(10), 861-864.

Wobus, C. W., Whipple, K. X., & Hodges, K. V. (2006). Neotectonics of the central Nepalese Himalaya: Constraints from geomorphology, detrital 40Ar/39Ar thermochronology, and thermal modeling. *Tectonics, 25*(4), TC4011.

FIGURE 1.1

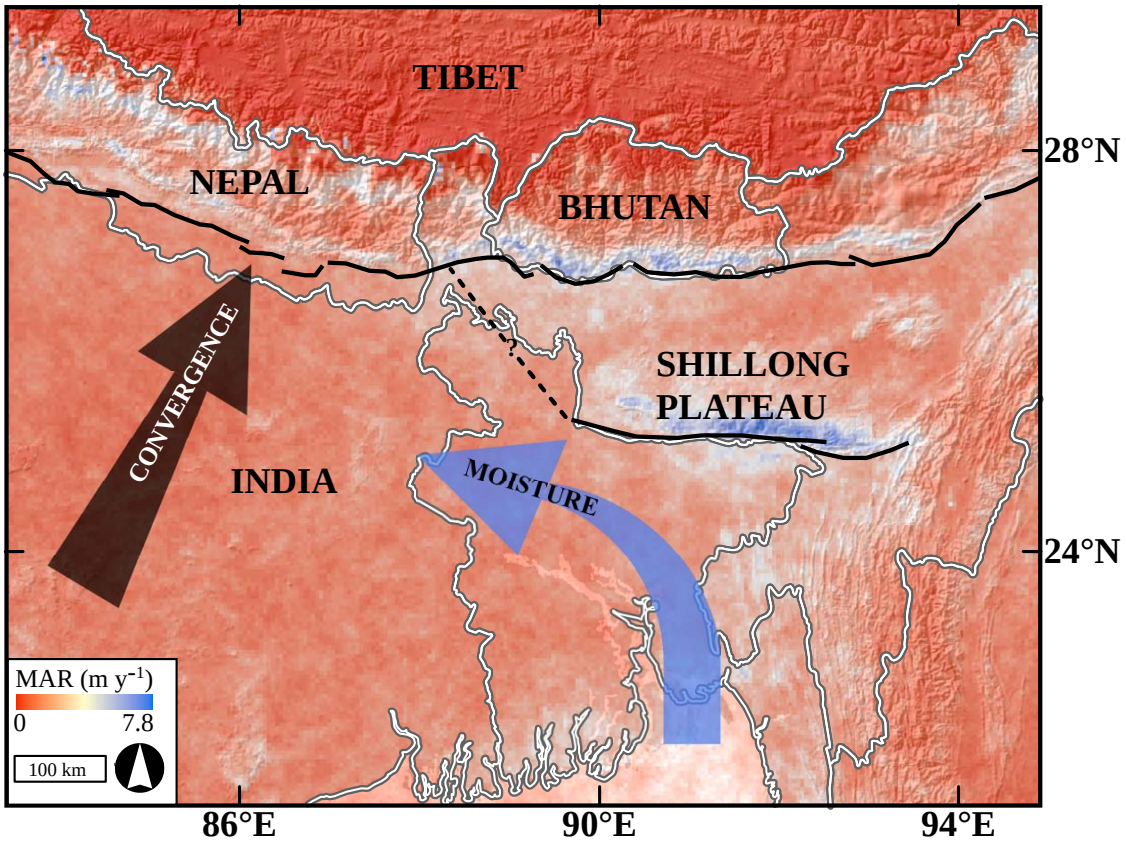
TIBET
NEPAL
BHUTAN
SHILLONG
PLATEAU
INDIA
CONVERGENCE
MOISTURE
MAR (m y-1)
0
7.8
100 km
28°N
24°N
86°E
90°E
94°E

CHAPTER 2

EVIDENCE FOR PLIOCENE-QUATERNARY NORMAL FAULTING IN THE HINTERLAND OF THE BHUTAN HIMALAYA

ABSTRACT

In the central Himalaya, past researchers have identified a distinctive transition from the physiographic Lower Himalayan ranges to the south to the Higher Himalayan ranges to the north. Local relief, hillslope gradient, as well as erosion and surface uplift rates increase abruptly across this transition to the north. In the eastern Himalaya, the same physiographic transition exists but is less dramatic. We describe here a previously undocumented steep, north-dipping, brittle structure that is roughly coincident with this physiographic transition in eastern Bhutan - the Lhuentse fault. Low-temperature (U-Th)/He apatite data suggest that the Lhuentse fault has been active since the Pliocene, and (U-Th)/He dates on offset hydrothermal hematite deposits from within the fault zone demonstrate a component of Quaternary slip. Although we identified no definitive evidence of fault kinematics based on field or petrographic analysis of the fault rocks, the disrupted pattern of (U-Th)/He apatite dates suggest normal-sense displacement, contrary to what was expected given previous studies of an analogous transition in the central Himalaya. We regard the existence and activity of the Lhuentse fault as evidence of 1) a recent evolution in the tectonic regime of the eastern Himalaya from one of near-exclusive N-S shortening to one in which both transcurrent and normal faulting are increasingly important in the region north of the Himalayan deformation front, or 2) an active duplex south of the physiographic transition in the middle latitudes of Bhutan.

INTRODUCTION

The transition from the Indo-Gangetic Plains northward to the Tibetan Plateau is a dramatic, 5 km-high escarpment (Figure 2.1). The Himalayan landscape in between rises thousands of meters across a set of steps, or physiographic transitions (Figure 2.1), that have been correlated to regions of focused uplift. The northern most physiographic transition – Physiographic Transition 1 (PT_1) - marks the dramatic change from the rugged and high peaks of the Himalayan range to the lower relief of the Tibetan Plateau. The most dramatic of these transitions, PT_2, generally separates the Physiographic Lower Himalaya to the south from the Higher Himalaya to the north. The southernmost, PT_3, denotes the meeting of the edge of the Himalayan range and the Indo-Gangetic Plains. See Hodges et al. (2001) and Hodges and Adams (2013) for a more thorough discussion.

In central Nepal, PT_2 corresponds spatially with a discontinuity of vertical rock and surface uplift rates that are higher to the north than to the south (Jackson and Bilham, 1994). A variety of geological, geochemical, geodetic, and geophysical datasets have been employed to interpret this discontinuity as a manifestation of one of three possible tectonic processes: 1) a simple ramp in the north-dipping sole thrust at the base of the Himalayan orogenic wedge (Figure 2.2A; e.g. Lyon-Caen and Molnar, 1983; Lyon-Caen and Molnar, 1985; Cattin et al., 2001; Lave and Avouac, 2001); 2) an actively growing thrust duplex (Figure 2.2B; e.g. Robinson et al., 2003; Bollinger et al., 2004; 2006; Pearson and DeCelles, 2005); or 3) a Quaternary, out-of-sequence, south-vergent thrust fault (Figure 2.2C; Wobus et al., 2003; 2005; 2006a; Hodges et al., 2004).

PT_2 has been studied in less detail in other sectors of the Himalaya. For example, it is possible to identify a distinctive PT_2 in Bhutan (Duncan et al., 2003), even though

the topographic profile is quite different than central Nepal. Like Duncan et al. (2003), we recognize that the front of the range in Bhutan exhibits ruggedness similar to the High Himalaya in central Nepal (Figure 2.1B). This observation gives the sense that Bhutan is "missing" the typical Lower Himalayan topography. However, Grujic et al. (2006) have proposed that a zone of low relief in the middle latitudes of Bhutan represents Pliocene to Quaternary uplifted surfaces of Lower Himalayan topography. These perched low-relief landscapes abut a zone of high relief to the north (Figure 2.1B). This juxtaposition of high and low relief topographies creates a physiographic transition analogous to that of central Nepal.

Because PT_2 in central Nepal is so closely related – in a spatial sense – to buried or emergent deformational structures that have played important roles in the evolution of the Himalaya, it is reasonable to posit that observation of this landform in other parts of the orogen could serve as indicators of the existence of similarly important structures, and could help focus future structural studies in less well-characterized sectors. However, such a hypothesis needs to be tested in each location where PT_2 is observed. Variability in the consistency or form of PT_2 along strike could suggest a change in tectonic mechanism, or magnitude and duration of tectonic forcing. The study of PT_2 along the strike of the range could illuminate architectural or temporal variations in the development of the orogen.

Here we describe the topographic and geologic character of PT_2 in central and eastern Bhutan and evaluate whether or not it marks a zone of active deformation in this sector of the orogen as it does in central Nepal. Bedrock mapping in Bhutan has revealed the existence of a major north-dipping, contractional fault in the vicinity of PT_2 – the

Kakhtang thrust (KT; Figures 2.3 and 2.4) – but previous workers have ascribed a Miocene age to all activity on the structure (Gansser, 1983; Swapp and Hollister, 1991; Davidson et al., 1997; Grujic et al., 2002; Kellett et al., 2009). We present evidence here that PT_2 is also coincident with the trace of a steep, N-dipping structure with activity extending into the Quaternary, which is referred to here as the Lhuentse fault. Although there is no direct structural evidence indicative of the kinematics of the fault, a (U-Th)/He thermochronometric dataset for samples collected across the structure is interpreted as evidence of a component of normal-sense displacement, with rocks to the south having been exhumed more rapidly than rocks of the higher relief terrains to the north during the past 2-3 million years. This unanticipated result is interpreted as evidence of a Pliocene to Quaternary transition in the kinematic evolution of the Himalayan hinterland at this latitude.

CHARACTERISTICS OF PT_2 IN THE BHUTAN HIMALAYA

Morphometric Observations

Although Duncan et al. (2003) first established the general position of PT_2 in Bhutan; our search for field evidence of structural disruption along this transition required a more precise location effort. Following the approach of Wobus et al. (2006a), we conducted a topographic analysis of the region using a ca. 30 m per pixel-resolution, Advanced Spaceborne Thermal Emission Reflection Radiometer (ASTER) digital elevation model (DEM).

We focused our geomorphic analyses on three metrics: 1) local relief, 2) hillslope gradient, and 3) channel steepness. Our local relief map (Figure 2.4A) was calculated by

finding the difference between the highest and lowest elevations within a 5 km-diameter circular moving window. The slope map (Figure 2.4B) was calculated across a ca. 90 m square and then smoothed using a 1 km-diameter circular moving window. We used the normalized channel steepness index (k_{sn}) to quantify patterns of river gradients that are scale-independent, allowing us to compare river gradients across Bhutan (Figure 2.4C) regardless of drainage basin size or location (e.g. Wobus et al., 2006b). We calculated k_{sn} over 10 km lengths of channel using a reference concavity index of 0.45 (e.g. Wobus et al., 2006b). The patterns of channel steepness revealed from this analysis can help constrain how landscapes are responding to external forcing factors (e.g. uplift, rock strength, and climate; e.g. Wobus et al., 2006b).

Our analysis shows that PT_2 within Bhutan is completely contained within the mapped extent of the Greater Himalayan sequence of rocks, which corresponds to the metamorphic hinterland of the Bhutan Himalaya (Figure 2.3, Long et al., 2011a). PT_2 can be readily observed as an abrupt, but discontinuous increase in hillslope gradient, local relief, channel steepness, and mean elevation to the north. In most cases, the mountains directly to the north of PT_2 climb rapidly to elevations in excess of 5000 m. Here the regional mean elevation and local relief appear to be limited by glacial erosion (Brozović et al., 1997; Meigs and Sauber, 2000) rather than fluvial valley incision. Glacial erosion in these high northern regions is evident in visible satellite imagery and previously published maps (Gansser, 1983; Komori, 2008) in the form of cirques, tarns, moraines and active glaciers. Such evidence for extensive glacial activity limits the utility of attempts to infer differential exhumation from simple morphometric comparisons of landscapes north and south of PT_2 (Brocklehurst and Whipple, 2007).

In comparison to PT_2 in central Nepal (Wobus et al., 2003; 2005; 2006a), the north-south gradient across PT_2 in Bhutan in any morphometric parameter is subdued and less abrupt, and it is segmented and more difficult to trace continuously along its trend. It is not possible to follow the trace of PT_2 across the deep canyons that surround these perched low-relief landscapes. Curiously, the two well-constrained segments in central Bhutan are located near the northern edge of the perched low-relief surfaces (Grujic et al., 2006; Figure 2.4). This may imply that these low-relief surfaces and PT_2 have a shared history.

Spatial Relationship of PT_2 with Previously Mapped or Inferred Structures

Of all the major structures previously mapped in Bhutan (Gansser, 1983; McQuarrie et al., 2008; Grujic et al., 2011), PT_2 most closely follows the Kakhtang thrust. However, there is a considerable uncertainty regarding the trace (Figure 2.3), throw, and timing of the Kakhtang thrust. Gansser's (1983) initial observations of the Kakhtang thrust lacked a clear description of the structure or its trace. In 1991, Swapp and Hollister observed a previously undocumented inversion in metamorphic grade that they argued was created by displacement on a thrust fault, and roughly coincident with the shear zone proposed by Gansser (1983). No exposures of the Kakhtang thrust have been described in the literature but it is often generally mapped near the position of a change in abundance of leucogranitic anatexites or the second sillimanite isograd within the Greater Himalayan sequence (e.g. Swapp and Hollister, 1991).

The rough coincidence of PT_2 and the Kakhtang thrust is particularly good in eastern Bhutan (Figure 4d). However, the trace of PT_2 and most previously mapped

traces of the Kakhtang thrust in central Bhutan (e.g. Long et al., 2011a; Grujic et al., 2011) differ substantially. In areas where the mapped position of the Kakhtang thrust is not coincident with PT_2, there is no geomorphic signature of differential uplift across the thrust. This may not be surprising as previous interpretations of U-Pb dates from luecogranites deformed by the Kakhtang thrust suggest an exclusively Miocene deformation history (Grujic et al., 2002; Kellett et al., 2009). Combined, these observations suggest that PT_2 is not simply a physiographic manifestation of hanging wall uplift of the Kakhtang thrust (i.e. this does not seem to support the hypothesis in Figure 2.2C), but may have a more complex relationship with the tectonic architecture of Bhutan.

While some research groups have interpreted the transition in uplift rate across PT_2 in central Nepal as a consequence of hanging wall deformation associated with a deep-seated ramp in the Himalayan sole thrust (Figure 2.2A; e.g. Lyon-Caen and Molnar, 1983; Jackson and Bilham, 1994; Lave and Avouac, 2001), a similar interpretation of the phenomenon in Bhutan is more difficult. There is considerable debate regarding the existence and along-strike extent of a ramp in the Himalayan sole thrust beneath Bhutan. Hauck et al. (1998) proposed a ramp in the Himalayan Sole thrust in western Bhutan, but their preferred position of that ramp is far north of PT_2 and could not explain the inferred differential uplift across the transition. Recent balanced sections of McQuarrie et al. (2008) and Long et al. (2011b; 2012) have provided evidence for a prominent Miocene ramp within transects of eastern Bhutan. However, the positions of these ramps and duplexes at depth are to the south of PT_2 and cannot be related to uplift north of PT_2 relative to the perched low-relief landscapes. The presence of a ramp in central or

western Bhutan is not as clear from balanced sections (Long et al. 2011b; 2012). Conversely, inversions of thermochronologic data by Robert et al. (2011) suggest the Himalayan sole thrust is a listric structure throughout Bhutan and that there is no evidence for a significant ramp in this part of the orogen.

FIELD OBSERVATIONS OF PT_2 – THE LHUENTSE FAULT

As is the case throughout much of the central and eastern Himalaya, the area of PT_2 in Bhutan is heavily vegetated and rocks are highly weathered. Outcrops are generally poor and restricted to river gorges or sparse road cuts. In order to better evaluate the causal mechanism for PT_2 in Bhutan, we studied one transect along the Kuri Chu in detail where PT_2 could be projected on the basis of our morphometric analysis (Figure 5a) and where the prospects for bedrock exposures seemed promising. At this projected point in the Kuri Chu valley, located ca. 4 km south of the mapped trace of the Kakhtang thrust (Figure 2.5A; Long et al., 2011b), we found a distinctive zone of brittle deformation in Greater Himalayan sequence rocks that we refer to here as the Lhuentse fault.

Most of our observations regarding the structural character of the Lhuentse fault are based on a continuous bedrock outcrop, parallel to the Kuri Chu drainage, which has a structural thickness of about 20 meters. The fault zone is expressed as a series of closely spaced, sub-parallel faults with a mean orientation of 063º/80º (Figure 2.5B). Each fault is marked by several tens of centimeters of cataclasite, including coarsely fragmented bedrock, fault gouge, and (typically) syn- to post-kinematic hydrothermal mineralization (Figures 2.5C and 2.5D). On closer inspection, the faults are marked by

anastomosing zones of finer-grained fragmented rock and gouge surrounding larger (ca. 1-2 m) phacoidal blocks of less-deformed rock. In outcrop, the crush zones are more easily eroded, leaving the more-resistant phacoids as prominent knobs. Despite a concerted effort, we were unable to identify any convincing slickenlines or asymmetric features on any of the structures in the Kuri Chu outcrop that would permit kinematic interpretation.

A thin section from the fault zone shows variously comminuted quartz grains (Figure 2.6A and 2.6B). This style of quartz deformation is consistent with grain size reduction principally by cataclasis at temperatures likely < 300°C and relatively high strain rates (Passchier and Trouw, 1996). We saw no indication of crystallographic grain-shape preferred orientation in the quartz, and found no useful kinematic indicators in thin section.

Petrographic analysis of the hydrothermal precipitates revealed that most consisted of an aggregate of quartz and an opaque mineral. Raman spectroscopy revealed that the opaque mineral is hematite (α-Fe_2O_3; see Appendix A). Based on the absence of hydrothermal mineralization in the rocks outside the fault zone, we infer that the fault zone itself served as the principal conduit for mineralizing fluids. Both outcrops and the thin section display clear evidence of multiple generations of hydrothermal mineralization. In section, fine-grained precipitates appear as speckled and rounded clusters. They are surrounded by younger, coarse-grained quartz + hematite masses. These quartz + hematite masses are also cross cut by younger microfaults (Figures 2.6C and 2.6D), which unfortunately exhibited no preferred orientation or consistent offsets of pre-existing hydrothermal veins that might indicate slip direction. We infer that

hydrothermal quartz + hematite precipitation commenced after the earliest stages of deformation and continued at least episodically during slip, but had largely ceased prior to the latest stages of deformational activity. Although we have no direct constraints on the crystallization temperatures of the syn-deformational hydrothermal minerals in the Kuri Chi cataclasites, we note that fluid inclusion studies of hydrothermal quartz deposits elsewhere along the Himalayan front suggests temperatures ca. 300˚C (Derry et al., 2009).

ALONG STRIKE EXTENT OF THE LHUENTSE FAULT

Attempts in the field to follow the Lhuentse fault along strike to the west and east out of the Kuri Chu valley were unsuccessful due to poor exposure. However, high-resolution (ca. 0.5 m per pixel) WorldView satellite imagery indicate that the fault may be the southernmost manifestation of a broader domain of high-angle faulting up to 13 km in width (Figures 2.5A). The images reveal spaced lineaments with an average strike (070º) similar to the Lhuentse fault (Figure 5e). These lineaments were also observed in remote sensing datasets by Das (2004), who interpreted them as potential strike-slip faults. However, we found no evidence of lateral offsets of drainages on the Lhuentse or any other ENE-trending lineaments in the course of our remote sensing study.

(U-Th)/He THERMOCHRONOLOGY – INDICATIONS OF NORMAL FAULT OFFSET

By analogy with PT_2 in central Nepal (Wobus et al., 2003; 2005 2006a), we anticipated that PT_2 in Bhutan might also mark a discontinuity in bedrock cooling ages as

determined by noble gas thermochronometry. To explore this possibility, we collected bedrock samples (para- and orthogneisses and fine-grained schists) for (U-Th)/He thermochronology along a ca. 13 km transect that crosses the Lhuentse fault in the Kuri Chu drainage (Figure 2.5A). Six samples were found to obtain datable apatite, but only three of those contained datable zircon. Using facilities in Arizona State University's Noble Gas Geochronology and Geochemistry Laboratories (NG^3L), we measured 21 (U-Th)/He apatite (AHe) dates and 14 zircon (ZHe) dates on single, hand-picked crystals (Table 2.1; Figure 2.7A). Analytical procedures closely followed those described in Schildgen et al. (2009) and van Soest et al. (2011).

For each sample, zircon and apatite single-crystal dates clustered reasonably well, but – as is frequently the case in (U-Th)/He thermochronometry – the dispersion of dates for a particular mineral in a particular sample was greater than would be predicted by analytical imprecision alone. We elected to interpret the AHe or ZHe date for a specific sample as the analytical error-weighted mean for all dated crystals, where the number of crystals (*n*) ranged from three to five depending on the sample. The reported error for the mean dates (Table 1) represents both the propagated analytical errors as well as an error magnification factor based on the Mean Square of Weighted Deviates (MSWD) and Student's *t* test for *n*-1 degrees of freedom (Wendt and Carl, 1991; Cooper et al., 2011). These mean dates and their calculated errors (reported at the 95% confidence level) form the basis for interpretations of the low temperature cooling history presented in the following paragraphs.

Compared to the central Nepal region where PT_2 has been studied in detail, the Kuri Chu AHe dates are older, suggesting less aggressive erosional exhumation since the

Late Pliocene in Bhutan, particularly north of PT_2. For example, in the Annapurna range of Nepal, AHe dates north of PT_2 are uniformly less than 1 Ma (Blythe et al., 2007; Nadin and Martin, 2012). In the Kuri Chu transect, AHe dates for samples collected north of the Lhuentse fault trace ranged from 2.78 ± 0.41 to 3.6 ± 1.3 Ma. Two samples collected south of the trace yielded younger dates of 2.41 ± 0.47 and 2.42 ± 0.35 Ma. Zircon dates for three samples collected north of the fault range from 4.23 ± 0.27 to 4.793 ± 0.085 Ma. Although we found no datable zircons in any samples collected south of the fault, Long et al. (2012) report a ZHe date of 4.05 ± 0.07 Ma for a sample collected ca. 7.5 km south of the trace (Figure 2.7A).

In order to estimate variations in exhumation rate across the transect from the thermochronometric data, we pursued 1D thermal modeling (AGE2EDOT; Brandon et al., 1998) of the AHe data that involved simultaneous solution of steady-state advection and diffusion equations and assumed uniform constant exhumation rates for each sample and reasonable values for material properties. Our assumptions regarding material properties were similar to those of Whipp et al. (2009): thermal conductivity = 2.75 W/m K; radiogenic heat production = 0.8 mW/m^3; specific heat = 1000 J/kg K; rock density = 2700 kg/m^3; a surface temperature of 10˚C; and a constant temperature boundary condition of 490 ˚C at 30 km. In addition, we employed the experimental data of Farley (2000) in order to model the diffusive loss of helium in apatite during exhumation. For simplistic 1D models, a thermochronometric date – taken here as the error-weighted mean AHe date for each sample – uniquely specifies a time-averaged exhumation rate (ε). Our justification for not employing more complex 2D or 3D models for such calculations is based on the work of Whipp et al. (2007), who concluded that the thermal

field in active orogens such as the Himalaya is predominantly controlled by the vertical (i.e., 1D) advection and conduction.

Time-averaged exhumation rates modeled in this way from the Kuri Chu apatites range from 0.58 ± 0.14 to 0.93 ± 0.15 km m.y.$^{-1}$ (Figure 7b). When erosion rates are in this range, assumptions regarding material properties have significant influence on 1D modeling results, and conductive heat transfer becomes more significant relative to advective heat transfer. However, the quoted 95% confidence interval for these calculated exhumation rates reflects only propagated analytical uncertainties in the thermochronologic data. We feel that this is reasonable because it is unlikely that material properties vary substantially along the ca. 13 km length of the transect. Nevertheless, the exhumation rate values themselves should be viewed only as rough estimates. A much more robust result is the apparent difference in rates north and south of the trace of the Lhuentse fault trace. Samples to the north can be reasonably interpreted as indicating an average erosion rate (ε_n) of 0.686 ± 0.049 km m.y.$^{-1}$, whereas the two samples to the south indicate an average erosion rate (ε_s) that is statistically distinctive at 0.922 ± 0.096 km m.y.$^{-1}$.

A distinction between the cooling histories of samples north and south of the fault is less obvious from the distribution of AHe dates in Figure 2.7A than from the distribution of modeled exhumation rates in Figure 2.7B. This reflects the fact that the samples were collected over a range of elevations, from 1254 m (BT0970) to 2360 m (BT0962). In order to better illustrate the distinctions, we have used ε_n and ε_s to normalize the AHe cooling dates to the mean elevation of the transect (1740 m). The elevation-corrected dates are shown in Figure 2.7C (see Appendix A for method and

discussion). North of the fault, the normalization process results in a much smaller scatter in corrected AHe dates (AHe_n), with a mean of 2.67 ± 0.16 Ma. South of the fault, corrected AHe dates (AHe_s) are younger, with a mean of 1.92 ± 0.28 Ma.

We conclude from this exercise that the apatite (U-Th)/He thermochronologic data from the Kuri Chu transect indicate preferential uplift of lithologies exposed south of the Lhuentse fault trace relative to those north of the trace over the past ca. 2 Ma. Given the observed dip direction of the fault, we interpret the data as indicative of normal-sense offset on the structure. Using the mean exhumation rates from each side of the fault to calculate the elevation for a cooling date, we find an offset of ca. 500 m in the AHe isochrones across the Lhuentse fault. Whether this reflects pure normal slip or possibly normal-oblique slip is presently unknown.

CONSTRAINTS ON THE AGE OF THE LHUENTSE FAULT FROM HEMATITE (U-Th)/He GEOCHRONOLOGY

Although the disruption of AHe cooling age patterns across the Lhuentse fault indicates slip subsequent to 2 Ma, an additional constraint is provided by (U-Th)/He dating of syn-deformational hydrothermal hematite in the Lhuentse fault cataclasites. Although the usefulness of hematite as a (U-Th)/He chronometer has been noted elsewhere (e.g., Kula and Baldwin, 2012), our study may be the first published application of the technique to dating fault activity. Since procedures for such work at NG^3L have not been published previously, they are detailed briefly here. We began by breaking a large, centimeter-sized piece of ore-rich cataclasite sample into millimeter-sized fragments. In order to eliminate the need for alpha ejection corrections of measured

^{4}He concentrations, interior fragments were enclosed in a pneumatic chamber and self-abraded for three days to eliminate the outer several tens of microns material from each fragment. Four well-rounded, polished fragments were selected and loaded into Nb tubes for analysis. Our approach to analyzing the hematite samples followed closely the protocols described by van Soest et al. (2011) for zircon analysis, although we found that high concentrations of H_2O and CO_2 liberated from the hydrothermal samples required our use of a cryotrap and longer gas purification times (ca. 6 minutes) to purify the extracted gasses in preparation for helium measurement on an Australian Scientific Instruments *Alphachron* system at NG^{3}L. The samples were then dissolved in a mixture of HF, HNO_3, and HCl in Parr digestion vessels prior to parent element measurements on a *ThermoElectron X-Series* inductively coupled, plasma source mass spectrometer.

The four specular hematite fragments yielded (U-Th)/He dates ranging from 70 ± 8 to 130 ± 15 ka (Table 2.2; dates reported at the 95% confidence level), with a variation larger than would be anticipated based on analytical imprecision alone. One plausible interpretation of these results is that the variation reflects variable post-crystallization loss of ^{4}He. We consider this unlikely, however, based on presently available experimental constraints on the diffusivity of ^{4}He in hematite (Kula and Baldwin, 2012). Using the kinetic parameters from that paper and assuming rapid cooling of the fault zone subsequent to hydrothermal precipitation (at rates of greater than 1000˚C per million years, in all likelihood), we calculated bulk ^{4}He closure temperatures of around 300˚C for all samples for an effective diffusion dimension of 500 mm. Inasmuch as this is comparable to the maximum temperatures consistent with the quartz deformation textures observed in the cataclasites, we suggest that the measured dates are crystallization ages

rather than cooling dates. We interpret the variability of dates to reflect polyphase precipitation of hematite in an evolving brittle shear zone. While the data do not constrain the duration of deformation, we infer that the Lhuentse fault was experiencing brittle deformation during the Pleistocene. Beyond the significance of these data for understanding Lhuentse fault activity, they generally affirm the utility of hematite (U-Th)/He chronology for dating the activity of faults that served as conduits for Fe-rich hydrothermal fluids.

THE EVOLUTIONARY GEODYNAMICS OF PT_2 IN BHUTAN

As is the case in the central Nepal Himalaya, PT_2 in Bhutan may indicate comparatively rapid uplift of the Higher Himalaya to the north in late Tertiary time. However, we found no evidence in the course of our study that this has been the case over the past 2 Ma. Thermochronometrically constrained palinspastic reconstructions of the Himalayan thrust belt in Bhutan imply that both the Kakhtang thrust and several more deep-seated structures of the Lesser Himalayan duplexes were active in this sector of the orogen between 15 and 9.5 Ma (Long et al., 2012). Although PT_2 in Bhutan maybe a relict Miocene physiographic feature, it seems likely that either the formation or the preservation of PT_2 may have been associated with the creation of the perched low-relief landscapes that lie to the south.

A variety of lines of evidence suggest a Late Miocene-Holocene change in the tectonics of Bhutan concomitant with the development of the Shillong Plateau to the south and partitioning of a significant component of India-Eurasia convergence to structures south of the Himalayan thrust belt of Bhutan (e.g., Clark and Bilham, 2008).

We infer that this north-to-south broadening of the region of convergence south of PT_2 had an important effect on deformational patterns in our study area by Pliocene time, such that a greater amount of rock uplift (and consequent exhumation) occurred south of PT_2. We regard the Lhuentse fault as, at least in part, a structure that initiated in response to differential uplift on either side of PT_2.

We postulate that the underlying cause of local uplift south of PT_2 was increasing structural relief at depth due to the activity of a blind duplex (Figure 2.8). Long et al. (2011b) have suggested the existence of such a structure south of the trace of the Kakhtang thrust near the location of our cross section A-A' based on palinspastic reconstruction of the Himalayan thrust belt in Bhutan. We propose that the Lhuentse fault developed as a very steep normal fault on the backside of the duplex, dipping toward the hinterland, to accommodate duplex growth and its southward migration as the orogenic wedge grew toward the foreland (Platt, 1986; Roure et al., 1991).

Whether or not the existence of a recently active fault at PT_2 is only a local phenomenon or of regional significance in the eastern Himalayan region is unclear. Seismic studies in Bhutan reveal a complex modern deformation field that includes components of both N-S shortening and transcurrent slip (predominantly right-lateral) on structures that strike NW-SE at various angles relative to the overall E-W trend of the Bhutanese Himalaya (Figure 2.9; De and Kayal, 2003; Rajendran et al., 2004; Andronicos et al., 2007; Drukpa et al., 2006; Velasco et al., 2007; Hazarika et al., 2010). We know of no evidence that transcurrent deformation played an important role in the largely Miocene construction of the primary tectonic architecture of Bhutan (Gansser, 1983; Grujic et al., 1996; McQuarrie et al., 2008; Long et al., 2011a), which suggests that

that seismic evidence for transcurrent deformation in Bhutan may be a recent phenomenon. It is plausible that the Lhuentse fault has accommodated both transcurrent and normal slip during its history, although field or remote sensing evidence for the latter is presently lacking. If it occurred, transcurrent slip along a fault of its orientation would have enabled progressive eastward extrusion of the southeastern Tibetan Plateau and easternmost Himalaya in a manner similar to that inferred by Antolín et al. (2012).

A change in the distribution and/or mode of strain in the eastern Himalaya associated with a transfer of slip to the Shillong Plateau (e.g. Clark and Bilham, 2008) or a focus of uplift created by a reactivated duplex; need to be accounted for within models of mountain building and landscape evolution, as well as geohazard potential maps. This hypothesis is counter to models of fold and thrust belts that suggest the most active loci of deformation are near the foreland of the range.

CONCLUSIONS

Morphometric analysis of central and eastern Bhutan has led to the definition of a sharp transition between topographically subdued landscapes to the south and rugged landscapes of the Higher Himalaya to the north, analogous to, but discontinuous and more subdued than the PT_2 feature studied more extensively in central Nepal (e.g., Hodges et al., 2001; Wobus et al., 2006b). Field studies in the Kuri Chu drainage of central Bhutan demonstrated the existence of a previously unrecognized brittle deformational structure at PT_2: the ENE-WSW-striking, steeply N-dipping Lhuentse fault. Remote sensing analysis of the region suggests that the Lhuentse fault may be one structure of a family of high-angle, ENE-WSW striking faults in the hinterland of Bhutan

Himalaya. Although exposures of the Lhuentse fault zone are good, we were unable to determine the structure's kinematics on the basis of outcrop or thin section analyses of the associated cataclasites. Regional patterns of seismicity are consistent with structures oriented similarly to the Lhuentse fault having right-lateral transcurrent slip components, but we found no direct structural or geomorphic evidence of such kinematics. However, the results of zircon and (especially) apatite (U-Th)/He thermochronometry across the fault are consistent with ca. 500 m of normal-sense displacement over the past ca. 2 Ma. Dating of syn-deformational specular hematite precipitates in the fault zone by the (U-Th)/He method yielded results indicative of Quaternary deformation on the structure at least as recently as a few tens of thousands of years. We postulate that the Lhuentse fault, while having only minor displacement, is related to a larger-scale reorganization of the tectonic regime of the eastern Himalaya caused by southward expansion of the Himalayan orogenic wedge. Increasing complexity of the deformation field in what had been the hinterland of the Himalayan thrust belt in recent times should influence our assessments of seismic hazards in the region.

ACKNOWLEDGMENTS

This work was supported by a National Science Foundation Tectonics Program grant EAR 0708714 to K.V.H. and a joint Tectonics and Geomorphology and Landuse Dynamics Programs grant EAR 1049888 to K.XW. We thank Emmanuel Soignard of the LeRoy Eyring Center for Solid State Science at Arizona State University for his help with the Raman spectrometer. This work was greatly strengthened by the assistance and conversations with Frances Cooper (School of Earth Sciences, University of Bristol) and

Arjun Heimsath (School of Earth and Space Sciences, Arizona State University) both in the field and lab. Fieldwork would not have been possible without support of our friends and colleagues in Bhutan: Peldon Tshering (National Environment Commission), Ugyen Wanda (Department of Geology and Mines), Karma Choden and Ugyen Rinzen (Yangphel Adventure Travel). We thank Arlo Weil, Nadine McQuarrie and two anonymous reviewers for their helpful comments on an earlier version of this manuscript.

FIGURE CAPTIONS

Figure 2.1. Topographic swath profiles from A) central Nepal and B) central Bhutan. Black lines denote the mean elevation across a 30 km swath. The grey region represents 2 standard deviations of the mean. PT_1 – Physiographic Transition 1; PT_2 – Physiographic Transition 2; PT_3 – Physiographic Transition 3.

Figure 2.2. Generalized cross sections from central Nepal emphasizing the three models for producing increased uplift rates in the Higher Himalaya. In all frames a vertical grey box denotes the focus of uplift at the surface. A) Simplified cross section of the orogen depicting a simple ramp in the Himalayan Sole thrust (HST). B) The growth of a Lesser Himalayan duplex. C) Active deformation along a new or reactivated out-of-sequence thrust fault.

Figure 2.3. A) Digital elevation model of the Himalayan-Tibetan orogen. The N-S black and white dashed lines show the locations of the transects from Nepal and Bhutan shown in Figure 1. The white box denotes the location of B. The white oval highlights the

Shillong Plateau (SP). B) Map of major fault systems after Cooper et al. (2013). STF – South Tibetan fault; KT – Kakhtang thrust; MCT- Main Central thrust; MBT – Main Boundary thrust; MFT - Main Frontal thrust; YCS – Yadong Cross Structure; LF – Lhuentse fault; TSS – Tibetan Sedimentary Sequence; GHS – Greater Himalayan Sequence; LHS - Lesser Himalayan Sequence; DCK - Dang Chu killpe; PW – Paro Window; SK – Sakteng klippe. The smaller solid black box marks the location of Figure 5a. The larger dashed black box marks the location of Figure 2.4. Line A-A' marks the location of the cross section in Figure 8.

Figure 2.4. Morphometric maps calculated with ca. 30 m resolution elevation data. A) Local relief calculated over a 5 km diameter circular window. B) Hillslope gradient calculated using a 3 x 3 pixel window and then smoothed using a 1 km circular averaging window. C) Channel steepness values (see text for description) overlaying a shaded relief map. D) Elevation map. White points mark the location of bedrock thermometer samples. The trace of the Kakhtang thrust is shown in white, as mapped by Long et al. (2011a). The trace of the Lhuentse fault is shown as a black and white line. In all maps thick black lines mark the location of Physiographic Transition 2, and blue lines outline the perched low-relief landscapes of Grujic et al. (2006).

Figure 2.5. Satellite imagery and outcrop photos from the Lhuentse fault. A) DigitalGlobe panchromatic data from the WorldView 1 and 2 satellites (ca. 0.5 m resolution). The black box marks the location of E. Paired black lines mark the potential thickness of the Lhuentse fault zone. A white line shows the location of the Kakhtang

thrust. The black and white line is Physiographic Transition 2. Bedrock thermometric sample locations are shown as black points. A white point marks the location of the outcrop in D and E, and the location of the hydrothermal hematite sample. B) An equal area stereonet of the fabrics within the study area. Regional foliation of the Greater Himalayan Sequence calc-silicate gneiss is shown in grey. The cross cutting cleavage of the Lhuentse fault is shown in black. C) An outcrop photograph looking northeast (parallel to strike) within the Lhuentse fault zone. Notice the steeply dipping packages of fault gouge and ore deposits (exhibited by recessed portions of the outcrop) that cut the regional shallowly north dipping ductile fabric. A ca. 2 m tall KXW is present for scale. D) An illustrated and annotated interpretation of C. E) An expanded view of the satellite imagery. Note the ENE-WSW trending structural fabric, some of which is marked with black arrows for emphasis.

Figure 2.6. Plain polar light photomicrographs of a cataclasite within the Lhuentse fault. A) Fractured and microfaulted quartz grains surrounded by coarse hematite and resin filled expanded microfaults. B) Simplified interpretation of a. Quartz grains are outlined in black, filled with a light grey and marked with q. Dark grey lines denote major cracks. The interstitial material dominated by hematite is shown with an irregular stipple. Resin filled expanded microfaults (marked with r) are white. C) Multiple generations of quartz and hematite precipitation. Pods of fine-grained quartz and hematite precipitation are surrounded by younger growths of coarse-grained quartz and hematite. D) Simplified interpretation of C. Regions of fine and coarse-grained quartz and hematite are labeled with f and c, respectively. Both phases are perturbed by expanded microfaults, denoted

by hatching. We suggest these phases of hydrothermal mineralization were syn-deformational.

Figure 2.7. A) Bedrock cooling dates from (U-Th)/He thermochronometric systems. Data from the zircon (U-Th)/He system (ZHe) are filed black circles. Data from the apatite (U-Th)/He system (AHe) are filed grey circles. B) Modeled exhumation rates from apatite dates (see text for description). C) Elevation-corrected apatite cooling dates (see Data Repository for method and discussion). Sample locations have been projected onto a transect trending ca. 325º. All error bars are 95% confidence intervals. LF – Lhuentse fault.

Figure 2.8. Schematic cross section of central Bhutan showing the spatial relationships of the Kakhtang thrust – KT, Lhuentse fault – LF, Physiographic Transition 2 – PT_2 and Himalayan Sole thrust (HST). A cartoon of a duplex within the hanging wall of the HST shows the possible geometry and uplift vector that could have initiated the LF. Black arrows denoted active slip on faults. Grey arrows show relative motions on structures thought to be inactive. The position of this duplex is similar to that of Long et al. (2011b).

Figure 2.9. Seismic map of the Bhutanese hinterland. Filled circles are relocated events from Drukpa et al. (2006). Focal mechanisms are calculated from first motion data (larger spheres) and waveform modeling (smaller spheres; Drukpa et al., 2006). There is a strong strike-slip signal within Bhutan, but the dominant mode of motion is unclear. The black dashed line marks the location of the Lhuentse fault (LF).

REFERNCES

Andronicos, C. L., Velasco, A. A., & Hurtado Jr, J. M. (2007). Large-scale deformation in the India-Asia collision constrained by earthquakes and topography. *Terra Nova, 19*(2), 105-119.

Antolín, B., Schill, E., Grujic, D., Baule, S., Quidelleur, X., Appel, E., & Waldhör, M. (2012). EW extension and block rotation of the southeastern Tibet: Unravelling late deformation stages in the eastern Himalayas (NW Bhutan) by means of pyrrhotite remanences. *Journal of Structural Geology, 42*, 19-33.

Blythe, A. E., Burbank, D. W., Carter, A., Schmidt, K., & Putkonen, J. (2007). Plio-Quaternary exhumation history of the central Nepalese Himalaya: 1. Apatite and zircon fission track and apatite [U-Th]/He analyses. *Tectonics, 26*(3), TC3002.

Bollinger, L., Avouac, J. P., Beyssac, O., Catlos, E. J., Harrison, T. M., Grove, M., Goffé, B., & Sapkota, S. (2004). Thermal structure and exhumation history of the Lesser Himalaya in central Nepal. *Tectonics, 23*(5), TC5015.

Bollinger, L., Henry, P., & Avouac, J. P. (2006). Mountain building in the Nepal Himalaya: Thermal and kinematic model. *Earth and Planetary Science Letters, 244*(1), 58-71.

Brandon, M. T., Roden-Tice, M. K., & Garver, J. I. (1998). Late Cenozoic exhumation of the Cascadia accretionary wedge in the Olympic Mountains, northwest Washington State. *Geological Society of America Bulletin, 110*(8), 985-1009.

Brocklehurst, S. H., & Whipple, K. X. (2007). Response of glacial landscapes to spatial variations in rock uplift rate. *Journal of Geophysical Research: Earth Surface*

(2003–2012), 112(F2).

Brozović, N., Burbank, D. W., & Meigs, A. J. (1997). Climatic limits on landscape development in the northwestern Himalaya. *Science, 276*(5312), 571-574.

Cattin, R., Martelet, G., Henry, P., Avouac, J. P., Diament, M., & Shakya, T. R. (2001). Gravity anomalies, crustal structure and thermo-mechanical support of the Himalaya of central Nepal. *Geophysical Journal International, 147*(2), 381-392.

Clark, M. K., & Bilham, R. (2008). Miocene rise of the Shillong Plateau and the beginning of the end for the Eastern Himalaya. *Earth and Planetary Science Letters, 269*(3), 337-351.

Cooper, F. J., Hodges, K. V., & Adams, B. A. (2013). Metamorphic constraints on the character and displacement of the South Tibetan fault system, central Bhutanese Himalaya. *Lithosphere, 5*(1), 67-81. doi: 10.1130/l221.1

Cooper, F. J., van Soest, M. C., & Hodges, K. V. (2011). Detrital zircon and apatite (U-Th)/He geochronology of intercalated baked sediments: A new approach to dating young basalt flows. *Geochemistry Geophysics Geosystems, 12*(7), Q07003.

Das, J. D. (2004). Active tectonics of the Eastern Himalayan foothills region and adjoining Brahmaputra Basin based on satellite images. *International Journal of Remote Sensing, 25*(3), 549-557.

Davidson, C., Grujic, D. E., Hollister, L. S., & Schmid, S. M. (1997). Metamorphic reactions related to decompression and synkinematic intrusion of leucogranite, High Himalayan Crystallines, Bhutan. *Journal of Metamorphic*

Geology, 15(5), 593-612.

De, R., & Kayal, J. R. (2003). Seismotectonic model of the Sikkim Himalaya: Constraint from microearthquake surveys. *Bulletin of the Seismological Society of America, 93*(3), 1395-1400.

Derry, L. A., Evans, M. J., Darling, R., & France-Lanord, C. (2009). Hydrothermal heat flow near the Main Central thrust, central Nepal Himalaya. *Earth and Planetary Science Letters, 286*(1), 101-109.

Drukpa, D., Velasco, A. A., & Doser, D. I. (2006). Seismicity in the Kingdom of Bhutan (1937–2003): Evidence for crustal transcurrent deformation. *Journal of geophysical research, 111*(B6), B06301.

Duncan, C., Masek, J., & Fielding, E. (2003). How steep are the Himalaya? Characteristics and implications of along-strike topographic variations. *Geology, 31*(1), 75-78.

Farley, K. A. (2000). Helium diffusion from apatite: General behavior as illustrated by Durango fluorapatite. *Journal of Geophysical Research, 105*(B2), 2903-2914.

Gansser, A. (1983). *Geology of the Bhutan Himalaya*. Basel: Birkhauser Verlag.

Grujic, D., Casey, M., Davidson, C., Hollister, L. S., Kündig, R., Pavlis, T., & Schmid, S. (1996). Ductile extrusion of the Higher Himalayan Crystalline in Bhutan: evidence from quartz microfabrics. *Tectonophysics, 260*(1), 21-43.

Grujic, D., Hollister, L. S., & Parrish, R. R. (2002). Himalayan metamorphic sequence as an orogenic channel: insight from Bhutan. *Earth and Planetary Science Letters, 198*(1), 177-191.

Grujic, D., Warren, C. J., & Wooden, J. L. (2011). Rapid synconvergent exhumation of Miocene-aged lower orogenic crust in the eastern Himalaya. *Lithosphere, 3*(5), 346-366.

Hauck, M. L., Nelson, K. D., Brown, L. D., Zhao, W., & Ross, A. R. (1998). Crustal structure of the Himalayan orogen at~ 90 east longitude from Project INDEPTH deep reflection profiles. *Tectonics, 17*(4), 481-500.

Hazarika, P., Kumar, M. R., Srijayanthi, G., Raju, P. S., Rao, N. P., & Srinagesh, D. (2010). Transverse tectonics in the Sikkim Himalaya: evidence from seismicity and focal-mechanism Data. *Bulletin of the Seismological Society of America, 100*(4), 1816-1822.

Hodges, K. V., & Adams, B. A. (2013). The influence of middle and lower crustal flow on the landscape evolution of orogenic plateaus: Insights from the Himalaya and Tibet. In L. Owen (Ed.), *Treatise on Geomorphology* (Vol. 5). San Diego: Academic Press.

Hodges, K. V., Hurtado, J. M., & Whipple, K. X. (2001). Southward extrusion of Tibetan crust and its effect on Himalayan tectonics. *Tectonics, 20*(6), 799-809.

Hodges, K. V., Wobus, C., Ruhl, K., Schildgen, T., & Whipple, K. (2004). Quaternary deformation, river steepening, and heavy precipitation at the front of the Higher Himalayan ranges. *Earth and Planetary Science Letters, 220*(3), 379-389.

Jackson, M., & Bilham, R. (1994). Constraints on Himalayan deformation inferred from vertical velocity fields in Nepal and Tibet. *Journal of Geophysical Research, 99*(B7), 13897-13813,13912.

Kellett, D. A., Grujic, D., & Erdmann, S. (2009). Miocene structural reorganization of the South Tibetan detachment, eastern Himalaya: Implications for continental collision. *Lithosphere, 1*(5), 259-281.

Komori, J. (2008). Recent expansions of glacial lakes in the Bhutan Himalayas. *Quaternary International, 184*(1), 177-186.

Kula, J., & Baldwin, S. L. (2012). On hematite as a target for dating aqueous conditions on Mars. *Planetary and Space Science, 67*, 101-108.

Lave, J., & Avouac, J. P. (2001). Fluvial incision and tectonic uplift across the Himalayas of central Nepal. *Journal of Geophysical Research-Solid Earth, 106*(B11), 26561-26591. doi: 10.1029/2001jb000359

Long, S., McQuarrie, N., Tobgay, T., & Grujic, D. (2011). Geometry and crustal shortening of the Himalayan fold-thrust belt, eastern and central Bhutan. *Geological Society of America Bulletin, 123*(7-8), 1427-U1244. doi: 10.1130/b30203.1

Long, S., McQuarrie, N., Tobgay, T., Grujic, D., & Hollister, L. (2011). Geologic Map of Bhutan. *Journal of Maps*, 184-192. doi: 10.4113/jom.2011.1159

Long, S. P., McQuarrie, N., Tobgay, T., Coutand, I., Cooper, F. J., Reiners, P. W., Wartho, J. A., & Hodges, K. V. (2012). Variable shortening rates in the eastern Himalayan thrust belt, Bhutan: Insights from multiple thermochronologic and geochronologic data sets tied to kinematic reconstructions. *Tectonics, 31*, 23. doi: 10.1029/2012tc003155

Lyon-Caen, H., & Molnar, P. (1983). Constraints on the structure of the Himalaya from an analysis of gravity anomalies and a flexural model of the lithosphere.

Journal of Geophysical Research, 88(B10), 8171-8191.

Lyon-Caen, H., & Molnar, P. (1985). Gravity anomalies, flexure of the Indian plate, and the structure, support and evolution of the Himalaya and Ganga basin. *Tectonics, 4*(6), 513-538.

McQuarrie, N., Robinson, D., Long, S., Tobgay, T., Grujic, D., Gehrels, G., & Ducea, M. (2008). Preliminary stratigraphic and structural architecture of Bhutan: Implications for the along strike architecture of the Himalayan system. *Earth and Planetary Science Letters, 272*(1), 105-117.

Meigs, A., & Sauber, J. (2000). Southern Alaska as an example of the long-term consequences of mountain building under the influence of glaciers. *Quaternary Science Reviews, 19*(14), 1543-1562.

Nadin, E. S., & Martin, A. J. (2012). Apatite thermochronometry within a knickzone near the Higher Himalaya front, central Nepal: No resolvable fault motion in the past one million years. *Tectonics, 31*(2), TC2010.

Passchier, C. W., & Trouw, R. A. J. (2005). *Microtectonics*. Berlin: Springer.

Pearson, O. N., & DeCelles, P. G. (2005). Structural geology and regional tectonic significance of the Ramgarh thrust, Himalayan fold-thrust belt of Nepal. *Tectonics, 24*(4), TC4008.

Platt, J. (1986). Dynamics of orogenic wedges and the uplift of high-pressure metamorphic rocks. *Geological Society of America Bulletin, 97*(9), 1037-1053.

Rajendran, C. P., Rajendran, K., Duarah, B. P., Baruah, S., & Earnest, A. (2004). Interpreting the style of faulting and paleoseismicity associated with the 1897 Shillong, northeast India, earthquake: Implications for regional

tectonism. *Tectonics, 23*, TC4009.

Robert, X., Van Der Beek, P., Braun, J., Perry, C., & Mugnier, J. L. (2011). Control of detachment geometry on lateral variations in exhumation rates in the Himalaya: Insights from low-temperature thermochronology and numerical modeling. *Journal of Geophysical Research, 116*(B5), B05202.

Robinson, D. M., DeCelles, P. G., Garzione, C. N., Pearson, O. N., Harrison, T. M., & Catlos, E. J. (2003). Kinematic model for the Main Central thrust in Nepal. *Geology, 31*(4), 359-362.

Roure, F., Casero, P., & Vially, R. (1991). Growth processes and melange formation in the southern Apennines accretionary wedge. *Earth and Planetary Science Letters, 102*(3), 395-412.

Schildgen, T. F., Hodges, K. V., Whipple, K. X., Pringle, M. S., van Soest, M., & Cornell, K. (2009). Late Cenozoic structural and tectonic development of the western margin of the central Andean Plateau in southwest Peru. *Tectonics, 28*(4), TC4007.

Swapp, S. M., & Hollister, L. S. (1991). Inverted metamorphism within the Tibetan slab of Bhutan; evidence for a tectonically transported heat-source. *The Canadian Mineralogist, 29*(4), 1019-1041.

van Soest, M. C., Hodges, K. V., Wartho, J. A., Biren, M. B., Monteleone, B. D., Ramezani, J., Spray, J. G., & Thompson, L. M. (2011). (U-Th)/He dating of terrestrial impact structures: The Manicouagan example. *Geochemistry Geophysics Geosystems, 12*(null), Q0AA16.

Velasco, A. A., Gee, V. L., Rowe, C., Grujic, D., Hollister, L. S., Hernandez, D., D., Miller,

K. C., Tobgay, T., Fort, M., & Harder, S. (2007). Using small, temporary seismic networks for investigating tectonic deformation: Brittle deformation and evidence for strike-slip faulting in Bhutan. *Seismological Research Letters, 78*(4), 446-453.

Wendt, I., & Carl, C. (1991). The statistical distribution of the mean squared weighted deviation. *Chemical Geology: Isotope Geoscience section, 86*(4), 275-285.

Whipp Jr, D. M., Ehlers, T. A., Blythe, A. E., Huntington, K. W., Hodges, K. V., & Burbank, D. W. (2007). Plio-Quaternary exhumation history of the central Nepalese Himalaya: 2. Thermokinematic and thermochronometer age prediction model. *Tectonics, 26*(3), TC3003.

Whipp Jr, D. M., Ehlers, T. A., Braun, J., & Spath, C. D. (2009). Effects of exhumation kinematics and topographic evolution on detrital thermochronometer data. *Journal of Geophysical Research, 114*(F4), F04021.

Wobus, C., Heimsath, A., Whipple, K., & Hodges, K. (2005). Active out-of-sequence thrust faulting in the central Nepalese Himalaya. *Nature, 434*(7036), 1008-1011.

Wobus, C., Whipple, K. X., Kirby, E., Snyder, N., Johnson, J., Spyropolou, K., Crosby, B. & Sheehan, D. (2006). Tectonics from topography: Procedures, promise, and pitfalls. *Special papers-Geological Society of America, 398*, 55-74.

Wobus, C. W., Hodges, K. V., & Whipple, K. X. (2003). Has focused denudation sustained active thrusting at the Himalayan topographic front? *Geology, 31*(10), 861-864.

Wobus, C. W., Whipple, K. X., & Hodges, K. V. (2006). Neotectonics of the central Nepalese Himalaya: Constraints from geomorphology, detrital $^{40}Ar/^{39}Ar$ thermochronology, and thermal modeling. *Tectonics, 25*(4), TC4011.

Table 2.1. Apatite and zircon (U-Th)/He data.

Sample/ Aliquot	Latitude (°N)	Longitude (°E)	Elevation (m)	Lithology	^{4}He* (fmol)	1σ (fmol)	^{238}U* (fmol)	1σ (fmol)	^{232}Th* (fmol)	1σ (fmol)	Raw Date (Ma)	1σ (Ma)	F_{τ}†	Corr. Date§ (Ma)	2σ (Ma)	Mean Date (Ma)	2σ (Ma)
BT0962	*27.768389*	*91.133306*	*2360*	*paragnesis*													
a1					1.795	0.030	512.4	5.4	7.2	1.0	2.705	0.052	0.713	3.794	0.073		
a2					3.469	0.051	903.6	8.8	47.4	1.9	2.938	0.051	0.695	4.226	0.073	3.6	1.2
a4					0.702	0.017	331.9	4.8	6.30	0.83	1.631	0.045	0.688	2.371	0.066		
a5					0.984	0.019	204.7	2.6	3.3	2.1	3.709	0.087	0.652	5.69	0.13		
z1					326.2	3.7	75063	998	489	12	3.360	0.059	0.703	4.783	0.083		
z2					321.4	3.8	74937	1074	686	13	3.314	0.061	0.684	4.845	0.089	4.793	0.085
z3					437.5	4.3	98493	1511	2307	37	3.423	0.062	0.715	4.784	0.086		
z4					508.3	5.4	114116	1600	3991	73	3.423	0.059	0.718	4.766	0.083		
BT0963	*27.74961*	*91.13331*	*2309*	*paragneiss*													
a2					3.378	0.051	961.2	9.0	75.3	2.7	2.674	0.047	0.732	3.65	0.13		
a3					0.856	0.017	307.5	3.6	17.33	0.64	2.130	0.049	0.636	3.35	0.15	3.52	0.17
a4					1.102	0.020	364.4	4.0	11.9	1.3	2.325	0.048	0.662	3.51	0.15		
z1					387.6	4.6	95230	1393	2389	41	3.135	0.059	0.738	4.25	0.16		
z2					731.0	8.6	150091	2328	3435	58	3.752	0.074	0.750	5.00	0.20		
z3					175.7	2.1	46506	668	4016	57	2.869	0.053	0.774	3.71	0.14	4.41	0.54
z4					382.7	4.5	80167	1188	2956	39	3.666	0.070	0.746	4.91	0.19		
z5					1318	16	261581	3772	5987	96	3.881	0.073	0.794	4.89	0.18		
BT0964	*27.74289*	*91.13753*	*1882*	*orthogneiss*													
a1					0.548	0.016	284.6	3.2	14.3	1.6	1.475	0.048	0.670	2.20	0.14		
a2					0.507	0.011	224.9	3.0	6.8	1.3	1.736	0.045	0.595	2.92	0.15	2.78	0.41
a3					0.615	0.012	258.4	3.1	7.3	1.2	1.833	0.043	0.680	2.69	0.13		
a4					1.876	0.030	593.6	6.0	29.8	1.8	2.421	0.046	0.761	3.18	0.12		
z1					105.1	1.2	23545	324	2211	34	3.387	0.060	0.750	4.52	0.16		
z2					52.76	0.55	12598	175	553	19	3.213	0.056	0.723	4.44	0.16		
z3					58.13	0.66	15283	225	980	18	2.904	0.054	0.756	3.84	0.14	4.23	0.27
z4					150.6	1.7	35918	516	1615	29	3.216	0.059	0.764	4.21	0.16		
z5					40.48	0.47	9919	143	1252	26	3.073	0.056	0.729	4.21	0.15		
BT1022	*27.72302*	*91.14889*	*1335*	*orthogneiss*													
a2					0.731	0.022	185.8	4.1	11.7	1.5	3.00	0.11	0.653	4.60	0.34		
a3					0.606	0.021	255.5	3.2	14.1	1.3	1.815	0.067	0.703	2.58	0.19	3.25	0.81
a4					0.527	0.017	156.1	2.2	5.2	1.4	2.593	0.091	0.648	4.00	0.28		
a5					0.699	0.020	255.7	4.2	20.9	1.8	2.079	0.068	0.662	3.14	0.21		
BT0969	*27.67427*	*91.17685*	*1301*	*schist*													
a1					0.380	0.011	170.9	2.0	20.8	1.5	1.674	0.052	0.714	2.34	0.15		
a2					0.323	0.012	142.0	2.9	11.1	1.2	1.732	0.072	0.729	2.38	0.20	2.42	0.35
a3					0.172	0.011	41.4	1.2	70.8	2.0	2.31	0.16	0.678	3.41	0.46		
BT0970	*27.66740*	*91.18995*	*1254*	*orthogneiss*													
a1					0.426	0.014	144.9	6.1	15.0	2.0	2.22	0.12	0.757	2.94	0.31		
a2					0.311	0.010	142.7	6.6	17.9	1.4	1.642	0.091	0.765	2.15	0.24	2.41	0.47
a3					0.278	0.012	117.6	6.0	17.2	1.5	1.78	0.12	0.758	2.34	0.31		

*Absolute measured abundances. ^{4}He measurement used to calculate the "raw date," which was not corrected for the effects of ^{4}He loss due to alpha particle recoil. †The mean Fτ correction calculated following Farley et al. (1996) for apatite and Hourigan et al. (2005) for zircon (see Table DR1 for crystal dimensions). §The Fτ corrected date of the crystal. This age was recalculated with a Fτ corrected 4He measurement (see Table DR1).

Table 2.2. (U-Th)/He data from 4 pieces of the hematite within the Lhuentse fault.

Sample/ Aliquot	Latitude (°N)	Longitude (°E)	Elevation (m)	Lithology	^{4}He (fmol)	1σ (fmol)	^{238}U (fmol)	1σ (fmol)	^{232}Th (fmol)	1σ (fmol)	Date (ka)	2σ (ka)
BTORE	*27.71540*	*91.15156*	*1253*	*hydrothermal hematite*								
h7					0.229	0.013	1678	16	4094	44	67.6	7.7
h8					0.397	0.025	1563	17	6362	86	102	13
h9					0.348	0.020	558.4	9.1	6760	111	128	15
h10					0.364	0.021	1678	17	6107	59	91	10

Figure 2.1

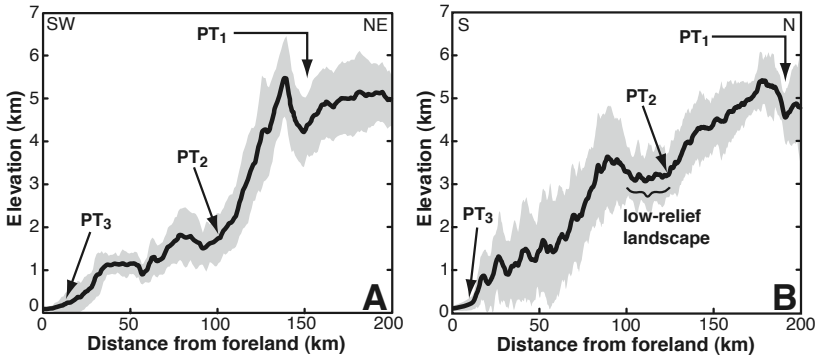
SW
NE
PT1
PT2
PT3
A
Elevation (km)
Distance from foreland (km)
S
N
PT1
PT2
PT3
low-relief
landscape
B
Elevation (km)
Distance from foreland (km)

Figure 2.2

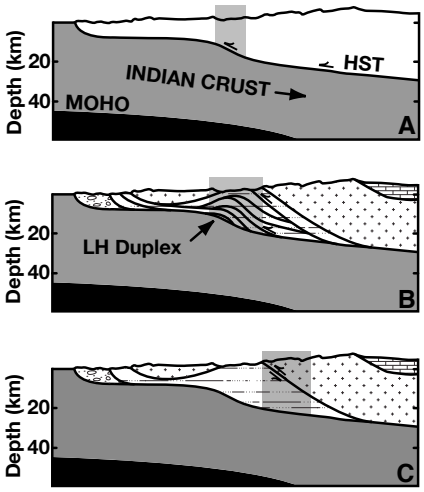
Depth (km)
20
40
INDIAN CRUST
HST
MOHO
A
Depth (km)
20
40
LH Duplex
B
Depth (km)
20
40
C

Figure 2.3

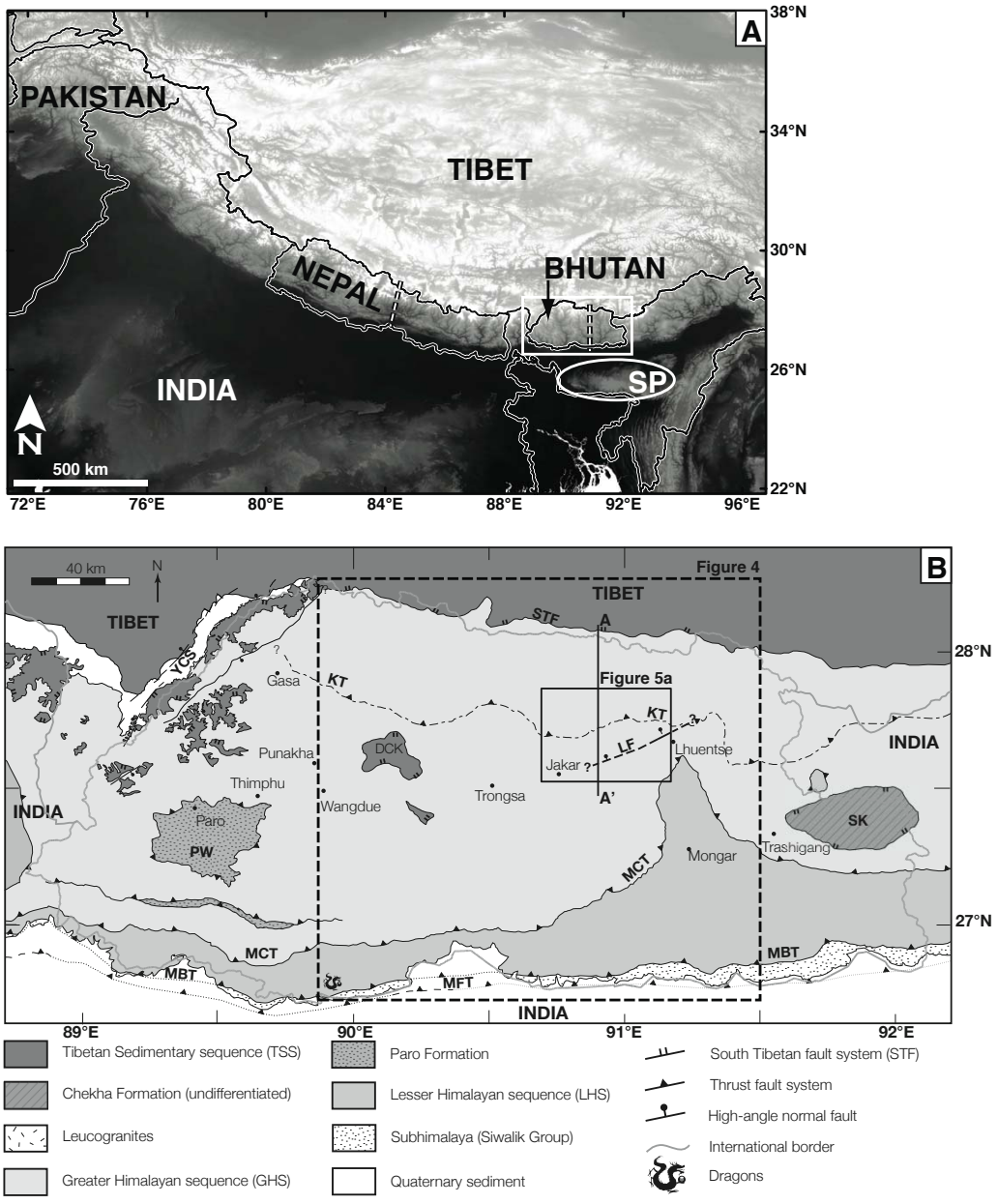
A
PAKISTAN
TIBET
NEPAL
BHUTAN
INDIA
SP
N
500 km
38°N
34°N
30°N
26°N
22°N
72°E
76°E
80°E
84°E
88°E
92°E
96°E
B
40 km
N
Figure 4
TIBET
STF
A
28°N
Gasa
KT
Figure 5a
Punakha
DCK
Jakar
LF
Lhuentse
INDIA
Thimphu
Wangdue
Trongsa
A'
IND!A
Paro
PW
SK
Trashigang
Mongar
MCT
27°N
MBT
MFT
89°E
90°E
91°E
92°E
Tibetan Sedimentary sequence (TSS)
Chekha Formation (undifferentiated)
Leucogranites
Greater Himalayan sequence (GHS)
Paro Formation
Lesser Himalayan sequence (LHS)
Subhimalaya (Siwalik Group)
Quaternary sediment
South Tibetan fault system (STF)
Thrust fault system
High-angle normal fault
International border
Dragons

Figure 2.4

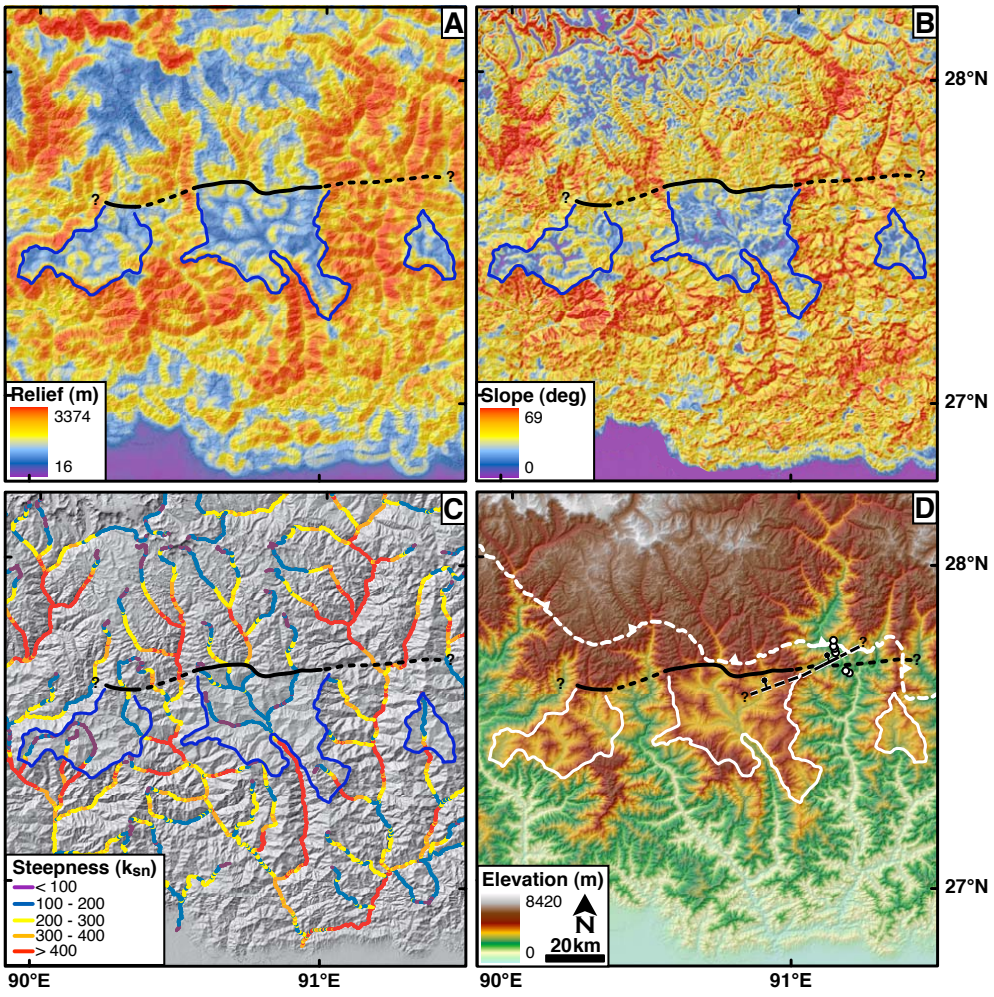
A
B
C
D
Relief (m)
3374
16
Slope (deg)
69
0
Steepness (ksn)
< 100
100 - 200
200 - 300
300 - 400
> 400
Elevation (m)
8420
0
N
20km
28°N
27°N
90°E
91°E

Figure 2.5

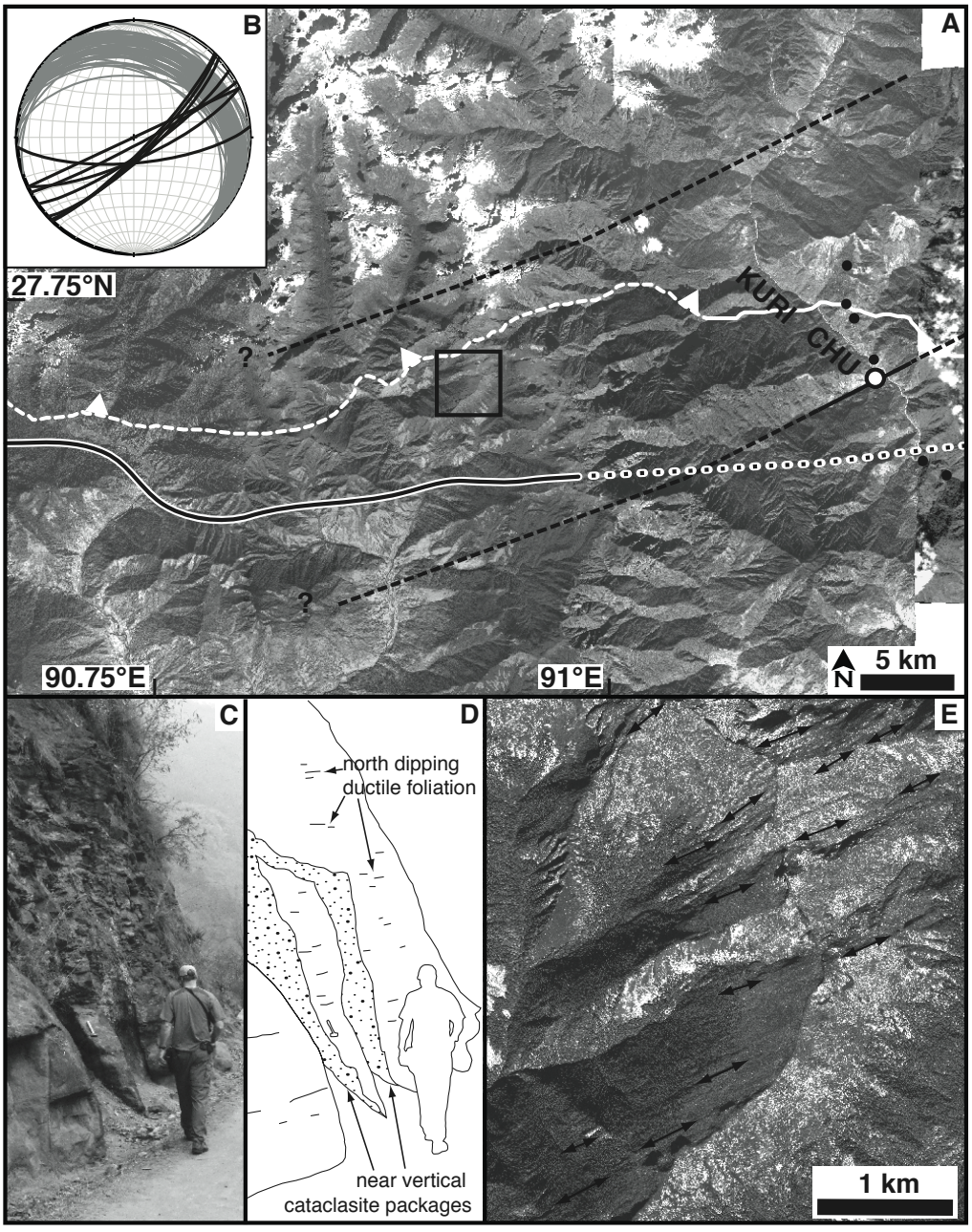
A
B
27.75°N
90.75°E
91°E
KURI CHU
?
?
5 km
N
C
D
north dipping
ductile foliation
near vertical
cataclasite packages
E
1 km

Figure 2.6

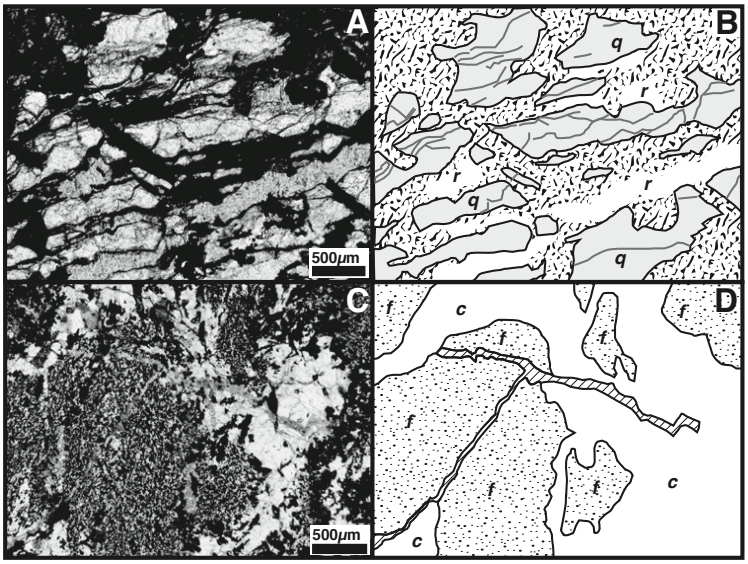

Figure 2.7

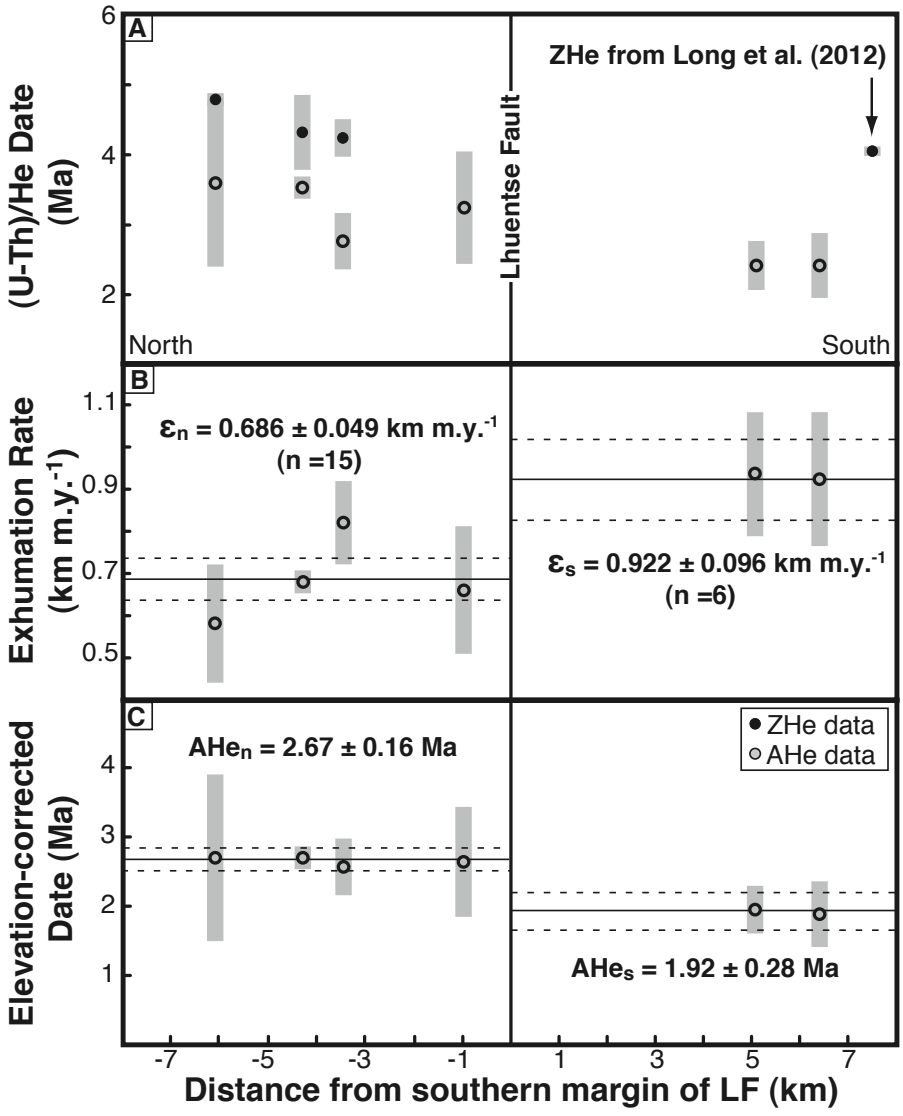
A
B
C
(U-Th)/He Date (Ma)
Exhumation Rate (km m.y.-1)
Elevation-corrected Date (Ma)
Lhuentse Fault
North
South
ZHe from Long et al. (2012)
εn = 0.686 ± 0.049 km m.y.-1
(n =15)
εs = 0.922 ± 0.096 km m.y.-1
(n =6)
AHen = 2.67 ± 0.16 Ma
AHes = 1.92 ± 0.28 Ma
ZHe data
AHe data
Distance from southern margin of LF (km)

Figure 2.8

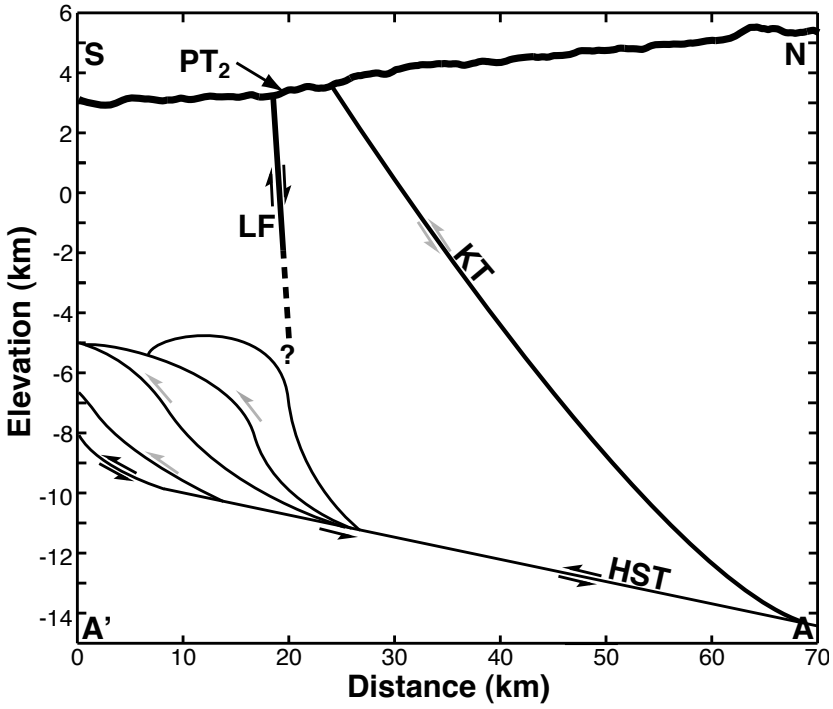
S
N
PT2
LF
?
KT
HST
A'
A
Elevation (km)
Distance (km)
6
4
2
0
-2
-4
-6
-8
-10
-12
-14
0
10
20
30
40
50
60
70

Figure 2.9

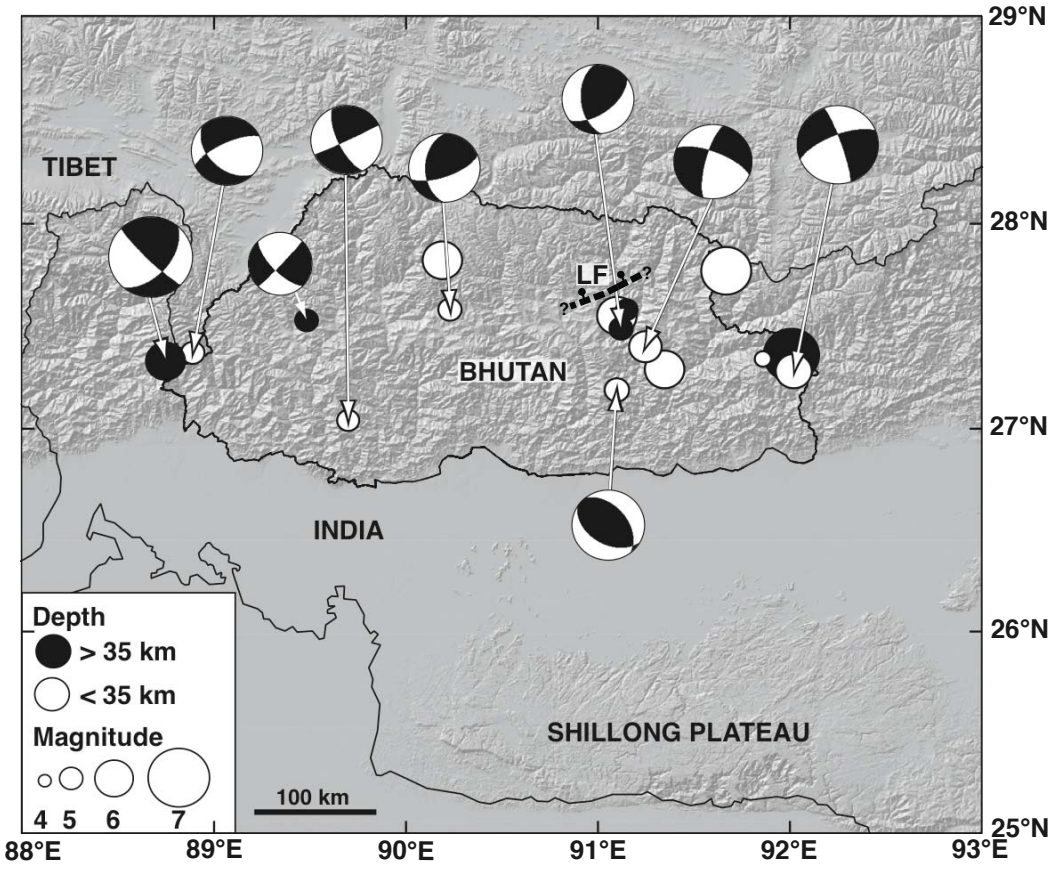
TIBET
BHUTAN
INDIA
SHILLONG PLATEAU
LF
?
?
Depth
> 35 km
< 35 km
Magnitude
4 5 6 7
100 km
29°N
28°N
27°N
26°N
25°N
88°E
89°E
90°E
91°E
92°E
93°E

CHAPTER 3

TECTONIC COUPLING OF THE EASTERN HIMALAYA AND SHILLONG PLATEAU

ABSTRACT

The eastern quarter of the Himalayan range appears to have a very different tectonic regime and topographic character than the rest of the range. The initiation of shortening structures associated with the Shillong Plateau to the south has greatly widened the zone of convergence between India and Eurasia, and decreased the rate of deformation in the Himalaya proper. New multi-chronometer (apatite (U-Th)/He; zircon (U-Th)/He; muscovite $^{40}Ar/^{39}Ar$) bedrock thermochronometric data from Bhutan have helped constrain the timing, magnitude, and the spatial distribution of these effects.

We compared observed cooling ages from each sample with synthetic cooling ages predicted by a 1D thermal-kinematic model, sampling across a wide range of possible erosion rate histories. We found that the data are most consistent with a protracted, roughly monotonic decrease in long-term erosion rate from the Late Miocene to the present. This pattern, found throughout Bhutan, suggests a decrease in fault slip rates and rock uplift rates subsequent to activation of Shillong Plateau structures in the Middle Miocene. While our lowest-temperature thermochronometers typically yielded Pliocene dates, the geomorphology of Bhutan suggests significant Pleistocene changes in the tectonic pattern of deformation. In particular, perched low-relief fluvial landscapes in the hinterland of the range represent surface uplift likely due to a recent increase in rock uplift rates. Our

findings paint a coherent picture of significant Miocene-Pliocene structural and thermal adjustment to decreased fault slip rates after the development of the Shillong Plateau, followed by a Pleistocene-Recent rejuvenation of deformational activity in both the foreland and the hinterland of the Bhutan Himalaya.

INTRODUCTION

The range-scale topographic expression of a convergent mountain belt is dictated by the contraction rate across the range, via an accretionary flux, and the climate- and lithology-modulated erosional efficiency of the range (e.g. Willett et al. 2001, Whipple and Meade, 2004; 2006). Changes in either, or both, of these forcing factors can cause the mountain range to reorganize internally (structurally), and change its external form to adjust toward a new stress-balanced topographic steady-state (Davis et al., 1983). The response time of an orogen to reach a new steady-state – if such a state can be achieved and maintained – depends on many factors, but is generally argued to be on the order of a few million years for active ranges such as the Himalaya (e.g., Whipple and Meade, 2006).

Of particular interest here is the striking difference in tectonic style observed in the eastern Himalaya as compared to better-studied regions farther west (Figure 3.1). Geodetic, geophysical, geochemical, and geological investigations have suggested that the Eastern Himalaya are undergoing deformation that has a significant component of transverse motion – broadly parallel to the Himalayan arc – in addition to the canonical N-S shortening component emphasized in most conceptualizations of Himalayan orogenesis (Andronicos et al., 2007; Styron et al., 2011; De Sarkar et al., 2013). In conjunction with this transition, the zone over which Indio-Eurasia convergence is distributed widens abruptly to the east of 90˚E by ca. 300% (Seeber and Armbruster, 1981). Transverse river systems within the Bhutan Himalaya, unlike those farther west, have significant convex, slope-break knickpoints that give the appearance of landscapes adjusting to an acceleration in

the rate of rock uplift relative to baselevel (Duncan et al., 2003; Baillie and Norbu, 2004; Grujic et al., 2006; Adams et al., 2013). One explanation that has been offered for these west-to-east changes in the character of the orogen has been the rise of a large uplifted region south of the Eastern Himalaya, the Shillong Plateau (Figure 3.1). For example, Clark and Bilham (2008) suggested that the development of structures associated with Shillong Plateau uplift could be linked with a fundamental change in the partitioning of convergence between India and Eurasia within the Himalayan-Tibetan orogenic system. From their analysis of Shillong Plateau structures, they argued that this structural reorganization led to spatial and temporal changes in shortening in the Eastern Himalaya, and changed the style of deformation in the Tibetan Plateau. In short, the Shillong Plateau may have led to the "dismemberment" of the Eastern Himalaya, and perhaps initiated the demise of this portion of the range due to a decrease in shortening rates within the range (Clark and Bilham, 2008). However, to date it is still unclear exactly how the emergence of the Shillong Plateau impacted deformational and exhumational patterns and rates in the Bhutan Himalaya.

The trade off between deformation along the structures of the Shillong Plateau and Himalaya should lead to detectable changes in the fault slip rates and topography of the Eastern Himalaya. The conversion of plate convergence into rock uplift, and therefore erosion, allowed us to detect changes in structural architecture or displacement rates via cooling histories of rocks (e.g. Wobus et al., 2003; 2005; 2006; Bollinger et al., 2004; 2006; McQuarrie et al., 2014; Long et al., 2012). In this paper we have utilized thermochronometric data from the Bhutan Himalaya to

analyze temporal and spatial variation in erosion rates. We focused our sampling strategy around several perched, low-relief surfaces that are thought to have been uplifted by a recent change in the tectonic or climate forcing of the Eastern Himalaya (Duncan et al., 2003; Baillie and Norbu, 2004; Grujic et al., 2006; Adams et al., 2013). We have calculated new apatite and zircon (U-Th)/He, and muscovite $^{40}Ar/^{39}Ar$ thermochronometric cooling ages from samples collected both on these perched, low-relief landscapes and in the rugged canyons that dissect them. These multi-chronometer data have permitted the exploration of spatial and temporal variations in plausible erosion rates using a Monte Carlo approach developed by Theide and Ehlers (2013). To broaden our region of analysis, we performed the same analysis on previously published thermochronologic data from eastern Bhutan (Long et al., 2012; Adams et al. (2013).

BACKGROUND

Changes in deformation patterns

While the age of collision between India and Eurasia is still debated (e.g., Yin and Harrison, 2000; Aitchison et al., 2007), it is commonly accepted that the major contractional structures south of the Himalayan crest have been active since the Early Miocene (e.g. Hodges, 2000), suggesting the range has developed to a mature state. The regional geology of the south flank of the Himalaya can be simplified into three tectonostratigraphic units that increase in metamorphic grade northward, and are divided by three south-vergent thrust systems. The Main Frontal thrust system carries essentially unmetamorphosed rocks of the Sub-Himalayan foreland in its

hanging wall over Gangetic basin units in its footwall. Moving up section, and northward, are the Main Boundary and Main Central thrust systems (Figure 3.2). The Main Boundary thrust sheet contains predominantly metasedimentary rocks of the Lesser Himalayan sequence. The metamorphic grade of these rocks increases northward toward to lower amphibolite facies near the trace of the overlying Main Central thrust sheet. The hanging wall of that structure contains higher-grade (amphibolite to granulite facies) ortho- and paragneisses of the Greater Himalayan sequence. Ages of initiation of the Main Central, Main Boundary, and Main Frontal thrust systems are thought to be ca. 23, 10, and 5 Ma, respectively (e.g. Hodges et al., 2000; Long et al., 2012).

South of the eastern Himalaya, a number of structures related to the emergence of the Shillong Plateau add complexity to the regional deformational pattern. Many of these structures are covered by young sediments of the Ganges and Brahmaputra river systems and their precise geometries and kinematics are not well known. A particularly significant deformational feature is the north-dipping Dauki thrust system, the trace of which marks the southern margin of the Shillong Plateau (Figure 3.1; Biswas and Grasemann, 2005). The system of faults associated with Shillong Plateau uplift broadens and extends northeastwards from the western edge of the plateau (ca. 90˚E) to the Indo-Burman ranges (Seeber and Armbruster, 1981; Biswas et al., 2007; Clark and Bilham, 2008; Banerjee et al., 2008). Previous estimates of the timing of exhumation of the Shillong Plateau have ranged from about 8 to about 15 Ma (Biswas et al., 2007; Clark and Bilham, 2008). However, only a million years separate the mean apatite fission track and (U-Th)/He dates for

samples collected near the southern edge of the plateau – 10.7 vs. 9.7 Ma (Biswas et al., 2007). Given roughly 40˚C difference between the nominal bulk closure temperatures of the two chronometers (Hodges, 2014), these data suggest that the Dauki thrust system hanging wall experienced rapid cooling over the 10.7-9.7 Ma interval. This implies that Shillong Plateau deformation was well underway by 10.7 Ma and most likely initiated in Middle Miocene time. The observation that the apatite (U-Th)/He dates are Late Miocene further suggests a dramatic decrease in Dauki hanging wall exhumation rates after 9.7 Ma. Nevertheless, global positioning satellite constraints on the regional modern velocity fields suggest that contractional structures south of the Main Frontal thrust trace may accommodate ca. 6 mm $y.^{-1}$ of continental convergence in the eastern portions of the orogenic system (Paul et al., 2001; Banerjee et al., 2008). This rate is also in agreement with leveling data presented by Bilham and England (2001). Geodetic data from the eastern and central Himalaya suggest no significant difference in convergence velocity across the Himalayan arc, such that the addition of convergence across structures of the Shillong Plateau and within the Himalayan range imply higher net convergence rates east of 90˚E (e.g. Styron et al., 2011).

Contraction rates across the Shillong Plateau estimated on geological time scales using thermochronometric techniques have ranged from 0.65 – 2.3 mm $y.^{-1}$ since the Late Miocene (Biswas et al., 2007; Clark and Bilham, 2008) – a minimum of a factor of 3 less that the geodetic rate. The discrepancy between these long-term rates and the modern rates from geodetic analysis may be a function of assumed fault geometries within the Indian plate (Clark and Bilham, 2008), or it may imply a

recent acceleration in slip on Shillong Plateau structures (Banerjee et al., 2008). Additionally, the work of Long et al. (2012) have shown spatially and temporally variable contraction rates across the Himalaya within Bhutan, which they suggested may be the result of temporal variability of slip on the Shillong Plateau structures themselves. Significantly, at longitudes east of the western edge of the Shillong Plateau, seismicity in the Himalaya implies a predominantly transpressive modern deformation field (Drukpa et al., 2006; Velasco et al., 2007; Baruah et al., 2013; De Sarkar et al., 2013).

A recent study in Bhutan offered new insight into the thrusting velocities and geometries of the Himalayan basal decollement (Coutand et al., 2014). For this study the authors implemented a 2D thermal-kinematic model to invert a large suite of thermochronometric data to find best-fit parameters of overthrusting characteristics in western and eastern Bhutan. The 2D model results suggested that spatial patterns in cooling rates are well explained by the distribution of ramps and flats within the basal decollement, and the velocity history of the overthrusting plate. However, Coutand et al. (2014) concluded that fitting cooling age data in eastern Bhutan required a two-part velocity history, where the overthrusting velocity is nearly halved around 6 Ma, and attributed this slow down to shortening accommodated by the Shillong Plateau. The data from western Bhutan was well described by a constant overthrusting velocity since 10 Ma (Coutand et al., 2014). This finding is quite provocative, as it requires a significant Himalayan structure that allows for eastern Bhutan to deform independently of western Bhutan.

Changes in the topography

Digital topographic analysis and field studies have illuminated low-relief landscapes that are perched above deeply incised canyons and widespread throughout the middle latitudes of Bhutan (Duncan et al., 2003, Baillie and Norbu, 2004; Grujic et al., 2006; Adams et al., 2013). We have used the topographic metrics (hillslope angle, local relief, channel steepness, mean elevation) and methods of Adams et al. (2013) to analyze all of Bhutan. These analyses revealed that perched fluvial low-relief landscapes with similar characteristics and occurring at similar elevations, extend into western Bhutan (Figure 3.2). Of these analyses, we found the perturbed nature of the longitudinal channel profiles of rivers to be the most diagnostic observation of the location of these low-relief landscapes (Figure 3.3). Downstream of the low-relief landscapes, mean elevations quickly fall and local-relief increases where landscapes are responding to the northward propagation of a convex slope-break knickpoint (Figure 3.3; Baillie and Norbu, 2004; Grujic et al., 2006; Adams et al., 2013). These knickpoints, which separate terrains of varying channel steepness, suggest there has been significant surface uplift (e.g. Whipple and Tucker, 1999; Crosby et al., 2007) across the length of the Bhutan Himalaya, ca. 89°E – 91.5°E.

As laid out by Grujic et al. (2006), the uplift of these landscapes can be explained either tectonically, by increasing rock uplift rates, or climatically, by decreasing the erosivity of river systems in the Shillong Plateau rain shadow. Erosion response to changes in tectonic rock uplift and climate-moderated erosivity of rugged topography as laid out below has been explored in physical and numerical

models (e.g. Bonnet and Crave, 2003; Whipple and Meade, 2006). These models predicted that a sudden increase in rock uplift rate in the foreland would create a wave of incision as the lower river reaches steepened to increase local erosion rates. The upper reaches of the landscape would be uplifted as rock uplift rate was increased, and erosion rates did changed above the knickpoint. Eventually, the entire landscape would erode at the new rate set by the new rock uplift rate, once the knickpoint passed through the fluvial system. The response to a decrease in climate-moderated erosivity would have a much different effect on the erosion rate history. Reduction of erosivity would result in a sudden decrease in erosion rate across the landscape. A wave of incision would propagate upstream as lower river reaches steepened to continue eroding at a rate equal to the rock uplift rate, as discharge decreased.Therefore, landscape erosion rates would only deviate from the constant background rock uplift rate until the knickpoint moved through the fluvial system. Much like the tectonic scenario above, a decrease in erosivity would cause surface uplift in the upper reaches of the landscape as the rock uplift rate would remain high, but the erosion rate would have decreased. These two hypotheses make very different predictions for the long-term erosion rate histories throughout the Bhutan Himalaya. The tectonic hypothesis would require that erosion rates increased synchronously with increased rock uplift rates. Alternatively, the climate hypothesis would require a sharp decrease in erosion rates at the time that precipitation decreased, *and* that local erosion rates later rebounded to their previous rates as the knickpoint passed through the system (e.g. Bonnet and Crave, 2003; Whipple and Meade, 2006).

Previous studies utilized a regionally expansive apatite fission track cooling age dataset to constrain regional long-term erosion rates and mechanism of surface uplift in Bhutan (Grujic et al., 2006). Grujic et al. (2006) interpreted from these data that erosion rates decreased ca. 5.9 Ma, from 1800 – 1000 to 850 – 500 m m.y.$^{-1}$. They further pointed out that the apatite fission track cooling ages were older than what would be predicted by an erosion rate of 1800 – 1000 m m.y.$^{-1}$ since ca. 5.9 Ma, implying a long-term decrease was required. The other option, a reduction in erosion rates caused by a slowing of uplift rates as the Shillong Plateau structures were activated, could not explain the surface uplift noted in Bhutan. Therefore, Grujic et al. (2006) concluded that the climate scenario was the most likely for producing the enigmatic low-relief landscapes of Bhutan. Subsequently, the formation of Shillong Plateau as a topographic barrier was proposed post 3-4 Ma by Biswas et al. (2007) based on the cessation of marine facies deposition on the foothills of the Shillong Plateau (Worm et al., 1998).

As mentioned above, Coutand et al. (2014) concluded that the erosion rate patterns in Bhutan are mostly the result of décollement geometries and overthrusting velocities. Furthermore, they were not able to detect any clear signal of climate change driven erosion in the core of the range, but instead suggested a strong erosion rate increase at the front of the range where rainfall rates are highest (Coutand et al., 2014). However, it is worth nothing that neither of the above thermochronometric studies have the temporal resolution to discern between the two models of surface uplift and erosion rate response.

Furthermore, our geomorphic observations of transient landscapes across the entire length of Bhutan (ca. 89°E – 91.5°E) call into question the hypothesis that Late Miocene – Early Pliocene climate change, associated with the formation of the Shillong Plateau rainshadow, triggered surface uplift in the Bhutan hinterland. Previous studies have defined the Shillong Plateau rain shadow as a position in the Himalaya range at the same longitude where moisture is intercepted by the Shillong Plateau (Bookhagen et al., 2005; Grujic et al., 2006; Adlakha et al., 2013). However, the footprint of the rain shadow only extends from the Indo-Burman ranges to ca 90°E, in central Bhutan (Bookhagen et al., 2005; Grujic et al., 2006; Adlakha et al., 2013). The clear existence of transient landscapes in western Bhutan suggests that the hypothesis that surface uplift was driven by the rain shadow is tenuous.

THERMOCHRONOMETRY

As a framework for understanding the spatial and temporal distributions of rock uplift rates in the Bhutan Himalaya, we constrained long-term erosion rates using thermochronometric data. In the analysis presented here, we combined previously published data from within the Kuri Chu valley in eastern Bhutan (Long et al., 2012; Adams et al., 2013) with new data from western and central Bhutan. For ease of discussion we divided Bhutan into four regions (Regions A-D) based on the locations of samples that we expected to behave similarly because of proximity (see Figure 3.4). We calculated new $^{40}Ar/^{39}Ar$ muscovite (MsAr) and biotite (BtAr), as well as new (U-Th)/He zircon (ZrnHe) and apatite (ApHe) cooling ages for seventeen bedrock samples (Figure 3.4). Samples were collected on top of elevated

low-relief landscapes, on the flanks of these landscapes, and in deep canyons that do not exhibit transient geomorphic signatures (e.g. in the Kuri Chu valley). Nearly all of our samples (15), were located in the higher-grade Greater Himalayan sequence rocks, the remainder are located in the Lesser Himalayan sequence of rocks. Our sample locations were all located in the middle latitudes of the Himalaya, spanning a geographic distance of ca. 160 km across Bhutan. The elevation difference between our highest and lowest samples is ca. 1700 m.

(U-Th)/He bedrock cooling ages from apatite and zircon

Single mineral crystals were handpicked from the 80-120 μm size fractions and loaded into niobium tubes for helium isotope-dilution analysis using a diode laser on an ASI Alphachron instrument in the Noble Gas, Geochronology, and Geochemistry Laboratories at Arizona State University. Degassed zircon crystals were dissolved in Parr digestion vessels with nitric and hydrofluoric acids. Apatites were dissolved in nitric acid in an ultrasonic bath. Uranium and thorium concentrations in the solutions were measured by isotope-dilution, inductively coupled, plasma-source, mass spectrometer in the W. M. Keck Foundation Laboratory for Environmental Geochemistry at Arizona State University. More details on our analytical protocols may be found in van Soest et al. (2011). (U-Th)/He dates were calculated following the method of Meesters and Dunai (2005).

Cooling ages for each bedrock sample calculated as a weighted mean of replicate single grain results. As is frequently the case with helium thermochronometric data, replicate single crystal analyses from individual bedrock

samples frequently exhibited scatter in excess of that anticipated on the basis of formally calculated analytical uncertainties. We dealt with this excess scatter in two ways. First, we employed the Hampel identifier method (reviewed by Pearson, 2011) to discard outliers with dates more than four mean average deviations from the median. We then calculated an uncertainty weighted mean, its standard deviation, and mean square of weighted deviates (MSWD) for all of the remaining dates for the sample (three or more crystals in each case). If the MSWD for the weighted-mean was found to be more than two standard deviations higher than its expected value of 1.0 (Wendt and Carl, 1991), we magnified the reported error on the weighted mean by a factor of $(MSWD)^{0.5}$. Mean dates and calculated uncertainties (at the ca. 95% confidence interval) are reported in Table 1. Raw aliquot data can be found in Appendix B.

New ZrnHe mean cooling ages from twelve Greater Himalayan sequence and two Lesser Himalayan sequence bedrock samples ranged from ca. 8 – 4.5 Ma. New ApHe mean cooling ages from eleven Greater Himalayan sequence and two Lesser Himalayan sequence bedrock samples ranged from ca. 6.5 – 4.5 Ma. We did not observe any clear spatial trend in our data, nor a strong positive correlation between age and elevation in most regions. Furthermore, there was no discernable trend in cooling ages in relation to lithology or stratigraphic/structural position.

$^{40}Ar/^{39}Ar$ bedrock cooling ages from muscovite and biotite

Muscovite and biotite crystals were handpicked from the 250-1000 μm size fractions and irradiated for 0.20 – 0.67 hours in the medium flux-positions

McMaster University nuclear reactor along with HD-B1 biotite as a neutron fluence monitor. Assuming an age of 24.18 ± 0.18 Ma (2σ) for the monitor (Swartz and Trieloff, 2007), we calculated J values ranging from 1.89×10^{-4} – 5.77×10^{-4} for these samples. A variety of salts were also irradiated along with the samples to estimate the production rate of interfering isotopes. Individual age standards were fused for J-value determinations and salt corrections, while multigrain aliquots of unknown grains were incrementally heated using a 60 W IPG Photonics infrared (970 nm) diode laser operating at successively higher power levels until fusion was achieved. The released gases were purified using one hot and one cold SAES NP10 getter, and analyzed via a Faraday detector or an ion counting multiplier (depending on signal size) on a Nu Instruments *Noblesse* a sector-field, multi-collector mass spectrometer. Detector intercalibration was determined via $^{40}Ar/^{36}Ar$ measurements of air standards on each detector. Cooling ages were calculated using Isoplot 3.75 (Table 2; Ludwig, 2012). Most muscovite incremental heating experiments resulted in plateau ages as traditionally defined (McDougall and Harrison, 1999), or – in one instance – a release behaviour that was easily interpreted using the inverse isotope correlation method. Unfortunately, many biotites exhibited signs of contamination by excess ^{40}Ar and we were generally unable to resolve the trapped $^{40}Ar/^{36}Ar$ ratio using the inverse isochron method. Plateau and inverse isochron dates, with uncertainties reported at the ca. 95% confidence level, are reported in Table 2; raw data and plots of release spectra and inverse isochron diagrams may be found in Appendix B.

Fifteen Greater Himalayan sequence and two Lesser Himalayan sequence bedrock samples yielded MsAr plateau ages – or an inverse isochron age in the case of BT0850 – ranging from ca. 12.3 – 7.9 Ma. Biotite spectra for six Greater Himalayan sequence and two Lesser Himalayan sequence bedrock samples were far more complex, and often yielded apparent ages older than muscovite from the same rock sample, something we did not expect based on the known diffusion kinematics of Ar in these minerals (Grove and Harrison, 1996; Harrison et al., 2009). We attributed this behavior to a high degree of contamination of biotites with excess Ar, and we were unable to successfully resolve what we would regard as meaningful $^{40}Ar/^{39}Ar$ ages from these samples. While the BtAr data are presented for the sake of thoroughness, we used only MsAr dates, in conjunction with ZrnHe and ApHe dates, for the erosion rate modeling exercise described in the next section.

THERMAL-KINEMATIC MODELING

Model formulation

Previous research has shown that the primary path of heat flow is in a direction perpendicular to the surface of Earth, even in active orogens (e.g. Braun et al., 2006; Whipp et al., 2007). Because of this, 1D models of erosion effectively capture the competition of advection and conduction within the crust. Moreover, 1D models alleviate the need to address temporal variation in fault activity, define fault geometries, or assume steady-state topography, all parameters that have been demonstrated to be in flux throughout the evolution of the Bhutan Himalaya (e.g. Grujic et al., 2006; Long et al., 2012; Adams et al., 2013; McQuarrie et al., 2014;

Coutand et al., 2014). The fast nature of a 1D model allows for a large number (hundreds of thousands) of erosion histories to be tested, providing a more thorough exploration of parameter space. Furthermore, as demonstrated in subsequent sections, the results of our 1D model are comparable to the results of more complex 2D models (e.g. Coutand et al., 2014). For this reason we elected to use a 1D thermal-kinematic model based on the transient solution to the advective-conductive heat transfer equation. To best determine the erosion histories of our samples we adopted the protocol of Thiede and Ehlers (2013), which employs a modified version of the Pecube finite element scheme (Braun, 2003; Whipp et al., 2007).

We used Pecube as a forward model to predict MsAr, ZrnHe, ApHe, and ApFT (for the samples of Long et al., 2012) cooling ages from 500,000 randomly selected erosion rate histories. Modeled erosion rate histories were determined by randomly selecting a rate between 0 and 4 km $m.y.^{-1}$, assuming erosion rates did not exceed 4 km $m.y.^{-1}$ in the past. Our models utilized implicit time steps where erosion rates changed at time steps, but not within them. We initiated the model at 23 Ma assuming that regional erosion has been active since the initiation of the Main Central thrust system ca. 23 Ma (Chambers et al., 2011, Tobgay et al., 2012; Stuwe and Foster, 2001; Daniel et al., 2003). We allowed for over 10 m.y. of 'spin-up' time over the course of several time steps (three steps on average) before our oldest cooling age. Because our ApHe and ZrnHe cooling ages were in some samples only separated by one million years, we chose a time step spacing of one million years from the time of the majority of our MsAr cooling ages (11 Ma) to the present (0

Ma). However, when modeling the data of Long et al. (2012), a time step of two million years was used, as the ApFT and ZrnHe cooling ages from these samples were not closer than this spacing. Only modeling results for the time steps beginning with that which includes the measured MsAr cooling age and ending with the 1-0 Ma step were considered. The other free parameters of our model design were selected from the suite of conditions associated with Greater Himalayan rocks as laid out by Thiede and Ehlers (2013). We used the following boundary conditions: model depth – 30 km; temperature at model depth – 650 °C; temperature at the surface – 5 °C; heat capacity – 800 J kg^{-1} K^{-1}; density – 2750 kg m^{-3}; conductivity – 2.5 W m^{-1} K^{-1}; heat production – 2 μW m^{-3}.

As a means to determine which erosion histories predicted our observed cooling ages well we adopted the reduced chi-squared test for each chronometric system, such that:

$$\chi^2 = \frac{(t_o - t_p)^2}{\sigma_n^2}$$

where χ^2 is the chi-squared misfit, t_o is the observed chronometric age, t_p is the predicted cooling age. Laboratories which frequently calculate (U-Th)/He cooling ages often calculate uncertainties as 10% of the mean, based on the long-term reproducibility of age standards, rather than on analytical imprecision alone. Here we follow this common practice by calculating the uncertainties used in the chi-squared test, σ_n, as $\sigma_n = 0.1t_o$. This procedure was used on all thermochronometers to equally weight cooling ages within our modeled solutions. The chi-squared misfit of a sample was calculated as the mean of the individual chronometer chi-squared

values in that sample. A sample chi-squared value less than or equal to three was considered an acceptable fit and implied an erosion history predicted cooling ages within the 99.7% (i.e. 3σ) confidence interval of the actual observed thermochronometric ages. The erosion rate histories of our samples were calculated as the mean and standard deviation of the erosion rates at each step for all acceptable histories (e.g. Thiede and Ehlers, 2013).

Results

We have summarized our modeling results in Figure 3.5. Despite some sample-to-sample variations in derived exhumation rates for any specific time slices, best-fit models for all samples indicate a monotonic decrease in exhumation rate – interpreted as a decrease in erosion rate – between MsAr closure (ca. 12.3 – 7.9 Ma) and ApHe closure (ca. 6.5 – 4.5 Ma). In our numerical experiments as well as others recently published by Coutand et al. (2014), the only quantitative constraint on modeled exhumation rates subsequent to ApHe closure was that the samples must have cooled to surface temperatures in no more than the elapsed time since ApHe closure. This constrained the minimum exhumation rate since the latest Miocene, but it did not provide a robust constraint on variations in exhumation rate between then and now. However, a large, sustained increase in exhumation rate after the ca. 6.5 – 4.5 Ma interval seemed improbable given the low nominal closure temperature of the ApHe chronometer (ca. 70˚C). Rapid erosion for a significant period after 6.5 – 4.5 Ma would have resulted in significantly younger ApHe closure ages. For example, the erosion histories from Region B suggest that ca. 2.5 km has

been removed from this location in the past ca. 5 million years (around the time of closure of the ApHe systems locally), and therefore, a rebound to a rate of ca. 1 km m.y.$^{-1}$ could have only occurred in the Quaternary. While our explicit modeled erosion rate histories extend from the Late Miocene to Recent time steps, we urge readers to keep in mind that neither our models nor those of Coutand et al. (2014) may be robust regarding latest-stage exhumation in the absence of thermochronometric data for the Pliocene and Quaternary.

Our 1D model results from Regions A, B and D, show a gradual decrease in erosion rate starting at high rates ca. 2-3 km m.y.$^{-1}$ at 11-10 Ma and slowing to rates perhaps as low as ca. 0.25-0.5 km m.y.$^{-1}$ over the Quaternary (Figure 3.4A, B and D). These results are similar to the 2D model results of Coutand et al. (2014), supporting the notion that our 1D models captured much of the information content from multi-chronometer datasets regarding regional and temporal patterns in exhumation rate.

Data from the central portions of Bhutan and from atop a low-relief surface, referred to as Region C, yielded a more complicated erosion history (Figure 3.5C). Sample BT0920 lacked datable apatite crystals, and therefore the erosion rate history was not constrained well after ZrHe closure at ca. 4.5 Ma. This could have greatly affected the shape of the best-fit erosion history. Sample BT0914 has a very complicated erosion rate history; it is possible that the thermal structure at its locality was affected by young activity on the Lhuentse fault (Adams et al., 2013). The most robust erosion history from this region was calculated from sample BT0919, which was determined using all three thermochronometers and does not

appear to be as perturbed. It shows a reduction in erosion rates similar to samples in Regions A, B and D.

To expand our observations, we also modeled erosion rate histories from two samples collected by Long et al. (2012) in the Kuri Chu valley. These samples were collected in the southern portions of Region D within Lesser Himalayan sequence rocks and selected for modeling because both samples contained three thermochronometers: ApFT, ZrnHe, and MsAr (Figure 3.5). These two samples exhibit much less variable erosion rate history curves, where Middle Miocene erosion rates are much lower, and Quaternary erosion rates are much higher than any other samples in Bhutan (Figure 3.5). Like the data from other regions, the modeling results of these data also show a reduction in erosion rate after the Middle Miocene despite being from a much different geographic (further south than our data), and geologic (in a large N-S antiform of the Main Boundary thrust sheet) location. However, it is worth noting that because of the large uncertainties associated with the ApFT technique, the most recent erosion rates are poorly constrained.

DISCUSSION

As Coutand et al. (2014) did before us, we interpreted the steady decrease in erosion rates between Middle and Late Miocene as an indication of decreased shortening in the eastern Himalaya related to a N-S broadening of the region of India-Eurasia shortening to include the Shillong Plateau. However, unlike those authors, we saw no obvious variation in erosion rate histories from eastern to

western Bhutan within samples north of 27.4°N. These inconsistencies may be readily explained by the 2D nature of the Coutand et al. (2014) models, which required specific structural geometries and kinematic evolutions of those structures in order to define a search range for best-fits to the modeling results. The different geometries in the Main Himalayan thrust they assumed for eastern and western Bhutan undoubtedly influenced their modeling best-fits and thus their conclusion of significantly different exhumation histories for eastern and western Bhutan despite the fact that the two areas yield very similar patterns of cooling ages. Our 1D models, which did not require assumptions regarding structural configurations, fault kinematics, or topographic steady-state, yielded consistent results for comparable thermochronometric datasets from eastern and western Bhutan and eliminated the need to invoke different subsurface architectures in the east and west.

Based on our findings, and in the absence of better constraints on the variation in subsurface structural geometries across Bhutan, we contend that the simplest interpretation of all available thermochronometric data is that all of the Bhutan Himalaya experienced a reduction in erosion rate between Middle and Late Miocene and not simply those regions north of the Shillong Plateau (i.e., east of 90˚E). This implies that the region of the eastern Himalaya over which a reduction in shortening rate after the Middle Miocene is larger than previously assumed. In particular, this reduction may have included areas west of 90˚E (e.g., western Bhutan and Sikkim) where transcurrent faulting appears to have played a more

important role in Himalayan tectonics than it has in the central Himalaya (e.g. De and Kayal, 2003; Velasco et al., 2007).

Notwithstanding the evidence for tectonic slow down, another geologic event/process was required to create the widespread surface uplift recorded in Bhutan. The existence of perched low-relief surfaces outside of the rain shadow of the Shillong Plateau is confounding to the hypothesis that a reduction in orographic precipitation led to the transient landscapes. Unfortunately, because the orographic rain shadow of the Shillong Plateau may have initiated after 3-4 Ma (Biswas et al., 2007), and few of the existing thermochronometric dates for Bhutan are younger than 3-4 Ma, we were not able to adequately test if erosion rates responded after the rain shadow may have set in, or how the erosion rates might have adjusted over time. However, a recent study from northeastern India, just to the east of Bhutan, showed that recent erosion rates have not responded to a possible decrease in precipitation due to the rise of the Shillong Plateau. Adlakha et al. (2013) presented a suite of ApFT data from the Himalayan hinterland, which exhibited widespread Quaternary cooling ages. These young ages suggest that even in areas where much of the annual precipitation from the South Asian Monsoon falls in the foothills of the Shillong Plateau (Adlakha et al., 2013), recent erosion rates have been high in the Himalaya to the north over the past few million years.

While the Quaternary cooling histories of the Bhutan Himalaya were not generally constrained by the thermochronometric data presented here, there are many lines of evidence for a very young increase in deformation rate and consequent increase in erosion rate. McQuarrie et al. (2014) utilized Plio-

Pleistocene ApFT and ZrnHe cooling ages to demonstrate an increase in cooling rates in south of 27.3 °S in western Bhutan. They went on to suggest that these fast cooling histories suggested accelerations in fault slip rates since 2 Ma. Indeed, such acceleration could account for the nearly uniform GPS-constrained convergence velocities along the central and eastern portions of the Himalayan range (Figure 3.1). Similarly, Adlakha et al. (2013) used Quaternary ApFT data to suggest out-of-sequence uplift rate patterns caused by young fault activity in Arunachal Pradesh, India. Adams et al. (2013) showed evidence of a change in the fault activity in the hinterland of the Bhutan Himalaya during the Quaternary. They demonstrated that the north-dipping Lhunetse fault accommodated differential uplift rates near the back limb of an active hinterland duplex and the northern extent of the low-relief surfaces.

The perched low-relief landscapes of Bhutan have clearly undergone significant surface uplift (e.g. Baillie and Norbu, 2004; Grujic et al., 2006). Both the tectonic and climatic hypothesis require an increase in erosion rate toward more recent times where landscapes have adjusted to the new forcing factors (i.e. in deeply incised canyons). Unfortunately, the erosion rates histories from our new data have only recorded evidence of a reduction toward the present. The lack of a signature of an erosion history indicative of surface uplift in our thermochronometric data has restricted the possible timing to after ca. 4.5 Ma. Then again, our data have at least confirmed that the perched low-relief surfaces in Bhutan cannot be older.

The erosion rate histories modeled from the data of Long et al. (2012), nearer the southern extent of the low-relief landscapes, hinted at a slightly different story. The relatively young ApFT cooling ages from these samples suggest higher recent erosion rates around 27.3-27.4°N. We interpreted the north to south increase in recent erosion rates from Region D is the result of a non-uniform rock uplift rate of similar pattern. While this hypothesis requires testing using techniques that are better able to capture more recent erosion rates, these samples may allude as a recent increase in rock uplift rates, which may be responsible for the surface uplift of the low-relief landscapes in Bhutan. However, because of the uncertainties associate with these southerly histories we hesitate to suggest anything more definitive.

Changes in the erosional and structural history of Bhutan during the Pliocene and Pleistocene suggest a dynamic system that has feedbacks likely associated with changes in plate convergence velocities and directions (e.g. Molnar and Stock, 2009; Styron et al., 2011), the internal reorganization of fold-and-thrust belts due to changes in accretionary flux (e.g. Davis et al., 1983), redistributions of stress related to heterogeneities within the Indian plate (e.g. Clark and Bilham, 2008), and the transient nature of responses to changes in uplift rates and erosional efficiencies (Whipple and Meade, 2006; Crosby et al., 2007; Grujic et al., 2006). While the eastern portions of the Himalayan-Tibetan orogen is an excellent location to test the coupling of the tectonic and climatic influences on mountain ranges (e.g. Grujic et al., 2006; Adlakha et al., 2013), more information is needed regarding the spatial extent (both into and along the range) and magnitude of the Shillong Plateau rain shadow,

recent spatial patterns in erosion rate, and quantitative demonstration of the coupling between mean annual rainfall and erosivity, before firm conclusions can be drawn regarding the possible influence of climate on eastern Himalayan orogenesis.

CONCLUSIONS

The tectonic and climatic influence of the Shillong Plateau and its associated structures has significant implications of orogenic processes in the regions of northeastern India and Bangladesh. However, because of the position and orientation of the Shillong Plateau, there is a need to understand how the evolution of this range has influenced the Eastern Himalaya. We have utilized the cooling histories of bedrock samples to analyze the spatial and temporal patterns in long-term erosion rate histories across the Bhutan Himalaya. We have provided evidence for a protracted reduction in erosion rates between the Middle Miocene and the Miocene-Pliocene boundary throughout the range. We have concluded that this decrease in erosion rates was caused by the accommodation of convergence between India and Eurasia on structures outside the Himalayan orogenic wedge *sensu stricto* (i.e., south of the trace of the Himalayan Frontal thrust system). Such structures include, but are not restricted to, the specific structures responsible for uplift of the Shillong Plateau. Several lines of evidence suggested a more recent rejuvenation of deformation and erosional activity throughout Bhutan.

ACKNOWLEDGMENTS

This work was supported by a National Science Foundation Tectonics Program grant EAR 0708714 to K.V.H. and a joint Tectonics and Geomorphology and Landuse Dynamics Programs grant EAR 1049888 to K.X.W. and Arjun Heimsath. B.A.A. would like to thank Frances Cooper (School of Earth Sciences, University of Bristol) for her assistance and discussions. Arjun Heimsath (School of Earth and Space Sciences, Arizona State University) was an invaluable asset and supporter of this work. Fieldwork would not have been possible without support of our friends and colleagues in Bhutan: Peldon Tshering (National Environment Commission), Ugyen Wanda (Department of Geology and Mines), Karma Choden and Ugyen Rinzen (Yangphel Adventure Travel).

FIGURE CAPTIONS

Figure 3.1. Digital elevation model of the Himalayan-Tibetan orogen. Fill patterns denote dominant style of deformation, as determined by the strain field of Andronicos et al. (2007). Circles - contraction; horizontal lines - transtension; diagonal lines - transpression. Thick white lines mark the locations of primary extensional structures at the crest of the range, from Hodges et al. (2000) and Long et al. (2012). Thick black lines mark the locations of primary contractional structures at the foreland of various ranges, from Styron et al. (2011). SP - Shillong Plateau. Numbers within upper arrows show the contraction component of convergence between India and Eurasia in mm $y.^{-1}$, as determined from global positioning satellite studies. (A) Data from Banerjee and Burgmann (2002). (B) Data

from Jouanne et al. (1999). (C) Data from Larson et al. (1999). (D) Data from Banerjee et al. (2008). (E) Data from Paul et al. (2001) and Banerjee et al. (2008).

Figure 3.2. Digital elevation model of the Bhutan Himalaya. White lines demarcate the boundaries of perched low-relief fluvial landscapes. Grey lines mark political boundaries. JF – Jomolhari fault; STF – South Tibetan fault system; KT – Kakhtang thrust; MCT – Main Central thrust system; MBT – Main Boundary thrust system; MFT – Main Frontal thrust system; LF – Lhuentse fault. Faults based on the maps of Long et al. (2012); Cooper et al. (2012); Cooper et al. (2013) and Adams et al. (2013).

Figure 3.3. River profiles from the Bhutan Himalaya. See Figure 3.2 for river locations. Note the significant slope-break knickpoints in each profile.

Figure 3.4. Bedrock thermochronometry sample locations in Bhutan. White points are sample locations of new data in this paper. Italicized data are taken from Adams et al. (2013). Red points are sample locations of data from Long et al. (2012). See Figure 3.2 for panel locations. Sample names, apatite (U-Th)/He, apatite fission track, zircon (U-Th)/He and muscovite $^{40}Ar/^{39}Ar$ cooling ages are shown in black, red, orange, green and blue text, respectively. Region demarcation is shown at the bottom of the panels. White lines represent the boundaries of perched low-relief fluvial landscapes. STF – South Tibetan fault; KT – Kakhtang thrust; MCT – Main Central thrust; LF – Lhuentse fault.

Figure 3.5. Erosion rate histories from 1D thermal-kinematic modeling. Bold solid lines show mean histories. Transparent envelopes show one standard deviation on the mean history. Panels A, B, C and D show erosion rate histories from samples located in Region A, B, C and D, respectively. See Figure 3.3 for sample and region locations, and thermochronometric cooling ages used in models. Arrows mark the extent of cooling ages and associated one standard deviation uncertainties of each region.

REFERNCES

Adams, B. A., Hodges, K. V., van Soest, M. C., & Whipple, K. X. (2013). Evidence for Pliocene-Quaternary normal faulting in the hinterland of the Bhutan Himalaya. *Lithosphere, 5*(4), 438-449. doi: 10.1130/l277.1

Adlakha, V., Lang, K. A., Patel, R. C., Lal, N., & Huntington, K. W. (2013). Rapid long-term erosion in the rain shadow of the Shillong Plateau, Eastern Himalaya. *Tectonophysics, 582*, 76-83. doi: 10.1016/j.tecto.2012.09.022

Aitchison, J. C., Ali, J. R., & Davis, A. M. (2007). When and where did India and Asia collide? *Journal of Geophysical Research-Solid Earth, 112*(B5), 19. doi: 10.1029/2006jb004706

Andronicos, C. L., Velasco, A. A., & Hurtado Jr, J. M. (2007). Large-scale deformation in the India-Asia collision constrained by earthquakes and topography. *Terra Nova, 19*(2), 105-119.

Baillie, I. C., & Norbu, C. (2004). Climate and other factors in the development of

river and interfluve profiles in Bhutan, Eastern Himalayas. *Journal of Asian Earth Sciences, 22*(5), 539-553. doi: 10.1016/s1367-9120(03)00092-0

Banerjee, P., Burgmann, R., Nagarajan, B., & Apel, E. (2008). Intraplate deformation of the Indian subcontinent. *Geophysical Research Letters, 35*(18), 5. doi: 10.1029/2008gl035468

Banerjee, P., & Bürgmann, R. (2002). Convergence across the northwest Himalaya from GPS measurements. *Geophysical Research Letters, 29*(13), 30-31-30-34.

Baruah, S., & Kayal, J. R. (2013). State of Tectonic Stress in Northeast India and Adjoining South Asia Region: An Appraisal. *Bulletin of the Seismological Society of America, 103*(2A), 894-910. doi: 10.1785/0120110354

Bilham, R., & England, P. (2001). Plateau 'pop-up' in the great 1897 Assam earthquake. *Nature, 410*(6830), 806-809. doi: 10.1038/35071057

Biswas, S., Coutand, I., Grujic, D., Hager, C., Stockli, D., & Grasemann, B. (2007). Exhumation and uplift of the Shillong plateau and its influence on the eastern Himalayas: New constraints from apatite and zircon (U-Th- Sm)/He and apatite fission track analyses. *Tectonics, 26*(6), 22. doi: 10.1029/2007tc002125

Biswas, S., & Grasemann, B. (2005). Quantitative morphotectonics of the southern Shillong plateau (Bangladesh/India). *Aust. J. Earth Sci, 97*, 82-93.

Bollinger, L., Avouac, J. P., Beyssac, O., Catlos, E. J., Harrison, T. M., Grove, M., Goffé, B., & Sapkota, S. (2004). Thermal structure and exhumation history of the Lesser Himalaya in central Nepal. *Tectonics, 23*(5), TC5015.

Bollinger, L., Henry, P., & Avouac, J. P. (2006). Mountain building in the Nepal

Himalaya: Thermal and kinematic model. *Earth and Planetary Science Letters, 244*(1), 58-71.

Bonnet, S., & Crave, A. (2003). Landscape response to climate change: Insights from experimental modeling and implications for tectonic versus climatic uplift of topography. *Geology, 31*(2), 123-126. doi: 10.1130/0091-7613(2003)031<0123:lrtcci>2.0.co;2

Braun, J. (2003). Pecube: A new finite-element code to solve the 3D heat transport equation including the effects of a time-varying, finite amplitude surface topography. *Computers & Geosciences, 29*(6), 787-794.

Braun, J., Van Der Beek, P., & Batt, G. (2006). *Quantitative thermochronology: numerical methods for the interpretation of thermochronological data*: Cambridge University Press.

Chambers, J., Parrish, R., Argles, T., Harris, N., & Horstwood, M. (2011). A short-duration pulse of ductile normal shear on the outer South Tibetan detachment in Bhutan: Alternating channel flow and critical taper mechanics of the eastern Himalaya. *Tectonics, 30*, 12. doi: 10.1029/2010tc002784

Clark, M. K., & Bilham, R. (2008). Miocene rise of the Shillong Plateau and the beginning of the end for the Eastern Himalaya. *Earth and Planetary Science Letters, 269*(3), 337-351.

Cooper, F. J., Adams, B. A., Edwards, C. S., & Hodges, K. V. (2012). Large normal-sense displacement on the South Tibetan fault system in the eastern Himalaya. *Geology, 40*(11), 971-974. doi: 10.1130/g33318.1

Cooper, F. J., Hodges, K. V., & Adams, B. A. (2013). Metamorphic constraints on the

character and displacement of the South Tibetan fault system, central Bhutanese Himalaya. *Lithosphere, 5*(1), 67-81. doi: 10.1130/l221.1

Coutand, I., Whipp, D. M., Grujic, D., Bernet, M., Fellin, M. G., Bookhagen, B., Landry, K. R., Ghalley, S. K. & Duncan, C. (2014). Geometry and kinematics of the Main Himalayan Thrust and Neogene crustal exhumation in the Bhutanese Himalaya derived from inversion of multithermochronologic data. *Journal of Geophysical Research: Solid Earth, 119*(2), 1446-1481.

Crosby, B. T., Whipple, K. X., Gasparini, N. M., & Wobus, C. W. (2007). Formation of fluvial hanging valleys: Theory and simulation. *Journal of Geophysical Research-Earth Surface, 112*(F3), 20. doi: 10.1029/2006jf000566

Daniel, C., Hollister, L., Parrish, R. t., & Grujic, D. (2003). Exhumation of the Main Central Thrust from lower crustal depths, eastern Bhutan Himalaya. *Journal of Metamorphic Geology, 21*(4), 317-334.

Davis, D., Suppe, J., & Dahlen, F. A. (1983). Mechanics of fold-and-thrust belts and accretionary wedges. *Journal of Geophysical Research, 88*(NB2), 1153-1172. doi: 10.1029/JB088iB02p01153

De Sarkar, S., Mathew, G., & Pande, K. (2013). Arc parallel extension in Higher and Lesser Himalayas, evidence from western Arunachal Himalaya, India. *Journal of Earth System Science, 122*(3), 715-727.

Drukpa, D., Velasco, A. A., & Doser, D. I. (2006). Seismicity in the Kingdom of Bhutan (1937–2003): Evidence for crustal transcurrent deformation. *Journal of geophysical research, 111*(B6), B06301.

Duncan, C., Masek, J., & Fielding, E. (2003). How steep are the Himalaya?

Characteristics and implications of along-strike topographic variations. *Geology, 31*(1), 75-78.

Gansser, A. (1983). Geology of the Bhutan Himalaya (Vol. 96, pp. 181). Basel: Birkhäuser Verlag.

Grove, M., & Harrison, T. M. (1996). 40Ar* diffusion in Fe-rich biotite. *American Mineralogist, 81*, 940-951.

Grujic, D., Coutand, I., Bookhagen, B., Bonnet, S., Blythe, A., & Duncan, C. (2006). Climatic forcing of erosion, landscape, and tectonics in the Bhutan Himalayas. *Geology, 34*(10), 801-804. doi: 10.1130/g22648.1

Harrison, T. M., Celerier, J., Aikman, A. B., Hermann, J., & Heizler, M. T. (2009). Diffusion of Ar-40 in muscovite. *Geochimica Et Cosmochimica Acta, 73*(4), 1039-1051. doi: 10.1016/j.gca.2008.09.038

Hodges, K. V. (2000). Tectonics of the Himalaya and southern Tibet from two perspectives. *Geological Society of America Bulletin, 112*(3), 324-350.

Hodges, K. V. (2014). Thermochronology in Orogenic Systems. In H. D. Holland & K. K. Turekian (Eds.), *Treatise on Geochemistry* (2 ed., Vol. 4, pp. 281-308). Oxford: Elsevier.

Hodges, K. V., Hurtado, J. M., & Whipple, K. X. (2001). Southward extrusion of Tibetan crust and its effect on Himalayan tectonics. *Tectonics, 20*(6), 799-809.

Jouanne, F., Mugnier, J. L., Pandey, M. R., Gamond, J. F., Le Fort, P., Serrurier, L., Vigny, C., Avouac, J. P. & Idylhim (1999). Oblique convergence in the Himalayas of western Nepal deduced from preliminary results of GPS measurements. *Geophysical Research Letters, 26*(13), 1933-1936. doi:

10.1029/1999gl900416

Larson, K. M., Bürgmann, R., Bilham, R., & Freymueller, J. T. (1999). Kinematics of the India-Eurasia collision zone from GPS measurements. *Journal of Geophysical Research: Solid Earth (1978–2012), 104*(B1), 1077-1093.

Long, S. P., McQuarrie, N., Tobgay, T., Coutand, I., Cooper, F. J., Reiners, P. W., Wartho, J. A. & Hodges, K. V. (2012). Variable shortening rates in the eastern Himalayan thrust belt, Bhutan: Insights from multiple thermochronologic and geochronologic data sets tied to kinematic reconstructions. *Tectonics, 31*, 23. doi: 10.1029/2012tc003155

Ludwig, K. R. (2012). *User's manual for Isoplot 3.75: a geochronological toolkit for Microsoft Excel* (Vol. 5): Kenneth R. Ludwig.

McDougall, I., & Harrison, T. M. (1999). *Geochronology and Thermochronology by the 40Ar/39Ar Method*: Oxford University Press.

McQuarrie, N., Tobgay, T., Long, S. P., Reiners, P. W., & Cosca, M. A. (2014). Variable exhumation rates and variable displacement rates: Documenting recent slowing of Himalayan shortening in western Bhutan. *Earth and Planetary Science Letters, 386*, 161-174.

Meesters, A., & Dunai, T. (2005). A noniterative solution of the (U-Th)/He age equation. *Geochemistry, Geophysics, Geosystems, 6*(4).

Molnar, P., & Stock, J. M. (2009). Slowing of India's convergence with Eurasia since 20 Ma and its implications for Tibetan mantle dynamics. *Tectonics, 28*(3).

Paul, J., Bürgmann, R., Gaur, V., Bilham, R., Larson, K., Ananda, M., Jade, S., Mukal, M., Anupama, T. S., Satyal, G. & Kumar, D. (2001). The motion and active

deformation of India. *Geophysical Research Letters, 28*(4), 647-650.

Pearson, R. K. (2011). *Exploring data in engineering, the sciences, and medicine*: Oxford Univ Pr.

Robert, X., van der Beek, P., Braun, J., Perry, C., & Mugnier, J. L. (2011). Control of detachment geometry on lateral variations in exhumation rates in the Himalaya: Insights from low-temperature thermochronology and numerical modeling. *Journal of Geophysical Research-Solid Earth, 116*, 22. doi: 10.1029/2010jb007893

Schwarz, W. H., & Trieloff, M. (2007). Intercalibration of $^{40}Ar/^{39}Ar$ age standards NL-25, HB3gr hornblende, GA1550, SB-3, HD-B1 biotite and BMus/2 muscovite. *Chemical Geology, 242*(1), 218-231.

Seeber, L., & Armbruster, J. G. (1981). Great detachment earthquakes along the Himalayan arc and long-term forecasting. *Maurice Ewing Series, 4*, 259-277.

Stuwe, K., & Foster, D. (2001). Ar-40/Ar-39, pressure, temperature and fission track constraints on the age and nature of metamorphism around the main central thrust in the eastern Bhutan Himalaya. *Journal of Asian Earth Sciences, 19*(1-2), 85-95. doi: 10.1016/s1367-9120(00)00018-3

Styron, R. H., Taylor, M. H., & Murphy, M. A. (2011). Oblique convergence, arc-parallel extension, and the role of strike-slip faulting in the High Himalaya. *Geosphere, 7*(2), 582-596.

Thiede, R. C., & Ehlers, T. A. (2013). Large spatial and temporal variations in Himalayan denudation. *Earth and Planetary Science Letters, 371*, 278-293. doi: 10.1016/j.epsl.2013.03.004

Tobgay, T., McQuarrie, N., Long, S., Kohn, M. J., & Corrie, S. L. (2012). The age and rate of displacement along the Main Central Thrust in the western Bhutan Himalaya. *Earth and Planetary Science Letters, 319*, 146-158. doi: 10.1016/j.epsl.2011.12.005

van Soest, M. C., Hodges, K. V., Wartho, J. A., Biren, M. B., Monteleone, B. D., Ramezani, J., Spray, J. G. & Thompson, L. M. (2011). (U-Th)/He dating of terrestrial impact structures: The Manicouagan example. *Geochemistry Geophysics Geosystems, 12*(null), Q0AA16.

Velasco, A. A., Gee, V. L., Rowe, C., Grujic, D., Hollister, L. S., Hernandez, D., D., Miller, K. C., Tobgay, T., Fort, M., & Harder, S. (2007). Using small, temporary seismic networks for investigating tectonic deformation: Brittle deformation and evidence for strike-slip faulting in Bhutan. *Seismological Research Letters, 78*(4), 446-453.

Wendt, I., & Carl, C. (1991). The statistical distribution of the mean squared weighted deviation. *Chemical Geology: Isotope Geoscience section, 86*(4), 275-285.

Whipp Jr, D. M., Ehlers, T. A., Blythe, A. E., Huntington, K. W., Hodges, K. V., & Burbank, D. W. (2007). Plio-Quaternary exhumation history of the central Nepalese Himalaya: 2. Thermokinematic and thermochronometer age prediction model. *Tectonics, 26*(3), TC3003.

Whipple, K., & Meade, B. (2004). Controls on the strength of coupling among climate, erosion, and deformation in two-sided, frictional orogenic wedges at steady state. *Journal of Geophysical Research: Earth Surface (2003–2012), 109*(F1).

Whipple, K. X., & Meade, B. J. (2006). Orogen response to changes in climatic and tectonic forcing. *Earth and Planetary Science Letters, 243*(1-2), 218-228. doi: 10.1016/j.epsl.2005.12.022

Whipple, K. X., & Tucker, G. E. (1999). Dynamics of the stream-power river incision model: Implications for height limits of mountain ranges, landscape response timescales, and research needs. *Journal of Geophysical Research-Solid Earth, 104*(B8), 17661-17674. doi: 10.1029/1999jb900120

Willett, S. D., Slingerland, R., & Hovius, N. (2001). Uplift, shortening, and steady state topography in active mountain belts. *American journal of Science, 301*(4-5), 455-485.

Wobus, C., Heimsath, A., Whipple, K., & Hodges, K. (2005). Active out-of-sequence thrust faulting in the central Nepalese Himalaya. *Nature, 434*(7036), 1008-1011.

Wobus, C. W., Hodges, K. V., & Whipple, K. X. (2003). Has focused denudation sustained active thrusting at the Himalayan topographic front? *Geology, 31*(10), 861-864.

Wobus, C. W., Whipple, K. X., & Hodges, K. V. (2006). Neotectonics of the central Nepalese Himalaya: Constraints from geomorphology, detrital $^{40}Ar/^{39}Ar$ thermochronology, and thermal modeling. *Tectonics, 25*(4), TC4011.

Yin, A., & Harrison, T. M. (2000). Geologic evolution of the Himalayan-Tibetan orogen. *Annual Review of Earth and Planetary Sciences, 28*(1), 211-280.

Table 3.1. New apatite and zircon (U-Th)/He data.

Sample	Latitude (°N)	Longitude (°E)	Elevation (m)	Lithology	ApHe (Ma)	2_ (Ma)	n	ZrnHe (Ma)	2_ (Ma)	n
BT0847	27.51336	90.58742	3522	leucogranite	5.41	0.98	7	6.57	0.76	5
BT0848	27.53239	90.57289	3213	orthogneiss	5.15	0.67	5	7.27	0.50	5
BT0849	27.50850	90.54692	2914	orthogneiss	5.35	0.17	5	7.06	0.12	4
BT0850	27.49989	90.53558	2622	paragneiss	5.6	1.1	4	6.95	0.53	5
BT0851	27.49350	90.52133	2243	paragneiss	5.26	0.27	3	6.22	0.42	4
BT0852	27.50411	90.48383	2025	paragneiss	4.99	0.45	3	5.99	0.73	5
BT0853	27.52039	90.45964	1876	leucogranite	4.412	0.091	3	6.29	0.11	3
BT0914	27.69694	90.72881	2882	orthogneiss	4.69	0.12	3	5.06	0.18	5
BT0919	27.66614	90.74593	2763	orthogneiss	5.34	0.13	3	5.84	0.54	5
BT0920	27.64550	90.73758	2779	orthogneiss	--	--	--	4.53	0.54	4
BT0987	27.46520	89.51972	2805	pelitic schist	5.89	0.38	4	6.89	0.66	5
BT0988	27.44978	89.52432	2655	orthogneiss	5.90	0.99	3	6.62	0.48	5
BT0989	27.42062	89.55662	2405	pelitic schist	6.4	1.8	5	6.63	0.42	4
BT1024	27.49695	90.50137	1827	orthogneiss	4.96	0.25	8	7.9	1.4	5

Apatite (U-Th)/He - ApHe; zircon (U-Th)/He - ZrnHe.

Table 3.2. New muscovite and biotite $^{40}Ar/^{39}Ar$ data.

Sample/ Aliquot	Latitude (°N)	Longitude (°E)	Elevation (m)	Lithology	Total gas age (Ma)	2σ (Ma)	Plateau Age* (Ma)	2σ (Ma)	MSWD	Inverse Isochron Age† (Ma)	2σ (Ma)	MSWD	Initial $^{40}Ar/^{36}Ar$	2σ
BT0847	27.51336	90.58742	3522	leucogranite										
Muscovite					10.70	0.30	**10.638**	**0.059**	0.71	10.70	0.29	2.1	299	11
BT0848	27.53239	90.57289	3213	orthogneiss										
Muscovite					10.70	0.18	**10.565**	**0.060**	0.57	10.53	0.17	0.97	311.8	3.3
BT0849	27.50850	90.54692	2914	orthogneiss										
Muscovite					10.50	0.30	**10.565**	**0.040**	1.7	10.63	0.26	3	289	11
BT0850	27.49989	90.53558	2622	paragneiss										
Muscovite					10.33	0.18	--	--	--	**10.30**	**0.20**	14	303.7	8.7
BT0851	27.49350	90.52133	2243	paragneiss										
Muscovite					10.59	0.18	**10.590**	**0.044**	2.1	10.85	0.39	33	300	39
BT0852	27.50411	90.48383	2025	paragneiss										
Muscovite					10.76	0.18	**10.753**	**0.057**	3.1	10.80	0.19	3.6	292.7	6.5
BT0853	27.52039	90.45964	1876	leucogranite										
Muscovite					10.05	0.18	**10.602**	**0.064**	1.3	10.9	0.67	143	294	33
BT0914	27.69694	90.72881	2882	orthogneiss										
Biotite					10.39	0.10	9.70	0.10	1.7	9.70	0.18	2.1	284.2	9.5
Muscovite					10.10	0.20	**10.800**	**0.029**	1.5	10.03	0.24	2.2	305.0	4.7
BT0919	27.66614	90.74593	2763	orthogneiss										
Biotite					8.73	0.05	8.720	0.025	1.7	8.731	0.068	2.1	297.9	8.8
Muscovite					9.50	0.30	**9.420**	**0.038**	1.5	9.53	0.31	17	300	15
BT0920	27.64550	90.73758	2779	orthogneiss										
Biotite					10.31	0.16	--	--	--	10.37	0.3	27	293	20
Muscovite							**9.974**	**0.066**	2.1	9.87	0.47	9.1	297	10
BT0962	27.76839	91.13331	2360	paragnesis										
Biotite					7.53	0.10	--	--	--	7.51	0.13	14	301	14
Muscovite					7.79	0.14	**7.860**	**0.024**	2.1	8.00	0.11	5.8	266.3	9.1
BT0963	27.74961	91.13331	2309	paragnesis										
Biotite					9.43	0.08	9.426	0.029	2.1	9.45	0.11	8.1	293	15
Muscovite					8.22	0.13	**8.215**	**0.035**	0.97	8.19	0.14	0.92	298.6	4.1
BT0964	27.74289	91.13753	1882	orthogneiss										
Biotite					17.60	0.20	--	--	--	17.58	0.33	40	298	32
Muscovite					9.4	1.0	**8.499**	**0.078**	2.0	8.24	0.37	10	374	46
BT0987	27.46520	89.51972	2805	pelitic schist										
Muscovite					9.71	0.13	**9.689**	**0.038**	1.9	9.63	0.13	1.9	303.9	4.7
BT0988	27.44978	89.52432	2655	orthogneiss										
Biotite					9.90	0.14	9.835	0.024	1.5	9.85	0.14	10	317	15
Muscovite					9.47	0.07	**9.451**	**0.031**	1.8	9.45	0.10	2.6	298.8	8.7
BT0989	27.42062	89.55662	2405	pelitic schist										
Biotite					8.66	0.09	8.660	0.027	1.7	8.66	12	1.9	296.3	5.6
Muscovite					9.61	0.18	**9.576**	**0.090**	1.6	9.7	0.18	2.1	284.2	9.5
BT1024	27.49695	90.50137	1827	orthogneiss										
Muscovite					12.10	0.20	**12.309**	**0.052**	2.3	12.1	1.9	1128	355	81

*Defined as 3 or more contiguous steps whose dates overlap at the 2σ level and represent at least 50% of the released ^{39}Ar. †Uses all steps. Cooling ages in bold were used in thermal modeling.

FIGURE 3.1

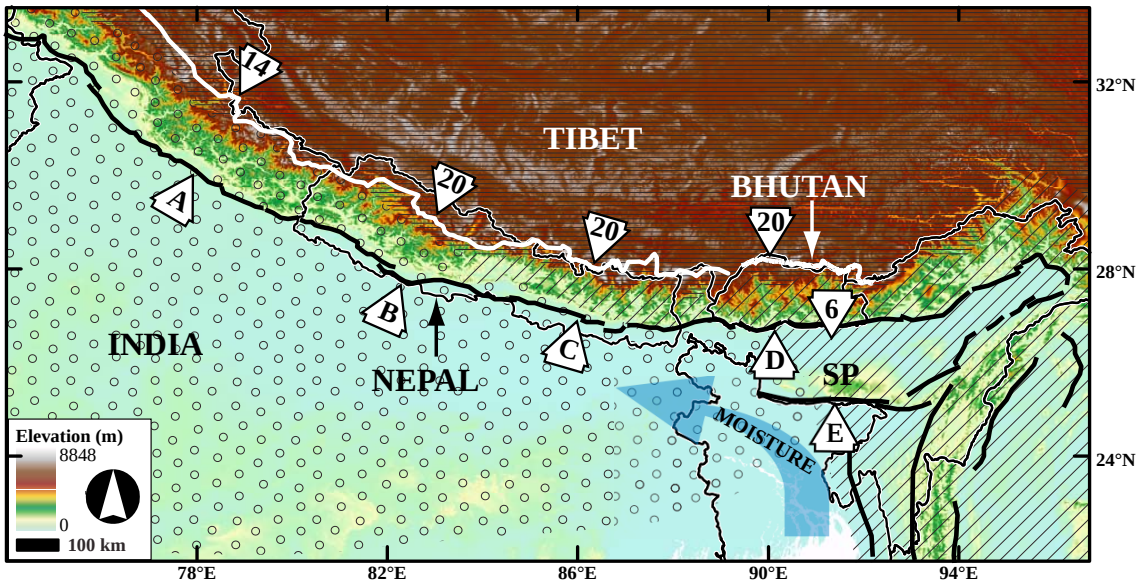
TIBET
BHUTAN
INDIA
NEPAL
SP
MOISTURE
A
B
C
D
E
14
20
20
20
6
Elevation (m)
8848
0
100 km
32°N
28°N
24°N
78°E
82°E
86°E
90°E
94°E

FIGURE 3.2

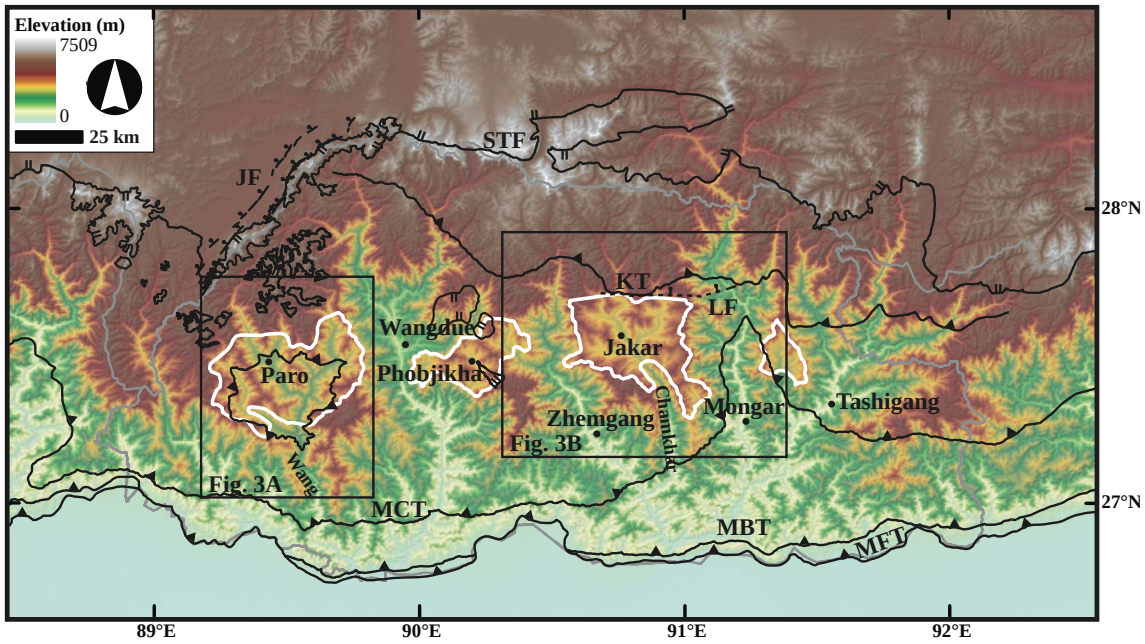
Elevation (m)
7509
0
25 km
JF
STF
KT
LF
Wangdue
Phobjikha
Paro
Jakar
Zhemgang
Chamkhar
Mongar
Tashigang
Fig. 3A
Fig. 3B
Wang
MCT
MBT
MFT
28°N
27°N
89°E
90°E
91°E
92°E

FIGURE 3.3

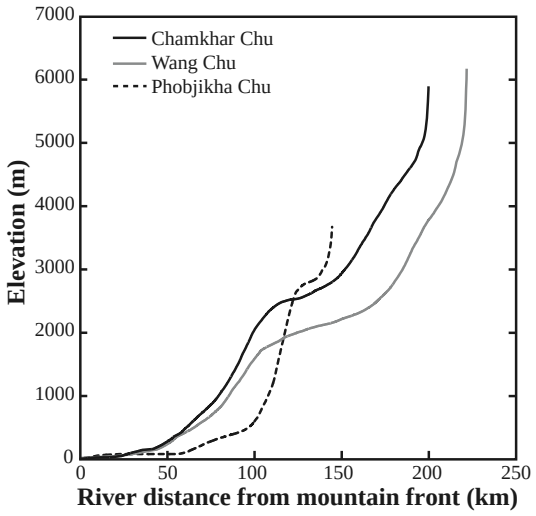
Chamkhar Chu
Wang Chu
Phobjikha Chu
Elevation (m)
River distance from mountain front (km)
0
1000
2000
3000
4000
5000
6000
7000
0
50
100
150
200
250

FIGURE 3.4

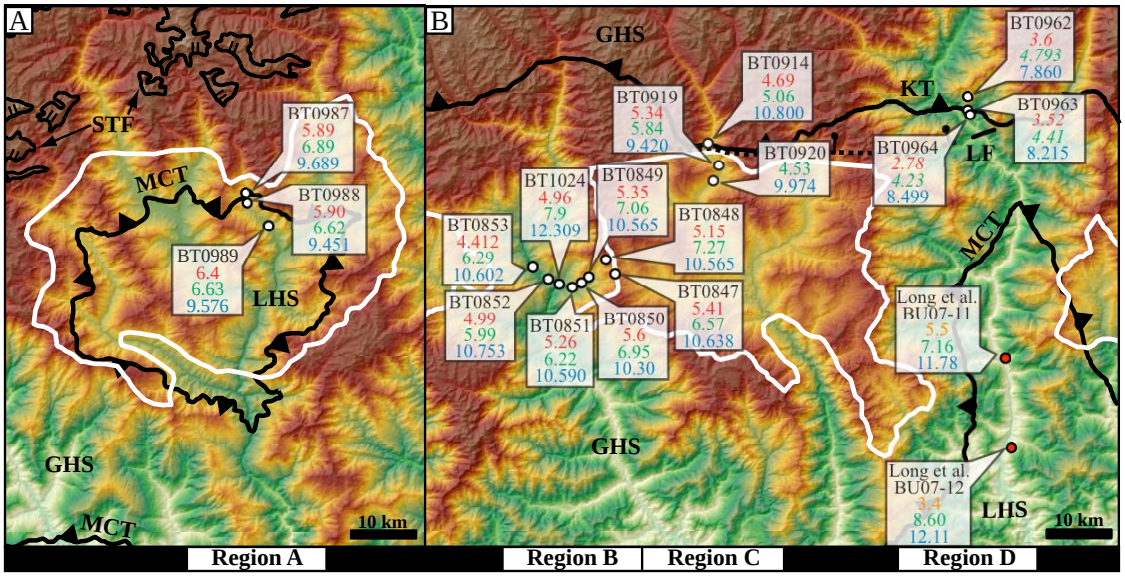
A
B
STF
MCT
GHS
LHS
KT
LF
BT0987
5.89
6.89
9.689
BT0988
5.90
6.62
9.451
BT0989
6.4
6.63
9.576
BT0914
4.69
5.06
10.800
BT0919
5.34
5.84
9.420
BT0920
4.53
9.974
BT0962
3.6
4.793
7.860
BT0963
3.52
4.41
8.215
BT0964
2.78
4.23
8.499
BT1024
4.96
7.9
12.309
BT0849
5.35
7.06
10.565
BT0848
5.15
7.27
10.565
BT0853
4.412
6.29
10.602
BT0852
4.99
5.99
10.753
BT0851
5.26
6.22
10.590
BT0850
5.6
6.95
10.30
BT0847
5.41
6.57
10.638
Long et al.
BU07-11
5.5
7.16
11.78
Long et al.
BU07-12
3.4
8.60
12.11
10 km
Region A
Region B
Region C
Region D

FIGURE 3.5

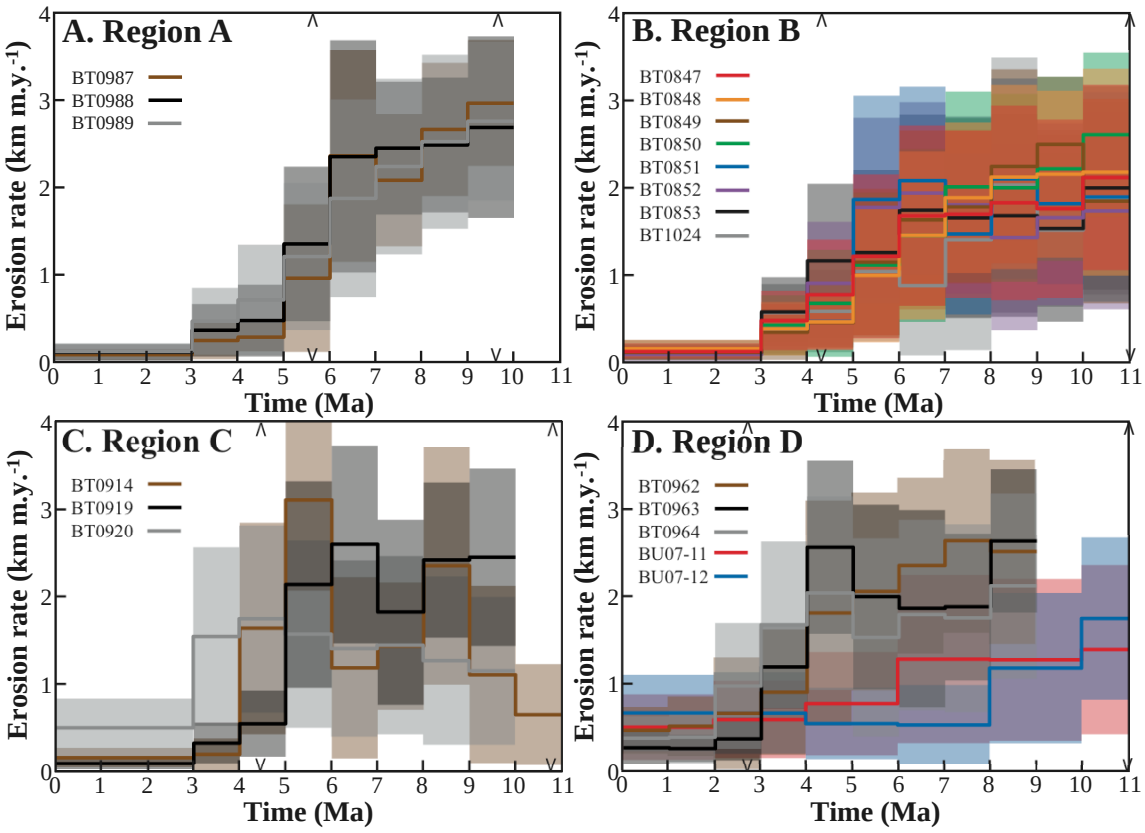
A. Region A
BT0987
BT0988
BT0989
B. Region B
BT0847
BT0848
BT0849
BT0850
BT0851
BT0852
BT0853
BT1024
C. Region C
BT0914
BT0919
BT0920
D. Region D
BT0962
BT0963
BT0964
BU07-11
BU07-12
Erosion rate (km m.y.-1)
Time (Ma)

CHAPTER 4

LANDSCAPE RESPONSE TO ACTIVE DUPLEX GROWTH IN THE EASTERN HIMALAYAN HINTERLAND

ABSTRACT

Along-strike variation in the topography of the Himalayan orogenic wedge has been explained by variation in the rheology of materials, the architecture of major structures, and climate. The Bhutan Himalaya have an unusual topographic profile characterized by large, isolated, low-relief landscapes, perched kilometers above deeply incised canyons, which interrupt an otherwise steep range front. Quantitative analysis of topography from spacebourne imagery, field geomorphology, and the distribution of millennial scale erosion rates, suggests that these landscapes did not develop at an ancient range front that was subsequently uplifted to high elevations, as has been previously proposed. Instead we have concluded that these landscapes developed in a hinterland position within the mountain belt as a consequence of backtilting and surface uplift above active structural duplexes at depth.

Millennial-scale erosion rates determined using basin-averaged cosmogenic radionuclide techniques have demonstrated that the low-relief landscapes in Bhutan are transient features. The low-relief surfaces are eroding at a rate ca. 70 m m.y.$^{-1}$, while basins from surrounding steep landscapes near major convex knickpoints yielded erosion rates ca. 550 m m.y.$^{-1}$. We have utilized these new erosion rates and reconstructed paleo-river profiles to calculate the magnitude and timing of surface

uplift, and concluded that the low-relief surfaces have been uplifted ca. 800 m, in the past ca. 1.5 Ma.

We have tested the influence of an active duplex on the overlying topography using a landscape evolution model to simulate the activation of an antiform uplift pattern within a previously steady-state mountain range. Our experiment showed that low-relief landscapes with thick alluvial fills were formed upstream of large convex knickpoints as rivers adjusted to higher uplift rates downstream. In addition, concave knickpoints were formed at the upstream boundaries of these sediment packages where river channels are still eroding into bedrock. Both of these types of knickpoints were transient and continuously moving headward and upward. The upward movement of the convex knickpoint led to surface uplift. The topographic patterns created during this numerical experiment match well with those observed in Bhutan.

MOTIVATION

Although mean elevation of orogenic systems generally increases toward the hinterland in a topographic taper, local factors can affect the details of this pattern. The pattern of local relief within a mountain belt is influenced by changes in the dip of the décollement, out-of-sequence deformation, the length of transverse tributaries, changes in fluvial dynamics, glaciation, and influences of precipitation or lithology (Whipple and Tucker, 1999; 2002; Whipple et al., 1999; Sklar and Dietrich, 2001). Along the length of the Himalayan mountain belt there is a significant amount of variation in topographic profile (e.g. Duncan et al., 2003; Hodges and Adams, 2013). Dahlen (1990), for example, noted a distinctive increase in the apparent critical taper of the Himalaya in central Nepal from the foothills (or foreland) region to the higher Himalayan (or hinterland) region (Figure 4.1A). He attributed this to the affects of a transition from brittle to ductile deformation at the depth of the basal detachment beneath the wedge. Subsequent researchers have invoked a ramp in the basal detachment, a blind structural duplex above the basal detachment, or out-of-sequence thrusting to explain this pattern (Lyon-Caen and Molnar, 1983; 1985; Cattin et al., 2001; Lave and Avouac, 2001; Robinson et al., 2003; Bollinger et al., 2004; 2006; Pearson and DeCelles, 2005; Wobus et al., 2003; 2005; 2006; Hodges et al., 2004).

The profile of the eastern Himalaya in Bhutan is characterized in many places by low-relief landscapes ("benches") in the hinterland (Figure 4.1A; Duncan et al., 2003; Baillie and Norbu, 2004; Grujic et al., 2006; Adams et al., 2013; Adams et al., Chapter 3). Because fluvial relief sets most of the relief in mountain ranges, the

differences between the mean topography of the central Nepal Himalaya and that of the Bhutan Himalaya are also expressed in the longitudinal profiles of transverse rivers (Figure 4.1B). Although strong precipitation and – in all likelihood – erosion gradients do occur across the this landscape, the N-S pattern of precipitation does not correlate strongly to changes in topographic slope or stream gradients from the Bhutanese hinterland to the foreland (Bookhagen and Burbank, 2010). It seems more probable that the unusual profile of Bhutan owes its origin to an unusual tectonic architecture (Adams et al., Chapter 3). Here we have explored the hypothesis that this profile resulted from surface uplift over recently active blind duplex structures such as those that have been invoked recently by McQuarrie et al. (2008), Long et al., (2011), Tobgay et al. (2012), and Adams et al. (2013) to explain observed surface structures in Bhutan.

APPROACH AND SCOPE

We used observations of the geology and geomorphology of Bhutan, and a cosmogenic radionuclide erosion rate dataset to develop a new conceptual model of how the development of blind duplexes within a mountain range could lead to the establishment of low-relief surfaces. Second, we used the Channel Hillslope Integrated Landscape Development (CHILD) landscape evolution model (Tucker et al., 2001) to predict the landscape response (e.g. the evolution of river channel steepening, landscape relief, and erosion rate patterns) across a landscape with hinterland low-relief surfaces built by an antiformal uplift pattern and compare the result with observations from Bhutan. Third, we reconstructed paleo-river profiles

from existing data to calculate the magnitude of surface uplift, which allowed us to constrain the rate and timing of surface uplift using our suite of basin averaged erosion rates.

TECTONIC SETTING

The structural architecture of the Bhutan Himalaya is one of nested tectonostratigraphic packages separated by three major south-vergent thrust systems (Heim and Gansser, 1939; Gansser, 1983); from the south to north, these are the Main Frontal (MFT), Main Boundary (MBT) and Main Central thrust (MCT) systems (Figure 4.2A). The active MFT system, which places unmetamorphosed foreland molasse sediments on top of stable Indian cratonal units, is thought to be younger than 5 Ma (Long et al., 2012). The MBT system, plausibly having a slip history spanning ca. 10 to 3 Ma (Long et al., 2012), has carried amphibolite and greenschist facies rocks of the Lesser Himalayan sequence over the molasse sequence of the MFT hanging wall. The structurally higher MCT system carries amphiboite to granulite facies units of the Greater Himalayan sequence in its hanging wall. Various researchers have estimated a slip history for this system that began as far back as at least 23 Ma and continued until ca. 10 Ma (Chambers et al., 2011; Tobgay et al., 2012; Stuwe and Foster, 2001; Daniel et al., 2003). In general, the developmental sequence of the MCT, MBT, and MFT systems implies southward propagation of the locus of major thrusting, toward the orogenic foreland, with time, as predicted by the canonical model of orogenic wedge development. One complication is the existence of a significant shortening structure – the Kakhtang

thrust (e.g., Grujic et al., 1996) – within the Greater Himalayan sequence and striking broadly subparallel to the MCT system (Figure 4.2A). The age of Kakhtang thrusting has been estimated as ca. 14 - 10 Ma (Grujic et al., 2002), making it an out-of-sequence structure, but the tectonostratigraphic throw on this structure appears to be less than the throws of the MCT, MBT, and MFT systems below.

LOW-RELIEF LANDSCAPES OF BHUTAN

Duncan et al. (2003) made three key observations regarding the geomorphology of the Bhutan Himalaya:

> 1) The physiographic Lower Himalaya, well-known in Nepal, is lacking in the front ranges of the Bhutan (Figure 4.1A);
>
> 2) There is a belt of high-elevation (ca. 3000 m) terrain with low hillslope gradients and low local relief in the middle latitudes of the country (Figures 4.1A and 4.2) and;
>
> 3) Most longitudinal river profiles in Bhutan have large convex-up[1] knickpoints (see Figures 4.2B and 4.3). Duncan et al. (2003) further suggested that variable tectonic forcing created geomorphic variability along the strike of the range.

Baillie and Norbu (2004) noted that the wide valleys upstream of major convexities contained thick, sometimes dissected packages of sediment. The tops of these sediment packages corresponded to the major low-relief surfaces in Bhutan (Figure 4.3). Filled landscapes were initially identified beneath the Thimphu and

[1] Following convention, henceforth convex-up and concave-up will be simply referred to as convex and concave, respectively.

Bumthang surfaces (Figure 4.2B; Baillie and Norbu, 2004). Similar landscapes were subsequently identified at Phobjikha and Yarab (Grujic et al., 2006). Evidence of a fifth example may exist in the upper Kunglung Chu valley. Large N-S rivers have incised deep canyons that have isolated these surfaces: the Puna Tsang Chu, Mangde Chu, Kuri Chu, and Kunglung Chu (Figure 4.2B and 4.5). Interestingly, despite the considerable relief in these canyons, there are broad, aggraded reaches of the Puna Tsang and Kunglung Chu valleys (Figure 4.4).

The abundance of aeolian, colluvial, and alluvial deposits, as well as saprolites, on these low-relief surfaces suggest very low erosion rates. Baillie et al. (2003) documented the development of saprolites > 8 m deep at elevations up to ca. 4000 m in the Puna Tsang valley, and on the Thimphu and Bumthang surfaces. In addition, they observed paleosols interbedded with colluvial deposits, suggesting long periods of landscape stability between mass wasting events. Caspari et al. (2004) described a large flight of fluvial terraces reaching heights of over 360 m above current river elevations on the Bumthang surface. Unfortunately, the only quantitative time constraint from this suite of terraces is a ^{14}C date of 27,340 ± 180 y. BP from wood remnants found within a fill terrace ca. 41 m above the modern river (Gurung, 2001). However, the terraces above this level have more significant weathering profiles and polygenetic soils (demonstrating interruptions in soil production by climate fluctuations), indicating they are significantly older (Caspari et al., 2004). Caspari et al. (2009) later explored the Phobjikha surface and found the eastern valley was very broad and flat, and smoothed by thick colluvial and loess packages with few terrace levels.

Grujic et al. (2006) noted that the Phobjikha, Bumthang and Yarab surfaces are not correlated with any particular lithology or structure, and suggested that they are remnants of an ancient landscape. Furthermore, they postulated that the perched nature of these landscapes and the surrounding slope-break knickpoints defining pronounced convexities in river profiles indicated significant surface uplift. Grujic et al. (2006) utilized the low-temperature apatite fission track thermochronometer (closure temperature ca. 110°C; Hodges, 2014) to conclude that the mechanism of surface uplift was a reduction in erosional efficiency in the presence of constant rock uplift rates. They suggested the rain shadow cast by the rising Shillong Plateau to the south created the change in erosional efficiency after 5.9 Ma based on the fission-track results.

Hodges and Adams (2013) and Adams et al. (2013) attempted to simplify the enigmatic topography of Bhutan by separating it into 2 landforms to better understand and constrain their origin: (1) the low-relief landscape and associated downstream knickpoint and canyons; and (2) the step in topography upstream of these landscapes (Figure 4.1 and 4.2B). The later landform was referred to in those papers as Physiographic Transition 2 (PT_2) using a terminology originally developed to describe a point in the nominal topographic profile for central Nepal where mean elevations and ruggedness increases sharply to the north from the physiographic lower Himalaya to the physiographic higher Himalaya (Hodges et al., 2001). Hodges and Adams (2013) suggested that PT_2 in Bhutan might be associated with an active structure generating higher uplift rates to the north like PT_2 in central Nepal (Wobus et al., 2003; 2005; 2006; Hodges et al., 2004). Adams et al. (2013) did

locate a young structure coincident with PT_2 in Bhutan, the Lhuentse fault, which did not exhibit diagnostic kinematic indicators. However, the thermal histories of the bedrock north and south of this north-dipping fault suggested a normal-sense displacement – opposite the sense required to create the observed step in topography. While the origin of PT_2 in Bhutan remained uncertain, Adams et al. (2013) suggested that the position of PT_2 at the northern edge of the low-relief landscapes could mean that the two landforms had a related formation mechanism.

Figure 4.2B summarizes the observations made above. In this figure, we used a ratio of mean elevation to local relief (Z/R; Formento-Trigilio and Pazzaglia, 1998) to highlight the position of these landscapes across Bhutan as shown by Adams et al. (Chapter 3). This metric is useful because the low-relief landscapes of Bhutan are found at high elevations. We have highlighted outliers of glaciated topography adjacent to the southern portions of the fluvial low-relief landscapes. However, we have noted that there are also significant lobes of high, glaciated terrains that extend to ca. 40 km from the foreland of the range to the east and west of our study area.

The variation in topographic form across Bhutan is also highlighted in a map of channel steepness (Figure 4.2B). Steady-state longitudinal river profiles often have a form set by a power law relationship between channel slope and drainage area (e.g., Hack, 1957; Flint, 1974; Tarboton et al., 1989): $S = k_s A^{-\theta}$, where k_s is the channel steepness and θ is the channel concavity. We used a reference value of $\theta = 0.45$, to normalize measures of S for the change in A along the length of the channel profile and calculate a normalized channel steepness, k_{sn}. In this way were able to compare channel gradients at all drainage areas (Wobus et al., 2006).

Changes exhibited by regional topography are discretely apparent in simple river profiles. Much like the morphometric map in Figure 4.2B, prominent transverse river profiles are highly variable across Bhutan, where every large trunk stream has at least one major convex knickpoint (Figure 4.3). However, these knickpoints range in style, magnitude, and elevation. We identified two styles of knickpoints in Bhutan – vertical-step and slope-break. Vertical-step knickpoints are defined as a local, discrete increase in channel gradient, while slope-break knickpoints are identified by spatially extensive changes in channel gradient along the longitudinal profile (e.g. Haviv et al., 2010). The fluvial systems that drain the perched low-relief landscapes (e.g. Wang, Kissna, Chamkhar, and Yarab) contain major slope-break knickpoints that split the basin into two distinct relief regimes (Figure 4.2B and 4.3). Because these knickpoints are not correlated with local changes in lithology we hypothesized that they were mobile (as has been suggested previously by Grujic et al., 2006), and that they represented a dichotomy in erosion rate within the landscape. The upper reaches of these fluvial systems appear to be on the verge of becoming hanging valleys. That is, downstream of slope-break knickpoints the channels become significantly over-steepened (much higher channel steepness values than less affected tributaries and large trunk streams) and cataract. This over-steepening was likely created by an amplification of the steepness of the lower reach responding to the apparent lowering of base level (set by the elevation at the foreland for large rivers, or main stem junction for tributaries), and a lag in the response of the upper reaches due to extremely low erosion rates above the knickpoint. This condition may be created as diminished

sediment transportation across the knickpoint inhibits incision of the channel downstream (Gasparini et al., 2006; Crosby et al., 2007). Low erosion rates and sediment trapping are not unexpected for the boggy, low-relief, upper portions of these basins.

The topographic form and thick surface deposits of the low-relief landscapes of Bhutan are suggestive of an increase in uplift rate downstream, which caused back tilting. Additionally, we interpreted the abundance of high, glaciated mountain peaks in the central latitudes of the Himalaya away from crest of the range, and near the southern edges of the low-relief surfaces, as strongly suggestive that these peaks have been the focus of high rock uplift rates.

GEOMORPHIC RESPONSE TO TECTONIC FORCING

One way to produce a non-uniform uplift rate pattern in mountain belt is for a structural duplex to develop as a consequence of thrust sheets moving over ramps (Mitra, 1986). The formation and growth of duplex systems at depth result in a pattern of rock uplift similar to that across a generic detachment fold (Plesch et al., 2007), specifically the establishment of an antiform roughly orthogonal to the thrust transport direction.

In preparing interpretive geologic cross sections consistent with observed surface geology in Bhutan, McQuarrie et al. (2008) and Long et al. (2012) proposed the existence of two major duplex systems resulting in the imbrication of Lesser Himalayan rocks. A 'lower' duplex is exhumed and exposed at the foreland of the range in the hanging wall of the MBT system. The 'upper' duplex is blind (i.e., not

exposed at the surface) and positioned under the outcrop extent MCT sheet in eastern and central Bhutan (McQuarrie et al., 2008; Long et al., 2012), or beneath other Lesser Himalayan structural packages in western Bhutan (Tobgay et al., 2012; McQuarrie et al., 2014). It has been suggested that the youngest activity of this upper duplex may date to the Middle or Late Miocene (Long et al., 2012; Tobgay et al., 2012; McQuarrie et al., 2014) based on geochronometric and thermochronometric data. Invoking upper duplex development as a possible causative mechanism for demonstrably Quaternary normal faulting in the hinterland of central Bhutan, Adams et al. (2013) suggested that the upper duplex may have been active recently. If so, the evolving upper duplex would be expected to have an impact on recent surface uplift patterns and fluvial processes. We hypothesized that one response might be establishment of the low-relief landscapes in the hinterland of the Bhutan Himalaya.

The response of fluvial systems to increased downstream rock uplift has been described in foreland basins (e.g. Burbank et al., 1996; Humphrey and Konrad, 2000). Models created to illustrate this behavior predicted that some rivers would maintain their course and become antecedent systems, while others would deflect around the impinging zones of higher rock uplift rate. Indeed, under some circumstances, river incision models predicted that fluvial systems could be entirely defeated and create internally drained basins. The likelihood of tectonic defeat of rivers could additionally be enhanced by aridification as catchment headwaters are uplifted (Sobel et al., 2003).

Once a new foreland structure is active, the older thrust sheets and basins contained within those thrust sheets would be passively piggybacked (e.g. Dahlstrom, 1970; Ori and Friend, 1984), and old foreland basins would become intermontane basins. However, fluvial systems behave dynamically by aggrading to maintain, or change their course, in the face of an impinging zone of higher rock uplift downstream, (Burbank et al., 1996). In the Himalayan foreland, antiformal deformation patterns are common, but river systems exhibit variable ability to incise their substrate efficiently and maintain an antecedent position (Gupta, 1997; Lave and Avouac, 2000; 2001). The peak of river incision is co-located with the peak of the rock uplift rate, and the incision rate sharply falls upstream of the peak rock uplift where rivers must aggrade to maintain a sufficient gradient and counteract the upstream tilting on the back limb of the antiform, producing a wedge of detritus that propagates upstream as downstream uplift continues.

Models of fluvial system response can be complicated by hinterland-focused uplift patterns within intermontane basins (e.g. Mortimer et al., 2007). Because these basins likely have higher relief, the fluvial system may not be able to migrate laterally away from the focus of uplift, and will therefore be limited in its ability to respond. In such a scenario, it becomes increasingly likely that that the fluvial system will continue to aggrade upstream behind the zone of high rock uplift. In fact, aggradation upstream must keep up with net uplift at the knickpoint (e.g. Burbank et al., 1996). These predictions suggest that a non-uniform rock uplift rate pattern should be recognized from a spatially expansive suite of erosion rates in landscapes

where rock uplift is balanced by erosion. To create such a dataset we turned to cosmogenic radionuclide techniques.

MILLENNIAL-SCALE EROSION RATES

Erosion rates were estimated based on measured concentrations of cosmogenic ^{10}Be in amalgamated quartz grains from modern fluvial systems in Bhutan. This approach is designed to reveal the average erosion rate integrated across a drainage basin (e.g. Granger et al. 1995; Bierman and Stieg, 1996). Sampled basins were selected that had channel profiles indicative that the fluvial system was in a quasi-steady state, and thus likely eroding all parts of the basin at similar rates (e.g. we selected only catchments have uniform hillslope gradients, local relief, and did not have major knickpoints). We also avoided sampling basins whose bed load was dominated by recent landslides, flood deposits, and glacial detritus. Our basins were all sampled within the Greater Himalayan sequence where quartz is ubiquitous at the basin scale, or within quartz rich portions of the Lesser Himalayan sequence. As noted earlier, there is a very strong precipitation gradient from north to south in Bhutan created by the effects of orographic precipitation dynamics at the front of the range (Figure 4.6). To avoid any complicating signals of variable erosivity due to variation in climate, we only analyzed basins from the drier (mean annual rainfall from 0.43 – 1.2 m $y.^{-1}$) interior of the country. The size of the twenty-nine sampled basins ranged from ca. 2 to 132 km^2.

All samples were processed at the Arizona State University, Surface Processes WOMBAT Laboratory. Quartz grains were separated and cleaned from the

250 – 1000 μm fraction of fluvial sands utilizing standard acid and gravimetric techniques. Sieved sediments were placed in aqua regia at room temperature for 12 hours. The samples were then leached in a 5% hydrofluoric and nitric acid solution and rolled on heat for 24 hours. Feldspars and micas were floated off using a wetting technique, and dense minerals were removed via heavy liquids. During the cleaning and separation process, quartz grains were leached at least five times with hydrofluoric and nitric acids. The quartz separates were then spiked with ^{9}Be, and digested with concentrated hydrofluoric and nitric acid. We removed interfering cations and anions using liquid chromatography techniques. Oxidized beryllium, was mixing with a matrix of niobium and loaded into cathodes for analysis on an accelerator mass spectrometer at PRIME Lab, Purdue University. Beryllium isotope ratios were referenced to the isotope ratio standards described in Nishiizumi et al. (2007).

Calculating basin average erosion rates

In a recent publication, Portenga and Bierman (2011) suggested a new method to make the calculation of basin average erosion rates more transparent and comparable between studies and other regions of Earth's surface. We utilized this approach to calculate an effective elevation, latitude, and longitude value that can be used for all samples using the CRONUS online calculator (Balco et al., 2008). Based on the Advanced Spaceborne Thermal Emission Radiometer (ASTER) 30 m resolution digital elevation dataset, we calculated the scaled production rate based on the elevation and latitude of each pixel in a basin. To be internally consistent with

the procedures of the CRONUS calculator, we calculated the production rate from spallation reactions using the scheme of Stone (2000), and the production rate from muon reactions using the equations of Heisinger et al. (2002a; 2002b). We then calculated the mean of all total production rates (e.g. spallation and muon) within the basin and found the elevation and latitude values corresponding to this mean scaling factor, referred to here as the effective elevation and latitude of the basin. We then used the CRONUS calculator to calculate our erosion rates (see Appendix C for CRONUS input data). Because we were not able to adjust the production rate of muons for the erosion rate at each pixel in the basin, it is not accurate to report any time-dependent erosion rate as calculated by the CRONUS calculator for this study. We, therefore, only report the constant production rate results as determined by the models of Lal (1991) and Stone (2000) from the CRONUS online calculator.

^{10}Be basin averaged erosion rate results

Our calculated erosion rates vary between ca. 30 and 1130 m m.y.$^{-1}$ (Table 1). We estimated the timescales over which these erosion rates integrate by dividing the e-folding depth of the penetration of cosmic particles in solid rock (ca. 0.6 m) by the erosion rate. These calculations suggest that our erosion rates yielded mean rates over the past ca. 0.5 – 20 ka. The median erosion rate from the samples collected from the low-relief surfaces is 69 m m.y.$^{-1}$ with a median absolute deviation from the median of 10 m m.y.$^{-1}$. The median erosion rate from the high-relief canyons is 208 m m.y.$^{-1}$ with a median absolute deviation from the median of 77 m m.y.$^{-1}$.

Our basin average erosion rates revealed two interesting patterns. First, the catchments on the low-relief surfaces are eroding much slower than the catchments within the steep flanking terrains (Figure 4.6 and 4.7). This pattern confirms that low-relief landscapes are not eroding at the same rates as regional rock uplift rates, and that they are actively being incised and erased as river reaches down stream steepen to erode at higher rates. Second, the erosion rates of the higher-relief catchments are highest near the southern margins of the low-relief landscapes adjacent to high, isolated glacial terrains (ca. 27.2 – 27.4°N), and decrease to the north. The second pattern further suggests that recent erosion rates are driven by rock uplift rates that are non-uniform and likely highest in the middle latitudes of Bhutan (ca. 27.2 – 27.4°N). In addition, these findings imply that higher rock uplift rates in the hinterland of the range may have promoted the development of high terrain such as the abundant glacial landscapes flanking the low-relief surfaces and near the western and eastern boarders of Bhutan. Therefore, these terrains may manifest the spatial extent of duplex activity in the Eastern Himalaya (see Figure 4.2). To test our hypothesis that the topography of Bhutan may be adjusting to an antiformal uplift pattern, we turned to a landscape evolution model.

LANDSCAPE EVOLUTION MODELING

We used the CHILD landscape evolution model (Tucker et al., 2001) to explore quantitatively how fluvial systems in mountainous landscapes responded to the onset of duplex formation midway between the crest of the range and the range front. Our purpose was to test the hypothesis that rock uplift associated with the

onset of duplex formation could produce landforms analogous to the enigmatic low-relief, high-elevation surfaces described above. We did not attempt to recreate all the complexity of the Bhutanese landscapes, aiming rather for a general analysis of the role of antiformal uplift over a growing blind duplex. In particular, we did not attempt to recreate landscapes with isolated, perched patches of low relief landscapes surrounded on three sides by deep canyons, but rather focus on systems analogous to the Chamkhar, Wang, and Phobjikha rivers that developed low-relief, aggradational surfaces upstream of major slope-break knickpoints that bound over-steepened reaches downstream (Figures 4.1-5.5). Moreover, we did not attempt to simulate or constrain the rates or timing of low-relief landscape formation with our models; we are interested here in only the patterns of landscape response. Rates and timing of Bhutanese landscape evolution are addressed independently using a combination of topographic analysis and detrital cosmogenic radionuclide concentrations in later sections.

As described earlier, river bed aggradation upstream of migrating slope-break knickpoints is required for rivers to maintain their courses across a transverse, antiformal zone of rock uplift during river response to the onset of rock uplift (Burbank et al., 1996; Humphrey and Konrad, 2000). Thus to model landscape response to blind duplex growth, we represented both river incision into bedrock, and the transport and deposition of the sediment load. Moreover, as slope-break knickpoints continue to migrate upstream (both laterally and vertically) as uplift progresses (e.g., Burbank et al., 1996), the model will need to be able to simulate the erosion of weak, recently deposited, river gravels. The simplest model that meets

these requirements is the mixed or hybrid detachment and transport model (e.g., Whipple and Tucker, 2002).

Model Formulation

In mixed or hybrid mode, our model tracked the evolution of surface elevations using the conservation of mass:

$$\frac{dz(x,y)}{dt} = U(x,y) - E(x,y) \quad (1)$$

where *z(x,y)*, *U(x,y)*, and *E(x,y)* are the spatial patterns of elevation, rock uplift relative to baselevel, and erosion (defined as positive downward – where deposition is negative erosion). The erosion rate, *E(x,y)*, was dictated by either detachment of bed material or the divergence of sediment transport capacity, whichever predicted the slower, and thus limiting rate. With this formulation erosion rates were determined as detachment-limited incision whenever volumetric sediment transport capacity, Q_c, exceeded volumetric sediment flux, Q_s, and as transport-limited erosion or deposition whenever $Q_c \leq Q_s$ (e.g., Whipple and Tucker, 2002).

In our experiments detachment-limited incision was computed using the well-known stream power incision model (e.g., Howard and Kerby, 1983; Whipple and Tucker, 1999):

$$E = K_b Q^{mb} S^{nb} \quad (2)$$

where K_b is the bedrock erodibility coefficient, Q is discharge, S is the channel slope, and *mb* and *nb* are dimensionless constants, held fixed at 0.5 and 1, respectively, in our experiments. A value of 0.5 for the mb/nb ratio is consistent with theory and

observed steady-state channel concavity (e.g., Whipple and Tucker, 1999; Tucker and Whipple, 2002). K_b was assigned a higher value when previously deposited sediments (tracked and termed regolith in CHILD) were incised under detachment-limited conditions ($Q_c > Q_s$) because these were more easily eroded. This higher value of the detachment coefficient is referred to as K_r, with subscript *r* denoting erosion of regolith rather than bedrock). Under transport-limited conditions, fluvial erosion, E, was calculated as the downstream divergence of sediment transport capacity (e.g. Willgoose et al., 1991; Tucker and Bras, 1998):

$$E = -\frac{dQ_c}{dx} \tag{3a}$$

where

$$Q_c = K_f Q^{mf} S^{nf} \tag{3b}$$

K_f is the sediment transport coefficient, and *mf* and *nf* are dimensionless constants held fixed at values of 1.5 and 1, respectively, following Whipple and Tucker (2002), again to approximate typically observed concavities of steady-state or graded channels (e.g., Tucker and Whipple, 2002). K_f was assigned the same value as K_r (2.5 times K_b) in all our experiments, both for internal consistency as basins aggraded and were re-incised, and to ensure that discrete slope-break knickpoints developed during transient channel-profile adjustment to an increase in rock uplift rate (i.e., detachment-limited incision would prevail at steady-state and during a response to renewed or accelerated rock uplift).

At steady-state ($E = U$) channel slope, S, increased monotonically with rock uplift rate relative to baselevel, regardless of whether incision was detachment-limited or transport-limited:

$$S = \left(\frac{U}{K'}\right)^{\frac{1}{n'}} A^{-\theta'} \tag{4}$$

where the first term on the right hand side is the channel steepness index, k_s, $K' = K_b$ (or K_r if incising regolith), $n' = nb$, and $q' = mb/nb$ if incision is detachment-limited and $K' = K_f$, $n' = nf$, and $q' = (mf - 1)/nf$ if incision is transport-limited.

Experimental setup and initial steady-state landscape

Our experiments were designed to explore just one problem: how mountainous landscapes respond to the onset of an antiformal uplift pattern associated with blind duplex formation. For simplicity, in all cases the antiformal duplex uplift pattern was imposed upon the same initial steady-state landscape. All numerical experiments were performed on a 30 x 30 km, regular triangular lattice of 250 m node spacing with a southern open boundary. Our initial condition was a random topography described by a mean elevation of 10 m and a standard deviation of 0.5 m. We first imposed a uniform regional uplift rate and evolved the experiment until a steady-state topography associated with uniform channel steepness and erosion rate was reached (Figure 4.8A). All grid cells were initially in a detachment-limited condition. A selection of longitudinal river channel profiles of varying lengths illustrated the smooth, concave-up profiles of a landscape with uniform channel steepness values. Fluvial relief scaled with channel steepness and

catchment size (e.g., Whipple and Tucker, 1999) and thus increased steadily towards the crest of the modeled mountain range (Figure 4.8B).

Imposing an active duplex

Figure 4.8C shows the duplex uplift rate pattern that we applied to our initial steady-state topography. The pattern of uplift above the duplex was modeled as a triangular (isosceles) ridge 20 km wide across-strike. The front limb was pinned to the southern edge of the landscape. Uplift rates increased linearly toward the hinge on each limb of the antiform. North of the back limb of the duplex was a 10 km wide section of the landscape that was uniformly uplifted at the same rate as the base of the duplex (U_l), which was set equal to the initial uniform rock uplift rate such that the only perturbation to the steady-state landscape was the increase in uplift rate centered above the modeled duplex. The maximum uplift rate at the crest of the duplex (U_h) was varied between 1.5 and 10 times greater than the initial, background uplift rate. The model run with $U_h = 4 \times U_l$ was selected for illustration (Figure 4.9) as this condition effectively created slope-break knickpoints separating steep, rapidly eroding downstream reaches from aggradational upstream reaches, but was not so severe as to tectonically defeat rivers and cause drainage reversal and the formation of internally-drained basins (e.g., Sobel et al, 2003) behind a new drainage divide at the position of maximum uplift rate.

However, there may be additional processes dictating the erosion of bedrock channels or transport of sediment occurring in actual landscapes that are not possible to constrain in our model. We noted that landscape dynamics such as: the

magnitude of baselevel rise at the hinge of the duplex, the upstream smoothing of the incision signal, the lag time of the sediment flux response, and thresholds associated with changes in the drainage area, are essential for properly modeling the formation of hanging valleys (Crosby et al., 2007). On the other hand, had we included these dynamics into our model would have only increased the propensity for upstream basins to become hanging valleys as uplift rates were increased downstream.

Landscape response to duplex growth

Figure 4.9 (panels A-C) shows the initial response of our experimental landscape. The elevation of mountain peaks near the hinge of the duplex has increased and deep canyons with higher channel steepness values have formed. All channel reaches in the front limb of the duplex, and a few on the back limb, have remained detachment-limited. Local relief has increased greatly near the hinge of the duplex and decreased in parts of the back limb and behind the duplex. However, the local relief near the back of the modeled landscape has not changed because the rivers are still detachment-limited and the rock uplift rate relative to baselevel has not changed.

A map of erosion rates exhibits a similar pattern, but only a small fraction of the landscape has adjusted to a new erosion rate set by the new higher uplift rate. Figure 4.9B shows focused incision has occurred in the front limb near the hinge of the duplex. However, in the back limb deposition has been prominent as rivers have adjusted to the new high uplift rate downstream by raising their bed elevations via

aggradation. Failure to match the rising local baselevel set by the migrating knickpoint with a similar deposition rate along reaches behind the hinge of the duplex would have led to defeated river and an internally drained basin.

River profiles within the front limb of the duplex have steepened and fluvial relief has increased (Figure 4.9C). Convex knickpoints have formed in the longitudinal profiles of channels that cross the hinge of the duplex. As the knickpoints migrated headward they moved vertically, and set the rate of baselevel rise upstream. This knickpoint also tracked an important boundary between detachment- and transport-limited reaches within the landscape. The vertical movement is associated with continued surface uplift, created by disequilibrium of erosion rates and rock uplift rate and deposition upstream of the knickpoint. The surface uplift rate of landscapes changed with the variation of the rock uplift rate at the position of the convex knickpoint, as the knickpoint migrated laterally through the non-uniform uplift rate pattern. Larger basins that extended to the back of the modeled landscape also showed transient concave knickpoints where upper detachment-limited river basins became transport-limited as they aggraded their beds. The landscape created by this dichotomy in local relief and fluvial character created a physiographic transition to gentler slopes and local relief downstream; however, this transition is subtle.

Figure 4.9 (panels D – F) shows further response of our experimental landscape. The development of low-relief landscapes continued behind the hinge of the duplex, and detachment-limited channel reaches behind the duplex nearly disappeared. However, convex knickpoints have migrated farther upstream into the

back limb and have removed thick packages of sediment that were previously deposited. The elevation of mountain peaks and local relief has increased in the front limb and near the hinge of the duplex. The region near the foreland has eroded rapidly, and the very upper portions of the basins have been eroding at the background rate, but the landscapes behind the hinge of the duplex have been dominated by active deposition.

The sediment wedge that has formed from continued deposition has migrated farther upstream, and in turn the concave knickpoint and associated physiographic transition has moved headward. This knickpoint migration decreased the area of steeper landscapes above the low-relief landscape, and reduced the ability to resolve the associated physiographic transition. Surface uplift has continued, but the magnitude was not the same for all rivers. The magnitude of surface uplift was greater for rivers with convex knickpoints that remained close to the hinge of the duplex, as the rock uplift rate was greater at these positions. Fluvial relief no longer simply increased from the front to the back of the modeled landscape, and large peaks near the hinge of the duplex reached similar elevations as the back of the modeled landscape.

Model comparison with Bhutan

To compare our model output with observed data, we focused on the patterns of channel steepness, mean elevation, and local relief from our resultant elevation data. We monitored channel steepness because this metric contains information regarding the state of the river (i.e. if it is in, or out of, equilibrium), the

uplift rate it is experiencing, and its sediment transport regime (i.e. K'). Despite not directly attempting to model the evolution of the Bhutan Himalaya, our modeled landscape was strikingly similar in form, except for our inability to create intermingled aggraded valleys and deeply incised canyons across the uplift pattern. The digital elevation models exhibit high mountain peaks much closer to the front of the range coincident with the region of highest uplift rate at the hinge of the antiform uplift pattern. These high peaks are analogous to the regions of glaciated peaks outboard of the Himalayan crest in Bhutan. To the north of these peaks, the landscapes are filled with fluvial sediments and local relief is reduced, this is very similar to our observations of the low-relief landscapes of Bhutan. A pattern of high-to-low-to-high channel steepness and local relief, from the front to the back of the model, is developed much like that observed in Bhutan. The south transition (high-to-low channel steepness and local relief) marks the position of transient convex knickpoints in the model and in Bhutan. The northern transition (low-to-high channel steepness and local relief) marks the position of a transient concave knickpoint in the model and in Bhutan, where it is called PT_2.

Armed with the observations from our experimental landscape, and our morphometric analysis and field observations, we developed a new conceptual model for the formation of the low-relief landscapes of the Bhutan Himalaya. Figure 4.10 shows a cartoon of our new conceptual model and highlights a few key points. First, and foremost, the low-relief landscapes of Bhutan are not relicts of an uplifted portion of the Himalayan foothills. This means that magnitude of surface uplift cannot be measured by assuming the low-relief landscapes once graded to the

current elevation of the mouth of the river at the foreland of the range. Second, the idea behind this cartoon implies that the best method for calculating the magnitude of surface uplift is by subtracting the difference between the modern river profile and the profile of the paleo-river profile before deformation by the antifromal uplift pattern.

MAGNITUDE AND TIMING OF SURFACE UPLIFT

Quantifying surface uplift

To calculate the magnitude of surface uplift, we reconstructed the shape of the river profiles that characterized the landscape before surface uplift occurred, and then calculated the difference between the paleo-river profiles and the modern river profiles. We conducted our paleo-river reconstruction using the technique described by Shoenbohm et al. (2004) where a channel profile is projected downstream using the relationship between drainage area and channel gradient along an upstream segment that has preserved the pre-surface uplift form. We calculated the channel steepness and concavity of selected river reaches and used these values to predict elevations, where we assumed that the drainage area along the length of the fluvial system has remained largely unchanged since the onset of duplex formation. To produce the most accurate reconstructions of the rivers of Bhutan, we selected channel reaches within regions not apparently affected by recent uplift, aggradation or glaciation. Comparisons with our landscape evolution model suggested that the low-relief landscapes of Bhutan were actively aggrading as they adjust to the local baselevel rise created by a migrating convex knickpoint, and

are therefore not useful for reconstruction of paleo-river profiles. Thus, we restricted the downstream extent of reaches selected for analysis to upstream of the concave knickpoints found at the physiographic transition of Adams et al. (2013). The Lhuentse fault may lie at or near the concave knickpoints at the northern boundary of the low-relief landscapes. As we took special care to avoid the use of these reaches for our reconstructions, this fault is unlikely to affect the characteristics of our selected reaches (e.g. channel steepness or concavity) or the channel profile reconstructions. Similarly, we omitted upstream reaches where channels appear to have been influenced by glacial incision.

Of the four perched, low-relief landscapes highlighted in this study, the Yarab and Phobjikha surfaces could not be reconstructed due to lack of suitable river reaches upstream of the aggraded low-relief benches. Consequently, we focused our river profile reconstructions on the channels of the Thimpu and Bumthang surfaces (Figure 4.11). The projected outlet elevations at the foreland are very close to the modern outlet elevations. This result is remarkable and suggests the technique is robust, as our projections were not tuned to nor fixed at a constant foreland elevation. We then used the difference between the modern river profile and the reconstructed profile to calculate the surface uplift along the length of the fluvial system (Figure 4.11). The surface uplift magnitude of an individual river profile was calculated by taking the maximum difference between the modern river profile and reconstructed river profile. The magnitude of surface uplift of a perched low-relief landscape was calculated as the mean surface uplift value of multiple river profiles within that landscape. The mean surface uplift magnitudes from the Thimpu and

Bumthang surfaces are ca. 831 ± 116 m (1 standard deviation, N = 5) and 767 ± 60 m (1 standard deviation, N = 3), respectively. The slight, difference in surface uplift magnitudes between the two low-relief landscapes is likely due to: variability in rock uplift rate along strike of the duplex; signal to noise ratio within the small amount of digital elevation data used to define a short river reach; and the degree to which selected reaches faithfully record pre-surface uplift channel profiles.

Timing of initiation of surface uplift

While Adams et al. (Chapter 3) suggested that the low-relief landscapes may have started to form as early as the Pliocene based on thermochronometric data, we used the magnitude of our surface uplift of these landscapes and the pattern of erosion rates to predict the time of the initiation of surface uplift independently, and thus constrained the time of initiation of the duplex if that is indeed the causative mechanism. We used the definition of the magnitude of surface uplift:

$$\Delta Z = (U - E_h) \times t \tag{6}$$

where U is the rock uplift rate, E_h is the erosion rate in the low-relief headwaters, and t is the duration of surface uplift. We assumed that the high-relief basins adjacent to the low-relief surfaces have adjusted to a new rock uplift rate and substituted the erosion rates in the canyons with the rock uplift rate yielding:

$$t = \frac{\Delta Z}{E_c - E_h} \tag{7}$$

where E_c is the characteristic erosion rate in the deep canyons near the convex knickpoint. We calculated the timing of surface uplift using data from the two

transects shown in Figure 4.7, for which we have erosion rates at the latitudes of the high, glaciated peaks and convex knickpoints. For the Puna Tsang transect we used the following values: ΔZ = 831 m, E_c = 527 m m.y.$^{-1}$, and E_h = 53 m m.y.$^{-1}$. For the Mangde transect we used the following values: ΔZ = 767 m, E_c = 563 m m.y.$^{-1}$, and E_h = 83 m m.y.$^{-1}$. With these estimates, Equation 7 yielded initiation of surface uplift ca. 1.49 and 1.51 Ma for the Paro and Bumthang surfaces, respectively.

A caveat of this calculation is the assumption that our cosmogenic radionuclide erosion rates represent erosion rates that have been steady since the timing of surface uplift initiation ca. 1.5 Ma. We were confident that our careful analysis and selection of basins that have smooth concave profiles ensures that these landscapes must have been in quasi-steady state over the past 1-2 Ma given the response time of landscape adjustment (Whipple and Meade, 2006). It has also been demonstrated that cosmogenic nuclide erosion rates track well with independently measured estimates of rock uplift or longer-term erosion rates (Cyr and Granger, 2008; Matmon et al., 2003; Ouimet et al., 2009; Wittmann et al., 2007). Similarly, modeled erosion rates from low-temperature thermochronometers averaged over the Quaternary yield similar values as nearby millennial scale erosion rates within the Mangde and Kuri Chu valleys, (ca. 120 – 270 m m.y.$^{-1}$; Figure 4.6) (Adams et al., Chapter 3). As stated by Adams et al. (Chapter 3), the modeled, long-term erosion rate histories could also permit an increase in erosion rate (ca. 1000 m m.y.$^{-1}$) during the Quaternary, which might have been the case where basin average erosion rates are higher near glaciated peaks.

DISCUSSION

Blind duplexes underlying the hinterland of the Bhutan Himalaya have been suggested by studies involving balanced cross sections (McQuarrie et al., 2008; Long et al., 2011; Long et al., 2012; Tobgay et al., 2012; Bhargava, 1995). The tectonic significance of active or reactivated duplexes in the hinterland of mountain ranges has been explored for many decades (e.g. Robinson et al., 2003; DeCelles et al., 1995; Erickson et al., 2001; Mitra and Sussman, 1997; Ferril and Dunne, 1989), and it is thought that this method of crustal thickening is important for the hinterland to maintain a critical taper. When active, these blind duplexes uplift and deform the overlying rocks to varying degrees depending on the nature of the blind thrusting (e.g. Ferril and Dune, 1989). However, the response of surface processes to such a tectonic condition has not been thoroughly studied.

The results from our landscape evolution experiments suggest that an active duplex dramatically changes the surface cover (e.g. alluvial and colluvial sediments, bedrock, saprolite) and topography of a mountain range. We designed these experiments with two important boundary conditions. The sediment transport coefficient was higher than the bedrock erodibility coefficient, and the uplift at the hinge of the duplex was four times larger than the uplift rates at the ends of the limbs. The flexibility of river reaches to act as transport- or detachment-limited changed the relief structure spatially and temporally within the experimental landscape. The lower sediment transportation efficiency yielded lower relief in detachment-limited basins as compared to detachment-limited basins with the same rock uplift rate. The erodibilty contrast between bedrock, regolith and sediment also

acted to attenuate and retard knickpoint migration (e.g. Crosby et al., 2007), which slowed landscape response. The ratio of uplift rates set the equivalent of a rotational velocity of the backtilting in the back limb of the duplex. This uplift rate ratio was required to create a knickpoint that moved slow enough to allow low-relief landscapes form upstream, but ensure that rivers were not completely defeated, causing drainage reversal in our experiments. Save the initial testing to ensure low-relief landscapes were formed, subsequent changing of these boundary conditions modified the landscape response time and the scale of topographic parameters; however, the pattern of landscape response, which we considered to be the most meaningful result of our modeling, remained steady.

By design, all drainages that crossed the active duplex in our experiments developed large convex knickpoints and the upper portions of the drainage appeared to be at least temporarily disconnected from the baselevel of the entire fluvial system by an extremely steep reach of the river (Figure 4.9F). This quasi-hanging valley condition was forced by the selection of the uplift rate at the hinge of the duplex. It was necessary to select a large uplift ratio because the basic rules for sediment transport and river incision (i.e. Eqs. 2 and 3) did not provide an adequate mechanism for the creation of hanging valleys in our model. Consequently, a lower uplift rate ratio could have created hanging valley systems under a more complicated fluvial regime, which might better explain why not all N-S trending rivers in Bhutan that cross the blind duplexes form perched low-relief landscapes (Figure 4.2B).

Despite the simplicity of our landscape evolution model, the results of our experiments were very informative. Our landscape evolution experiment confirmed the hypothesis that a hinterland duplex would create actively infilling and uplifting piggyback basins. There are many examples of similar processes occurring near the foreland of the Himalaya where actively growing antiforms impede drainages, and form sediment filled intermontane basins (e.g. Valdiya, 1993). Among these examples, is the spectacular and well-known Kathmandu Basin, which has at times been the site of swallow lakes and gentle rivers from the Pliocene through the Quaternary (e.g. Dill et al., 2003). The many generations of lacustrian and alluvial and colluvial fills have dramatically reduced the local relief in this portion of the Central Nepal Himalaya.

Our landscape evolution experiment also supported the hypothesis that these low-relief landscapes were transient features incised by a headward migrating convex knickpoint, as evident from the dichotomy in erosion rates between the low-relief surfaces and adjacent canyons. Most importantly, we found that these low-relief surfaces were formed during uplift (Figure 4.10). This point is an important reinterpretation of the evolution of the Bhutan Himalaya, and suggests that the low-relief landscapes never formed a terrain that was analogous to the foothills of the central Himalaya.

Our experiments also provided interesting insight into the formation of PT_2 in Bhutan. A break in local relief and mean elevation formed upstream of the duplex in our experiment. Mountain peaks upstream of the duplex continued to erode, but the resulting sediments were stored locally in broad alluvial valleys because of the

impinging zone of high rock uplift rate downstream. The results of our experiments suggested that the boundary of deposition and relief reduction migrates headward, and that the strength of this signal as detected in the local relief was decreased as a function of time. If PT_2 in Bhutan was formed by a similar mechanism, then it is not structurally controlled, and is instead a transient landform whose position is dictated by the migration of a concave knickpoint at the north edge of the low-relief surfaces. While Adams et al. (2013) did note a correlation of PT_2 and the Lhuentse fault, they concluded the kinematics of the fault were not suggestive of a forming mechanism. We have concluded that the correlation of PT_2 and the Lhuentse fault could be expected if both were formed near the northern edge of an active blind duplex. In addition, the timing of surface uplift is provocative as it is around the same time that Adams et al. (2013) suggested that the Lhuentse fault (Quaternary), which was likely created by the recent activity of a blind duplex.

As laid out by Adams et al. (Chapter 3), there has been a disconnect in Bhutan between the temporal constraints of long-lived tectonic process, measured with geo- and thermochronometry data, the more recent landscape response to tectonic and climatic processes, which are too young for these techniques, and the modern deformation field that can be measured using geodesy. In this study we have bridged the gap between these observations and processes to develop a more complete image of the evolution of the Bhutan Himalaya. Analyses of geo- and thermochronometric data have led past authors to suggest that shortening across Bhutan decreased due to the partitioning of slip between Himalayan and Shillong Plateau structures in the Miocene (Long et al., 2012; Coutand et al., 2014; Adams et

al., Chapter 3). While the effect of this slow down, would manifest as a slow wearing down of the Eastern Himalaya (e.g. Clark and Bilham, 2008), the observation of surface uplift calls for a more recent rejuvenation of the range. Unfortunately, constraints on the timing and mechanism of surface uplift were beyond the reach of the older chronometers used in the above studies. We have presented here a new tectonic mechanism for surface uplift based on observations and millennial-scale erosion rates, and backed by a landscape evolution model governed by empirical and physics based relationships. The creation of low-relief landscapes of Bhutan, and the associated physiographic transition, PT_2, can be explained by the activation of a young (ca. 1.5 Ma) antiformal uplift pattern, similar to what might be expected by a blind duplex. This young duplex growth may be associated with a structural adjustment within the Himalaya after returning to previous shortening rates. This recent rejuvenation of deformation in Bhutan may explain the nearly uniform convergence rates across the central and eastern Himalaya revealed in modern geodetic data (e.g. Jouanne et al., 1999; Larson et al., 1999; Banerjee et al., 2008).

CONCLUSION

The variability in the surface deposits, fluvial dynamics and mean elevation in the Bhutan Himalaya suggests a dynamic landscape where all facets may not be explained by simple foreland fault activity or climate change. However, we have found that the creation of high, sediment filled, low-relief, fluvial landscapes, and high, glaciated landscapes in the middle latitudes of the Bhutan Himalaya can be explained by landscape adjustment to a complex uplift rate pattern created by an

active duplex. To explore the plausibility of this hypothesis we utilized a landscape evolution model. We have demonstrated that landscapes with similar patterns of topography and erosion rate are readily formed when using a very simple triangular uplift pattern.

A similar uplift pattern in Bhutan is supported by the spatial pattern in millennial scale, basin average cosmogenic nuclide erosion rates. These erosion rates also revealed that the low-relief landscapes are, in fact, transient and undergoing surface uplift. We capitalized on preserved reaches of rivers that have not experienced syn-surface uplift deposition or glacial incision, to reconstruct river profiles that are representative of the form of landscapes before recent duplex deformation. With these paleo-river profiles we calculated the surface uplift magnitude of the low-relief surfaces in Bhutan, where the mean magnitude of uplift is ca. 800 m. With the magnitude of surface uplift constrained, and estimates of the current and former uplift rates from our basin average erosion rates, we found that surface uplift was initiated ca. 1.5 Ma. The recent activation of a duplex in the hinterland of the Bhutan Himalaya may suggest the range is adjusting to increase the after a protracted period of decreased fault slip rates due to the development of the Shillong Plateau to the south during the Miocene (Adams et al., Chapter 3).

ACKNOWLEDGEMENTS

This work was supported by a National Science Foundation Tectonics Program grant EAR 0708714 to K.V.H. and a joint Tectonics and Geomorphology and Landuse Dynamics Programs grant EAR 1049888 to K.X.W. and A.M.H. B.A.A. is

grateful for the efforts of Frances Cooper (School of Earth Sciences, University of Bristol) both in the field and at the drawing board. Fieldwork would not have been possible without support of our friends and colleagues in Bhutan: Peldon Tshering (National Environment Commission), Ugyen Wanda (Department of Geology and Mines), Karma Choden and Ugyen Rinzen (Yangphel Adventure Travel).

FIGURE CAPTIONS

Figure 4.1. A) Thirty kilometer-wide swath profiles, perpendicular to the strike of the range, from central Bhutan and central Nepal (see Figure 4.2 for locations). The solid black line represents the mean elevation the Bhutan swath and the surrounding dark grey envelope denotes 2 standard deviations. The dashed black line represents the mean elevation of the Nepal swath and the surrounding light grey envelope denotes 2 standard deviations. White dots mark the Physiographic Transition 2 in Nepal and Bhutan. B) Longitudinal profiles of river systems within the swath profiles from A. The solid black line shows the form of the Chamkhar Chu and its tributaries that drain the Bumthang surface of Bhutan. The dashed black line shows the form of the Modi Khola and its tributaries that drain the Annapurna region of Nepal. A black dot marks the major convex knickpoint on the Chamkhar Chu. A white dot marks the convex knickpoint associated with Physiographic Transition 2.

Figure 4.2. Geography, geology and geomorphology of Bhutan. A) Elevation map from 30 m Advanced Spaceborne Thermal Emission Radiometer data. Grey lines

denote the political boarders. Red and white dots mark the locations of the photos in Figures 4.4 and 4.5. White box denotes the swath area of data in Figure 4.1. Red dotted line on inset map is the location of the Nepal swath in Figure 4.1. Cities are shown as black dots. MFT - Main Frontal thrust system; MBT - Main Boundary thrust system; Main Central thrust system; KT - Kakhtang thrust; STF - South Tibetan fault system; PW - Paro Window; JF - Jomolhari fault system; LF - Lhuentse fault. B) Map of Z/R calculated as the ratio of mean elevation to local relief where both metrics are calculated using a 5 km radius moving window. Note that high surfaces with low relief are light colored. The river channels are colored by channel steepness values (see text for description). Black lines mark the location of Physiographic Transition 2. Solid white lines show the extent of the low-relief landscapes. Dotted white lines highlight the high, glaciated terrains adjacent to the low-relief landscapes. Magenta ellipses highlight additional high, glacial terrains near the foreland. TS - Thimpu surface; PS - Phobjikha surface; BS - Bumthang surface; YS - Yarab surface; WA - Wang Chu; PT - Puna Tsang Chu; MA - Mangde Chu; CH - Chamkhar Chu; KR - Kuri Chu; KL - Kunglung Chu.

Figure 4.3. Examples of longitudinal river profiles of the Bhutan Himalaya (see Figure 4.2B for locations). A) Profiles from the four low-relief landscapes. B) Profiles from the fluvial systems that dissect the low-relief surfaces.

Figure 4.4. Examples of the low-relief landscapes and alluvial reaches of otherwise deeply incised valleys (see Figure 4.2A for locations). A) Looking north at the city of

Thimpu on the Thimpu surface. B) Looking east on the Phobjikha surface. C) Looking northwest near the town of Jakar on the Bumthang surface. D) Looking north at the Punakha Dzong on the Puna Tsang Chu. E) Looking north in the Kunglung Chu valley north of Tashigang.

Figure 4.5. Examples of the deep canyons that dissect low-relief surfaces in Bhutan (see Figure 4.2A for locations). A) Looking south (downstream) on the Puna Tsang Chu, south of the town of Wangdue. B) Looking south (downstream) on the Mangde Chu north of the town of Zhemgang. C) Looking northwest in a tributary basin of the Kuri Chu northwest of the town of Mongar. D) Looking north (upstream) on the Kunglung Chu north of the city of Tashigang.

Figure 4.6. Map of mean annual precipitation derived from Tropical Rainfall Measurement Mission data (Bookhagen, in review) and basin averaged erosion rates in Bhutan. Low-relief fluvial surfaces are outlined in bold black lines. Outliers of glacial terrains are outlines with dashed black lines. Dashed white boxes show the extent of transects in Figure 4.7. Magenta circles mark the locations of thermochronometric studies that yielded Quaternary erosion rates of ca. 120-270 m m.y.$^{-1}$ (Adams et al., Chapter 2). A collection of high erosion rates is located near the hinge of the duplex in the middle latitudes near high glacial landscapes. Low-relief surfaces are dominated by very low erosion rates. Note that mean annual precipitation significantly decreases away from the Himalayan range front, and generally remains constant in the middle latitudes of Bhutan.

Figure 4.7. Basin averaged erosion rates from three transects in Bhutan. See Figure 4.6 for locations. Basins are plotted by the elevation of the outlet where the samples were collected (ordinate), the mean latitude (abscissa; error bars denote range), and erosion rate (color). Vertical grey bars mark the latitudes of glacial terrain outliers in each transect. Diagonal lines denote the locations of the Thimpu surface in A, and the Bumthang surface in B and C.

Figure 4.8. (A) Initial steady-state topography created with a uniform uplift rate. Erosion rate and channel steepness values are equal in all parts of the landscape. Numbers mark the locations of basins in B. (B) Longitudinal profiles of rivers from the initial steady-state landscape. (C) Map of the rock uplift rate gradient later imposed on the initial steady-state landscape. Cross section shows the shape of the uplift rate function. U_h – high uplift rate of at the hinge of the duplex, U_l – low uplift rate at the base of the duplex.

Figure 4.9. (A and D) Transient topographies created after initial, and further response to an active duplex. River channels are colored by channel steepness. Numbers mark the locations of basins in C and F. (B and E) Erosion rate maps created after initial, and further response to an active duplex. (C & F) Longitudinal profiles created after initial, and further response to an active duplex. Red dots mark the locations of transient convex knickpoints. Blue dots mark the location of transient concave knickpoints and the juxtaposition of terrains similar to

Physiographic Transition 2 in Bhutan. The dashed lines represent the initial profiles of steady-state rivers (Figure 4.8B). The magnitude of surface uplift (ΔZ) at each time step can be measured directly. Lines mark the positions of changes in the rock uplift rate gradient seen in Figure 4.8C. U_h – high uplift rate of at the hinge of the duplex, U_l – low uplift rate at the base of the duplex.

Figure 4.10. Cartoon cross section showing the evolution of a landscape affected by an active duplex in the hinterland of a mountain range. Dashed gray line shows the initial river profile before duplex activity. The upper discontinuity in the profile is created by glacial incision. The black line denotes the shape of the perturbed river profile. The stippled pattern marks the packages of sediment accumulating upstream of a migrating convex knickpoint (black dot) and forming the migrating concave knickpoint upstream (white dot). Portions of the original fluvial landscape are preserved between the concave knickpoint and glacial terrains. The magnitude of surface uplift (ΔZ) can be easily calculated as the greatest difference between the former and current river profile. This magnitude calculated in this way (black markers) is much smaller than if the aggraded reaches are extrapolated to the foreland of the range (gray markers). A) Landscape soon after duplex activation. B) Landscape long after duplex activation. Note that older packages of sediment are cut and rotated as duplex activity continues.

Figure 4.11. Upper black solid lines are the longitudinal profiles sampled from 30 m digital elevation data. Dashed gray lines are the projected profiles of the preserved

reaches (thick gray lines). Lower thick black lines show the magnitude of surface uplift along the profiles. The bounding envelope of horizontal lines shows the range of surface uplift as recorded by multiple river profiles from each region. A) Data from the Thimpu surface. B) Data from the Bumthang surface.

REFERENCES

Adams, B. A., Hodges, K. V., van Soest, M. C., & Whipple, K. X. (2013). Evidence for Pliocene-Quaternary normal faulting in the hinterland of the Bhutan Himalaya. *Lithosphere, 5*(4), 438-449. doi: 10.1130/l277.1

Baillie, I. C., & Norbu, C. (2004). Climate and other factors in the development of river and interfluve profiles in Bhutan, Eastern Himalayas. *Journal of Asian Earth Sciences, 22*(5), 539-553. doi: 10.1016/s1367-9120(03)00092-0

Baillie, I. C., Tshering, K., Dorji, T., Tamang, H. B., Norbu, C., Hutcheon, A. A., & Baumler, R. (2004). Regolith and soils in Bhutan, Eastern Himalayas. *European Journal of Soil Science, 55*(1), 9-27. doi: 10.1046/j.1365-2389.2003.00579.x

Balco, G., Stone, J. O., Lifton, N. A., & Dunai, T. J. (2008). A complete and easily accessible means of calculating surface exposure ages or erosion rates from (10)Be and (26)Al measurements. *Quaternary Geochronology, 3*(3), 174-195. doi: 10.1016/j.quageo.2007.12.001

Baldwin, J. A., Whipple, K. X., & Tucker, G. E. (2003). Implications of the shear stress river incision model for the timescale of postorogenic decay of topography. *Journal of Geophysical Research-Solid Earth, 108*(B3), 17. doi:

10.1029/2001jb000550

Banerjee, P., Burgmann, R., Nagarajan, B., & Apel, E. (2008). Intraplate deformation of the Indian subcontinent. *Geophysical Research Letters, 35*(18), 5. doi: 10.1029/2008gl035468

Bhargava, O. (1995). *The Bhutan Himalaya, a geological account*: Geological Survey of India.

Bierman, P., & Steig, E. J. (1996). Estimating rates of denudation using cosmogenic isotope abundances in sediment. *Earth Surface Processes and Landforms, 21*(2), 125-139. doi: 10.1002/(sici)1096-9837(199602)21:2<125::aid-esp511>3.0.co;2-8

Bollinger, L., Avouac, J. P., Beyssac, O., Catlos, E. J., Harrison, T. M., Grove, M., Goffé, B., & Sapkota, S. (2004). Thermal structure and exhumation history of the Lesser Himalaya in central Nepal. *Tectonics, 23*(5), TC5015.

Bollinger, L., Henry, P., & Avouac, J. P. (2006). Mountain building in the Nepal Himalaya: Thermal and kinematic model. *Earth and Planetary Science Letters, 244*(1), 58-71.

Burbank, D., Meigs, A., & Brozovic, N. (1996). Interactions of growing folds and coeval depositional systems. *Basin Research, 8*(3), 199-223. doi: 10.1046/j.1365-2117.1996.00181.x

Caspari, T., Baumler, R., Dorji, T., Norbu, C., Tshering, K., & Baillie, I. (2004). Pedochemical characterisation and landscape history of the Thangbi river terrace system, central Bhutan. *Zeitschrift Fur Geomorphologie, 48*(2), 145-166.

Caspari, T., Baumler, R., Norbu, C., Tshering, K., & Baillie, I. (2009). Soil formation in Phobjikha Valley, Central Bhutan with special regard to the redistribution of loessic sediments. *Journal of Asian Earth Sciences, 34*(3), 403-417. doi: 10.1016/j.jseaes.2008.07.002

Cattin, R., Martelet, G., Henry, P., Avouac, J. P., Diament, M., & Shakya, T. R. (2001). Gravity anomalies, crustal structure and thermo-mechanical support of the Himalaya of central Nepal. *Geophysical Journal International, 147*(2), 381-392.

Chambers, J., Parrish, R., Argles, T., Harris, N., & Horstwood, M. (2011). A short-duration pulse of ductile normal shear on the outer South Tibetan detachment in Bhutan: Alternating channel flow and critical taper mechanics of the eastern Himalaya. *Tectonics, 30*, 12. doi: 10.1029/2010tc002784

Chapple, W. M. (1978). Mechanics of thin-skinned fold-and-thrust belts. *Geological Society of America Bulletin, 89*(8), 1189-1198. doi: 10.1130/0016-7606(1978)89<1189:motfb>2.0.co;2

Crosby, B. T., Whipple, K. X., Gasparini, N. M., & Wobus, C. W. (2007). Formation of fluvial hanging valleys: Theory and simulation. *Journal of Geophysical Research-Earth Surface, 112*(F3), 20. doi: 10.1029/2006jf000566

Cyr, A. J., & Granger, D. E. (2008). Dynamic equilibrium among erosion, river incision, and coastal uplift in the northern and central Apennines, Italy. *Geology, 36*(2), 103-106.

Dahlen, F. A. (1990). Critical taper model of fold-and-thrust belts and accretionary wedges. *Annual Review of Earth and Planetary Sciences, 18*, 55-99. doi:

10.1146/annurev.earth.18.1.55

Dahlstrom, C. D. (1970). Structural geology in the eastern margin in the eastern margin of the Canadian Rocky Mountains. *Bulletin of Canadian Petroleum Geology, 18*(3), 332-406.

Daniel, C., Hollister, L., Parrish, R. t., & Grujic, D. (2003). Exhumation of the Main Central Thrust from lower crustal depths, eastern Bhutan Himalaya. *Journal of Metamorphic Geology, 21*(4), 317-334.

Decelles, P. G., Lawton, T. F., & Mitra, G. (1995). Thrust timing, growth of structural culminations, and synorogenic sedimentation in the type Sevier Orogenic Belt, western United States. *Geology, 23*(8), 699-702. doi: 10.1130/0091-7613(1995)023<0699:ttgosc>2.3.co;2

Dill, H. G., Khadka, D. R., Khanal, R., Dohrmann, R., Melcher, F., & Busch, K. (2003). Infilling of the Younger Kathmandu-Banepa intermontane lake basin during the Late Quaternary (Lesser Himalaya, Nepal): a sedimentological study. *Journal of Quaternary Science, 18*(1), 41-60. doi: 10.1002/jqs.726

Duncan, C., Masek, J., & Fielding, E. (2003). How steep are the Himalaya? Characteristics and implications of along-strike topographic variations. *Geology, 31*(1), 75-78.

Erickson, S. G., Strayer, L. M., & Suppe, J. (2001). Initiation and reactivation of faults during movement over a thrust-fault ramp: numerical mechanical models. *Journal of Structural Geology, 23*(1), 11-23. doi: 10.1016/s0191-8141(00)00074-2

Ferrill, D. A., & Dunne, W. M. (1989). Cover deformation above a blind duplex – an

example from West Virginia, USA. *Journal of Structural Geology, 11*(4), 421-431. doi: 10.1016/0191-8141(89)90019-9

Flint, J. (1974). Stream gradient as a function of order, magnitude, and discharge. *Water Resources Research, 10*(5), 969-973.

Formento-Trigilio, M. L., & Pazzaglia, F. J. (1998). Tectonic geomorphology of the Sierra Nacimiento: Traditional and new techniques in assessing long-term landscape evolution in the Southern Rocky Mountains. *Journal of Geology, 106*(4), 433-453.

Gansser, A. (1983). Geology of the Bhutan Himalaya (Vol. 96, pp. 181). Basel: Birkhäuser Verlag.

Gasparini, N. M., Bras, R. L., & Whipple, K. X. (2006). Numerical modeling of non–steady-state river profile evolution using a sediment-flux-dependent incision model. In S. D. Willett, Hovius, N., Brandon, M.T., and Fisher, D. (Ed.), *Tectonics, climate, and landscape evolution: Geological Society of America Special Paper* (Vol. 398, pp. 127-141).

Granger, D. E., Kirchner, J. W., & Finkel, R. (1996). Spatially averaged long-term erosion rates measured from in situ-produced cosmogenic nuclides in alluvial sediment. *Journal of Geology, 104*(3), 249-257.

Grujic, D., Casey, M., Davidson, C., Hollister, L. S., Kündig, R., Pavlis, T., & Schmid, S. (1996). Ductile extrusion of the Higher Himalayan Crystalline in Bhutan: evidence from quartz microfabrics. *Tectonophysics, 260*(1), 21-43.

Grujic, D., Coutand, I., Bookhagen, B., Bonnet, S., Blythe, A., & Duncan, C. (2006). Climatic forcing of erosion, landscape, and tectonics in the Bhutan Himalayas.

Geology, 34(10), 801-804. doi: 10.1130/g22648.1

Grujic, D., Hollister, L. S., & Parrish, R. R. (2002). Himalayan metamorphic sequence as an orogenic channel: insight from Bhutan. *Earth and Planetary Science Letters, 198*(1), 177-191.

Gupta, S. (1997). Himalayan drainage patterns and the origin of fluvial megafans in the Ganges foreland basin. *Geology, 25*(1), 11-14.

Gurung, D. R. (2001). Quaternary system in the Chamkhar and Tang Valley floor. *Bhutan Geology Newsletter, 4*, 1-6.

Hancock, G. S., Anderson, R. S., Chadwick, O. A., & Finkel, R. C. (1999). Dating fluvial terraces with Be-10 and Al-26 profiles: application to the Wind River, Wyoming. *Geomorphology, 27*(1-2), 41-60. doi: 10.1016/s0169-555x(98)00089-0

Haviv, I., Enzel, Y., Whipple, K. X., Zilberman, E., Matmon, A., Stone, J., & Fifield, K. L. (2010). Evolution of vertical knickpoints (waterfalls) with resistant caprock: Insights from numerical modeling. *Journal of Geophysical Research-Earth Surface, 115*, 22. doi: 10.1029/2008jf001187

Heim, A., & Gansser, A. (1939). *Central Himalaya: Geological Observations of the Swiss Expedition 1936* (Vol. 73). Zurich: Mémoires de la Société Helvétique des Sciences Naturelles.

Heisinger, B., Lal, D., Jull, A. J. T., Kubik, P., Ivy-Ochs, S., Knie, K., & Nolte, E. (2002). Production of selected cosmogenic radionuclides by muons: 2. Capture of negative muons. *Earth and Planetary Science Letters, 200*(3-4), 357-369.

Heisinger, B., Lal, D., Jull, A. J. T., Kubik, P., Ivy-Ochs, S., Neumaier, S., . . . Nolte, E.

(2002). Production of selected cosmogenic radionuclides by muons 1. Fast muons. *Earth and Planetary Science Letters, 200*(3-4), 345-355. doi: 10.1016/s0012-821x(02)00640-4

Hodges, K. V. (2014). Thermochronology in Orogenic Systems. In H. D. Holland & K. K. Turekian (Eds.), *Treatise on Geochemistry* (2 ed., Vol. 4, pp. 281-308). Oxford: Elsevier.

Hodges, K. V., & Adams, B. A. (2013). The influence of middle and lower crustal flow on the landscape evolution of orogenic plateaus: Insights from the Himalaya and Tibet. In L. Owen (Ed.), *Treatise on Geomorphology* (Vol. 5). San Diego: Academic Press.

Hodges, K. V., Hurtado, J. M., & Whipple, K. X. (2001). Southward extrusion of Tibetan crust and its effect on Himalayan tectonics. *Tectonics, 20*(6), 799-809.

Hodges, K. V., Wobus, C., Ruhl, K., Schildgen, T., & Whipple, K. (2004). Quaternary deformation, river steepening, and heavy precipitation at the front of the Higher Himalayan ranges. *Earth and Planetary Science Letters, 220*(3), 379-389.

Howard, A. D., Dietrich, W. E., & Seidl, M. A. (1994). Modeling fluvial erosion on regional to continental scales. *Journal of Geophysical Research: Solid Earth (1978–2012), 99*(B7), 13971-13986.

Humphrey, N. F., & Konrad, S. K. (2000). River incision or diversion in response to bedrock uplift. *Geology, 28*(1), 43-46. doi: 10.1130/0091-7613(2000)28<43:riodir>2.0.co;2

Jouanne, F., Mugnier, J. L., Pandey, M. R., Gamond, J. F., Le Fort, P., Serrurier, L., Vigny,

C., Avouac, J. P. & Idylhim (1999). Oblique convergence in the Himalayas of western Nepal deduced from preliminary results of GPS measurements. *Geophysical Research Letters, 26*(13), 1933-1936. doi: 10.1029/1999gl900416

Kirby, E., & Whipple, K. (2001). Quantifying differential rock-uplift rates via stream profile analysis. *Geology, 29*(5), 415-418. doi: 10.1130/0091-7613(2001)029<0415:qdrurv>2.0.co;2

Korup, O., Clague, J. J., Hermanns, R. L., Hewitt, K., Strom, A. L., & Weidinger, J. T. (2007). Giant landslides, topography, and erosion. *Earth and Planetary Science Letters, 261*(3-4), 578-589. doi: 10.1016/j.epsl.2007.07.025

Lal, D. (1991). Cosmic ray labeling of erosion surfaces – in situ nuclide production rates and erosion models. *Earth and Planetary Science Letters, 104*(2-4), 424-439. doi: 10.1016/0012-821x(91)90220-c

Larson, K. M., Bürgmann, R., Bilham, R., & Freymueller, J. T. (1999). Kinematics of the India-Eurasia collision zone from GPS measurements. *Journal of Geophysical Research: Solid Earth (1978–2012), 104*(B1), 1077-1093.

Lave, J., & Avouac, J. P. (2000). Active folding of fluvial terraces across the Siwaliks Hills, Himalayas of central Nepal. *Journal of Geophysical Research-Solid Earth, 105*(B3), 5735-5770. doi: 10.1029/1999jb900292

Lave, J., & Avouac, J. P. (2001). Fluvial incision and tectonic uplift across the Himalayas of central Nepal. *Journal of Geophysical Research-Solid Earth, 106*(B11), 26561-26591. doi: 10.1029/2001jb000359

Long, S., McQuarrie, N., Tobgay, T., & Grujic, D. (2011). Geometry and crustal

shortening of the Himalayan fold-thrust belt, eastern and central Bhutan. *Geological Society of America Bulletin, 123*(7-8), 1427-U1244. doi: 10.1130/b30203.1

Long, S. P., McQuarrie, N., Tobgay, T., Coutand, I., Cooper, F. J., Reiners, P. W., Wartho, J. A. & Hodges, K. V. (2012). Variable shortening rates in the eastern Himalayan thrust belt, Bhutan: Insights from multiple thermochronologic and geochronologic data sets tied to kinematic reconstructions. *Tectonics, 31*, 23. doi: 10.1029/2012tc003155

Lyon-Caen, H., & Molnar, P. (1983). Constraints on the structure of the Himalaya from an analysis of gravity anomalies and a flexural model of the lithosphere. *Journal of Geophysical Research, 88*(B10), 8171-8191.

Lyon-Caen, H., & Molnar, P. (1985). Gravity anomalies, flexure of the Indian plate, and the structure, support and evolution of the Himalaya and Ganga basin. *Tectonics, 4*(6), 513-538.

Matmon, A., Bierman, P., Larsen, J., Southworth, S., Pavich, M., & Caffee, M. (2003). Temporally and spatially uniform rates of erosion in the southern Appalachian Great Smoky Mountains. *Geology, 31*(2), 155-158.

McQuarrie, N., Robinson, D., Long, S., Tobgay, T., Grujic, D., Gehrels, G., & Ducea, M. (2008). Preliminary stratigraphic and structural architecture of Bhutan: Implications for the along strike architecture of the Himalayan system. *Earth and Planetary Science Letters, 272*(1-2), 105-117. doi: 10.1016/j.epsl.2008.04.030

McQuarrie, N., Tobgay, T., Long, S. P., Reiners, P. W., & Cosca, M. A. (2014). Variable

exhumation rates and variable displacement rates: Documenting recent slowing of Himalayan shortening in western Bhutan. *Earth and Planetary Science Letters, 386*, 161-174.

Mitra, G., & Boyer, S. E. (1986). Energy balance and deformation mechanisms of duplexes. *Journal of Structural Geology, 8*(3-4), 291-304. doi: 10.1016/0191-8141(86)90050-7

Mitra, G., & Sussman, A. J. (1997). Structural evolution of connecting splay duplexes and their implications for critical taper: An example based on geometry and kinematics of the Canyon Range culmination, Sevier Belt, central Utah. *Journal of Structural Geology, 19*(3-4), 503-521. doi: 10.1016/s0191-8141(96)00108-3

Mortimer, E., Carrapa, B., Coutand, I., Schoenbohm, L., Sobel, E. R., & Gomez, J. S. (2007). Fragmentation of a foreland basin in response to out-of-sequence basement uplifts and structural reactivation: El Cajon-Campo del Arenal basin, NW Argentina. *Geological Society of America Bulletin, 119*(5-6), 637-653. doi: 10.1130/b25884.1

Nishiizumi, K., Imamura, M., Caffee, M. W., Southon, J. R., Finkel, R. C., & McAninch, J. (2007). Absolute calibration of< sup> 10</sup> Be AMS standards. *Nuclear Instruments and Methods in Physics Research Section B: Beam Interactions with Materials and Atoms, 258*(2), 403-413.

Ori, G. G., & Friend, P. F. (1984). Sedimentary basins formed and carried piggyback on active thrust sheets. *Geology, 12*(8), 475-478. doi: 10.1130/0091-7613(1984)12<475:sbfacp>2.0.co;2

Ouimet, W. B., Whipple, K. X., & Granger, D. E. (2009). Beyond threshold hillslopes: Channel adjustment to base-level fall in tectonically active mountain ranges. *Geology, 37*(7), 579-582.

Pearson, O. N., & DeCelles, P. G. (2005). Structural geology and regional tectonic significance of the Ramgarh thrust, Himalayan fold-thrust belt of Nepal. *Tectonics, 24*(4), TC4008.

Plesch, A., Shaw, J. H., & Kronman, D. (2007). Mechanics of low-relief detachment folding in the Bajiaochang field, Sichuan Basin, China. *Aapg Bulletin, 91*(11), 1559-1575. doi: 10.1306/06200706072

Portenga, E. W., & Bierman, P. R. (2011). Understanding Earth's eroding surface with 10 Be. *GSA Today, 21*(8), 4-10.

Robinson, D. M., DeCelles, P. G., Garzione, C. N., Pearson, O. N., Harrison, T. M., & Catlos, E. J. (2003). Kinematic model for the Main Central thrust in Nepal. *Geology, 31*(4), 359-362.

Schoenbohm, L., Whipple, K., Burchfiel, B., & Chen, L. (2004). Geomorphic constraints on surface uplift, exhumation, and plateau growth in the Red River region, Yunnan Province, China. *Geological Society of America Bulletin, 116*(7-8), 895-909.

Sklar, L. S., & Dietrich, W. E. (2001). Sediment and rock strength controls on river incision into bedrock. *Geology, 29*(12), 1087-1090. doi: 10.1130/0091-7613(2001)029<1087:sarsco>2.0.co;2

Snyder, N. P., Whipple, K. X., Tucker, G. E., & Merritts, D. J. (2000). Landscape response to tectonic forcing: Digital elevation model analysis of stream

profiles in the Mendocino triple junction region, northern California. *Geological Society of America Bulletin, 112*(8), 1250-1263. doi: 10.1130/0016-7606(2000)112<1250:lrttfd>2.3.co;2

Sobel, E. R., Hilley, G. E., & Strecker, M. R. (2003). Formation of internally drained contractional basins by aridity-limited bedrock incision. *Journal of Geophysical Research-Solid Earth, 108*(B7), 23. doi: 10.1029/2002jb001883

Stone, J. O. (2000). Air pressure and cosmogenic isotope production. *Journal of Geophysical Research: Solid Earth (1978–2012), 105*(B10), 23753-23759.

Stuwe, K., & Foster, D. (2001). Ar-40/Ar-39, pressure, temperature and fission track constraints on the age and nature of metamorphism around the main central thrust in the eastern Bhutan Himalaya. *Journal of Asian Earth Sciences, 19*(1-2), 85-95. doi: 10.1016/s1367-9120(00)00018-3

Tarboton, D. G., Bras, R. L., & Rodriguez-Iturbe, I. (1989). Scaling and elevation in river networks. *Water Resources Research, 25*(9), 2037-2051.

Tobgay, T., McQuarrie, N., Long, S., Kohn, M. J., & Corrie, S. L. (2012). The age and rate of displacement along the Main Central Thrust in the western Bhutan Himalaya. *Earth and Planetary Science Letters, 319*, 146-158. doi: 10.1016/j.epsl.2011.12.005

Tucker, G., & Whipple, K. (2002). Topographic outcomes predicted by stream erosion models: Sensitivity analysis and intermodel comparison. *Journal of Geophysical Research: Solid Earth (1978–2012), 107*(B9), ETG 1-1-ETG 1-16.

Tucker, G. E., & Bras, R. L. (1998). Hillslope processes, drainage density, and landscape morphology. *Water Resources Research, 34*(10), 2751-2764. doi:

10.1029/98wr01474

Tucker, G. E., Lancaster, S. T., Gasparini, N. M., Bras, R. L., & Rybarczyk, S. M. (2001). An object-oriented framework for distributed hydrologic and geomorphic modeling using triangulated irregular networks. *Computers & Geosciences, 27*(8), 959-973. doi: 10.1016/s0098-3004(00)00134-5

Whipple, K. X., Kirby, E., & Brocklehurst, S. H. (1999). Geomorphic limits to climate-induced increases in topographic relief. *Nature, 401*(6748), 39-43. doi: 10.1038/43375

Whipple, K. X., & Tucker, G. E. (1999). Dynamics of the stream-power river incision model: Implications for height limits of mountain ranges, landscape response timescales, and research needs. *Journal of Geophysical Research-Solid Earth, 104*(B8), 17661-17674. doi: 10.1029/1999jb900120

Whipple, K. X., & Tucker, G. E. (2002). Implications of sediment-flux-dependent river incision models for landscape evolution. *Journal of Geophysical Research-Solid Earth, 107*(B2), 20. doi: 10.1029/2000jb000044

Willgoose, G., Bras, R. L., & Rodriguez-Iturbe, I. (1991). A coupled channel network growth and hillslope evolution model 1. Theory. *Water Resources Research, 27*(7), 1671-1684. doi: 10.1029/91wr00935

Wittmann, H., von Blanckenburg, F., Kruesmann, T., Norton, K. P., & Kubik, P. W. (2007). Relation between rock uplift and denudation from cosmogenic nuclides in river sediment in the Central Alps of Switzerland. *Journal of Geophysical Research: Earth Surface (2003–2012), 112*(F4).

Wobus, C., Heimsath, A., Whipple, K., & Hodges, K. (2005). Active out-of-sequence

thrust faulting in the central Nepalese Himalaya. *Nature, 434*(7036), 1008-1011.

Wobus, C., Whipple, K. X., Kirby, E., Snyder, N., Johnson, J., Spyropolou, K., Crosby, B. & Sheehan, D. (2006). Tectonics from topography: Procedures, promise, and pitfalls. *Special papers-Geological Society of America, 398*, 55.

Wobus, C. W., Hodges, K. V., & Whipple, K. X. (2003). Has focused denudation sustained active thrusting at the Himalayan topographic front? *Geology, 31*(10), 861-864.

Wobus, C. W., Whipple, K. X., & Hodges, K. V. (2006). Neotectonics of the central Nepalese Himalaya: Constraints from geomorphology, detrital $^{40}Ar/^{39}Ar$ thermochronology, and thermal modeling. *Tectonics, 25*(4), TC4011.

Table 4.1. Basin average erosion rate sample data.

Sample Name	Latitude (°N)*	Longitude (°E)*	Elevation (m)*	Basin Area (km^2)	[^{10}Be] (atoms/g)	[^{10}Be] 1σ (atoms/g)	Erosion Rate† ($m\ m.y.^{-1}$)	Erosion Rate 1σ† ($m\ m.y.^{-1}$)	Integration Time§ (ky)
BT0901	27.41836	90.60650	1083	80	44219	5683	652	97	0.92
BT0902	27.35374	90.66857	1029	132	39267	3230	473	53	1.3
BT0903	27.50617	90.55857	2101	42	94955	4890	208	19	2.9
BT0904	**27.53484**	**90.60214**	**2864**	**48**	**298794**	**11001**	**79.3**	**6.9**	**7.6**
BT0905	**27.53888**	**90.64625**	**2899**	**27**	**475140**	**21725**	**47.8**	**4.4**	**13**
BT0906	**27.47286**	**90.62557**	**2875**	**30**	**200487**	**16725**	**117**	**13**	**5.1**
BT0907	**27.52203**	**90.62083**	**2871**	**110**	**261393**	**18222**	**88.7**	**9.3**	**6.8**
BT0909	**27.66006**	**90.82805**	**2785**	**65**	**336625**	**26332**	**73.7**	**8.2**	**8.1**
BT0910	**27.62422**	**90.95410**	**2777**	**56**	**351628**	**20649**	**71.7**	**7.1**	**8.4**
BT0912	**27.68652**	**90.94741**	**2865**	**50**	**243388**	**11954**	**115**	**11**	**5.2**
BT0922	**27.61863**	**90.60584**	**2735**	**114**	**311891**	**26495**	**80.2**	**9.4**	**7.5**
BT0926	27.47059	91.24598	930	59	97598	5147	168	15	3.6
BT0927	27.50980	91.23062	1045	21	170952	5250	88.3	7.2	6.8
BT0928	27.54972	91.27051	1071	53	85463	2778	191	16	3.1
BT0929	27.67441	91.13576	1240	13	95408	3569	131	11	4.6
BT0931	27.67680	91.07116	1278	91	79985	3350	215	19	2.8
BT0973	**27.46368**	**90.97917**	**3444**	**20**	**642631**	**21388**	**41.6**	**3.6**	**14**
BT0974	**27.46313**	**90.11234**	**3182**	**2.1**	**792250**	**38474**	**29.6**	**2.8**	**20**
BT0993	27.52631	89.77748	1440	114	165244	10102	134	13	4.5
BT0994	27.66848	89.77435	1372	108	16682	1562	1130	137	0.53
BT0995	27.45004	89.81466	1190	74	109994	4843	132	11	4.5
BT0996	27.28347	89.92412	750	41	54706	3760	318	31	1.9
BT0998	27.33546	90.05133	696	65	26354	8401	736	265	0.82
BT09108	**27.40841**	**89.71839**	**2355**	**42**	**318378**	**14705**	**65.1**	**5.9**	**9.2**
BT1021	27.78506	91.18372	1283	72	170813	13217	193	21	3.1
BT1036	**27.30971**	**89.44209**	**2203**	**37**	**701376**	**30004**	**45.0**	**4.0**	**13**
BT1042	**27.44001**	**90.10559**	**2918**	**38**	**548906**	**41782**	**65.1**	**7.2**	**9.2**
BT1043	**27.44946**	**90.00967**	**2595**	**57**	**563798**	**63642**	**52.7**	**7.3**	**11**
BT1044	27.77093	89.64485	1714	89	68274	5037	644	69	0.93

*Actual sample location data. See Table DR1 for CRONUS input data. †Values calculated using the CRONUS calculator (see text and Data Repository for discussion). Results were calculated using the constant prodution rate model of Lal (1991)/Stone (2000). §Time over which the erosion rate is integrated. This value is calculated by dividing the e-folding depth of the production of cosmic nuclides via spallation (0.6 m) by the erosion rate. Bold samples are located on low-relief landscapes.

FIGURE 4.1

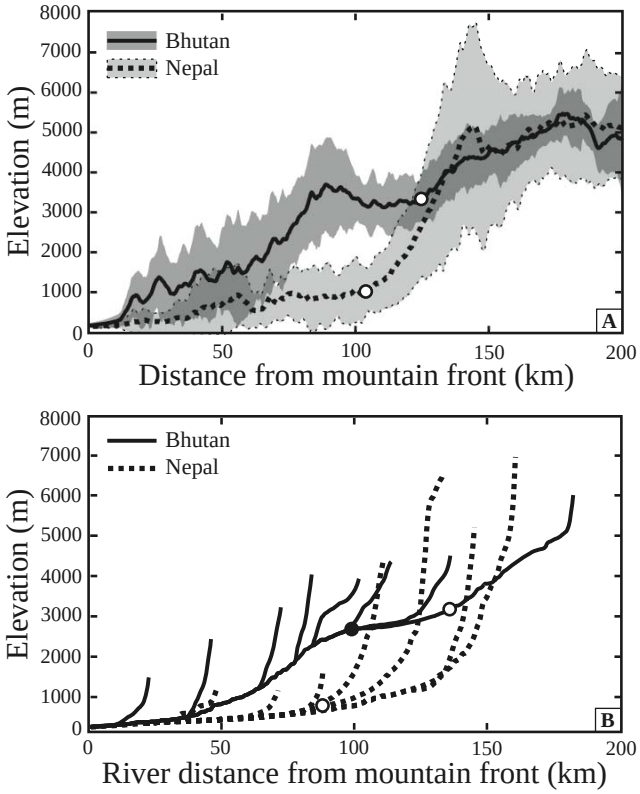
Bhutan
Nepal
Elevation (m)
Distance from mountain front (km)
A
B
River distance from mountain front (km)

FIGURE 4.2

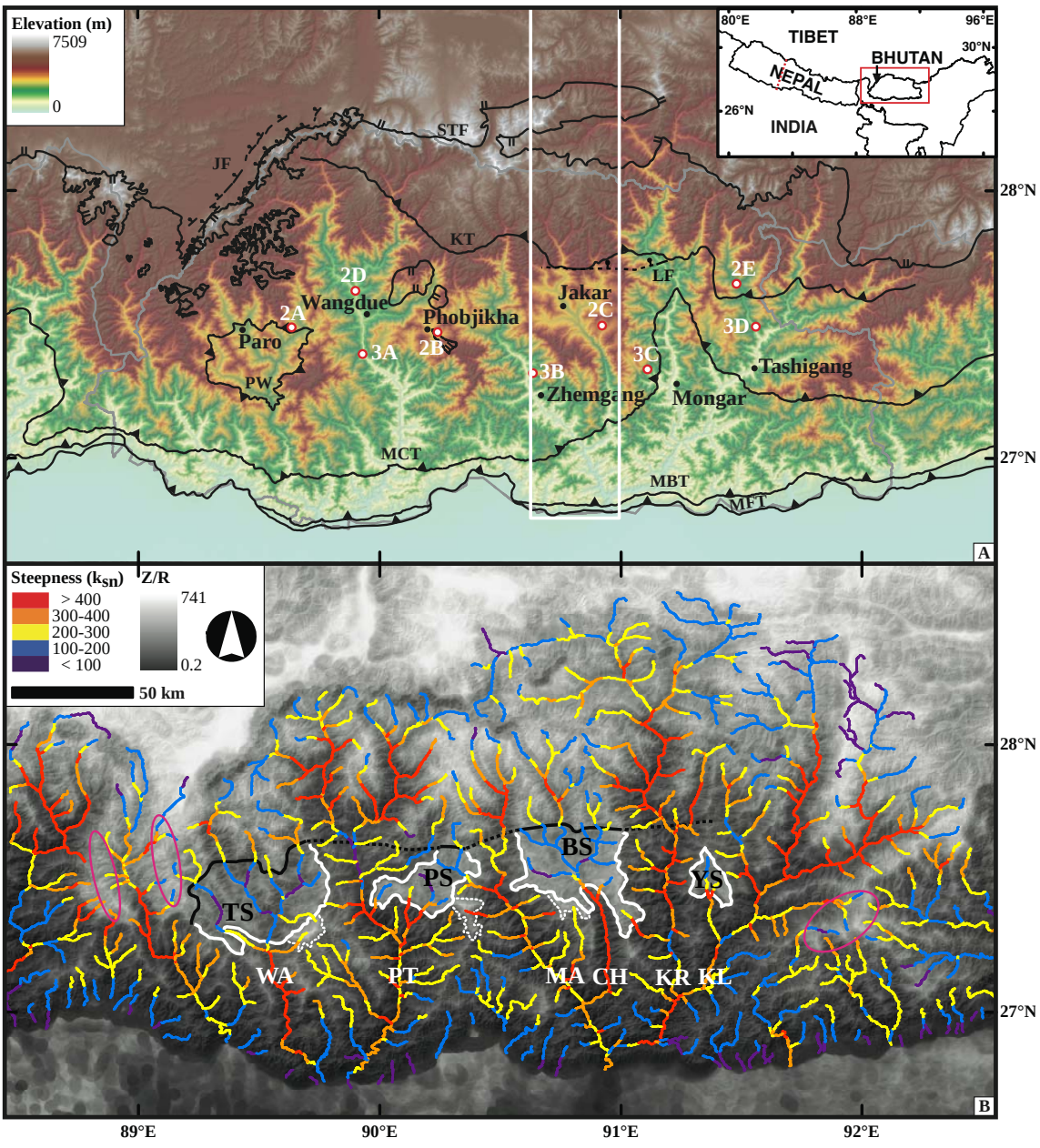
Elevation (m)
7509
0
STF
JF
KT
LF
MCT
MBT
MFT
Wangdue
Phobjikha
Paro
Jakar
Zhemgang
Mongar
Tashigang
2A
2B
2C
2D
2E
3A
3B
3C
3D
PW
80°E
88°E
96°E
30°N
26°N
TIBET
BHUTAN
NEPAL
INDIA
28°N
27°N
A
Steepness (k_SN)
> 400
300-400
200-300
100-200
< 100
Z/R
741
0.2
50 km
BS
PS
YS
TS
WA
PT
MA
CH
KR
KL
B
89°E
90°E
91°E
92°E

FIGURE 4.3

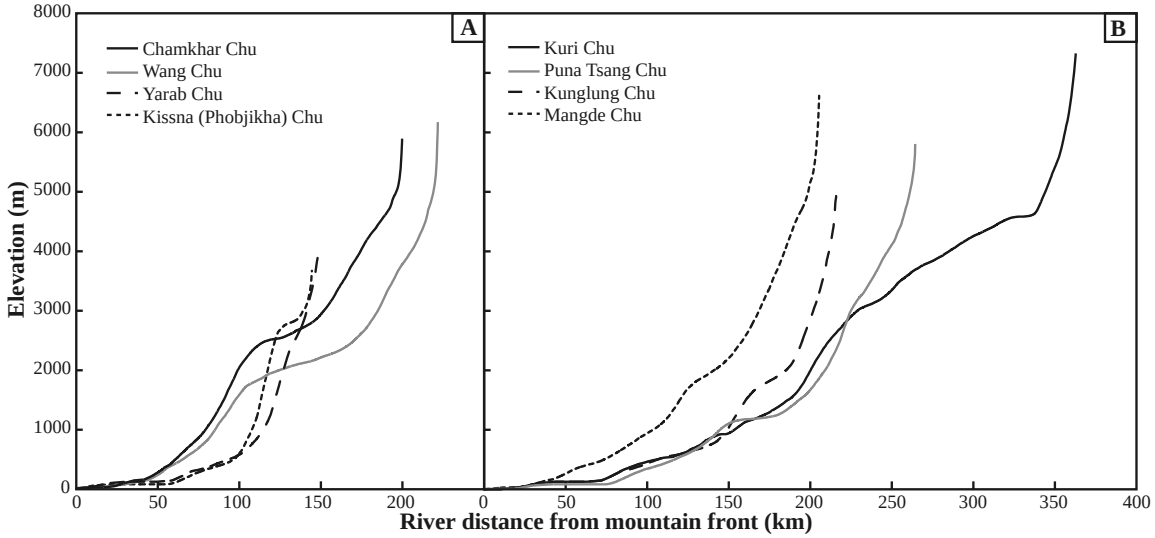
A
B
Chamkhar Chu
Wang Chu
Yarab Chu
Kissna (Phobjikha) Chu
Kuri Chu
Puna Tsang Chu
Kunglung Chu
Mangde Chu
Elevation (m)
River distance from mountain front (km)
0
1000
2000
3000
4000
5000
6000
7000
8000
0
50
100
150
200
250
300
350
400

FIGURE 4.4

FIGURE 4.5

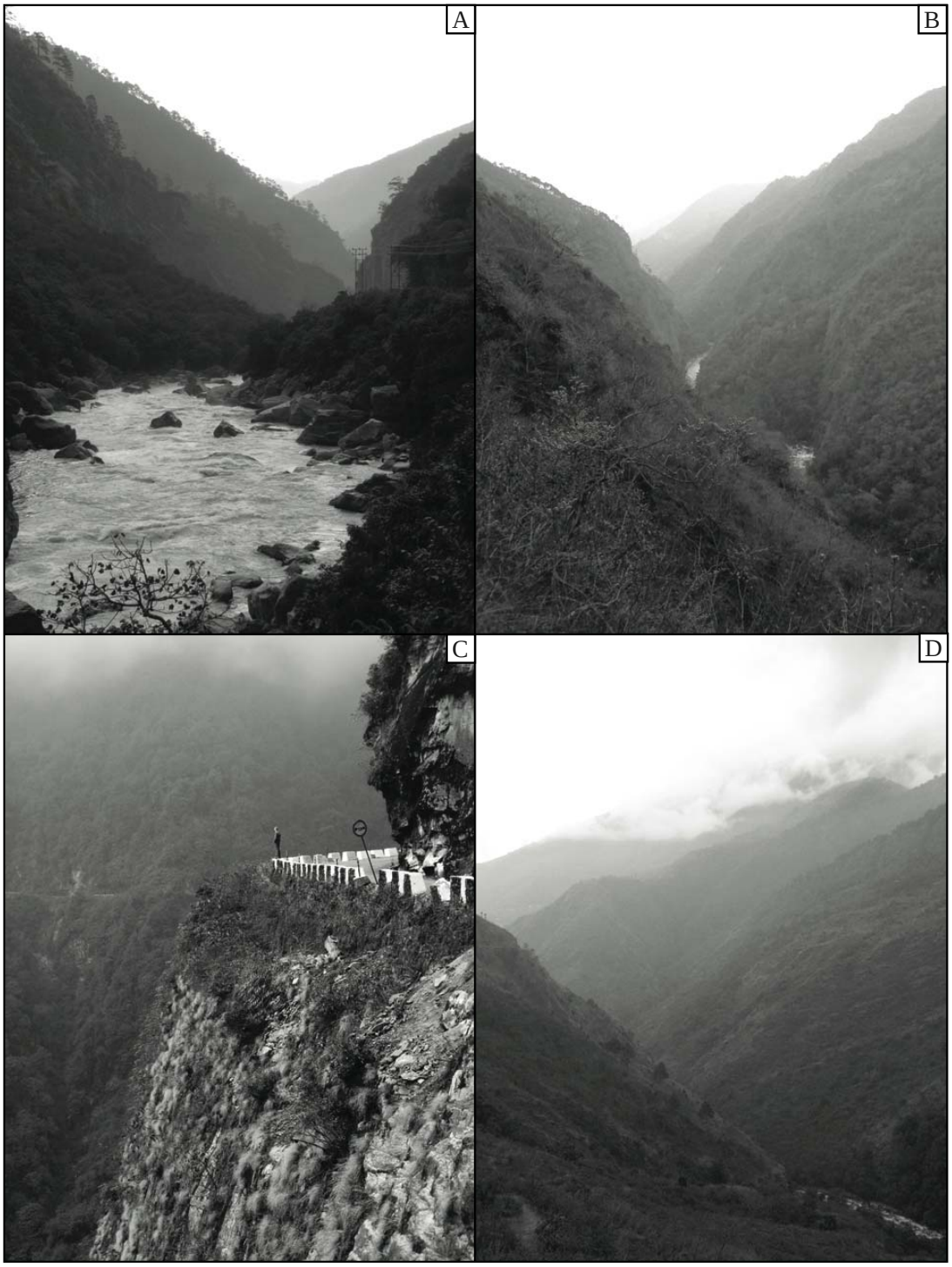

FIGURE 4.6

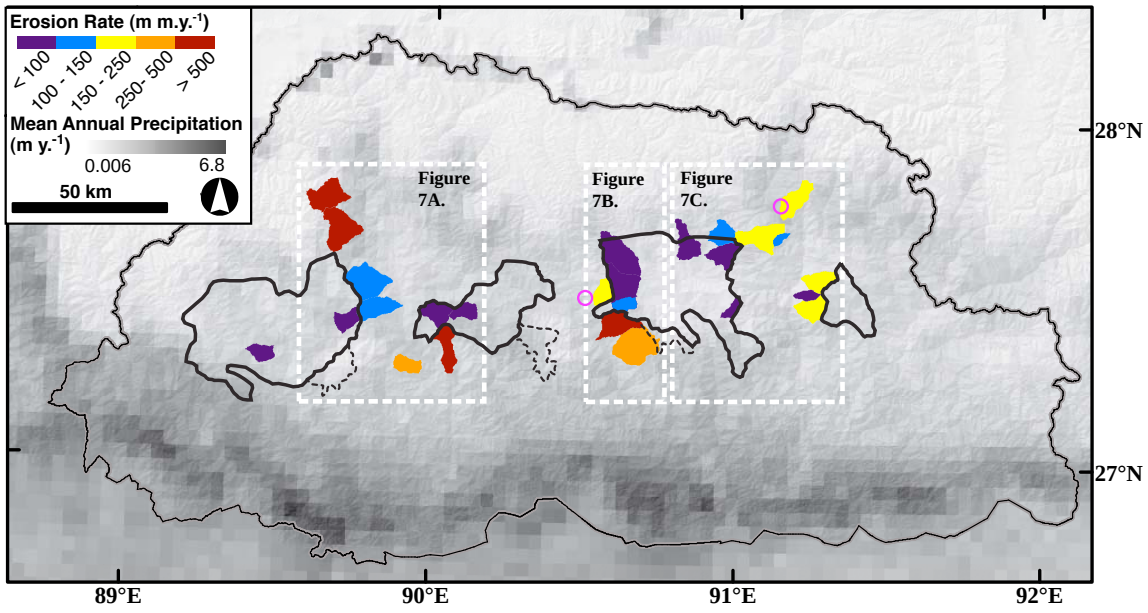
Erosion Rate (m m.y.-1)
< 100
100 - 150
150 - 250
250- 500
> 500
Mean Annual Precipitation (m y.-1)
0.006
6.8
50 km
Figure 7A.
Figure 7B.
Figure 7C.
28°N
27°N
89°E
90°E
91°E
92°E

FIGURE 4.7

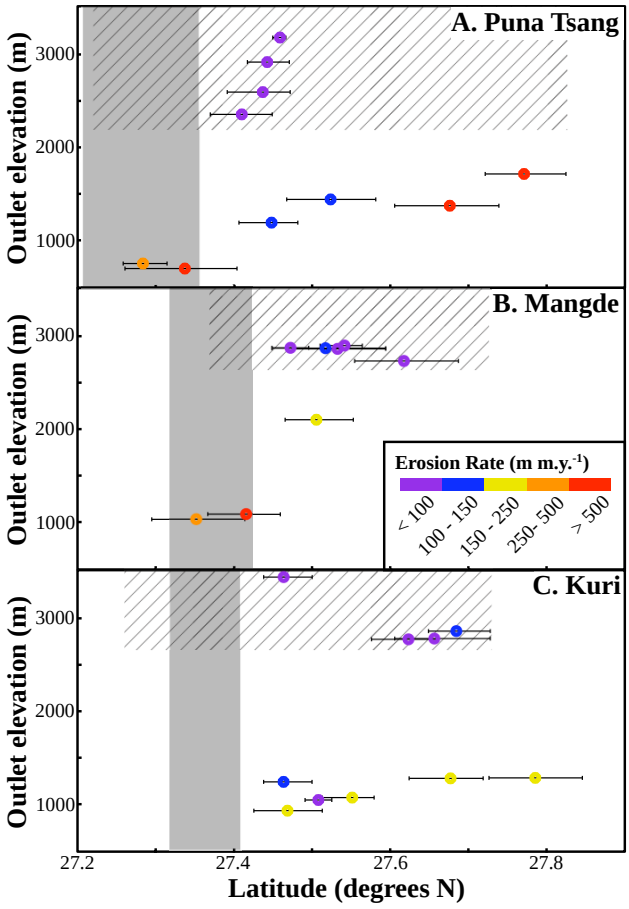
A. Puna Tsang
B. Mangde
C. Kuri
Outlet elevation (m)
3000
2000
1000
Erosion Rate (m m.y.-1)
< 100
100 - 150
150 - 250
250- 500
> 500
27.2
27.4
27.6
27.8
Latitude (degrees N)

FIGURE 4.8

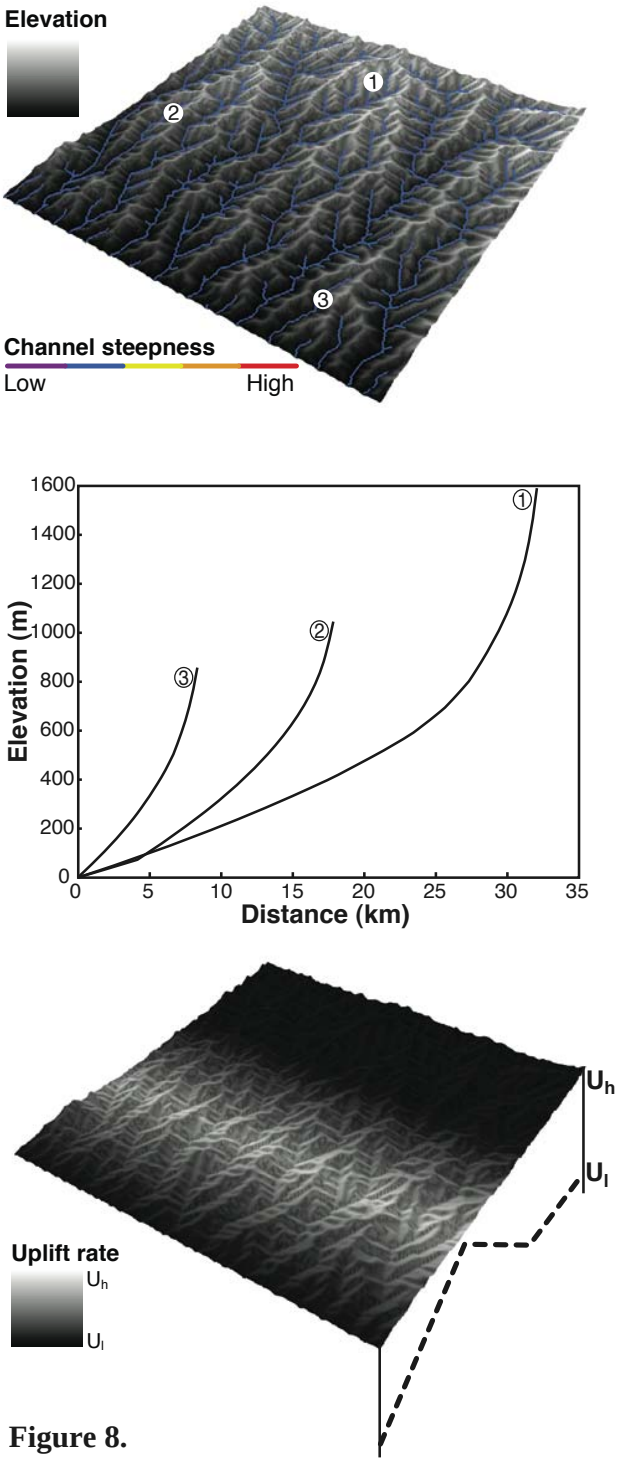

Figure 8.

FIGURE 4.9

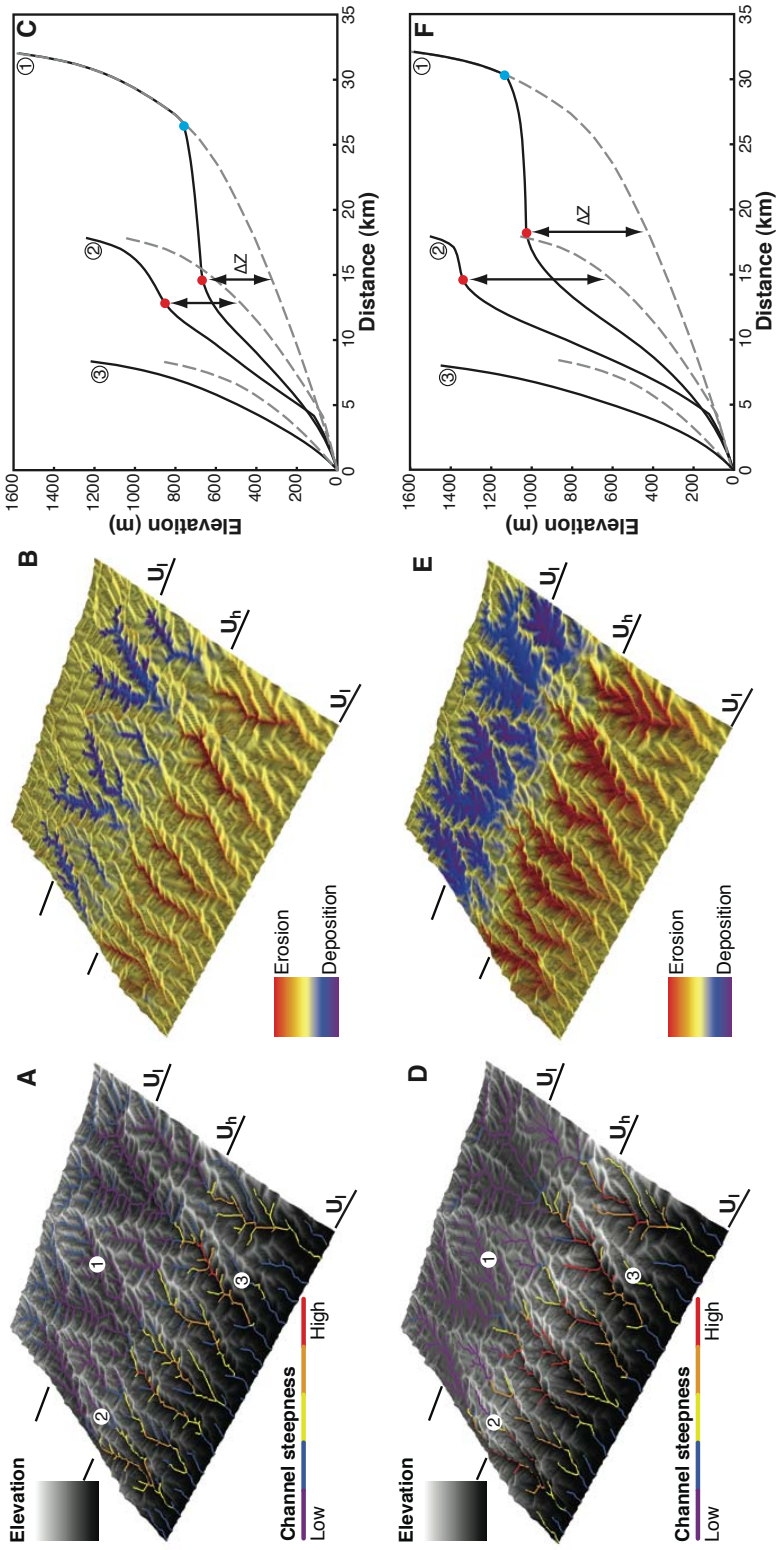
A
B
C
D
E
F
Elevation
Channel steepness
Low
High
Erosion
Deposition
Elevation (m)
Distance (km)
ΔZ
U_l
U_h
U_l
1
2
3

FIGURE 4.10

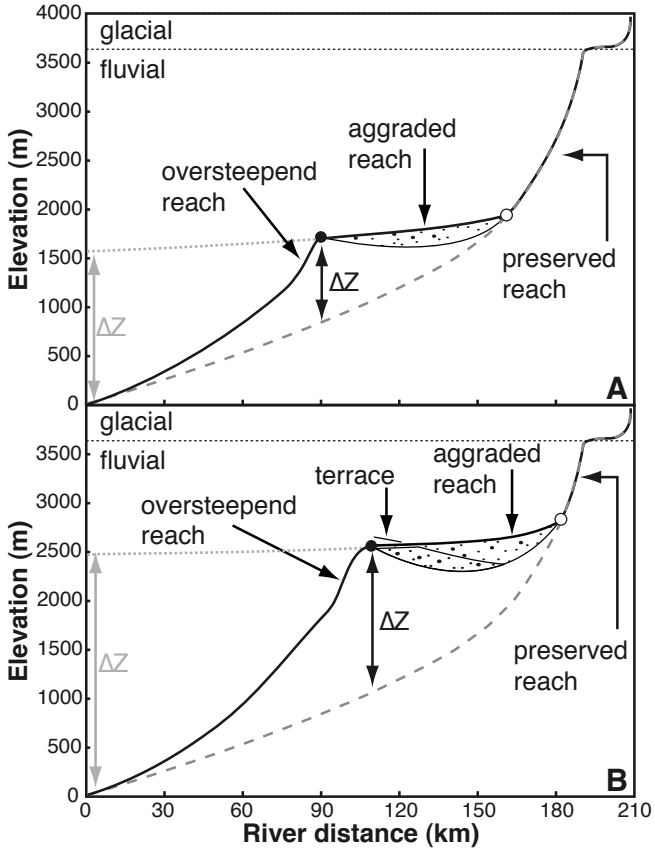
glacial
fluvial
oversteepend reach
aggraded reach
preserved reach
ΔZ
ΔZ
A
terrace
B
Elevation (m)
River distance (km)
0
500
1000
1500
2000
2500
3000
3500
4000
30
60
90
120
150
180
210

FIGURE 4.11

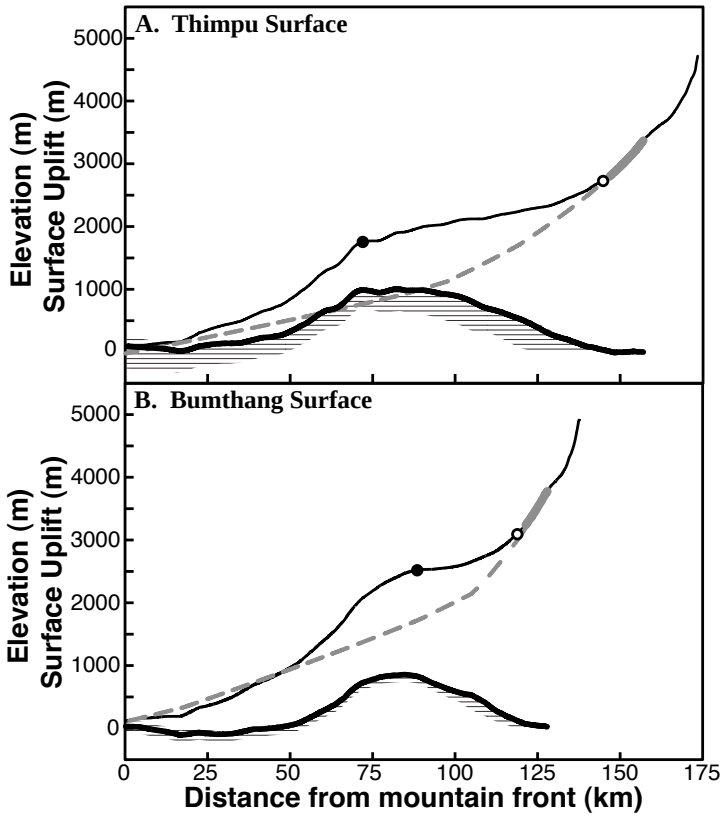
A. Thimpu Surface
B. Bumthang Surface
Elevation (m)
Surface Uplift (m)
5000
4000
3000
2000
1000
0
0
25
50
75
100
125
150
175
Distance from mountain front (km)

CHAPTER 5

DISENTANGLING TOPOGRAPHY, EROSION AND CLIMATE IN THE BHUTAN HIMALAYA

ABSTRACT

Prior studies relating topography to erosion rates from different climate regimes in the Himalayan-Tibetan orogenic system make predictions for how climate controls the steady-state relief at a given erosion rate and whether tectonic processes are coupled to climate. Range-scale topographic response to climate change has been proposed in the eastern Himalaya. Surface uplift of hinterland landscapes in Bhutan has been linked to a deep rain shadow cast by the rising Shillong Plateau in the foreland. A prerequisite to the testing of this hypothesis is confirmation that climate and erosion rate are coupled, or that there is a significant effect on the relationship between topography and erosion rates in different climate regimes. We exploited the large rainfall and topographic gradients across Bhutan to provide a comprehensive test of the linkages between topographic form, climate and erosion. We have calculated basin-averaged erosion rates determined from concentrations of ^{10}Be in modern river sands, and use the mean normalized channel steepness to characterize the topographic form of each sampled basin. The mean annual rainfall in sampled basins ranged from 0.4 to 4.5 m y.$^{-1}$.

We also found that the relationship between channel steepness and erosion rate in the drier interior regions of Bhutan (rainfall < 0.65 m y^{-1}) matched that found in similar climates along the eastern margin of the Tibetan Plateau (rainfall < 0.6 m y.$^{-1}$), while the wetter frontal ranges of Bhutan are consistent with observations from the central Nepal Himalaya under a similar climate. Non-linear relationships between topographic

metrics and erosion rates, suggested a fundamental difference in the mode of river incision within the drier interior of Bhutan and the wetter foothills. However, our data also suggested that the potential decrease in rainfall rates dues to the rain shadow of the Shillong Plateau would not be great enough to cause the dramatic slowing of erosion rates suggested to have initiate the surface uplift of low-relief landscapes in Bhutan.

MOTIVATION

Theory (e.g., Whipple & Tucker, 1999) and experiments (e.g., Bonnet & Crave, 2003) have suggested that the steady-state relief required for erosion rates to balance rock uplift rates is expected to depend strongly on climate state (e.g. mean annual rainfall and rainfall variability). Nevertheless, evidence for an unambiguous climatic control on erosion rate has been elusive. Some previous studies have emphasized an apparent link between erosion and climate (Reiners et al., 2003; Thiede et al., 2004; Grujic et al., 2006; Moon et al., 2011; Bookhagen and Strecker, 2012; Carretier et al., 2013). Others have suggested a negligible effect of climate on erosion rate (e.g. Ahnert, 1970; Burbank et al., 2003; von Blanckenburg, 2005; Aalto et al., 2006; Riebe et al., 2001; Adlakha et al., 2013; Godard et al., 2014). However, despite this body of work, no definitive relationships have emerged, perhaps in part because of a lack of topographic or lithologic controls across some of the study sites.

This topic has garnered special interest within the Himalayan-Tibetan orogenic research community because the results of various studies have supported (e.g. Wobus et al., 2003; Hodges et al., 2004; Thiede et al., 2004; Huntington et al., 2006) and contested (e.g. Burbank et al., 2003; Adlakha et al., 2013; Godard et al., 2014) coupling between tectonics and climate. In this study, we do not set out to resolve this issue directly, but instead to characterize the efficiency of fluvial erosion observed in the Himalayan-Tibetan orogeny, and the coupling between erosion rate and rainfall rate. We have calculated new basin-averaged ^{10}Be erosion rates in the Bhutan Himalaya in the context of similar data collected in central Nepal (Godard et al., 2014) and the eastern margin of the Tibetan Plateau (Ouimet et al., 2009).

The Himalayan-Tibetan orogenic system has variable rock type, surface processes, topographic characteristics, and rock uplift rates (e.g. Hodges, 2000; Hodges et al., 2001; Duncan et al., 2003; Jackson and Bilham, 1994; Lave and Avouac, 2001; Adams et al., Chapter 3; Adams et al., Chapter 4). These variations provide an opportunity to test the connections among climate, surface processes and tectonics. Several significant suites of cosmogenic radionuclide basin average erosion rate data have been presented from the orogen, which were focused within very different climate zones (Ouimet et al., 2009; Godard et al., 2014, Scherler et al., 2014). Data from the temperate (mean annual rainfall ca. 0.3-0.6 m $y.^{-1}$) eastern margin of the Tibetan Plateau suggest that high steady-state relief can be generated within landscapes where erosion rates are relatively low (Ouimet et al., 2009). However, at the wetter (mean annual rainfall ca. 1.5-5 m $y.^{-1}$) central Himalaya front, much higher uplift rates are required to maintain similar steady-state relief (Godard et al., 2014; Wobus et al., 2005). The data from the western (Scherler et al., 2014) and central Himalaya show a similar relationship between topography and erosion rate; however, for the sake of clarity, our data analysis focused on the larger of the two datasets, in Nepal.

The climate regime in Bhutan spans across the two end member regions above (Bookhagen & Burbank, 2010). We have used this climate gradient to test how well the relationships between topography and erosion rate observed in central Nepal and the eastern margin of the Tibetan Plateau explain patterns in erosion rates in this setting with stronger rainfall gradients (Figure 5.1) and the plausibility of significant surface uplift in response to a recent decrease in rainfall in Bhutan (e.g. Grujic et al., 2006). Our samples were collected in basins that experience mean annual rainfall amounts that span nearly

the entire range of variability of the orogenic system as a whole. Moreover, these basins exhibited a range of topographic relief. We have leveraged these variations to explore how functional relationships between topography and erosion rate vary as a function of rainfall.

THE BHUTAN HIMALAYA

Isolated, low-relief landscapes are prevalent across the hinterland of the Bhutan Himalaya. These landscapes contain broad, flat-bottomed valleys with thick alluvial fills and deep saprolites (e.g. Baillie et al., 2004). Rivers that are actively incising into these subdued landscapes exhibit major convex-up slope-break knickpoints (following convention, henceforth convex-up and concave-up will be simply referred to as convex and concave, respectively), where the lower river reaches form deep canyons with steep hillslopes and are eroding faster than the upper portions of the basin, demonstrating that these are transient landscapes (Adams et al., Chapter 4). Two leading hypotheses exist that give a causal formation mechanism of low-relief landscapes. Grujic et al. (2006) proposed that a reduction in erosion rates, caused by the rain shadow of the rising Shillong Plateau, resulted in surface uplift because of higher rock uplift rates. However, Adams et al. (Chapter 4) suggested that an increase in Quaternary rock uplift rates, due to an active hinterland duplex, caused back tilting and surface uplift of these low-relief landscapes.

The Shillong Plateau lies directly outboard of the eastern two-thirds of the Bhutan Himalaya to the south. Investigations using satellite-derived rainfall data suggested that the Shillong Plateau intercepts a significant amount of the moisture delivered by the

South Asian Monsoon in this portion of the orogen, essentially halving the mean annual rainfall in most of Bhutan (Grujic et al., 2006; Adlakha et al., 2013). These studies have also showed that the rain shadow of the Shillong Plateau creates a west to east reduction in the mean annual rainfall along the range front in Bhutan (from ca. 6 to 4 m $y.^{-1}$, respectively). However, the most remarkable rainfall gradient in the Himalayan is the south to north gradient between the Himalayan foothills, and the core of the range (Bookhagen and Burbank 2006; 2010). In the central and eastern Himalaya, at least half of the annual rainfall volume is concentrated in the foreland foothills (Figure 5.1 inset; Bookhagen and Burbank 2006; 2010).

Our analyses were spread throughout much of Bhutan, with focus on the tributaries of the primary N-S trunk streams of the Wang, Puna Tsang, Mangde, Chamkhar, and Kuri rivers, and small rivers that drain the front of the range, all of which merge with the Brahmaputra River in the foreland (Figure 5.1). The bedrock geology consists mostly of the high-grade schists, gneisses and migmatites of the Greater Himalayan sequence in the hanging wall of the Main Central thrust system, and greenschist-amphibolite grade phyllites, psammites and quartzites of the Lesser Himalayan sequence in the hanging wall of the Main Boundary thrust system (Figure 5.1).

METHODS AND DATA

We collected river sands for basin averaged erosion rates from the active banks and gravel bars of small- to medium-sized basins (ca. 2-130 km^2). Sampled basins were specifically selected to have normally distributed hillslope gradients and smooth, concave

river profiles that are indicative of quasi-equilibrium erosion. We avoided basins that contained significant slope-break knickpoints, strong patterns in hillslope gradients, or exhibited evidence of significant late Pleistocene glaciation or sediment that appeared to be dominated by recent flooding or mass-wasting debris.

While we have presented only one morphometric parameter here – normalized channel steepness – we also evaluated relationship with mean hillslope gradient (see Appendix D). By using the normalized channel steepness index, we were able to compare quantitatively the steepness of rivers within basins of all scales (reference concavity, θ_{ref} = 0.45, see the Data Repository for more details). In addition, the channel steepness metric is able to record landscape steepening beyond the point where threshold hillslopes dominate (Safran et al., 2005; Ouimet et al., 2009; DiBiase et al., 2010). Several studies have found that the functional relationship between erosion rate and mean hillslope gradient becomes invariant at rates greater than ca. 200-300 m m.y.$^{-1}$ (von Blanckenburg, 2005; Safran et al., 2005; Binnie et al., 2007; Ouimet et al., 2009; DiBiase et al., 2010; Godard et al., 2014). Much like in other regions on Earth, we have found that the relationship between mean hillslope and erosion rate in Bhutan, becomes invariant at rates greater than ca. 215 m m.y.$^{-1}$ (see Appendix D); therefore, we suggest that the more diagnostic metric to quantify the relationship between landscape form and erosion rate is the channel steepness index.

Our sampled basins were collected within the Greater Himalaya sequence (n = 25), Lesser Himalayan sequence (n = 4), and some spanned both tectono-stratigraphic units (n = 2) (Figure 5.1). Our mean normalized channel steepness values ranged from ca. 50-400 $m^{0.9}$ and did not show any correlation with lithology. We also selected basins that

covered a broad range of mean annual rainfall (0.4 to 4.5 m $y.^{-1}$) as determined from the Tropical Rainfall Measuring Mission (TRMM) 2B31 data set, a combined Precipitation Radar and Microwave Imager product with a resolution of 5 x 5 km (Bookhagen, in review)(see Appendix D).

As a means of quantifying erosion rates in Bhutan, we measured the concentration of *in situ* cosmogenic ^{10}Be in quartz grains separated from fluvial sediments. The concentration of *in situ* ^{10}Be in quartz is a function of the production rate and the time spent near the surface, thus erosion rates inversely scale with concentrations of acquired cosmogenic nuclides (e.g. Granger et al. 1995; Bierman and Stieg, 1996). Erosion rates were calculated using a technique similar to that proposed by Portenga and Biermann (2011), where spallogenic and muogneic production rates are calculated for every pixel in the basin digital elevation model, and effective elevations and latitudes are calculated to make sample characterization compatible with the CRONUS online calculator protocols (Balco et al., 2008). See Data Repository for more details on our methods.

Derived erosion rates range from 30 to 1130 m $m.y.^{-1}$, which yield representative integration time scales of 20,000 and 500 years, respectively (Figure 5.1). As suggested by Adams et al. (Chapter 4), the erosion rates in Bhutan showed a clear dichotomy between those of the upper reaches of basins with slope-break knickpoints (median of ca. 69 m $m.y.^{-1}$ and median absolute deviation from the median of 10 m $m.y.^{-1}$) and the adjacent deeply incised canyons (median of ca. 208 m $m.y.^{-1}$ and median absolute deviation from the median of 77 m $m.y.^{-1}$). Furthermore, they found there was an apparent N-S erosion rate gradient within the trellised basins of the Puna Tsang, Mangde, and Kuri rivers that is suggestive of hinterland focused uplift (Adams et al., Chapter 4).

Basin averaged erosion rates were highest (ca. 550 m m.y.$^{-1}$) at the latitudes of 27.2 – 27.4°N, inline with outliers of glaciated landscapes and major convex knickpoints, and decrease to the north (ca. 200 – 100 m m.y.$^{-1}$) (Adams et al., Chapter 4). New erosion rates derived from detrital samples collected near the Himalayan front are some of the highest within Bhutan. We attributed this to especially high precipitation (based on TRMM data) and active deformation near the sampling localities.

DISCUSSION AND CONCLUSIONS

Our basin-averaged erosion rates from Bhutan revealed considerable scatter when plotted against mean normalized channel steepness (Figure 5.2) – more scatter than in a number of recent studies. We first explored plausible explanations for this broad scatter. Our data, and the data from similar Himalayan or Tibetan Plateau studies, showed no systematic influence of bedrock substrate (Ouimet et al., 2009; Godard et al., 2014; Scherler et al., 2014); however, variable susceptibilities to erosion of substrate lithology may have introduced scatter into these datasets. To better evaluate our data we compared relationships between topography and erosion in Bhutan to similar, but much clearer relationships from landscapes discussed above, the eastern margin of the Tibetan Plateau and the central Nepal Himalaya (Figure 5.2; Ouimet et al., 2009; Godard et al., 2014).

The data from the eastern margin of the Tibetan Plateau and Nepal were well described by a power-law relationship expressed by $E \approx Ck_{sn}^{p}$, where E is the basin average erosion rate, k_{sn} is the mean normalized channel steepness index, and the coefficient, C, and exponent, p, vary with lithology and climate (see Appendix D) (e.g. Kirby and Whipple, 2001; DiBiase et al., 2010; Lague et al., 2005; DiBiase and Whipple,

2011). To find the best-fit climate parameters for these two data sets, we used a least squares power law regression wrapped in a Monte Carlo protocol that incorporated the uncertainties in k_{sn} and E. Best-fit values of p were calculated as 0.93 and 1.25 for the eastern margin of the Tibetan Plateau and the central Nepal Himalaya, respectively. Best-fit values of C were calculated as 1.24 and 0.71 for the eastern margin of the Tibetan Plateau and the central Nepal Himalaya, respectively. Because the exponent values for these relationships are different the units of coefficients are different, making them not directly comparable.

These best-fit parameters suggested that each region exhibits a different relationship between channel steepness and erosion rate. The central Nepal data show a more strongly non-linear relationship than the eastern Tibet data. The fit to the power law relationship inferred above to the eastern Tibet data is good, but Kirby and Ouimet (2011) showed that a linear fit is nearly as good. In the discussions that follow, we assumed that both datasets are described well by a non-linear relationship. Nonlinearity may arise in landscapes for a variety of reasons: 1) the relationship between incision and bed shear stress may be nonlinear (e.g. Whipple et al., 2000); 2) channel widths may decrease as incision rates increase (e.g. Lave and Avouac, 2001); 3) incision thresholds are expected to be exceeded more frequently on steeper slopes experiencing the same discharge regime (e.g. Lague et al., 2005). Recent advances have suggested that non-linear incision models capture the effects of the mean annual discharge and the variability (i.e. size and frequency) of large discharge events (i.e. large storms), which cause the most significant periods of incision, and the mean annual discharge (e.g. Synder et al., 2003; Lague et al., 2005; DiBiase and Whipple, 2011). We assumed that precipitation

was effectively transformed into river discharge, and that our observations of a shift between mean annual precipitation rates of < 0.65 and > 1.5 m $y.^{-1}$, were significant enough to have influenced the relationship between topography and erosion rates. However, previous studies have found that a reduction in discharge variability may diminish the influence of increases in mean discharge (Molnar et al., 2006; DiBiase and Whipple, 2011).

Our data from Bhutan overlapped with both previously published datasets from the eastern margin of the Tibetan Plateau and the Central Nepal Himalaya (Figure 5.2). We have divided our data from Bhutan into three groups based the mean annual rainfall ranges from the two other regions. We found that the basins receiving annual rainfall similar to that on the eastern margin of the Tibetan Plateau (< 0.65 m $y.^{-1}$) can be described well by a similar power-law relationship between erosion rate and channel steepness. The same was true for the basins in Bhutan that are as wet as the Nepal dataset (> 1.5 m $y.^{-1}$). However, the basins that receive between 0.65 and 1.5 m $y.^{-1}$ of precipitation were not as clearly separated, and form an intermediate group that was difficult to interpret within the scatter of the data.

Our results show that multiple non-linear relationships are required to explain the topographic response to erosion rate in the Bhutan Himalaya. These relationships are likely differentiated by climate-moderated erosivity and a change in incision processes that affect the non-linearity of the relationship between landscape steepness and erosion rate. In addition, these non-linear relationships, and our new data, provide a means to constrain the possible influence of a halving of rainfall in Bhutan due to the Shillong Plateau rain shadow.

One of the basic tenants of the climate induced surface uplift hypothesis is that low-relief foreland landscapes have been uplifted and dissected forming the current hinterland low-relief landscapes. Because the mean channel steepness of these landscapes is presumed to be stable during the uplift process (ca. 100 – 200 $m^{0.9}$) and an estimate of the reduction in rainfall rate due to the climate change in Bhutan has been proffered (Grujic et al., 2006), we were able to predict the possible response of the erosion rate using the non-linear relationships developed above. The amalgamated data from the Himalayan-Tibetan orogenic system suggested that given the mean channel steepness of the low-relief landscapes in Bhutan (ca. 150 $m^{0.9}$), halving of rainfall rate (switching from the blue curves to the red curves), would not have changed erosion rates enough to created the proposed magnitude of surface uplift. For instance, erosion rates would have changed from ca. 400 m $m.y.^{-1}$ when receiving more than 1.5 m of rain per year to ca. 100 m $m.y.^{-1}$ when receiving less than 0.65 m of rain per year. Using these values we have calculated the magnitude of surface uplift of 1500 m since 5 Ma (the possible timing of initiation from Grujic et al., 2006). However, this value is much lower than the 2500 m required to uplift the low-relief surfaces from a lower foreland position, as suggested by the climate change hypothesis (Grujic et al., 2006).

Instead, we have favored the conclusion of Adams et al. (Chapter 4), which suggested that recent hinterland focused uplift has caused the surface uplift of the low-relief landscapes in Bhutan. These findings demonstrated that the low-relief landscapes were formed *in situ* as fluvial systems were backtiliting, in-filled and uplifted (Adams et al., Chapter 4).

ACKNOWLEDGMENTS

This work was supported by a National Science Foundation Tectonics Program grant EAR 0708714 to K.V.H. and a joint Tectonics and Geomorphology and Landuse Dynamics Programs grant EAR 1049888 to K.XW. and A.M.H. We thank F. Cooper (School of Earth Sciences, University of Bristol) for her assistance in the field, and M. Rossi (School of Earth and Space Exploration, Arizona State University) for helpful discussions and feedback. Fieldwork would not have been possible without support of our friends and colleagues in Bhutan: Peldon Tshering (National Environment Commission), Ugyen Wanda (Department of Geology and Mines), Karma Choden and Ugyen Rinzen (Yangphel Adventure Travel).

FIGURE CAPTIONS

Figure 5.1. Digital elevation model and basin average erosion rates of Bhutan. River systems labeled in white. Uplifted low-relief surfaces are outlined with heavy white lines. Outliers of high, glaciated landscapes are outlined with dashed white lines. Political boundaries are shown with heavy gray/black lines. Lower inset shows a map of mean annual rainfall (MAR) in Bhutan derived from Tropical Rainfall Measuring Mission data (Bookhagen, in review). Sampled basins awaiting erosion rate data are outlined in green dashed lines. STF – South Tibetan fault system; KT – Kakhtang thrust; Lhuentse fault; MCT – Main Central thrust system; MBT – Main Boundary thrust system; MFT – Main Frontal thrust system. Faults based on the maps of Long et al. (2012); Cooper et al. (2012); Cooper et al. (2013) and Adams et al. (2013).

Figure 5.2. Variable erosivity within the Himalayan-Tibetan orogenic system. Light grey triangles represent data from the eastern margin of the Tibetan Plateau (Ouimet et al., 2009). Dark squares represent data from the Central Nepal Himalaya (Godard et al., 2014). Envelopes show the results of 5000 Monte Carlo least squares regressions, dark curves show median best-fit curve (equation shown). Best-fit curves from the Tibetan Plateau and Nepal data are shown in blue and red, respectively. Data from Bhutan are colored by Tropical Rainfall Measuring Mission mean annual rainfall data (Bookhagen, in review). Error bars are 1σ.

REFERENCES

Aalto, R., Dunne, T., & Guyot, J. L. (2006). Geomorphic controls on Andean denudation rates. *Journal of Geology, 114*(1), 85-99. doi: 10.1086/498101

Adams, B. A., Hodges, K. V., van Soest, M. C., & Whipple, K. X. (2013). Evidence for Pliocene-Quaternary normal faulting in the hinterland of the Bhutan Himalaya. *Lithosphere, 5*(4), 438-449. doi: 10.1130/l277.1

Adlakha, V., Lang, K. A., Patel, R. C., Lal, N., & Huntington, K. W. (2013). Rapid long-term erosion in the rain shadow of the Shillong Plateau, Eastern Himalaya. *Tectonophysics, 582*, 76-83. doi: 10.1016/j.tecto.2012.09.022

Ahnert, F. (1970). Functional relationships between denudation, relief, and uplift in large mid-latitude drainage basins. *American Journal of Science, 268*(3), 243-263.

Baillie, I. C., Tshering, K., Dorji, T., Tamang, H. B., Norbu, C., Hutcheon, A. A., & Baumler, R. (2004). Regolith and soils in Bhutan, Eastern Himalayas.

European Journal of Soil Science, 55(1), 9-27. doi: 10.1046/j.1365-2389.2003.00579.x

Balco, G., Stone, J. O., Lifton, N. A., & Dunai, T. J. (2008). A complete and easily accessible means of calculating surface exposure ages or erosion rates from (10)Be and (26)Al measurements. *Quaternary Geochronology, 3*(3), 174-195. doi: 10.1016/j.quageo.2007.12.001

Bierman, P., & Steig, E. J. (1996). Estimating rates of denudation using cosmogenic isotope abundances in sediment. *Earth Surface Processes and Landforms, 21*(2), 125-139. doi: 10.1002/(sici)1096-9837(199602)21:2<125::aid-esp511>3.0.co;2-8

Binnie, S. A., Phillips, W. M., Summerfield, M. A., & Fifield, L. K. (2007). Tectonic uplift, threshold hillslopes, and denudation rates in a developing mountain range. *Geology, 35*(8), 743-746.

Bookhagen, B., & Burbank, D. W. (2006). Topography, relief, and TRMM-derived rainfall variations along the Himalaya. *Geophysical Research Letters, 33*(8), 5. doi: 10.1029/2006gl026037

Bookhagen, B., & Burbank, D. W. (2010). Toward a complete Himalayan hydrological budget: Spatiotemporal distribution of snowmelt and rainfall and their impact on river discharge. *Journal of Geophysical Research: Earth Surface (2003–2012), 115*(F3).

Bookhagen, B., & Strecker, M. R. (2012). Spatiotemporal trends in erosion rates across a pronounced rainfall gradient: Examples from the southern Central Andes. *Earth and Planetary Science Letters, 327*, 97-110.

Bookhagen, B., in review, High resolution spatiotemporal distribution of rainfall seasonality and extreme events based on a 12-year TRMM time series.

Burbank, D., Blythe, A., Putkonen, J., Pratt-Sitaula, B., Gabet, E., Oskin, M., . . . Ojha, T. (2003). Decoupling of erosion and precipitation in the Himalayas. *Nature, 426*(6967), 652-655.

Carretier, S., Regard, V., Vassallo, R., Aguilar, G., Martinod, J., Riquelme, R., Pepin, E., Charrier, R., Hérail, G., Farías, M., Guyot, J-L, Vagas, G. & Lagane, C. (2013). Slope and climate variability control of erosion in the Andes of central Chile. *Geology, 41*(2), 195-198. doi: 10.1130/g33735.1

Cooper, F. J., Adams, B. A., Edwards, C. S., & Hodges, K. V. (2012). Large normal-sense displacement on the South Tibetan fault system in the eastern Himalaya. *Geology, 40*(11), 971-974. doi: 10.1130/g33318.1

Cooper, F. J., Hodges, K. V., & Adams, B. A. (2013). Metamorphic constraints on the character and displacement of the South Tibetan fault system, central Bhutanese Himalaya. *Lithosphere, 5*(1), 67-81. doi: 10.1130/l221.1

DiBiase, R. A., & Whipple, K. X. (2011). The influence of erosion thresholds and runoff variability on the relationships among topography, climate, and erosion rate. *Journal of Geophysical Research: Earth Surface (2003–2012), 116*(F4).

DiBiase, R. A., Whipple, K. X., Heimsath, A. M., & Ouimet, W. B. (2010). Landscape form and millennial erosion rates in the San Gabriel Mountains, CA. *Earth and Planetary Science Letters, 289*(1), 134-144.

Duncan, C., Masek, J., & Fielding, E. (2003). How steep are the Himalaya?

Characteristics and implications of along-strike topographic variations. *Geology, 31*(1), 75-78.

Godard, V., Bourlès, D. L., Spinabella, F., Burbank, D. W., Bookhagen, B., Fisher, G. B., Moulin, A. & Léanni, L. (2014). Dominance of tectonics over climate in Himalayan denudation. *Geology*, G35342. 35341.

Granger, D. E., Kirchner, J. W., & Finkel, R. (1996). Spatially averaged long-term erosion rates measured from in situ-produced cosmogenic nuclides in alluvial sediment. *Journal of Geology, 104*(3), 249-257.

Grujic, D., Coutand, I., Bookhagen, B., Bonnet, S., Blythe, A., & Duncan, C. (2006). Climatic forcing of erosion, landscape, and tectonics in the Bhutan Himalayas. *Geology, 34*(10), 801-804. doi: 10.1130/g22648.1

Hodges, K. V. (2000). Tectonics of the Himalaya and southern Tibet from two perspectives. *Geological Society of America Bulletin, 112*(3), 324-350.

Hodges, K. V., Hurtado, J. M., & Whipple, K. X. (2001). Southward extrusion of Tibetan crust and its effect on Himalayan tectonics. *Tectonics, 20*(6), 799-809.

Hodges, K. V., Wobus, C., Ruhl, K., Schildgen, T., & Whipple, K. (2004). Quaternary deformation, river steepening, and heavy precipitation at the front of the Higher Himalayan ranges. *Earth and Planetary Science Letters, 220*(3), 379-389.

Huntington, K. W., Blythe, A. E., & Hodges, K. V. (2006). Climate change and Late Pliocene acceleration of erosion in the Himalaya. *Earth and Planetary Science Letters, 252*(1-2), 107-118. doi: 10.1016/j.epsl.2006.09.031

Jackson, M., & Bilham, R. (1994). Constraints on Himalayan deformation inferred

from vertical velocity fields in Nepal and Tibet. *Journal of Geophysical Research, 99*(B7), 13897-13813,13912.

Kirby, E., & Ouimet, W. (2011). Tectonic geomorphology along the eastern margin of Tibet: Insights into the pattern and processes of active deformation adjacent to the Sichuan Basin. *Geological Society, London, Special Publications, 353*(1), 165-188.

Kirby, E., & Whipple, K. (2001). Quantifying differential rock-uplift rates via stream profile analysis. *Geology, 29*(5), 415-418. doi: 10.1130/0091-7613(2001)029<0415:qdrurv>2.0.co;2

Lague, D., Hovius, N., & Davy, P. (2005). Discharge, discharge variability, and the bedrock channel profile. *Journal of Geophysical Research: Earth Surface (2003–2012), 110*(F4).

Lave, J., & Avouac, J. P. (2001). Fluvial incision and tectonic uplift across the Himalayas of central Nepal. *Journal of Geophysical Research-Solid Earth, 106*(B11), 26561-26591. doi: 10.1029/2001jb000359

Long, S. P., McQuarrie, N., Tobgay, T., Coutand, I., Cooper, F. J., Reiners, P. W., Wartho, J. A. & Hodges, K. V. (2012). Variable shortening rates in the eastern Himalayan thrust belt, Bhutan: Insights from multiple thermochronologic and geochronologic data sets tied to kinematic reconstructions. *Tectonics, 31*, 23. doi: 10.1029/2012tc003155

Montgomery, D. R., & Brandon, M. T. (2002). Topographic controls on erosion rates in tectonically active mountain ranges. *Earth and Planetary Science Letters, 201*(3-4), 481-489. doi: 10.1016/s0012-821x(02)00725-2

Moon, S., Chamberlain, C. P., Blisniuk, K., Levine, N., Rood, D. H., & Hilley, G. E. (2011). Climatic control of denudation in the deglaciated landscape of the Washington Cascades. *Nature Geoscience, 4*(7), 469-473. doi: 10.1038/ngeo1159

Ouimet, W. B., Whipple, K. X., & Granger, D. E. (2009). Beyond threshold hillslopes: Channel adjustment to base-level fall in tectonically active mountain ranges. *Geology, 37*(7), 579-582.

Portenga, E. W., & Bierman, P. R. (2011). Understanding Earth's eroding surface with ^{10}Be. *GSA Today, 21*(8), 4-10.

Reiners, P. W., Ehlers, T. A., Mitchell, S. G., & Montgomery, D. R. (2003). Coupled spatial variations in precipitation and long-term erosion rates across the Washington Cascades. *Nature, 426*(6967), 645-647. doi: 10.1038/nature02111

Riebe, C. S., Kirchner, J. W., Granger, D. E., & Finkel, R. C. (2001). Minimal climatic control on erosion rates in the Sierra Nevada, California. *Geology, 29*(5), 447-450.

Scherler, D., Bookhagen, B., & Strecker, M. R. (2013). Tectonic control on 10Be-derived erosion rates in the Garhwal Himalaya, India. *Journal of Geophysical Research: Earth Surface*.

Snyder, N. P., Whipple, K. X., Tucker, G. E., & Merritts, D. J. (2003). Importance of a stochastic distribution of floods and erosion thresholds in the bedrock river incision problem. *Journal of Geophysical Research: Solid Earth (1978–2012), 108*(B2).

Thiede, R. C., Bookhagen, B., Arrowsmith, J. R., Sobel, E. R., & Strecker, M. R. (2004). Climatic control on rapid exhumation along the Southern Himalayan Front. *Earth and Planetary Science Letters, 222*(3), 791-806.

von Blanckenburg, F. (2005). The control mechanisms of erosion and weathering at basin scale from cosmogenic nuclides in river sediment. *Earth and Planetary Science Letters, 237*(3-4), 462-479. doi: 10.1016/j.epsl.2005.06.030

Whipple, K. X., Hancock, G. S., & Anderson, R. S. (2000). River incision into bedrock: Mechanics and relative efficacy of plucking, abrasion, and cavitation. *Geological Society of America Bulletin, 112*(3), 490-503.

Wobus, C., Heimsath, A., Whipple, K., & Hodges, K. (2005). Active out-of-sequence thrust faulting in the central Nepalese Himalaya. *Nature, 434*(7036), 1008-1011.

FIGURE 5.1

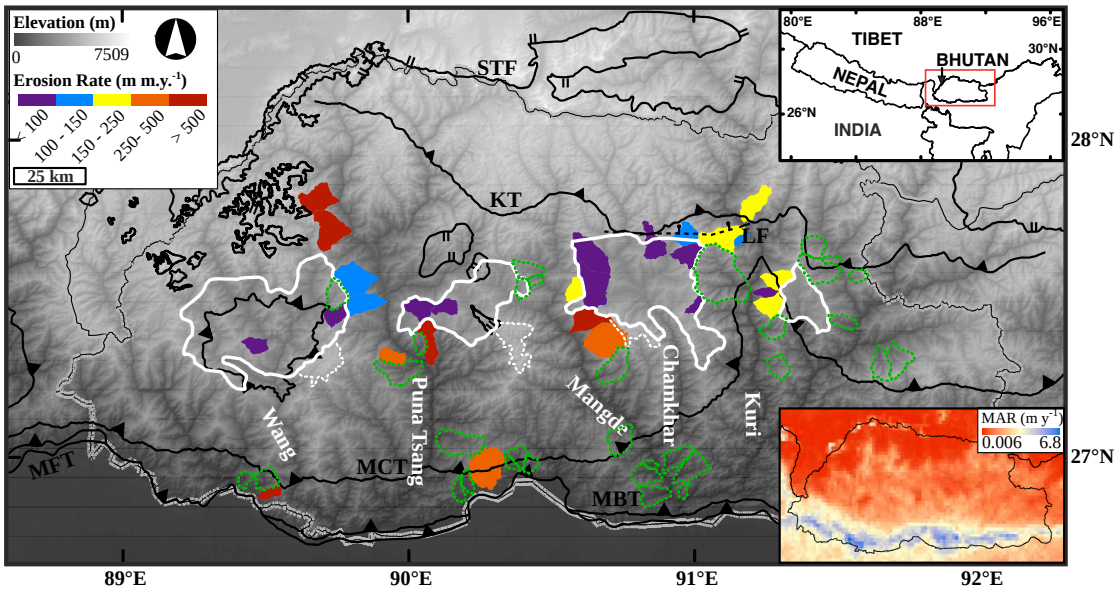
Elevation (m)
0
7509
Erosion Rate (m m.y.-1)
< 100
100 - 150
150 - 250
250- 500
> 500
25 km
STF
KT
LF
MFT
MCT
MBT
Wang
Puna Tsang
Mangde
Chamkhar
Kuri
80°E
88°E
96°E
30°N
26°N
TIBET
BHUTAN
NEPAL
INDIA
MAR (m y-1)
0.006
6.8
28°N
27°N
89°E
90°E
91°E
92°E

FIGURE 5.2

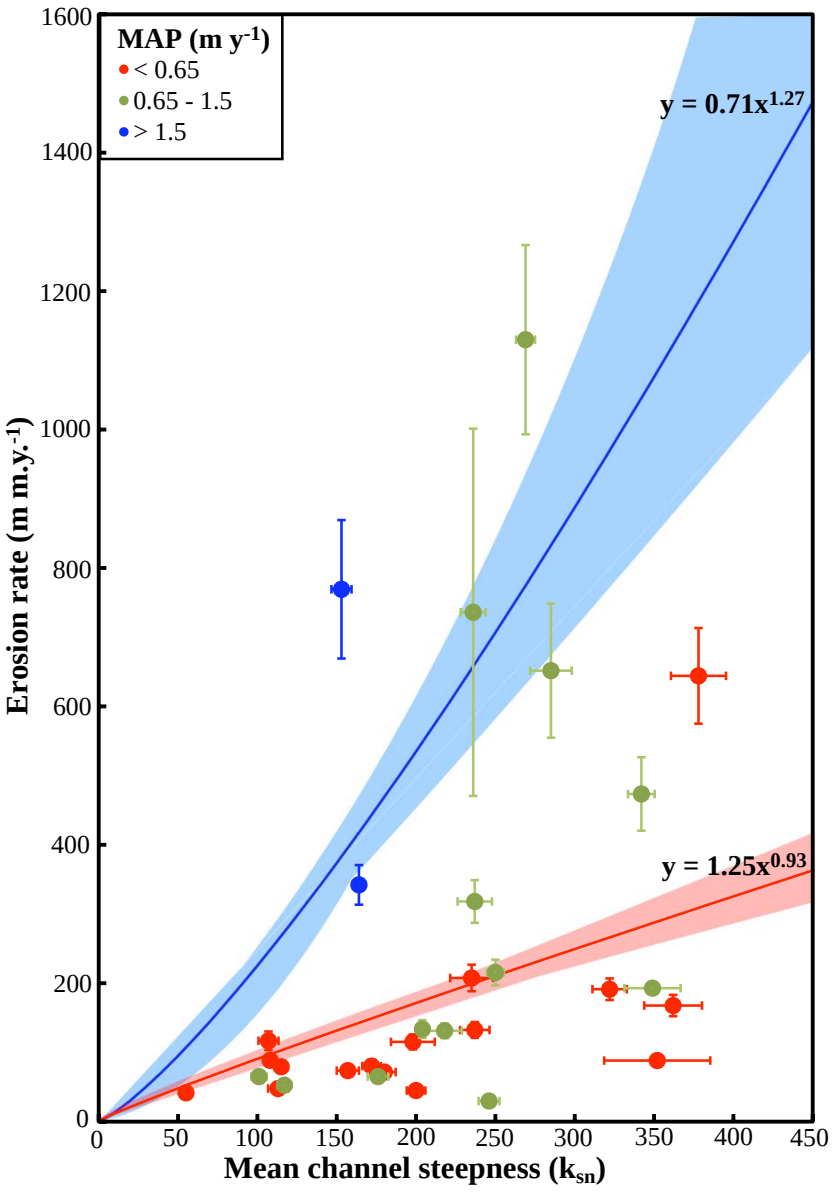
MAP (m y-1)
< 0.65
0.65 - 1.5
> 1.5
y = 0.71x1.27
y = 1.25x0.93
Erosion rate (m m.y.-1)
Mean channel steepness (ksn)
0
200
400
600
800
1000
1200
1400
1600
0
50
100
150
200
250
300
350
400
450

CHAPTER 6

SYNTHESIS

This dissertation approached the problems in the Bhutan Himalaya from a holistic perspective, and demonstrated how this treatment can lead to a more complete understanding of mountain range evolution. In this final chapter I have summarized my main findings and identified directions for future research.

THE NATURE AND ORIGIN OF PT_2 IN BHUTAN

Chapter 2 focused on a physiographic transition in the Bhutan Himalaya, which has a similar form to a physiographic transition in the central Nepal Himalaya that has been called PT_2 (Hodges et al., 2001). In Nepal, PT_2 is co-located with a steep gradient in uplift and erosion, where rates increase to the north with higher elevations (e.g. Lave and Avouac, 2001; Wobus et al., 2003; 2005; 2006; Godard et al., 2014). However, our study of PT_2 in Bhutan revealed the opposite trend, where lower exhumation rates were found in the more rugged terrains on the north side of the transition. This study also marked the discovery of a steep, brittle fault dipping to the north near the position of PT_2 in Bhutan, the Lhuentse fault. The discrepancy in exhumation rates across this fault suggested a normal sense of motion, which implied that the Lhuentse fault had the wrong sense of motion to have created PT_2. We used both apatite (U-Th)/He thermochronometry, and a newly developed technique involving the dating of deformed hydrothermal hematite using the (U-Th)/He system, to show that fault activity likely started in the Pliocene and continued into the Pleistocene. Our data indicated that the throw of the Lhuentse

fault was limited to ca. 500 m. We concluded that the Lhuentse fault was created by young activity on a rotated roof thrust associated with a blind duplex at depth.

With our morphometric analyses in Chapter 2 we demonstrated that PT_2 was only observed on the northern boundaries of uplifted low-relief landscapes (Figure 6.1). In Chapter 4 we used a landscape evolution model to simulate the production of aggraded low-relief landscapes and found the formation of a landform similar to PT_2 in Bhutan. A physiographic transition between low- and high-relief landscapes was created at a concave knickpoint where sediment-filled valleys encroached on bedrock channels that were still actively eroding high peaks. The knickpoint migrated headward and reduced relief by moving the position of aggradation upstream, and thus reduced the sharpness of the physiographic transition. This formation mechanism explained why PT_2 was co-located with the upstream limits of the low-relief landscapes, and why it was not co-located with a steep increase in rock uplift rates toward the north.

THE EFFECTS OF SHILLONG PLATEAU SHORTENING IN BHUTAN

The Miocene activation of contractional structures within the Indian plate, associated with the Shillong Plateau, is an interesting circumstance that may have complicated the evolution of the eastern 25% of Himalayan mountain belt (Figure 1.1). Studies have suggested that the accommodation of Indo-Eurasian convergence on Shillong Plateau structures may have variously: slowed down Himalayan exhumation rates, but only in eastern Bhutan (Coutand et al., 2014); slowed down

contraction and exhumation rates across the eastern Himalaya (Clark and Bilham, 2008); or had little to no effect on the Himalayan range (Biswas et al., 2007).

To resolve the effects of the Shillong Plateau structures, we used a multi-chronometer (apatite (U-Th)/He, zircon (U-Th)/He, muscovite $^{40}Ar/^{39}Ar$) approach and a 1D thermal-kinematic model to constrain the temporal and spatial patterns in long-term exhumation rates in Bhutan. We demonstrated protracted reduction in erosion rates across the hinterland of the Bhutan Himalaya after the inferred timing of initiation of Shillong Plateau structures ca. 11 Ma. We attributed this slowing to decreased slip rates on regional E-W trending contractional structures in the Himalaya due to increased fault slip rates on Shillong Plateau structures outboard of the Himalaya. The slowing of exhumation rates across Bhutan suggested that any transfer structures communicating Shillong Plateau deformation to the Himalayan mountain belt must exist west of Bhutan, such that there is no meaningful division between eastern and western Bhutan.

THE NATURE AND ORIGIN OF LOW-RELIEF LANDSCAPES IN BHUTAN

Chapters 2, 3 and 4 all developed an increased understanding of the form of the low-relief landscapes in Bhutan. Using mean elevation, local relief, hillslope gradient, channel steepness, and longitudinal river profiles we have mapped subdued landscapes perched above major knickpoints and deeply incised canyons (Figure 6.1). These low-relief landscapes are found at the middle latitudes, along the entire length of Bhutan as isolated patches. Two of these surfaces were located in smaller tributary basins and the other two form “benches” within the basins of main

stem N-S rivers. While these low-relief landscapes have been long considered transient features (Grujic et al., 2006), a critical step toward understanding their origin was made in Chapter 4 where we demonstrated that the low-relief landscapes were eroding much slower than the steep canyons below. This implied that these landscapes are being erased by headward migrating slope-break knickpoints. In Chapter 3, we suggested that these landscapes were all likely formed by the same process and, therefore, not likely created by the Shillong Plateau Rain shadow, which is thought to terminate in central Bhutan (Figure 1.1, e.g. Grujic et al., 2006).

In Chapter 4, we highlighted three important observations: 1) the presence of thick alluvial fills within the low-relief landscapes, 2) high glaciated peaks near the southern boundaries of these landscapes (Figure 6.1), and 3) a pattern within the basin averaged erosion rates, where the highest rates were co-located with the glacial peaks and slope-break knickpoints. Taken together we suggested that these observations are compatible with backtilting and hinterland focused uplift rates, which could have formed the low-relief landscapes in Bhutan. We tested this idea by imposing an antiformal uplift pattern, similar to one that might be caused by a blind duplex, on a steady-state mountain landscape within a landscape evolution model. Though we did not attempt to reproduce the landscapes of Bhutan exactly, our experimental models produced patterns of landscape response that bared a striking resemblance to Bhutan. Figure 6.1 shows a schematic block diagram of the possible blind duplex that could have influenced the current form of the Bhutan Himalaya. In contrast to a previously published hypothesis (Grujic et al., 2006), we propose that the low-relief landscapes formed as they were uplifted, and are therefore not relict

landscapes. Combining estimates of the magnitude of surface uplift and erosion rates on the low-relief landscapes, and rock uplift rates at the knickpoint position, we found that these surfaces have been uplifted ca. 800 m over the past 1.5 Ma.

THE COUPLING OF EROSION AND CLIMATE IN BHUTAN

Quantifying the connection between topography, erosion, tectonics and climate is essential to test if the rain shadow of the Shillong Plateau has affected the evolution of the Bhutan Himalaya. In Chapter 5 we explored the relationships between mean normalized channel steepness, cosmogenic radionuclide basin averaged erosion rates, and mean annual rainfall values derived from satellite data. Our data suggest that basins receiving less than 0.65 m of rain per year are much steeper for a given erosion rate than basins receiving more than 1.5 m of rain per year. Furthermore, these two datasets were best described by different non-linear relationships implying different erosivity values and non-linear incision processes, which set the topographic form at similar erosion rates.

With these non-linear relationships we were able to constrain the effects of a reduction in rainfall rate on the evolution of the Bhutan Himalaya – the climate change hypothesis. At the channel steepness values of the current foreland basins and the uplifted low-relief surfaces (ca. 150 $m^{0.9}$), erosion rates would have changed from ca. 400 m $m.y.^{-1}$ when receiving more than 1.5 m of rain per year to ca. 100 m $m.y.^{-1}$ when receiving less than 0.65 m of rain per year. If this change occurred ca. 5 Ma, as suggested by Grujic et al. (2006), we would expect ca. 1500 m of surface uplift, which is much lower than the 2500 m required to uplift the low-relief

surfaces from a lower foreland position. These results showed that the climate change hypothesis is tenuous based on the current relationships between topography, erosion rate and climate in the Bhutan Himalaya.

FUTURE RESEARCH DIRECTIONS

Detrital thermochronometry studies in the Bhutan Himalaya.

Our bedrock thermochronometry data and geomorphic interpretations suggested that the topographic form of the Bhutan Himalaya might have varied significantly since the Miocene. The use of detrital thermochronometry of select basins from the low-relief landscapes and adjacent canyons could help constrain how much topography changed during the erosion rate decrease detected across Bhutan. A useful place to start would be in the basin in central Bhutan, where we have presented a multi-chronometer transect spanning ca. 1700 vertical meters, and also measured the recent erosion rates using cosmogenic radionuclide techniques.

Dating of low-relief surface alluvial deposits via cosmogenic nuclide techniques.

If our estimates of the low-relief surfaces are correct, then we may expect that very old alluvial deposits can be found on these surfaces. Independent age constraints of these surfaces would be beneficial for further testing of a formation mechanism. Because of this potentially old age, many conventional techniques (e.g. ^{14}C) may fall short of constraining such deposition. Instead, the use of multiple cosmogenic nuclides and the isochron method has shown promise in dating similarly old buried

sediments (Balco and Rovey, 2008). Of great importance would be finding the best sample locations (e.g. high above current river elevation, and recently exposed) and to evaluate timing consistency between low-relief landscapes.

FIGURE CAPTIONS

Figure 6.1. Oblique block model and elevation map of the central Bhutan Himalaya. Solid white lines denote the outline of perched low-relief surfaces. Grey lines denote the outline of southern glacial surfaces. Faults adapted from Cooper et al. (2012), Long et al. (2011), Cooper et al. (2013). MFT – Main Frontal thrust system; MBT – Main Boundary thrust system; MCT – Main Central thrust system; KT – Kakhtang thrust; STF - South Tibetan fault; SP - Shillong Plateau.

REFERENCES

Balco, G., & Rovey, C. W. (2008). An isochron method for cosmogenic-nuclide dating of buried soils and sediments. *American Journal of Science, 308*(10), 1083-1114.

Biswas, S., Coutand, I., Grujic, D., Hager, C., Stockli, D., & Grasemann, B. (2007). Exhumation and uplift of the Shillong plateau and its influence on the eastern Himalayas: New constraints from apatite and zircon (U-Th- Sm)/He and apatite fission track analyses. *Tectonics, 26*(6), 22. doi: 10.1029/2007tc002125

Bookhagen, B., in review, High resolution spatiotemporal distribution of rainfall seasonality and extreme events based on a 12-year TRMM time series.

Clark, M. K., & Bilham, R. (2008). Miocene rise of the Shillong Plateau and the beginning of the end for the Eastern Himalaya. *Earth and Planetary Science Letters, 269*(3), 337-351.

Cooper, F. J., Adams, B. A., Edwards, C. S., & Hodges, K. V. (2012). Large normal-sense displacement on the South Tibetan fault system in the eastern Himalaya. *Geology, 40*(11), 971-974. doi: 10.1130/g33318.1

Cooper, F. J., Hodges, K. V., & Adams, B. A. (2013). Metamorphic constraints on the character and displacement of the South Tibetan fault system, central Bhutanese Himalaya. *Lithosphere, 5*(1), 67-81. doi: 10.1130/l221.1

Coutand, I., Whipp, D. M., Grujic, D., Bernet, M., Fellin, M. G., Bookhagen, B., Landry, K. R., Ghalley, S. K. & Duncan, C. (2014). Geometry and kinematics of the Main Himalayan Thrust and Neogene crustal exhumation in the Bhutanese Himalaya derived from inversion of multithermochronologic data. *Journal of Geophysical Research: Solid Earth, 119*(2), 1446-1481.

Godard, V., Bourlès, D. L., Spinabella, F., Burbank, D. W., Bookhagen, B., Fisher, G. B., Moulin, A., & Léanni, L. (2014). Dominance of tectonics over climate in Himalayan denudation. *Geology*, G35342. 35341.

Grujic, D., Coutand, I., Bookhagen, B., Bonnet, S., Blythe, A., & Duncan, C. (2006). Climatic forcing of erosion, landscape, and tectonics in the Bhutan Himalayas. *Geology, 34*(10), 801-804. doi: 10.1130/g22648.1

Hodges, K. V., Hurtado, J. M., & Whipple, K. X. (2001). Southward extrusion of Tibetan crust and its effect on Himalayan tectonics. *Tectonics, 20*(6), 799-809.

Lave, J., & Avouac, J. P. (2001). Fluvial incision and tectonic uplift across the

Himalayas of central Nepal. *Journal of Geophysical Research-Solid Earth, 106*(B11), 26561-26591. doi: 10.1029/2001jb000359

Long, S., McQuarrie, N., Tobgay, T., Grujic, D., & Hollister, L. (2011). Geologic Map of Bhutan. *Journal of Maps*, 184-192. doi: 10.4113/jom.2011.1159

Wobus, C., Heimsath, A., Whipple, K., & Hodges, K. (2005). Active out-of-sequence thrust faulting in the central Nepalese Himalaya. *Nature, 434*(7036), 1008-1011.

Wobus, C. W., Hodges, K. V., & Whipple, K. X. (2003). Has focused denudation sustained active thrusting at the Himalayan topographic front? *Geology, 31*(10), 861-864.

Wobus, C. W., Whipple, K. X., & Hodges, K. V. (2006). Neotectonics of the central Nepalese Himalaya: Constraints from geomorphology, detrital $^{40}Ar/^{39}Ar$ thermochronology, and thermal modeling. *Tectonics, 25*(4), TC4011.

FIGURE 6.1

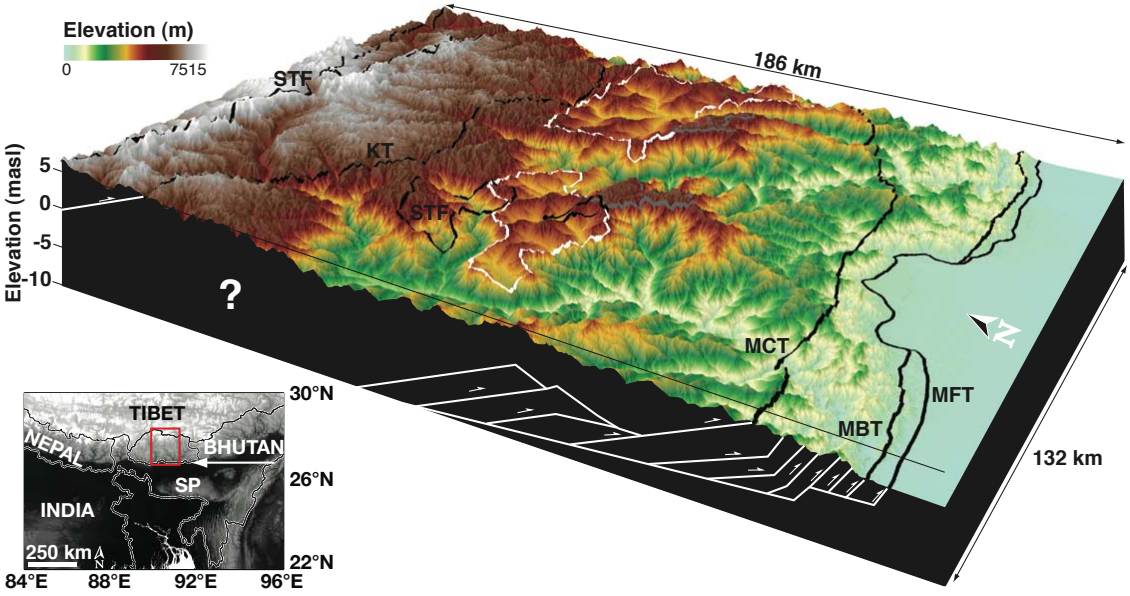
Elevation (m)
0
7515
STF
KT
STF
186 km
Elevation (masl)
5
0
-5
-10
?
MCT
MFT
MBT
132 km
N
TIBET
NEPAL
BHUTAN
SP
INDIA
250 km
30°N
26°N
22°N
84°E
88°E
92°E
96°E

APPENDIX A

CHAPTER 2 SUPPLEMENTARY MATERIALS

ORE IDENTIFIACTION VIA RAMAN SPECTOSCOPY

Before dating the ore deposit found within the Lhuentse fault, we first constrained the chemical composition of the sample. This is an important initial step that enables us to assess the complications of interpreting data from unknown or mixed mineralogical phases. Raman spectroscopy has been show to be a useful method for identifying and differentiating between different iron oxides (e.g. de Faria et al., 1997).

Samples of the hydrothermal ore located in the fault were broken into millimeter-sized particles with an agate motor and pestle. The grains were then self-abraded in a pneumatic chamber, without any additional abrading media, for 3 days until the grains looked polished and well rounded. Measurements were made using a custom-built Raman spectrometer in the LeRoy Eyring Center for Solid State Science at Arizona State University. The samples were analyzed using a Compass 532 nm laser utilizing neutral density filters. The laser was focused onto the samples using a x50 Mitutoyo objective, and the signal was discriminated from the laser excitation with a Kaiser laser band pass filter followed by a Semrock edge filter. The data were collected using an Acton 300i spectrograph and a back thinned Princeton Instruments liquid nitrogen cooled CCD detector. Grains of ore were analyzed with a 3 mW beam for 60 seconds over a spectral window of 100 to 1200 cm-1. Three scans were obtained at each spot and averaged. One of the averaged spectra is shown for comparison with a spectra of hematite (α-Fe_2O_3) from de Faria et al. (1997) in Figure S1. The samples were determined to be nearly entirely hematite.

ELEVATION NORMILIZATION OF THERMOCHONMETRY DATA

Our aim of the thermochronometric transect study was to measure a thermal perturbation created by the Lhuntse fault. However, do to accessibility issues our sample elevations varied by ca. 1100 m. So as not to conflate the issues of the influence of topography (e.g. the correlation of thermochronometric date and elevation), and the cutting of isocrones or advection of heat created by faulting, we have normalized our apatite (U-Th)/He data to the mean elevation of the transect (1740 m). This normalization ensured that the influence of topography did not complicate the interpretation of our data. To normalize the cooling dates to a single elevation samples that were collected above the mean elevation were reduced in age, and samples collected below the mean elevation were increased in age. The cooling dates of samples collected near the mean elevation were corrected less than those farther from the mean elevation.

To change a date based on its elevation we use an exhumation rate. To calculate exhumation rates we used a 1D thermal model (AGE2EDOT, Brandon et al., 1998). See main text for a discussion of this model and parameters used in this study. We calculated elevation corrected dates (t_{corr}; e.g. the dates denoted in Figure 7c) using the following equations:

$$t_{corr} = \frac{\Delta z}{\bar{\varepsilon}} + t_{\text{int}} \quad (1)$$

$$\Delta z = z_{\text{int}} - \bar{z} \quad (2)$$

where $\bar{\varepsilon}$ is the mean exhumation rate for the block in which the sample was collected (e.g. the exhumation rates denoted in Figure 7b), t_{int} is the initial cooling

date (e.g. the dates in Figure 7a), z_{int} is the elevation at the sample location, and $\bar{z}$ is the mean elevation of the sample locations along the entire transect. We emphasize that uncertainties also need be propagated through this calculation using analytical or Monte Carlo techniques.

FIGURE CAPTIONS

Figure A1. Upper Raman spectra is of hematite (α-Fe_2O_3) from de Faria et al. (1997). The lower Raman spectra is representative of the data recorded from the hydrothermal ore collected from the Lhuentse fault.

REFERNCES

Brandon, M. T., Roden-Tice, M. K., and Garver, J. I., 1998, Late Cenozoic exhumation of the Cascadia accretionary wedge in the Olympic Mountains, northwest Washington State: Geological Society of America Bulletin, v. 110, no. 8, p. 985-1009.

de Faria, D.L.A., Venâncio Silva, S., and de Oliveira, M.T., 1997, Raman Microspectroscopy of Some Iron Oxides and Oxyhydroxides: Journal of Raman Spectroscopy, v. 28, no. 11, p. 873-878.

Table A1. Additional thermochronometer sample infromation.

Sample/ Aliquot	Th/U[a]	R1[b] (μm)	R2[b] (μm)	L[b] (μm)	T1[b] (μm)	T2[b] (μm)	^{4}He F_τ[c] (fmol)	1σ (fmol)
BT0962								
a1	0.014	52.1	41.0	183.5	--	--	2.519	0.041
a2	0.052	32.1	50.5	232.2	--	--	4.990	0.071
a4	0.019	51.1	40.1	128.0	--	--	1.020	0.024
a5	0.016	39.0	39.5	124.7	--	--	1.510	0.029
z1	0.006	34.1	30.5	219.0	65.1	56.5	464.2	5.4
z2	0.009	24.8	35.3	241.0	55.9	63.5	469.8	5.6
z3	0.023	32.4	33.2	214.6	29.9	59.6	611.6	6.1
z4	0.035	33.0	32.5	268.9	49.3	74.7	707.8	7.5
BT0963								
a2	0.078	52.5	52.8	166.9	--	--	4.611	0.069
a3	0.056	42.9	27.7	151.1	--	--	1.347	0.027
a4	0.032	41.7	36.4	150.9	--	--	1.665	0.030
z1	0.025	37.6	37.6	217.1	63.4	58.6	525.4	6.2
z2	0.023	48.5	42.9	180.1	90.3	43.4	975	12
z3	0.086	50.2	55.9	189.7	60.8	88.8	227.0	2.7
z4	0.037	44.2	43.9	195.9	82.6	67.4	512.7	6.1
z5	0.023	46.9	46.0	293.3	63.2	60.2	1659	20
BT0964								
a1	0.050	29.8	52.0	143.6	--	--	0.817	0.025
a2	0.030	37.5	20.6	212.7	--	--	0.852	0.019
a3	0.028	43.6	34.3	226.3	--	--	0.904	0.018
a4	0.050	60.4	55.3	208.0	--	--	2.467	0.039
z1	0.093	36.4	37.7	273.3	55.0	53.4	140.2	1.5
z2	0.044	33.7	35.4	198.4	40.0	51.8	73.01	0.74
z3	0.064	47.5	42.1	204.0	68.3	77.2	76.86	0.86
z4	0.045	42.6	41.5	255.5	75.5	70.1	197.1	2.2
z5	0.125	31.6	36.0	283.1	59.7	51.2	55.52	0.63
BT1022								
a2	0.062	38.8	45.2	102.8	--	--	1.119	0.033
a3	0.055	48.6	40.8	180.4	--	--	0.863	0.030
a4	0.033	40.8	34.2	140.7	--	--	0.812	0.026
a5	0.081	41.8	39.7	127.6	--	--	1.057	0.030
BT0969								
a1	0.121	46.6	46.6	192.5	--	--	0.532	0.015
a2	0.078	52.5	52.0	160.6	--	--	0.443	0.016
a3	1.70	43.6	44.2	149.1	--	--	0.254	0.016
BT0970								
a1	0.103	56.4	59.9	188.4	--	--	0.562	0.019
a2	0.125	71.3	63.1	142.6	--	--	0.406	0.013
a3	0.146	67.1	61.3	142.1	--	--	0.367	0.017
BTORE								
h7	2.4	--	--	--	--	--	--	--
h8	4.1	--	--	--	--	--	--	--
h9	12	--	--	--	--	--	--	--
h10	3.6	--	--	--	--	--	--	--

[a]The Th/U ratio of the analyzed crystal. For this calculation the ^{235}U has been accounted for by dividing the measured ^{238}U by 137.88. [b]R1 and R2 describe the perpendicular half widths of the crystal. L describes the length of the c axis. T1 and T2 describe the height of the pyramidal terminations of the zircon crystals. [c]The F_τ corrected ^{4}He abundance.

FIGURE A1.

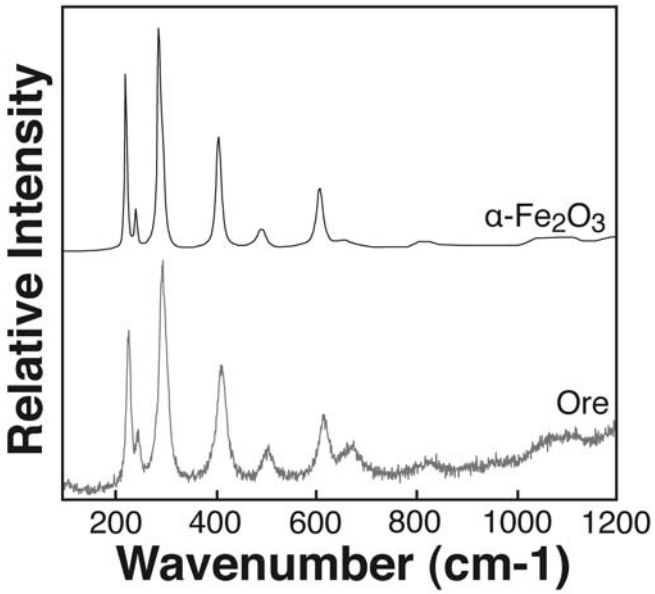
Relative Intensity
α-Fe2O3
Ore
200
400
600
800
1000
1200
Wavenumber (cm-1)

APPENDIX B

CHAPTER 3 SUPPLEMENTARY MATERIALS

Table A1. Apatite and zircon (U-Th)/He data.

Sample/ Aliquot	R1* (μm)	R2* (μm)	L* (μm)	T1* (μm)	T2* (μm)	^{4}He† (fmol)	2σ (fmol)	^{238}U† (fmol)	2σ (fmol)	^{232}Th† (fmol)	2σ (fmol)	Th/U§	Raw Date (Ma)	2σ (Ma)	F_{τ}«	^{4}He F_{τ} # (fmol)	2σ (fmol)	Corr. Date¥ (Ma)	2σ (Ma)	Mean Date (Ma)	2σ (Ma)
BT0847																					
a1	52.3	49.0	226.5	--	--	1.820	0.059	325	11	15.3	5.0	0.047	4.28	0.20	0.739	2.462	0.080	5.80	0.27		
a2	54.7	47.2	176.5	--	--	2.262	0.069	257	12	11.4	5.2	0.044	6.74	0.38	0.729	3.102	0.094	9.24	0.52		
a3	39.0	34.8	149.8	--	--	1.010	0.037	175.1	7.8	32.1	4.5	0.182	4.29	0.24	0.646	1.564	0.057	6.64	0.37		
a4	48.6	36.3	227.4	--	--	2.293	0.072	429	11	42.0	3.5	0.097	4.05	0.16	0.700	3.27	0.10	5.78	0.23	**5.41**	**0.98**
a5	43.1	59.5	172.2	--	--	1.471	0.050	358.8	8.8	60.4	4.3	0.167	3.06	0.13	0.728	2.020	0.068	4.20	0.17		
a6	49.8	33.0	130.0	--	--	1.083	0.041	179	15	23.3	2.6	0.129	4.55	0.41	0.666	1.626	0.062	6.83	0.62		
a7	48.0	41.9	230.3	--	--	1.858	0.057	346	23	35.7	2.5	0.102	4.06	0.29	0.714	2.602	0.079	5.69	0.41		
z1	40.4	29.5	237.7	45.2	61.8	32.98	0.81	6200	177	60	16	0.010	4.11	0.15	0.726	45.5	1.1	5.67	0.21		
z2	38.3	35.0	465.4	51.8	58.0	724	17	88244	2647	7348	226	0.083	6.24	0.23	0.762	951	22	8.19	0.30		
z3	31.4	32.9	209.2	53.6	45.7	93.1	2.1	13714	385	3773	126	0.273	4.95	0.17	0.705	132.0	3.0	7.01	0.24	**6.57**	**0.76**
z4	32.0	41.7	295.3	45.3	33.9	143.8	3.1	21707	643	3286	121	0.150	4.96	0.18	0.751	191.5	4.2	6.60	0.24		
z5	36.7	32.7	286.8	42.8	30.6	107.7	2.2	17165	518	2910	79	0.168	4.68	0.17	0.741	145.4	3.0	6.31	0.22		
BT0848																					
a1	55.5	47.5	136.5	--	--	0.387	0.023	81.6	3.8	13.9	5.1	0.170	3.54	0.27	0.716	0.541	0.032	4.94	0.38		
a2	44.7	43.0	148.5	--	--	0.403	0.023	59.4	4.1	11.6	5.4	0.194	5.03	0.45	0.687	0.586	0.033	7.32	0.66		
a3	53.0	46.0	182.0	--	--	0.550	0.029	98.4	6.2	16.9	7.9	0.170	4.17	0.34	0.724	0.760	0.039	5.76	0.48	**5.15**	**0.67**
a4	52.7	45.7	156.4	--	--	0.517	0.027	118.6	5.2	14.9	3.5	0.124	3.28	0.22	0.715	0.723	0.038	4.59	0.31		
a5	51.8	58.4	180.0	--	--	0.850	0.034	163.9	7.0	39.1	3.7	0.237	3.81	0.22	0.744	1.143	0.045	5.12	0.29		
z1	38.1	28.0	335.4	72.7	62.1	116.6	3.4	16085	281	2854	28	0.176	5.39	0.18	0.721	161.7	4.7	7.48	0.25		
z2	30.2	30.5	258.0	42.8	33.2	105.9	2.6	17351	285	1181	13	0.068	4.66	0.14	0.708	149.7	3.7	6.58	0.19		
z3	24.5	24.4	230.9	41.2	28.3	75.9	1.9	11140	188	2425	34	0.216	5.02	0.15	0.645	117.6	2.9	7.78	0.23	**7.27**	**0.50**
z4	27.4	33.7	230.6	43.8	41.7	202.6	5.3	31643	510	640.4	8.2	0.020	4.94	0.15	0.701	289.1	7.5	7.04	0.21		
z5	27.5	27.1	225.2	49.7	43.9	47.2	1.2	6697	101	1256	25	0.186	5.23	0.15	0.670	70.5	1.7	7.81	0.22		
BT0849																					
a1	52.8	56.8	191.0	--	--	4.18	0.12	812	14	15.8	1.6	0.019	3.96	0.13	0.747	5.59	0.16	5.30	0.18		
a2	63.2	52.7	155.2	--	--	6.20	0.16	1166	19	36.5	1.4	0.031	4.09	0.12	0.747	8.31	0.21	5.48	0.17		
a3	*45.7*	*41.6*	*365.0*	--	--	*6.50*	*0.16*	*1041*	*36*	*31*	*12*	*0.029*	*4.80*	*0.21*	*0.722*	*9.00*	*0.23*	*6.65*	*0.29*	**5.35**	**0.17**
a4	56.1	52.2	204.6	--	--	4.21	0.11	784	34	36	11	0.046	4.12	0.21	0.748	5.63	0.15	5.50	0.28		
a5	72.5	60.3	159.2	--	--	4.68	0.13	915	17	27.7	2.4	0.030	3.93	0.13	0.771	6.07	0.17	5.10	0.17		
a6	39.5	33.1	122.6	--	--	1.390	0.047	306.5	5.9	7.4	1.8	0.024	3.49	0.14	0.631	2.203	0.076	5.54	0.22		
z1	46.2	33.2	384.1	64.5	52.7	1515	25	215776	4389	1404	50	0.006	5.43	0.14	0.769	1970	33	7.06	0.19		
z2	42.2	32.8	395.1	77.1	59.4	1506	30	217596	4401	1317	40	0.006	5.35	0.15	0.758	1987	39	7.06	0.20		
z3	35.0	26.5	206.1	35.3	43.2	391.9	9.3	61624	1229	455	24	0.007	4.92	0.15	0.697	562	13	7.05	0.22	**7.06**	**0.12**
z4	*46.9*	*36.4*	*312.3*	*99.8*	*87.4*	*1338*	*29*	*180965*	*4003*	*1468*	*46*	*0.008*	*5.72*	*0.18*	*0.761*	*1759*	*39*	*7.52*	*0.24*		
z5	*39.1*	*34.3*	*334.5*	*47.6*	*55.8*	*1099*	*19*	*153709*	*3680*	*777*	*31*	*0.005*	*5.53*	*0.17*	*0.755*	*1455*	*26*	*7.32*	*0.22*		

Table A1. Apatite and zircon (U-Th)/He data.

Sample/ Aliquot	R1* (μm)	R2* (μm)	L* (μm)	T1* (μm)	T2* (μm)	^{4}He† (fmol)	2σ (fmol)	^{238}U† (fmol)	2σ (fmol)	^{232}Th† (fmol)	2σ (fmol)	Th/U§	Raw Date (Ma)	2σ (Ma)	F_T«	^{4}He F_T # (fmol)	2σ (fmol)	Corr. Date¥ (Ma)	2σ (Ma)	Mean Date (Ma)	2σ (Ma)
BT0850																					
a1	74.1	70.5	189.0	--	--	4.41	0.12	483	22	32	11	0.065	6.97	0.37	0.793	5.57	0.16	8.79	0.47		
a2	60.8	53.6	160.9	--	--	6.07	0.16	1038	42	91.5	8.1	0.087	4.44	0.21	0.746	8.14	0.21	5.95	0.29		
a3	*46.3*	*32.5*	*160.0*	--	--	*14.37*	*0.35*	*469*	*12*	*43.1*	*5.6*	*0.091*	*23.17*	*0.82*	*0.667*	*21.54*	*0.54*	*34.7*	*1.2*	**5.6**	**1.1**
a4	42.1	40.1	108.0	--	--	1.03	0.04	236	10	21.3	2.8	0.090	3.32	0.21	0.652	1.581	0.071	5.09	0.32		
a5	91.9	61.1	211.3	--	--	9.41	0.24	1702	32	138.7	6.5	0.081	4.20	0.14	0.806	11.68	0.31	5.21	0.17		
z1	42.8	40.4	384.9	88.0	64.1	1932	41	246088	7918	3440	115	0.014	6.06	0.23	0.779	2479	52	7.78	0.30		
z2	37.4	38.5	348.4	66.9	61.1	578	12	84558	2439	3076	88	0.036	5.25	0.19	0.761	760	16	6.90	0.24		
z3	42.7	38.3	384.5	71.5	66.3	487	11	69319	1377	1640	64	0.023	5.41	0.16	0.776	628	14	6.97	0.20	**6.95**	**0.53**
z4	40.9	31.4	278.7	51.7	45.1	234.1	5.5	32137	634	3398	85	0.105	5.51	0.17	0.743	315.0	7.4	7.41	0.22		
z5	47.2	48.7	450.1	72.4	70.1	2389	53	369038	9214	4552	113	0.012	5.00	0.17	0.811	2947	66	6.17	0.21		
BT0851																					
a1	49.8	42.7	164.1	--	--	2.150	0.070	449.7	7.6	30.5	1.4	0.067	3.64	0.13	0.705	3.048	0.097	5.17	0.19		
a2	51.0	40.4	177.1	--	--	2.71	0.11	570	10	41.8	1.5	0.073	3.62	0.16	0.707	3.84	0.15	5.13	0.23	**5.26**	**0.27**
a3	76.2	99.4	228.6	--	--	14.16	0.34	2342	89	137	12	0.058	4.62	0.20	0.827	17.12	0.41	5.59	0.25		
a4	*83.5*	*69.7*	*173.0*	--	--	*10.56*	*0.26*	*922*	*41*	*32.8*	*5.9*	*0.035*	*8.80*	*0.44*	*0.796*	*13.26*	*0.32*	*11.04*	*0.55*		
z1	62.4	39.8	546.6	70.6	60.2	721	15	95670	2847	10720	310	0.111	5.69	0.21	0.816	883	19	6.97	0.25		
z2	46.0	32.2	299.2	61.1	64.1	91.9	2.1	15614	490	2121	67	0.135	4.42	0.17	0.755	121.7	2.8	5.86	0.23		
z3	*31.1*	*30.2*	*272.0*	*46.4*	*53.0*	*450*	*11*	*15821*	*499*	*11641*	*588*	*0.730*	*18.81*	*0.70*	*0.703*	*639*	*15*	*26.73*	*0.99*	**6.22**	**0.42**
z4	38.2	43.6	372.3	95.1	50.5	292.0	5.4	45366	972	10794	269	0.236	4.73	0.13	0.774	377.5	7.0	6.11	0.17		
z5	36.3	39.0	278.2	63.7	62.0	164.6	4.0	27398	741	756	36	0.027	4.62	0.17	0.751	219.2	5.4	6.16	0.23		
BT0852																					
a1	92.1	86.1	207.4	--	--	3.260	0.094	635	11	103.9	3.5	0.162	3.83	0.13	0.824	3.95	0.12	4.65	0.16		
a2	88.5	70.4	216.4	--	--	7.26	0.19	1262	20	195.5	4.0	0.154	4.30	0.13	0.811	8.94	0.23	5.30	0.16	**4.99**	**0.45**
a3	*47.9*	*79.0*	*217.0*	--	--	*5.31*	*0.14*	*584*	*28*	*88.7*	*8.1*	*0.151*	*6.81*	*0.36*	*0.778*	*6.83*	*0.18*	*8.75*	*0.46*		
a4	51.5	50.5	171.0	--	--	1.512	0.050	296	16	57.7	7.8	0.194	3.79	0.23	0.727	2.080	0.070	5.22	0.32		
z1	24.9	23.1	187.3	48.2	34.1	189.7	5.0	29519	514	730.4	8.9	0.025	4.95	0.15	0.626	302.8	8.0	7.90	0.25		
z2	36.1	30.2	324.4	51.9	78.0	179.3	4.5	31425	568	2782	28	0.088	4.33	0.13	0.726	247.2	6.2	5.97	0.18		
z3	27.6	26.6	173.6	52.4	31.5	41.1	1.0	8820	157	634.6	7.2	0.071	3.55	0.11	0.656	62.6	1.6	5.41	0.17	**5.99**	**0.73**
z4	43.0	37.5	274.1	72.8	69.9	67.6	2.0	12121	187	1073	14	0.088	4.23	0.14	0.759	89.0	2.6	5.57	0.18		
z5	42.5	46.0	245.3	65.5	55.6	349.8	8.7	56341	901	4173	51	0.074	4.73	0.14	0.777	450	11	6.08	0.18		
BT0853																					
a1	51.3	47.5	201.5	--	--	2.62	0.12	626	10	28.1	1.5	0.045	3.20	0.16	0.729	3.59	0.17	4.39	0.22		
a2	65.2	68.8	169.7	--	--	3.09	0.10	692	11	26.9	1.3	0.039	3.43	0.12	0.776	3.99	0.13	4.42	0.16	**4.412**	**0.091**
a3	50.1	61.0	203.0	--	--	7.39	0.18	1702	29	96.7	5.8	0.056	3.320	0.098	0.752	9.82	0.24	4.41	0.13		
a4	*81.3*	*88.5*	*245.9*	--	--	*22.41*	*0.55*	*4448*	*70*	*312.0*	*6.5*	*0.070*	*3.84*	*0.11*	*0.826*	*27.15*	*0.66*	*4.65*	*0.13*		
z1	49.4	45.3	364.5	93.6	72.0	587	14	85713	1587	17791	186	0.206	5.06	0.15	0.798	735	18	6.34	0.19		
z2	41.1	45.5	288.5	68.9	62.2	417	10	63890	1155	4665	45	0.072	4.97	0.15	0.779	535	13	6.38	0.20	**6.29**	**0.11**
z3	43.0	37.5	274.1	72.8	69.9	405.4	9.8	66065	1119	3927	40	0.059	4.69	0.14	0.759	534	13	6.17	0.18		
z4	*42.5*	*46.0*	*245.3*	*65.5*	*55.6*	*157.2*	*4.1*	*28603*	*469*	*2596*	*29*	*0.090*	*4.17*	*0.13*	*0.777*	*202.4*	*5.3*	*5.37*	*0.17*		

Table A1. Apatite and zircon (U-Th)/He data.

Sample/ Aliquot	R1* (µm)	R2* (µm)	L* (µm)	T1* (µm)	T2* (µm)	^{4}He† (fmol)	2σ (fmol)	^{238}U† (fmol)	2σ (fmol)	^{232}Th† (fmol)	2σ (fmol)	Th/U§	Raw Date (Ma)	2σ (Ma)	F_T«	^{4}He F_T # (fmol)	2σ (fmol)	Corr. Date¥ (Ma)	2σ (Ma)	Mean Date (Ma)	2σ (Ma)
BT0914																					
a1	51.8	48.7	150.0	--	--	1.346	0.05	297.68	6.6	48.6	2.2	0.162	3.37	0.14	0.717	1.878	0.067	4.71	0.19		
a2	60.0	47.2	189.2	--	--	1.843	0.07	409.22	8.8	55.5	2.3	0.135	3.38	0.14	0.742	2.484	0.093	4.56	0.19	**4.69**	**0.12**
a3	52.9	59.0	163.4	--	--	1.468	0.06	304.70	6.8	48.0	1.6	0.156	3.60	0.17	0.742	1.978	0.081	4.85	0.22		
z1	41.4	44.1	203.1	42.4	41.7	64.29	1.70	12929	286	1969	46	0.151	3.72	0.13	0.768	83.7	2.2	4.84	0.17		
z2	45.6	33.7	175.1	57.8	47.5	68.12	1.88	12994	245	2428	55	0.185	3.89	0.13	0.731	93.1	2.6	5.32	0.18		
z3	55.4	37.5	235.3	45.1	52.0	72.35	1.84	13222	288	3142	73	0.236	4.02	0.13	0.781	92.7	2.4	5.15	0.17	**5.06**	**0.18**
z4	41.7	42.9	267.8	49.6	64.2	214.4	5.5	42811	997	4932	120	0.114	3.78	0.13	0.774	276.8	7.2	4.88	0.17		
z5	45.0	43.9	211.1	47.4	53.6	67.43	1.84	12366	256	2921	82	0.234	4.00	0.14	0.773	87.2	2.4	5.18	0.18		
BT0919																					
a1	52	50.7	260.4	--	--	3.66	0.12	700	12	110.3	2.8	0.157	3.91	0.14	0.746	4.90	0.16	5.24	0.19		
a2	*41.5*	*38.1*	*124.5*	--	--	*1.149*	*0.056*	*197.1*	*4.7*	*39.3*	*1.6*	*0.198*	*4.32*	*0.24*	*0.653*	*1.760*	*0.086*	*6.61*	*0.36*	**5.34**	**0.13**
a3	46.6	42.8	182.6	--	--	3.66	0.13	718	14	88.2	2.4	0.122	3.84	0.16	0.703	5.21	0.19	5.46	0.23		
a4	35.5	40.2	131.0	--	--	1.046	0.049	223.9	5.6	47.9	1.8	0.212	3.45	0.18	0.644	1.623	0.077	5.35	0.29		
z1	33.1	27.6	164.5	39.8	45.3	23.50	0.61	4443	76	399.4	5.4	0.089	4.01	0.13	0.679	34.61	0.92	5.91	0.19		
z2	44.9	35.7	157.4	42.0	46.2	22.00	0.56	4172	71	970	11	0.231	3.88	0.12	0.735	29.94	0.78	5.27	0.16		
z3	40.5	32.4	190.5	43.7	46.2	57.6	1.5	8375	135	2608	31	0.309	4.97	0.15	0.728	79.2	2.1	6.83	0.21	**5.84**	**0.54**
z4	43.4	39.5	182.6	41.4	44.6	48.7	1.3	7581	135	1766	19	0.231	4.72	0.15	0.755	64.6	1.7	6.26	0.20		
z5	44.9	32.6	197.7	33.3	45.8	44.5	1.2	7683	128	3549	35	0.459	4.06	0.12	0.742	60.0	1.6	5.47	0.17		
BT0920																					
z1	40.7	38.0	218.5	45.8	44.6	113.3	2.8	22897	470	6734	132	0.292	3.59	0.11	0.754	150.2	3.7	4.76	0.15		
z2	46.0	45.9	244.8	36.4	44.3	264.9	6.6	61207	1097	6945	169	0.113	3.266	0.098	0.790	335.2	8.3	4.13	0.12		
z3	39.3	39.5	230.8	46.8	64.2	238.3	6.0	50324	939	5186	111	0.102	3.58	0.11	0.754	316.1	8.0	4.75	0.15	**4.53**	**0.54**
z4	*48.5*	*49.2*	*293.7*	*42.0*	*61.0*	*477*	*12*	*123399*	*2917*	*8132*	*174*	*0.065*	*2.947*	*0.098*	*0.805*	*592*	*14*	*3.66*	0.12		
z5	48.5	40.6	215.8	40.6	55.9	93.5	2.4	19089	444	4770	104	0.248	3.59	0.12	0.774	120.7	3.0	4.63	0.15		
BT0987																					
a1	46.1	39.1	229.4	--	--	1.949	0.062	382.6	7.9	5.6	2.3	0.015	3.93	0.15	0.702	2.775	0.088	5.60	0.21		
a2	51.1	42.2	137.1	--	--	1.278	0.046	267	18	4.5	1.7	0.017	3.70	0.28	0.697	1.833	0.066	5.30	0.40	**5.89**	**0.38**
a3	46.2	46.0	231.8	--	--	3.087	0.085	538	16	5.2	3.8	0.010	4.43	0.18	0.721	4.28	0.12	6.15	0.24		
a4	40.4	29.5	252.2	--	--	2.287	0.064	436.1	9.7	1.0	2.2	0.002	4.06	0.14	0.656	3.488	0.097	6.19	0.22		
z1	39.3	32.1	208.4	42.8	46.8	49.9	1.0	6133	129	977	31	0.158	6.07	0.18	0.731	68.3	1.4	8.31	0.24		
z2	34.2	36.5	187.0	49.3	47.3	65.7	1.5	10066	215	726	33	0.072	4.97	0.15	0.722	91.0	2.0	6.89	0.21		
z3	41.1	39.4	227.1	64.7	67.9	51.9	1.2	8117	174	1356	49	0.166	4.77	0.15	0.750	69.1	1.6	6.35	0.20	**6.89**	**0.66**
z4	40.1	30.1	169.5	33.3	41.1	50.2	1.2	8215	165	1054	34	0.127	4.59	0.14	0.717	70.0	1.7	6.41	0.20		
z5	36.2	35.0	166.1	64.7	54.4	31.80	0.78	4821	111	1024	51	0.211	4.87	0.16	0.699	45.5	1.1	6.97	0.23		

Table A1. Apatite and zircon (U-Th)/He data.

Sample/ Aliquot	R1* (μm)	R2* (μm)	L* (μm)	T1* (μm)	T2* (μm)	^{4}He† (fmol)	2σ (fmol)	^{238}U† (fmol)	2σ (fmol)	^{232}Th† (fmol)	2σ (fmol)	Th/U§	Raw Date (Ma)	2σ (Ma)	F_τ«	^{4}He F_τ # (fmol)	2σ (fmol)	Corr. Date¥ (Ma)	2σ (Ma)	Mean Date (Ma)	2σ (Ma)
BT0988																					
a1	54.2	62.5	132.7	--	--	0.386	0.018	74.5	3.5	9.8	3.1	0.131	3.90	0.26	0.737	0.524	0.024	5.28	0.35		
a2	49.4	35.3	149.6	--	--	0.342	0.026	44.2	2.7	37.9	3.9	0.851	5.01	0.47	0.675	0.507	0.039	7.42	0.70	**5.90**	**0.99**
a3	*52.7*	*49.0*	*140.6*	--	--	*4.87*	*0.13*	*69.1*	*3.1*	*60.2*	*3.3*	*0.864*	*45.4*	*2.1*	*0.710*	*6.86*	*0.19*	*63.7*	*3.0*		
a4	49.8	46.2	162.7	--	--	1.064	0.045	146.5	8.2	187.6	8.7	1.271	4.34	0.27	0.705	1.509	0.064	6.16	0.38		
z1	46.4	40.7	223.3	62.3	45.9	463	11	77534	1526	9290	258	0.119	4.50	0.14	0.771	601	14	5.84	0.18		
z2	32.0	33.7	246.8	45.5	48.5	188.2	4.4	31795	618	2609	72	0.081	4.50	0.14	0.722	260.9	6.1	6.23	0.19		
z3	36.4	36.4	347.4	45.7	42.7	548.8	9.9	73834	1433	7518	211	0.101	5.62	0.15	0.756	726	13	7.44	0.20	**6.62**	**0.58**
z4	47.4	44.9	249.6	44.2	48.4	367.3	6.9	49208	1029	9930	314	0.200	5.52	0.15	0.790	465.2	8.8	6.99	0.19		
z5	37.9	39.0	274.4	61.0	48.5	682	15	100097	2249	10465	258	0.104	5.15	0.16	0.757	900	20	6.80	0.21		
BT0989																					
a1	51.0	43.8	270.1	--	--	2.487	0.074	466	11	17.7	3.4	0.038	4.09	0.16	0.732	3.40	0.10	5.59	0.21		
a2	45.7	42.0	230.0	--	--	3.315	0.096	304.3	7.1	24.1	2.3	0.078	8.28	0.31	0.708	4.68	0.14	11.68	0.44		
a3	51.4	42.4	186.7	--	--	1.811	0.059	294.3	7.5	7.6	2.9	0.026	4.74	0.20	0.715	2.533	0.084	6.62	0.28	**6.4**	**1.8**
a4	58.8	42.2	156.6	--	--	1.364	0.050	286.2	8.2	6.8	5.0	0.024	3.67	0.17	0.721	1.891	0.071	5.09	0.24		
a5	42.4	41.5	145.2	--	--	1.240	0.043	180.1	5.4	3.0	3.9	0.017	5.31	0.25	0.677	1.832	0.065	7.84	0.36		
z1	22.8	22.9	219.4	28.9	35.7	29.74	0.69	5650	124	700	28	0.123	3.96	0.13	0.625	47.6	1.1	6.34	0.20		
z2	*31.8*	*30.3*	*261.9*	*46.2*	*46.7*	*39.76*	*0.96*	*9753*	*223*	*1254*	*39*	*0.128*	*3.07*	*0.10*	*0.710*	*56.0*	*1.4*	*4.32*	*0.14*		
z3	29.0	30.0	205.2	31.3	27.6	50.6	1.2	7074	176	2933	96	0.412	5.06	0.17	0.692	73.2	1.7	7.31	0.24	**6.63**	**0.42**
z4	28.6	26.3	160.3	35.1	25.6	20.07	0.47	3354	87	1317	38	0.390	4.25	0.15	0.661	30.39	0.73	6.44	0.22		
z5	30.7	22.5	165.5	22.5	34.9	20.21	0.50	3486	87	688	36	0.196	4.30	0.15	0.650	31.10	0.78	6.61	0.23		
BT1024																					
a1	34.1	34.8	249.2	--	--	1.036	0.040	247	12	7.8	4.6	0.031	3.23	0.20	0.651	1.59	0.06	4.95	0.30		
a2	52.3	47.3	233.2	--	--	3.63	0.12	708	17	33.4	5.2	0.047	3.92	0.16	0.737	4.92	0.17	5.32	0.22		
a3	51.2	49.1	272.0	--	--	3.48	0.13	672	20	32.8	5.2	0.048	3.96	0.19	0.744	4.68	0.18	5.33	0.25		
a4	37.8	39.5	286.7	--	--	1.627	0.062	380	11	13.9	3.1	0.036	3.29	0.15	0.686	2.37	0.09	4.79	0.22	**4.96**	**0.25**
a5	54.6	51.8	203.3	--	--	1.911	0.072	395	14	15.3	4.9	0.038	3.72	0.19	0.744	2.57	0.10	5.00	0.25		
a6	28.5	22.5	306.4	--	--	0.793	0.038	246.8	6.5	10.4	3.3	0.042	2.47	0.13	0.563	1.41	0.07	4.38	0.24		
a7	49.8	49.4	173.7	--	--	1.770	0.070	397	27	13.4	2.7	0.034	3.43	0.26	0.723	2.45	0.10	4.74	0.36		
a8	62.7	50.7	138.4	--	--	1.882	0.069	379	29	15	29	0.038	3.82	0.32	0.736	2.56	0.09	5.19	0.44		
z1	37.3	35.1	166.9	43.6	30.0	151.2	3.6	18897	441	6362	185	0.334	5.75	0.18	0.725	208.5	4.9	7.93	0.25		
z2	29.0	33.0	169.8	42.0	33.9	45.3	1.1	6840	175	5237	182	0.760	4.36	0.14	0.687	66.0	1.5	6.35	0.20		
z3	33.0	37.8	174.0	54.6	48.8	187.5	4.3	16701	393	6588	214	0.392	7.97	0.24	0.710	264.0	5.9	11.22	0.34	**7.9**	**1.4**
z4	47.0	39.7	182.3	49.8	39.9	396.0	9.4	47637	1169	15286	421	0.319	5.99	0.19	0.760	521	12	7.88	0.25		
z5	33.0	28.3	149.4	40.6	34.1	59.7	1.5	7670	179	935	43	0.121	5.86	0.19	0.679	88.0	2.1	8.63	0.28		

*R1 and R2 describe the perpendicular half widths of the crystal. L describes the length of the c axis. T1 and T2 describe the height of the pyramidal terminations of the zircon crystals. †Absolute measured abundances. ^{4}He measurement used to calculate the raw date, which was not corrected for the effects of ^{4}He loss due to alpha particle recoil. §The Th/U ratio of the analyzed crystal. For this calculation the ^{235}U has been accounted for by dividing the measured ^{238}U by 137.88. «The mean F_τ correction calculated following Farley et al. (1996) for apatite and Hourigan et al. (2005) for zircon. # The F_τ corrected ^{4}He abundance. ¥The F_τ corrected date of the crystal. This age was recalculated with a F_τ corrected ^{4}He measurement. Aliquots in intalics were omited from the mean.

Table A2: white mica $^{40}Ar/^{39}Ar$ data

Sample/ Lab ID	Laser Power (W)	$^{40}Ar^*/^{39}Ar$	1σ	$^{40}Ar/^{39}Ar$	2σ	$^{38}Ar/^{39}Ar$	2σ	$^{36}Ar/^{39}Ar$	2σ	Cl/K	^{39}Ar (fmol)	$\%^{40}Ar^*$	$\%^{39}Ar$	Date (Ma)	2σ (Ma)	J	2σ
BT4708																5.25E-04	1.3E-05
601-01A	4	11.22	0.26	33.23	0.13	0.02620	0.00071	0.0745	0.0018	0.0021	5.49	33.78	8.79	10.59	0.49		
601-01B	5	11.530	0.095	14.995	0.056	0.01417	0.00042	0.01169	0.00062	0.0020	8.21	76.98	13.14	10.88	0.18		
601-01C	5	11.547	0.070	13.645	0.042	0.01325	0.00034	0.00706	0.00046	0.0020	10.36	84.74	16.59	10.90	0.13		
601-01D	5	11.190	0.088	12.383	0.046	0.01200	0.00049	0.00399	0.00058	0.0019	5.75	90.51	9.21	10.56	0.17		
601-01E	5	11.46	0.11	11.856	0.054	0.01238	0.00053	0.00125	0.00070	0.0020	4.52	96.85	7.23	10.82	0.20		
601-01F	6	11.264	0.051	12.410	0.045	0.01270	0.00042	0.00379	0.00031	0.0020	7.10	90.91	11.37	10.633	0.096		
601-01G	7	11.32	0.10	12.385	0.056	0.01218	0.00046	0.00351	0.00067	0.0019	5.29	91.56	8.47	10.69	0.19		
601-01H	8	11.27	0.16	13.101	0.069	0.01345	0.00061	0.0061	0.0010	0.0021	3.48	86.12	5.57	10.64	0.29		
601-01I	9	11.18	0.23	12.255	0.088	0.01207	0.00088	0.0035	0.0015	0.0019	2.07	91.42	3.32	10.56	0.43		
601-01J	9	11.12	0.25	11.765	0.090	0.01297	0.00096	0.0021	0.0017	0.0021	1.72	94.67	2.75	10.50	0.48		
601-01K	11	11.41	0.20	12.071	0.078	0.01286	0.00081	0.0022	0.0013	0.0021	2.26	94.63	3.62	10.77	0.37		
601-01L	15	11.228	0.069	11.585	0.040	0.01149	0.00045	0.00113	0.00045	0.0019	6.21	97.07	9.94	10.60	0.13		
BT4808																5.415E-04	8.3E-06
603-01A	4	11.666	0.085	27.58	0.13	0.02147	0.00036	0.05381	0.00044	0.0019	13.42	42.32	22.52	11.36	0.16		
603-01B	5	11.016	0.058	12.902	0.030	0.01265	0.00030	0.00634	0.00038	0.0019	14.96	85.50	25.11	10.73	0.11		
603-01C	5	10.880	0.043	12.053	0.046	0.01225	0.00038	0.00396	0.00025	0.0019	8.31	90.40	13.94	10.597	0.084		
603-01D	5	10.77	0.20	12.129	0.093	0.01216	0.00078	0.0046	0.0013	0.0019	2.33	88.90	3.91	10.49	0.40		
603-01E	5	10.90	0.34	12.23	0.12	0.0136	0.0012	0.0045	0.0023	0.0022	1.36	89.22	2.29	10.61	0.66		
603-01F	6	10.821	0.086	12.879	0.062	0.01246	0.00061	0.00698	0.00056	0.0019	3.38	84.13	5.67	10.54	0.17		
603-01G	7	10.899	0.072	12.164	0.046	0.01234	0.00041	0.00424	0.00047	0.0019	7.42	89.73	12.44	10.62	0.14		
603-01H	8	10.73	0.10	11.56	0.11	0.01181	0.00075	0.00281	0.00054	0.0019	3.32	92.94	5.57	10.45	0.19		
603-01I	9	10.61	0.23	12.07	0.13	0.0121	0.0013	0.0050	0.0015	0.0019	1.09	87.98	1.83	10.33	0.44		
603-01J	9	10.77	0.52	11.82	0.14	0.0115	0.0019	0.0035	0.0035	0.0018	0.75	91.23	1.25	10.5	1.0		
603-01K	11	10.48	0.38	11.59	0.11	0.0116	0.0014	0.0038	0.0025	0.0018	1.11	90.51	1.86	10.21	0.73		
603-01L	15	10.75	0.19	11.485	0.072	0.01279	0.00088	0.0024	0.0013	0.0021	2.15	93.77	3.61	10.47	0.37		
BT4908																5.69E-04	1.3E-05
605-01A	4	10.7	1.1	113.32	0.87	0.0794	0.0022	0.3472	0.0076	0.0024	1.54	9.42	1.16	10.9	2.2		
605-01B	5	9.82	0.53	48.49	0.30	0.0368	0.0011	0.1308	0.0037	0.0021	2.39	20.25	1.80	10.0	1.1		
605-01C	5	10.31	0.17	21.530	0.079	0.01903	0.00049	0.0379	0.0012	0.0020	6.47	47.91	4.89	10.55	0.35		
605-01D	5	9.96	0.12	14.590	0.060	0.01434	0.00049	0.01560	0.00083	0.0019	5.91	68.38	4.47	10.20	0.25		
605-01E	5	10.430	0.086	13.212	0.043	0.01379	0.00042	0.00936	0.00057	0.0020	7.62	79.05	5.76	10.67	0.17		
605-01F	6	10.309	0.044	12.502	0.044	0.01320	0.00024	0.00737	0.00026	0.0020	19.51	82.58	14.74	10.549	0.090		
605-01G	7	10.323	0.035	11.794	0.039	0.01268	0.00020	0.00492	0.00020	0.0020	27.83	87.66	21.03	10.563	0.072		
605-01H	8	10.345	0.032	11.167	0.044	0.01196	0.00020	0.00272	0.00016	0.0019	27.84	92.79	21.04	10.586	0.065		
605-01I	9	10.185	0.066	11.545	0.040	0.01243	0.00042	0.00456	0.00043	0.0020	7.63	88.36	5.76	10.42	0.13		
605-01J	9	9.99	0.16	11.910	0.074	0.01244	0.00067	0.0065	0.0010	0.0019	2.68	84.01	2.02	10.23	0.32		
605-01K	11	10.58	0.15	12.733	0.064	0.01448	0.00063	0.0073	0.0010	0.0022	3.34	83.23	2.53	10.83	0.31		
605-01L	15	10.093	0.034	10.719	0.041	0.01220	0.00021	0.00207	0.00018	0.0020	19.59	94.32	14.80	10.329	0.068		

Table A2: white mica $^{40}Ar/^{39}Ar$ data

Sample/ Lab ID	Laser Power (W)	$^{40}Ar^*/^{39}Ar$	1σ	$^{40}Ar/^{39}Ar$	2σ	$^{38}Ar/^{39}Ar$	2σ	$^{36}Ar/^{39}Ar$	2σ	Cl/K	^{39}Ar (fmol)	$\%^{40}Ar^*$	$\%^{39}Ar$	Date (Ma)	2σ (Ma)	J	2σ
BT5008																5.450E-04	6.8E-06
606-01A	4	15.14	0.59	139.9	1.2	0.0927	0.0020	0.4220	0.0048	0.0023	1.82	10.82	1.05	14.8	1.2		
606-01B	5	10.17	0.22	40.03	0.25	0.0300	0.0011	0.1010	0.0016	0.0019	2.45	25.41	1.41	9.97	0.44		
606-01C	5	10.90	0.13	29.19	0.13	0.02321	0.00067	0.06184	0.00090	0.0020	4.72	37.37	2.71	10.69	0.25		
606-01D	5	10.742	0.089	17.732	0.068	0.01563	0.00057	0.02360	0.00059	0.0019	5.00	60.64	2.87	10.53	0.17		
606-01E	5	10.68	0.13	14.495	0.065	0.01451	0.00046	0.01288	0.00088	0.0020	5.39	73.75	3.10	10.47	0.26		
606-01F	6	10.860	0.053	13.226	0.067	0.01322	0.00025	0.00795	0.00028	0.0020	19.99	82.23	11.49	10.65	0.10		
606-01G	7	10.673	0.064	11.355	0.044	0.01207	0.00016	0.00225	0.00040	0.0020	42.17	94.14	24.24	10.46	0.12		
606-01H	8	10.473	0.066	11.012	0.047	0.01197	0.00018	0.00177	0.00042	0.0020	36.24	95.26	20.84	10.27	0.13		
606-01I	9	10.260	0.044	10.870	0.040	0.01202	0.00026	0.00200	0.00026	0.0020	14.08	94.55	8.10	10.060	0.085		
606-01J	9	10.06	0.10	11.289	0.051	0.01270	0.00049	0.00415	0.00064	0.0020	5.40	89.23	3.10	9.86	0.19		
606-01K	11	10.08	0.13	12.277	0.061	0.01320	0.00061	0.00738	0.00086	0.0020	4.26	82.24	2.45	9.89	0.25		
606-01L	15	10.543	0.027	11.123	0.039	0.01189	0.00017	0.00191	0.00013	0.0019	32.42	94.95	18.64	10.338	0.053		
BT5108																5.234E-04	8.3E-06
608-01A	4	14.3	2.5	184.0	2.6	0.1223	0.0056	0.574	0.018	0.0025	0.52	7.79	0.66	13.5	4.6		
608-01B	5	12.4	1.1	58.87	0.76	0.0418	0.0025	0.1571	0.0078	0.0021	0.68	21.08	0.87	11.7	2.1		
608-01C	5	12.07	0.42	29.40	0.19	0.0237	0.0010	0.0586	0.0028	0.0021	2.18	41.09	2.80	11.36	0.78		
608-01D	5	11.05	0.30	21.42	0.13	0.01828	0.00089	0.0351	0.0020	0.0020	2.44	51.63	3.14	10.41	0.56		
608-01E	5	10.94	0.20	15.756	0.093	0.01470	0.00056	0.0163	0.0014	0.0020	3.14	69.49	4.04	10.30	0.38		
608-01F	6	11.20	0.10	14.380	0.062	0.01360	0.00041	0.01072	0.00069	0.0020	6.69	77.99	8.60	10.55	0.20		
608-01G	7	11.142	0.059	13.024	0.080	0.01330	0.00026	0.00631	0.00030	0.0020	16.09	85.67	20.68	10.49	0.11		
608-01H	8	11.307	0.042	12.858	0.045	0.01254	0.00021	0.00520	0.00024	0.0020	21.32	88.06	27.39	10.646	0.078		
608-01I	9	11.165	0.058	11.736	0.041	0.01178	0.00034	0.00188	0.00037	0.0019	8.72	95.28	11.20	10.51	0.11		
608-01J	9	11.02	0.37	12.95	0.13	0.0134	0.0013	0.0065	0.0024	0.0021	1.32	85.21	1.70	10.37	0.69		
608-01K	11	10.85	0.32	12.82	0.11	0.0140	0.0012	0.0066	0.0021	0.0021	1.45	84.72	1.86	10.22	0.60		
608-01L	15	11.322	0.045	11.866	0.030	0.01179	0.00027	0.00179	0.00029	0.0019	13.28	95.56	17.06	10.660	0.084		
BT5208																5.521E-04	9.0E-06
610-01A	4	9.66	0.50	61.87	0.57	0.0447	0.0022	0.1767	0.0037	0.0019	1.06	15.62	1.34	9.60	0.99		
610-01B	5	10.62	0.14	27.56	0.14	0.02237	0.00077	0.05729	0.00096	0.0020	3.96	38.57	5.03	10.55	0.27		
610-01C	5	10.770	0.057	17.991	0.060	0.01549	0.00039	0.02440	0.00037	0.0018	9.24	59.92	11.74	10.70	0.11		
610-01D	5	10.991	0.053	14.130	0.052	0.01378	0.00047	0.01058	0.00033	0.0020	6.97	77.88	8.85	10.92	0.11		
610-01E	5	10.916	0.056	13.082	0.051	0.01293	0.00048	0.00726	0.00035	0.0020	6.42	83.57	8.16	10.84	0.11		
610-01F	6	10.900	0.046	16.275	0.049	0.01461	0.00042	0.01813	0.00030	0.0019	10.91	67.05	13.85	10.825	0.092		
610-01G	7	10.770	0.029	12.624	0.031	0.01275	0.00027	0.00621	0.00017	0.0020	15.65	85.44	19.87	10.696	0.057		
610-01H	8	10.927	0.056	13.067	0.052	0.01308	0.00045	0.00720	0.00035	0.0020	5.74	83.74	7.29	10.85	0.11		
610-01I	9	10.56	0.16	13.36	0.11	0.01368	0.00095	0.0094	0.0011	0.0020	1.69	79.16	2.14	10.49	0.32		
610-01J	9	10.59	0.15	12.66	0.10	0.0141	0.0010	0.00692	0.00094	0.0022	1.78	83.75	2.26	10.52	0.29		
610-01K	11	10.670	0.084	12.645	0.069	0.01306	0.00056	0.00656	0.00053	0.0020	3.84	84.52	4.88	10.60	0.17		
610-01L	15	10.844	0.029	11.519	0.032	0.01171	0.00030	0.00222	0.00017	0.0019	11.49	94.29	14.59	10.770	0.058		

Table A2: white mica $^{40}Ar/^{39}Ar$ data

Sample/ Lab ID	Laser Power (W)	$^{40}Ar^*/^{39}Ar$	1σ	$^{40}Ar/^{39}Ar$	2σ	$^{38}Ar/^{39}Ar$	2σ	$^{36}Ar/^{39}Ar$	2σ	Cl/K	^{39}Ar (fmol)	$\%^{40}Ar^*$	$\%^{39}Ar$	Date (Ma)	2σ (Ma)	J	2σ
BT5308																5.770E-04	8.1E-06
612-01A	4	10.88	0.63	61.20	0.85	0.0407	0.0029	0.1700	0.0048	0.0015	0.65	17.79	0.90	11.3	1.3		
612-01B	5	11.11	0.81	91.3	1.4	0.0610	0.0038	0.2712	0.0068	0.0017	0.58	12.17	0.79	11.5	1.7		
612-01C	5	9.67	0.51	62.33	0.59	0.0435	0.0025	0.1780	0.0038	0.0017	0.98	15.53	1.35	10.0	1.1		
612-01D	5	9.82	0.49	38.94	0.43	0.0268	0.0023	0.0985	0.0034	0.0014	0.80	25.24	1.10	10.2	1.0		
612-01E	5	10.16	0.33	31.94	0.25	0.0254	0.0016	0.0738	0.0022	0.0020	1.17	31.81	1.60	10.54	0.67		
612-01F	6	10.379	0.091	25.480	0.086	0.02143	0.00055	0.05106	0.00063	0.0020	7.12	40.76	9.78	10.77	0.19		
612-01G	7	10.219	0.039	14.688	0.057	0.01448	0.00026	0.01506	0.00020	0.0020	21.59	69.66	29.65	10.606	0.081		
612-01H	8	10.131	0.062	13.271	0.036	0.01369	0.00030	0.01058	0.00041	0.0020	15.03	76.44	20.64	10.52	0.13		
612-01I	9	10.46	0.10	16.567	0.076	0.01562	0.00066	0.02064	0.00067	0.0020	3.87	63.22	5.32	10.86	0.21		
612-01J	9	10.43	0.14	16.06	0.10	0.01488	0.00092	0.01905	0.00090	0.0019	2.19	64.99	3.00	10.82	0.28		
612-01K	11	10.06	0.17	19.00	0.12	0.01668	0.00092	0.0302	0.0011	0.0019	2.31	52.99	3.17	10.44	0.35		
612-01L	15	9.977	0.027	11.809	0.029	0.01299	0.00027	0.00616	0.00016	0.0020	16.53	84.62	22.70	10.356	0.056		
BT0914																1.888E-04	4.4E-06
485-01A	5.00	30.84	0.17	68.26	0.29	0.03672	0.00067	0.12655	0.00097	0.0022	7.54	45.20	19.57	10.47	0.11		
485-01B	5.20	29.88	0.13	42.53	0.22	0.02023	0.00058	0.04272	0.00061	0.0021	5.73	70.31	14.88	10.146	0.086		
485-01C	5.40	29.65	0.12	36.81	0.18	0.01690	0.00064	0.02416	0.00061	0.0021	3.87	80.60	10.04	10.067	0.079		
485-01D	5.50	29.64	0.12	35.84	0.18	0.01628	0.00066	0.02087	0.00061	0.0021	3.56	82.78	9.25	10.065	0.078		
485-01E	5.70	29.30	0.17	39.21	0.26	0.01865	0.00087	0.03345	0.00096	0.0021	2.15	74.78	5.59	9.95	0.12		
485-01F	5.90	29.54	0.14	33.08	0.20	0.01469	0.00079	0.01186	0.00075	0.0021	2.42	89.38	6.29	10.032	0.096		
485-01G	6.20	30.01	0.22	35.94	0.31	0.0157	0.0012	0.0200	0.0013	0.0020	1.42	83.57	3.69	10.19	0.15		
485-01H	7.75	29.67	0.11	35.69	0.17	0.01638	0.00062	0.02028	0.00059	0.0021	3.86	83.20	10.01	10.075	0.077		
485-01I	9.00	29.62	0.13	36.59	0.16	0.01713	0.00073	0.02349	0.00077	0.0021	2.85	81.01	7.38	10.058	0.088		
485-01J	9.10	29.61	0.21	31.01	0.27	0.0142	0.0013	0.0047	0.0011	0.0023	1.28	95.56	3.32	10.05	0.14		
485-01K	9.30	30.32	0.37	32.12	0.45	0.0135	0.0017	0.0060	0.0021	0.0021	0.73	94.48	1.89	10.30	0.25		
485-01L	15.00	29.81	0.11	32.02	0.17	0.01346	0.00070	0.00740	0.00055	0.0020	3.12	93.17	8.09	10.122	0.078		
BT0919																1.958E-04	5.3E-06
487-01A	5.00	28.61	0.28	76.92	0.49	0.04366	0.00113	0.1634	0.0019	0.0022	2.91	37.21	7.63	10.08	0.20		
487-01B	5.20	27.74	0.12	34.89	0.20	0.01672	0.00054	0.02410	0.00051	0.0021	5.33	79.58	13.97	9.776	0.082		
487-01C	5.40	26.88	0.11	33.63	0.18	0.01692	0.00059	0.02275	0.00054	0.0021	5.04	80.00	13.21	9.474	0.077		
487-01D	5.50	26.58	0.17	37.03	0.19	0.01880	0.00083	0.0353	0.0010	0.0021	2.38	71.82	6.24	9.37	0.12		
487-01E	5.70	26.67	0.13	31.83	0.17	0.01629	0.00083	0.01738	0.00077	0.0022	2.68	83.86	7.03	9.398	0.094		
487-01F	5.90	27.00	0.19	35.80	0.25	0.01841	0.00095	0.0297	0.0011	0.0022	2.20	75.48	5.76	9.52	0.13		
487-01G	6.20	26.60	0.25	38.26	0.30	0.0195	0.0014	0.0394	0.0016	0.0020	1.45	69.55	3.79	9.37	0.18		
487-01H	7.75	26.76	0.10	33.47	0.14	0.01660	0.00057	0.02261	0.00058	0.0021	4.49	80.02	11.77	9.429	0.072		
487-01I	9.00	26.42	0.16	36.62	0.22	0.01939	0.00079	0.03442	0.00093	0.0022	2.56	72.21	6.70	9.31	0.11		
487-01J	9.10	25.41	0.44	30.74	0.47	0.0144	0.0021	0.0180	0.0027	0.0019	0.59	82.73	1.55	8.96	0.31		
487-01K	9.30	27.72	0.61	30.95	0.56	0.0141	0.0030	0.0109	0.0037	0.0020	0.45	89.64	1.18	9.77	0.43		
487-01L	15.00	27.496	0.077	29.44	0.14	0.01310	0.00043	0.00648	0.00024	0.0020	8.09	93.50	21.19	9.689	0.054		

Table A2: white mica $^{40}Ar/^{39}Ar$ data

Sample/ Lab ID	Laser Power (W)	$^{40}Ar^*/^{39}Ar$	1σ	$^{40}Ar/^{39}Ar$	2σ	$^{38}Ar/^{39}Ar$	2σ	$^{36}Ar/^{39}Ar$	2σ	Cl/K	^{39}Ar (fmol)	$\%^{40}Ar^*$	$\%^{39}Ar$	Date (Ma)	2σ (Ma)	J	2σ
BT0920																1.897E-04	5.4E-06
489-04A	5.00	30.56	0.38	117.61	0.71	0.0681	0.0015	0.2945	0.0027	0.0022	2.93	25.99	12.55	10.42	0.26		
489-04B	5.20	27.25	0.40	86.05	0.58	0.0505	0.0019	0.1990	0.0029	0.0022	1.56	31.67	6.68	9.30	0.27		
489-04C	5.40	28.22	0.30	58.65	0.45	0.0328	0.0015	0.1029	0.0020	0.0023	1.48	48.13	6.36	9.63	0.20		
489-04D	5.50	27.29	0.36	60.04	0.55	0.0317	0.0015	0.1108	0.0025	0.0018	1.37	45.48	5.88	9.31	0.25		
489-04E	5.70	28.43	0.31	57.42	0.50	0.0293	0.0014	0.0980	0.0021	0.0018	1.51	49.53	6.48	9.70	0.21		
489-04F	5.90	28.90	0.28	53.33	0.43	0.0279	0.0013	0.0826	0.0019	0.0021	1.64	54.22	7.02	9.86	0.19		
489-04G	6.20	29.01	0.24	46.34	0.30	0.0236	0.0011	0.0586	0.0016	0.0021	1.81	62.63	7.76	9.90	0.17		
489-04H	7.75	29.26	0.28	51.62	0.29	0.02666	0.00080	0.0756	0.0018	0.0021	3.77	56.73	16.15	9.99	0.19		
489-04I	9.00	28.74	0.27	48.36	0.40	0.0254	0.0015	0.0663	0.0017	0.0022	1.53	59.46	6.56	9.81	0.18		
489-04J	9.10	28.48	0.69	48.78	0.88	0.0235	0.0030	0.0688	0.0045	0.0018	0.43	58.40	1.86	9.72	0.47		
489-04K	9.30	30.1	1.1	48.3	1.2	0.0243	0.0052	0.0619	0.0068	0.0022	0.28	62.30	1.20	10.27	0.72		
489-04L	15.00	29.56	0.15	51.41	0.23	0.02562	0.00066	0.07385	0.00086	0.0020	5.02	57.53	21.51	10.09	0.10		
BT0962																1.973E-04	1.9E-06
555-01A	5.00	20.30	0.11	39.90	0.17	0.02481	0.00049	0.06626	0.00064	0.0021	9.49	50.91	17.52	7.213	0.080		
555-01B	5.20	21.27	0.11	32.41	0.16	0.02004	0.00061	0.03764	0.00067	0.0022	4.79	65.66	8.85	7.556	0.079		
555-01C	5.40	22.07	0.24	37.39	0.18	0.02239	0.00071	0.0518	0.0016	0.0021	4.53	59.06	8.37	7.84	0.17		
555-01D	5.50	22.02	0.10	28.74	0.13	0.01562	0.00063	0.02268	0.00061	0.0019	4.45	76.66	8.22	7.822	0.073		
555-01E	5.70	22.13	0.12	26.98	0.14	0.01541	0.00086	0.01633	0.00067	0.0021	3.34	82.10	6.17	7.863	0.082		
555-01F	5.90	21.90	0.13	27.57	0.19	0.01628	0.00097	0.01912	0.00071	0.0021	2.49	79.50	4.60	7.779	0.094		
555-01G	6.20	22.21	0.10	25.69	0.13	0.01472	0.00064	0.01172	0.00059	0.0021	3.76	86.52	6.95	7.889	0.073		
555-01H	7.75	22.232	0.079	27.21	0.10	0.01577	0.00051	0.01676	0.00044	0.0021	6.30	81.78	11.64	7.897	0.056		
555-01I	9.00	22.00	0.12	26.61	0.15	0.01583	0.00072	0.01553	0.00069	0.0022	3.42	82.75	6.31	7.817	0.084		
555-01J	9.10	22.20	0.21	23.60	0.21	0.0139	0.0011	0.00469	0.00121	0.0022	1.57	94.13	2.89	7.88	0.15		
555-01K	9.30	21.77	0.48	24.75	0.41	0.0119	0.0025	0.0100	0.0030	0.0017	0.64	88.03	1.18	7.73	0.34		
555-01L	15.00	22.160	0.062	23.98	0.10	0.01340	0.00040	0.00609	0.00024	0.0021	9.37	92.49	17.30	7.872	0.044		
BT0963																1.914E-04	2.9E-06
490-01A	5.00	23.42	0.62	85.80	0.93	0.0564	0.0029	0.2110	0.0047	0.0028	0.78	27.30	3.19	8.07	0.43		
490-01B	5.20	24.45	0.34	49.19	0.44	0.0285	0.0018	0.0836	0.0023	0.0022	1.11	49.74	4.55	8.42	0.24		
490-01C	5.40	23.75	0.28	39.83	0.32	0.0224	0.0014	0.0544	0.0018	0.0021	1.23	59.68	5.04	8.18	0.19		
490-01D	5.50	23.43	0.45	37.71	0.49	0.0214	0.0022	0.0482	0.0029	0.0021	0.66	62.19	2.69	8.07	0.31		
490-01E	5.70	23.91	0.38	42.77	0.42	0.0254	0.0021	0.0637	0.0025	0.0023	0.85	55.96	3.49	8.24	0.26		
490-01F	5.90	24.13	0.30	40.55	0.34	0.0214	0.0017	0.0555	0.0020	0.0019	1.21	59.54	4.96	8.31	0.21		
490-01G	6.20	23.87	0.28	40.14	0.33	0.0230	0.0013	0.0549	0.0018	0.0021	1.50	59.52	6.13	8.23	0.19		
490-01H	7.75	24.09	0.15	43.03	0.20	0.02458	0.00064	0.06397	0.00085	0.0021	4.40	56.03	17.98	8.30	0.10		
490-01I	9.00	23.76	0.11	32.24	0.16	0.01781	0.00075	0.02862	0.00064	0.0021	3.80	73.75	15.52	8.186	0.077		
490-01J	9.10	23.79	0.17	33.16	0.22	0.01825	0.00095	0.0316	0.0011	0.0021	2.07	71.80	8.45	8.20	0.12		
490-01K	9.30	24.16	0.35	27.00	0.32	0.0141	0.0018	0.0095	0.0022	0.0021	0.76	89.60	3.08	8.32	0.24		
490-01L	15.00	23.771	0.081	28.64	0.12	0.01518	0.00048	0.01638	0.00041	0.0020	6.10	83.09	24.91	8.191	0.056		

Table A2: white mica $^{40}Ar/^{39}Ar$ data

Sample/ Lab ID	Laser Power (W)	$^{40}Ar^*/^{39}Ar$	1σ	$^{40}Ar/^{39}Ar$	2σ	$^{38}Ar/^{39}Ar$	2σ	$^{36}Ar/^{39}Ar$	2σ	Cl/K	^{39}Ar (fmol)	$\%^{40}Ar^*$	$\%^{39}Ar$	Date (Ma)	2σ (Ma)	J	2σ
BT0964																1.981E-04	1.8E-06
557-01A	5.00	36.19	0.19	77.21	0.36	0.03872	0.00077	0.1388	0.0011	0.0021	5.97	46.88	7.39	12.89	0.13		
557-01B	5.20	24.85	0.39	35.94	0.20	0.01929	0.00060	0.0375	0.0025	0.0021	5.33	69.18	6.60	8.86	0.27		
557-01C	5.40	24.50	0.46	30.73	0.15	0.01602	0.00053	0.0210	0.0031	0.0020	5.86	79.77	7.25	8.74	0.33		
557-01D	5.50	23.67	0.26	27.01	0.12	0.01524	0.00059	0.0113	0.0017	0.0022	5.28	87.67	6.53	8.44	0.18		
557-01E	5.70	22.98	0.53	27.78	0.13	0.01506	0.00051	0.0162	0.0035	0.0020	5.09	82.81	6.29	8.20	0.37		
557-01F	5.90	25.00	0.54	30.24	0.16	0.01521	0.00063	0.0177	0.0037	0.0020	4.54	82.71	5.61	8.91	0.39		
557-01G	6.20	24.00	0.28	27.44	0.14	0.01448	0.00049	0.0116	0.0018	0.0021	4.95	87.52	6.12	8.56	0.20		
557-01H	7.75	23.94	0.22	27.28	0.12	0.01423	0.00031	0.0112	0.0014	0.0020	13.78	87.83	17.04	8.54	0.15		
557-01I	9.00	23.56	0.21	27.01	0.17	0.01384	0.00043	0.0116	0.0013	0.0020	7.64	87.31	9.45	8.40	0.15		
557-01J	9.10	22.84	0.56	26.52	0.20	0.01395	0.00099	0.0124	0.0038	0.0020	2.28	86.18	2.82	8.14	0.40		
557-01K	9.30	24.74	0.62	26.04	0.24	0.0130	0.0013	0.0043	0.0042	0.0021	1.60	95.10	1.98	8.82	0.44		
557-01L	15.00	25.42	0.16	27.17	0.11	0.01378	0.00025	0.0059	0.0011	0.0021	18.52	93.63	22.91	9.06	0.12		
BT0987																1.944E-04	2.2E-06
566-02A	5.00	29.48	0.37	92.73	0.63	0.0544	0.0015	0.2139	0.0027	0.0024	1.73	31.80	4.01	10.31	0.26		
566-02B	5.20	28.70	0.34	65.35	0.56	0.0364	0.0016	0.1239	0.0024	0.0022	1.47	43.93	3.40	10.03	0.24		
566-02C	5.40	28.19	0.30	55.40	0.39	0.0320	0.0014	0.0920	0.0020	0.0025	1.81	50.92	4.18	9.86	0.21		
566-02D	5.50	27.66	0.25	46.20	0.31	0.0246	0.0012	0.0627	0.0016	0.0022	1.86	59.89	4.29	9.67	0.18		
566-02E	5.70	27.83	0.17	37.72	0.21	0.01868	0.00099	0.0334	0.0010	0.0021	2.53	73.84	5.84	9.73	0.12		
566-02F	5.90	28.18	0.20	44.85	0.25	0.0224	0.0011	0.0564	0.0013	0.0020	2.19	62.86	5.05	9.85	0.14		
566-02G	6.20	27.42	0.14	34.84	0.18	0.01763	0.00089	0.02504	0.00085	0.0022	2.96	78.75	6.84	9.59	0.10		
566-02H	7.75	27.76	0.11	35.23	0.19	0.01681	0.00051	0.02522	0.00051	0.0020	6.80	78.84	15.70	9.706	0.079		
566-02I	9.00	27.90	0.17	36.68	0.17	0.01804	0.00056	0.0296	0.0010	0.0021	6.55	76.11	15.14	9.76	0.12		
566-02J	9.10	27.27	0.22	38.93	0.28	0.0194	0.0012	0.0394	0.0014	0.0020	1.76	70.10	4.06	9.54	0.15		
566-02K	9.30	27.19	0.35	37.53	0.42	0.0188	0.0017	0.0349	0.0021	0.0021	1.07	72.47	2.47	9.51	0.24		
566-02L	15.00	27.721	0.072	32.70	0.12	0.01536	0.00033	0.01679	0.00030	0.0021	12.56	84.82	29.02	9.694	0.050		
BT0988																1.944E-04	1.2E-06
567-01A	5.00	27.152	0.078	40.17	0.14	0.02083	0.00036	0.04397	0.00037	0.0021	17.41	67.64	37.52	9.499	0.054		
567-01B	5.20	26.99	0.11	30.86	0.19	0.01447	0.00049	0.01304	0.00039	0.0020	7.41	87.51	15.96	9.442	0.075		
567-01C	5.40	26.76	0.14	30.08	0.18	0.01422	0.00084	0.01115	0.00078	0.0020	3.40	89.04	7.32	9.363	0.098		
567-01D	5.50	26.85	0.23	28.70	0.21	0.0133	0.0014	0.0062	0.0014	0.0021	1.61	93.61	3.48	9.39	0.16		
567-01E	5.70	27.39	0.29	29.64	0.30	0.0141	0.0015	0.0075	0.0017	0.0021	1.26	92.49	2.71	9.58	0.20		
567-01F	5.90	26.78	0.25	29.42	0.26	0.0125	0.0015	0.0088	0.0015	0.0018	1.29	91.12	2.78	9.37	0.17		
567-01G	6.20	27.26	0.24	29.80	0.20	0.01388	0.00089	0.0085	0.0015	0.0021	2.53	91.53	5.45	9.54	0.17		
567-01H	7.75	26.83	0.11	29.32	0.17	0.01380	0.00050	0.00835	0.00049	0.0021	5.13	91.59	11.05	9.386	0.076		
567-01I	9.00	27.13	0.13	29.18	0.15	0.01332	0.00078	0.00687	0.00074	0.0020	2.92	93.04	6.30	9.491	0.091		
567-01J	9.10	28.03	0.40	27.99	0.36	0.0136	0.0019	-0.0002	0.0025	0.0023	0.79	100.22	1.70	9.81	0.28		
567-01K	9.30	27.39	0.64	27.63	0.53	0.0117	0.0030	0.0007	0.0040	0.0020	0.45	99.23	0.97	9.58	0.45		
567-01L	15.00	27.43	0.17	28.96	0.21	0.01412	0.00086	0.00510	0.00091	0.0022	2.21	94.80	4.76	9.60	0.12		

Table A2: white mica $^{40}Ar/^{39}Ar$ data

Sample/ Lab ID	Laser Power (W)	$^{40}Ar^*/^{39}Ar$	1σ	$^{40}Ar/^{39}Ar$	2σ	$^{38}Ar/^{39}Ar$	2σ	$^{36}Ar/^{39}Ar$	2σ	Cl/K	^{39}Ar (fmol)	$\%^{40}Ar^*$	$\%^{39}Ar$	Date (Ma)	2σ (Ma)	J	2σ
BT0989																1.916E-04	2.5E-06
482-01A	3.00	21.9	1.5	132.1	3.5	0.0794	0.0070	0.373	0.014	0.0016	0.28	16.58	0.58	7.5	1.0		
482-01B	3.00	27.4	1.2	64.0	1.5	0.0304	0.0056	0.1238	0.0082	0.0012	0.26	42.81	0.55	9.45	0.82		
482-01C	3.80	27.73	0.52	53.40	0.66	0.0289	0.0027	0.0868	0.0035	0.0021	0.64	51.95	1.35	9.56	0.36		
482-01D	4.60	27.33	0.38	48.15	0.29	0.02557	0.00087	0.0704	0.0025	0.0021	2.65	56.80	5.58	9.43	0.26		
482-01E	5.00	28.56	0.42	33.63	0.14	0.01571	0.00044	0.0170	0.0028	0.0021	6.87	85.00	14.47	9.85	0.29		
482-01F	5.50	28.46	0.24	30.79	0.14	0.01392	0.00036	0.0078	0.0015	0.0021	7.79	92.52	16.40	9.81	0.16		
482-01G	6.00	28.06	0.31	30.82	0.15	0.01397	0.00048	0.0093	0.0020	0.0021	6.65	91.12	14.01	9.68	0.21		
482-01H	6.50	27.05	0.48	30.58	0.16	0.01431	0.00057	0.0119	0.0032	0.0020	4.22	88.53	8.89	9.33	0.33		
482-01I	7.50	27.41	0.43	31.70	0.13	0.01519	0.00056	0.0144	0.0029	0.0021	5.01	86.57	10.55	9.45	0.30		
482-01J	8.50	26.67	0.61	30.26	0.16	0.01364	0.00080	0.0120	0.0041	0.0019	2.93	88.22	6.18	9.20	0.42		
482-01K	9.50	27.88	0.24	30.94	0.26	0.0152	0.0013	0.0103	0.0014	0.0022	1.31	90.18	2.76	9.61	0.17		
482-01L	15.00	27.94	0.23	29.21	0.20	0.01283	0.00037	0.0042	0.0014	0.0020	8.87	95.73	18.68	9.63	0.16		
BT1024																5.509E-04	5.0E-06
613-01A	4	15.48	0.62	180.3	1.3	0.1172	0.0024	0.5577	0.0052	0.0021	1.94	8.59	1.74	15.3	1.2		
613-01B	5	12.84	0.28	64.50	0.35	0.0450	0.0012	0.1748	0.0021	0.0021	2.78	19.91	2.48	12.71	0.55		
613-01C	5	10.41	0.10	28.02	0.12	0.02303	0.00048	0.05955	0.00069	0.0020	6.97	37.17	6.23	10.31	0.21		
613-01D	5	12.365	0.092	22.730	0.097	0.01903	0.00057	0.03505	0.00061	0.0021	5.53	54.44	4.95	12.25	0.18		
613-01E	5	12.168	0.088	19.088	0.082	0.01572	0.00060	0.02338	0.00057	0.0019	4.96	63.81	4.43	12.05	0.17		
613-01F	6	12.282	0.090	18.426	0.071	0.01507	0.00033	0.02073	0.00057	0.0019	13.35	66.72	11.93	12.16	0.18		
613-01G	7	12.469	0.035	15.271	0.053	0.01353	0.00020	0.00943	0.00016	0.0020	20.84	81.75	18.63	12.349	0.069		
613-01H	8	12.395	0.044	14.066	0.048	0.01253	0.00023	0.00561	0.00025	0.0019	22.10	88.23	19.75	12.276	0.087		
613-01I	9	12.151	0.042	14.325	0.040	0.01305	0.00038	0.00729	0.00026	0.0020	9.35	84.94	8.35	12.036	0.083		
613-01J	9	12.13	0.10	15.670	0.074	0.01311	0.00058	0.01192	0.00061	0.0018	3.71	77.50	3.32	12.01	0.19		
613-01K	11	12.18	0.11	18.338	0.088	0.01533	0.00076	0.02082	0.00073	0.0019	3.45	66.48	3.08	12.06	0.22		
613-01L	15	12.170	0.040	14.437	0.062	0.01312	0.00027	0.00762	0.00018	0.0020	16.91	84.41	15.12	12.054	0.079		

Table A3: biotite $^{40}Ar/^{39}Ar$ data

Sample/ Lab ID	Laser Power (W)	$^{40}Ar^*/^{39}Ar$	2σ	$^{40}Ar/^{39}Ar$	2σ	$^{38}Ar/^{39}Ar$	2σ	$^{36}Ar/^{39}Ar$	2σ	Cl/K	^{39}Ar (fmol)	$\%^{40}Ar^*$	$\%^{39}Ar$	Date (Ma)	2σ	J	2σ
BT0914																1.9350E-04	8.5E-07
450-01A	3.0	29.70	0.35	50.55	0.29	0.02535	0.00080	0.07046	0.00094	0.0020	4.1320	58.79	12.02	10.34	0.12		
450-01B	3.0	29.54	0.21	35.79	0.16	0.01649	0.00060	0.02108	0.00056	0.0021	4.0141	82.59	11.68	10.281	0.074		
450-01C	3.8	29.79	0.23	35.88	0.18	0.01574	0.00063	0.02053	0.00060	0.0020	3.5979	83.09	10.47	10.367	0.080		
450-01D	4.6	29.92	0.21	33.83	0.17	0.01571	0.00056	0.01313	0.00050	0.0022	3.9282	88.53	11.43	10.413	0.073		
450-01E	5.0	29.93	0.17	32.30	0.14	0.01392	0.00052	0.00792	0.00040	0.0021	4.0012	92.75	11.64	10.415	0.060		
450-01F	5.5	29.64	0.20	31.18	0.15	0.01323	0.00065	0.00514	0.00046	0.0021	3.4460	95.13	10.03	10.314	0.069		
450-01G	6.0	29.97	0.20	31.15	0.15	0.01342	0.00069	0.00391	0.00045	0.0021	3.1473	96.31	9.16	10.430	0.069		
450-01H	6.5	29.98	0.26	31.09	0.19	0.01406	0.00089	0.00371	0.00064	0.0023	1.8665	96.50	5.43	10.431	0.091		
450-01I	7.5	30.01	0.25	30.92	0.19	0.01307	0.00081	0.00297	0.00056	0.0021	2.1469	97.17	6.25	10.444	0.086		
450-01J	8.5	29.75	0.30	30.99	0.22	0.01357	0.00093	0.00412	0.00073	0.0022	1.5503	96.09	4.51	10.35	0.11		
450-01K	9.5	31.21	0.75	31.61	0.39	0.0128	0.0020	0.0012	0.0022	0.0021	0.5075	98.84	1.48	10.86	0.26		
450-01L	15.0	30.79	0.90	84.92	0.69	0.0489	0.0017	0.1831	0.0029	0.0024	2.0319	36.28	5.91	10.72	0.31		
BT0919																1.9710E-04	4.7E-07
455-01A	3.0	24.72	0.25	37.81	0.18	0.02036	0.00062	0.04421	0.00077	0.0020	4.2589	65.43	11.80	8.770	0.090		
455-01B	3.0	24.81	0.17	29.68	0.12	0.01555	0.00061	0.01639	0.00048	0.0021	4.3457	83.69	12.04	8.803	0.061		
455-01C	3.8	24.67	0.18	27.92	0.13	0.01520	0.00045	0.01095	0.00045	0.0022	4.4484	88.42	12.33	8.752	0.062		
455-01D	4.6	24.65	0.15	27.42	0.11	0.01380	0.00046	0.00928	0.00036	0.0020	5.8310	89.99	16.16	8.744	0.052		
455-01E	5.0	24.47	0.14	26.51	0.11	0.01420	0.00051	0.00684	0.00034	0.0022	5.0678	92.39	14.04	8.681	0.051		
455-01F	5.5	24.59	0.18	26.73	0.12	0.01319	0.00068	0.00716	0.00049	0.0020	3.2277	92.09	8.94	8.723	0.064		
455-01G	6.0	24.41	0.27	26.85	0.18	0.01346	0.00080	0.00819	0.00073	0.0020	2.0205	91.00	5.60	8.660	0.095		
455-01H	6.5	24.59	0.35	26.79	0.21	0.0141	0.0010	0.00739	0.00099	0.0021	1.4789	91.86	4.10	8.72	0.12		
455-01I	7.5	24.74	0.32	27.05	0.18	0.0148	0.0010	0.00774	0.00092	0.0022	1.4749	91.55	4.09	8.78	0.11		
455-01J	8.5	25.00	0.48	27.26	0.27	0.0154	0.0013	0.0076	0.0014	0.0024	0.9853	91.82	2.73	8.87	0.17		
455-01K	9.5	23.61	0.90	25.97	0.40	0.0146	0.0023	0.0079	0.0028	0.0022	0.4513	91.01	1.25	8.38	0.32		
455-01L	15.0	24.34	0.65	50.85	0.31	0.0298	0.0015	0.0896	0.0022	0.0022	2.4954	47.89	6.92	8.64	0.23		
BT0920																1.9550E-04	5.6E-07
469-01A	3.0	29.38	0.31	58.08	0.25	0.03121	0.00060	0.09702	0.00089	0.0022	7.3317	50.61	18.35	10.33	0.11		
469-01B	3.0	29.71	0.24	37.16	0.20	0.01685	0.00052	0.02513	0.00050	0.0020	5.0657	80.01	12.68	10.447	0.083		
469-01C	3.8	30.29	0.27	37.77	0.24	0.01684	0.00057	0.02521	0.00053	0.0020	4.8106	80.27	12.04	10.651	0.093		
469-01D	4.6	30.47	0.27	39.00	0.23	0.01806	0.00047	0.02875	0.00057	0.0021	5.1763	78.20	12.95	10.713	0.094		
469-01E	5.0	28.74	0.21	36.74	0.17	0.01680	0.00071	0.02698	0.00055	0.0020	4.5590	78.29	11.41	10.106	0.075		
469-01F	5.5	28.95	0.21	35.58	0.17	0.01657	0.00057	0.02235	0.00054	0.0021	4.1815	81.43	10.46	10.181	0.074		
469-01G	6.0	28.79	0.28	35.20	0.20	0.01667	0.00075	0.02162	0.00076	0.0021	3.0690	81.85	7.68	10.123	0.098		
469-01H	6.5	28.67	0.38	35.90	0.25	0.01611	0.00085	0.0244	0.0011	0.0019	2.0246	79.94	5.07	10.08	0.13		
469-01I	7.5	28.78	0.44	35.80	0.26	0.0173	0.0011	0.0237	0.0013	0.0022	1.5282	80.44	3.82	10.12	0.15		
469-01J	8.5	29.38	0.97	36.43	0.53	0.0184	0.0023	0.0237	0.0029	0.0023	0.5368	80.71	1.34	10.33	0.339		
469-01K	9.5	30.1	1.3	37.18	0.73	0.0151	0.0030	0.0239	0.0039	0.0018	0.3804	81.05	0.95	10.588	0.455		
469-01L	15.0	27.08	0.94	77.96	0.71	0.0421	0.0021	0.1721	0.0034	0.0017	1.2988	34.75	3.25	9.52	0.331		

Table A3: biotite $^{40}Ar/^{39}Ar$ data

Sample/ Lab ID	Laser Power (W)	$^{40}Ar^*/^{39}Ar$	2σ	$^{40}Ar/^{39}Ar$	2σ	$^{38}Ar/^{39}Ar$	2σ	$^{36}Ar/^{39}Ar$	2σ	Cl/K	^{39}Ar (fmol)	$\%^{40}Ar^*$	$\%^{39}Ar$	Date (Ma)	2σ	J	2σ
BT0962																1.943E-04	1.4E-06
457-01A	3.0	21.93	0.31	49.40	0.25	0.03083	0.00071	0.09289	0.00089	0.0023	6.2543	44.41	10.43	7.67	0.11		
457-01B	3.0	21.87	0.18	28.20	0.15	0.01587	0.00042	0.02133	0.00040	0.0020	8.0731	77.63	13.46	7.647	0.062		
457-01C	3.8	21.88	0.16	26.06	0.13	0.01493	0.00043	0.01404	0.00036	0.0021	7.3713	84.08	12.29	7.653	0.056		
457-01D	4.6	22.01	0.17	26.34	0.14	0.01485	0.00049	0.01457	0.00038	0.0020	6.8915	83.64	11.49	7.696	0.061		
457-01E	5.0	21.17	0.14	25.54	0.10	0.01467	0.00049	0.01468	0.00038	0.0020	5.8326	83.00	9.72	7.405	0.050		
457-01F	5.5	21.43	0.18	25.00	0.12	0.01471	0.00049	0.01196	0.00049	0.0021	4.5996	85.84	7.67	7.496	0.063		
457-01G	6.0	21.56	0.18	24.58	0.12	0.01418	0.00061	0.01015	0.00050	0.0021	3.7242	87.79	6.21	7.539	0.063		
457-01H	6.5	21.34	0.21	24.66	0.15	0.01385	0.00061	0.01111	0.00057	0.0020	3.0741	86.67	5.12	7.465	0.074		
457-01I	7.5	21.47	0.18	24.43	0.12	0.01506	0.00059	0.00994	0.00050	0.0022	3.8483	87.98	6.42	7.507	0.064		
457-01J	8.5	21.21	0.21	24.79	0.14	0.01503	0.00070	0.01203	0.00060	0.0022	3.0553	85.65	5.09	7.418	0.074		
457-01K	9.5	20.78	0.27	25.26	0.15	0.01533	0.00085	0.01505	0.00082	0.0021	2.4058	82.36	4.01	7.269	0.095		
457-01L	15.0	21.25	0.57	40.06	0.20	0.02424	0.00080	0.0636	0.0019	0.0021	4.8594	53.08	8.10	7.43	0.20		
BT0963																1.985E-04	1.2E-06
459-01A	3.0	26.60	0.25	40.00	0.20	0.02179	0.00061	0.04523	0.00063	0.0022	5.7201	66.56	14.74	9.500	0.090		
459-01B	3.0	25.954	0.179	30.923	0.1439	0.01584	0.00055	0.01673	0.00044	0.0021	5.1499	84.01	13.27	9.269	0.064		
459-01C	3.8	26.382	0.194	29.580	0.1436	0.01425	0.00051	0.01072	0.00049	0.0021	4.4167	89.28	11.38	9.421	0.069		
459-01D	4.6	26.580	0.156	28.840	0.140	0.01446	0.00052	0.00755	0.00029	0.0022	4.5271	92.25	11.66	9.492	0.056		
459-01E	5.0	26.288	0.167	27.998	0.125	0.01387	0.00056	0.00569	0.00040	0.0022	4.5816	93.99	11.80	9.388	0.060		
459-01F	5.5	26.302	0.190	27.531	0.137	0.01367	0.00062	0.00406	0.00047	0.0022	3.3300	95.64	8.58	9.393	0.068		
459-01G	6.0	26.37	0.21	27.498	0.138	0.01406	0.00068	0.00372	0.00053	0.0023	2.7906	95.99	7.19	9.416	0.073		
459-01H	6.5	26.70	0.242	27.519	0.157	0.01351	0.00079	0.00271	0.00064	0.0022	2.1921	97.10	5.65	9.533	0.086		
459-01I	7.5	26.92	0.237	28.180	0.170	0.01360	0.00078	0.00418	0.00058	0.0022	2.5583	95.62	6.59	9.612	0.084		
459-01J	8.5	27.14	0.571	27.15	0.31	0.01460	0.00169	0.00000	0.00163	0.0025	0.8114	100.03	2.09	9.69	0.20		
459-01K	9.5	26.88	1.017	26.91	0.40	0.0133	0.0025	0.00000	0.0032	0.0022	0.4168	100.00	1.07	9.60	0.36		
459-01L	15.0	25.89	0.561	50.66	0.31	0.02888	0.00127	0.08374	0.00186	0.0022	2.3196	51.14	5.98	9.25	0.20		
BT0964																1.948E-04	1.5E-06
461-01A	3.0	49.91	0.32	72.05	0.30	0.03205	0.00064	0.07483	0.00075	0.0030	7.0340	69.30	13.55	17.45	0.11		
461-01B	3.0	50.07	0.26	54.52	0.25	0.02008	0.00052	0.01494	0.00036	0.0029	6.7605	91.90	13.02	17.509	0.091		
461-01C	3.8	49.59	0.29	54.28	0.28	0.02014	0.00058	0.01579	0.00040	0.0029	5.0491	91.41	9.72	17.34	0.10		
461-01D	4.6	50.54	0.30	54.37	0.28	0.02007	0.00059	0.01290	0.00040	0.0030	4.7445	92.99	9.14	17.67	0.10		
461-01E	5.0	52.19	0.31	55.67	0.29	0.01939	0.00062	0.01167	0.00050	0.0029	4.4746	93.81	8.62	18.25	0.11		
461-01F	5.5	50.96	0.37	54.07	0.34	0.01866	0.00074	0.01046	0.00057	0.0028	3.3276	94.29	6.41	17.82	0.13		
461-01G	6.0	48.94	0.33	52.66	0.31	0.01962	0.00082	0.01249	0.00055	0.0029	3.2076	92.99	6.18	17.11	0.12		
461-01H	6.5	49.75	0.31	52.12	0.28	0.01846	0.00078	0.00793	0.00051	0.0029	3.0154	95.51	5.81	17.40	0.11		
461-01I	7.5	51.04	0.34	52.96	0.32	0.01810	0.00066	0.00641	0.00042	0.0028	3.8544	96.43	7.42	17.84	0.12		
461-01J	8.5	50.03	0.34	51.93	0.31	0.01728	0.00078	0.00633	0.00059	0.0027	2.7135	96.39	5.23	17.49	0.12		
461-01K	9.5	50.28	0.38	52.48	0.32	0.01718	0.00090	0.00732	0.00073	0.0027	2.3121	95.87	4.45	17.58	0.13		
461-01L	15.0	52.06	0.40	66.62	0.30	0.02530	0.00065	0.04916	0.00099	0.0027	5.4340	78.19	10.46	18.20	0.14		

Table A3: biotite $^{40}Ar/^{39}Ar$ data

Sample/ Lab ID	Laser Power (W)	$^{40}Ar^*/^{39}Ar$	2σ	$^{40}Ar/^{39}Ar$	2σ	$^{38}Ar/^{39}Ar$	2σ	$^{36}Ar/^{39}Ar$	2σ	Cl/K	^{39}Ar (fmol)	$\%^{40}Ar^*$	$\%^{39}Ar$	Date (Ma)	2σ	J	2σ
BT0988																1.979E-04	2.2E-06
480-01A	3.0	28.98	0.22	43.51	0.18	0.02313	0.00044	0.04909	0.00054	0.0023	7.8862	66.64	15.23	10.319	0.077		
480-01B	3.0	27.78	0.19	29.74	0.14	0.01499	0.00058	0.00655	0.00045	0.0023	4.0698	93.49	7.86	9.893	0.068		
480-01C	3.8	27.53	0.19	29.40	0.15	0.01491	0.00051	0.00621	0.00044	0.0023	4.7204	93.75	9.12	9.805	0.068		
480-01D	4.6	27.73	0.18	29.50	0.15	0.01494	0.00050	0.00591	0.00037	0.0023	5.2308	94.07	10.10	9.874	0.063		
480-01E	5.0	27.49	0.16	28.93	0.12	0.01447	0.00055	0.00480	0.00036	0.0023	5.1530	95.10	9.95	9.789	0.056		
480-01F	5.5	27.54	0.15	28.76	0.12	0.01475	0.00056	0.00402	0.00036	0.0024	4.7743	95.87	9.22	9.810	0.055		
480-01G	6.0	27.64	0.19	28.68	0.14	0.01384	0.00054	0.00341	0.00043	0.0022	3.8907	96.49	7.51	9.846	0.066		
480-01H	6.5	27.68	0.19	28.72	0.13	0.01418	0.00069	0.00339	0.00048	0.0023	3.7191	96.49	7.18	9.858	0.068		
480-01I	7.5	28.05	0.18	29.16	0.14	0.01423	0.00057	0.00368	0.00042	0.0023	4.2793	96.27	8.26	9.988	0.064		
480-01J	8.5	27.94	0.23	28.75	0.15	0.01456	0.00076	0.00264	0.00057	0.0024	2.8145	97.28	5.44	9.949	0.080		
480-01K	9.5	28.39	0.29	28.68	0.18	0.01378	0.00085	0.00085	0.00077	0.0023	2.0114	99.09	3.88	10.11	0.10		
480-01L	15.0	27.63	0.47	45.41	0.27	0.0256	0.0011	0.0601	0.0015	0.0024	3.2321	60.87	6.24	9.84	0.17		
BT0989																1.906E-04	1.9E-06
478-01A	3.0	25.37	0.25	49.75	0.19	0.02846	0.00051	0.082	0.00070	0.0022	8.5333	51.02	21.37	8.703	0.085		
478-01B	3.0	25.21	0.25	34.31	0.16	0.01882	0.00062	0.031	0.00074	0.0022	3.9904	73.55	9.99	8.652	0.085		
478-01C	3.8	25.37	0.26	34.26	0.17	0.01725	0.00069	0.030	0.00077	0.0020	3.6116	74.11	9.04	8.705	0.090		
478-01D	4.6	24.97	0.21	35.33	0.15	0.01931	0.00060	0.035	0.00062	0.0021	4.6967	70.73	11.76	8.567	0.072		
478-01E	5.0	25.15	0.21	33.80	0.14	0.01737	0.00067	0.029	0.00061	0.0020	4.3049	74.45	10.78	8.628	0.071		
478-01F	5.5	25.22	0.23	32.94	0.15	0.01670	0.00062	0.026	0.00066	0.0020	3.7427	76.63	9.37	8.653	0.078		
478-01G	6.0	25.21	0.26	32.44	0.17	0.01737	0.00076	0.024	0.00077	0.0022	3.3137	77.79	8.30	8.650	0.089		
478-01H	6.5	25.37	0.28	31.43	0.18	0.01604	0.00078	0.020	0.00081	0.0021	2.4498	80.79	6.13	8.705	0.096		
478-01I	7.5	25.49	0.30	30.73	0.19	0.01638	0.00092	0.018	0.00086	0.0022	2.1860	83.04	5.47	8.75	0.10		
478-01J	8.5	25.25	0.58	30.21	0.32	0.0150	0.0014	0.0167	0.0017	0.0020	0.9208	83.65	2.31	8.66	0.20		
478-01K	9.5	26.7	1.3	29.26	0.50	0.0145	0.0036	0.0084	0.0043	0.0022	0.3835	91.48	0.96	9.17	0.46		
478-01L	15.0	25.33	0.79	66.65	0.49	0.0394	0.0019	0.1397	0.0027	0.0022	1.7981	38.03	4.50	8.69	0.27		

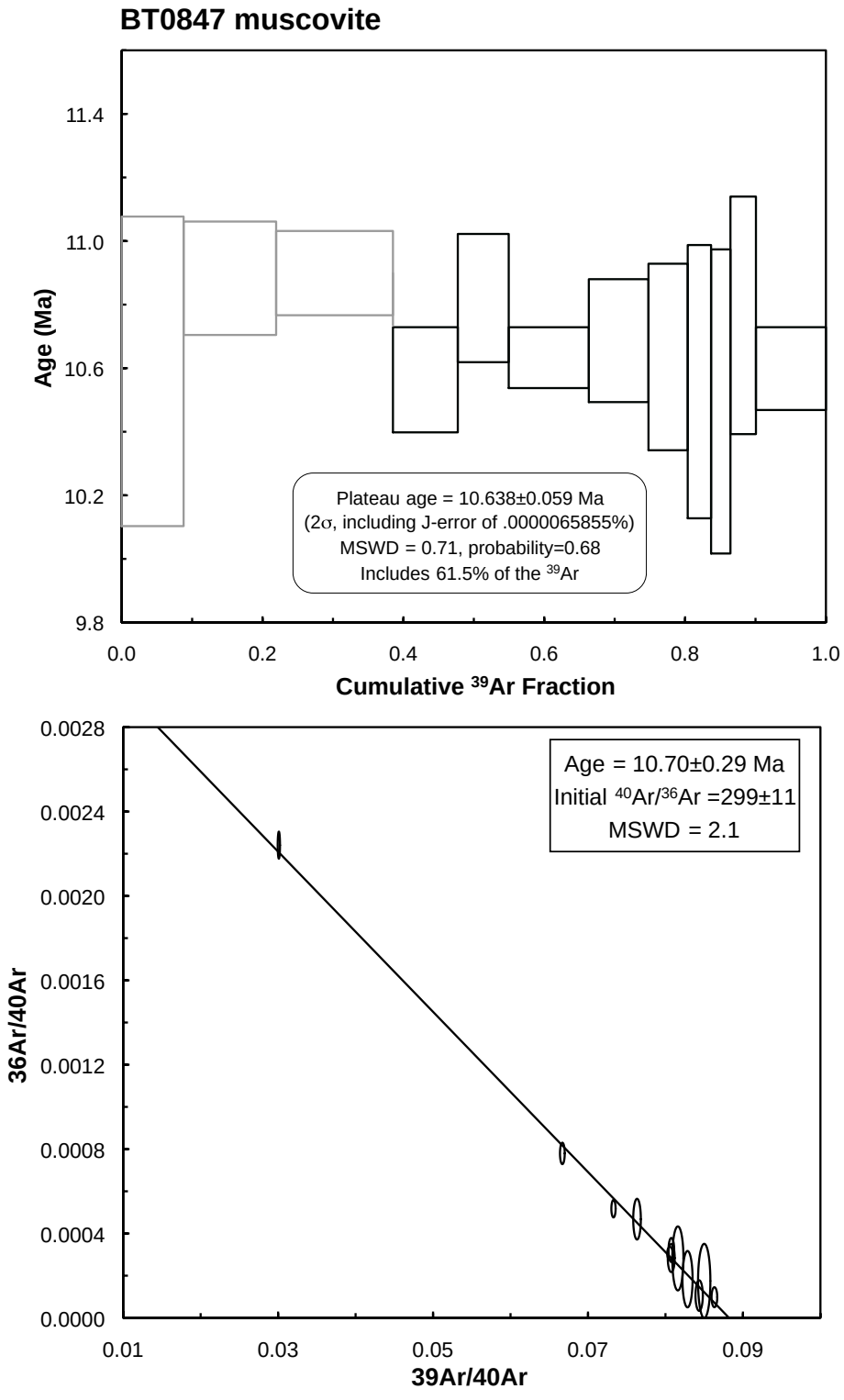
BT0847 muscovite
Age (Ma)
11.4
11.0
10.6
10.2
9.8
0.0
0.2
0.4
0.6
0.8
1.0
Cumulative 39Ar Fraction
Plateau age = 10.638±0.059 Ma
(2σ, including J-error of .0000065855%)
MSWD = 0.71, probability=0.68
Includes 61.5% of the 39Ar
36Ar/40Ar
0.0028
0.0024
0.0020
0.0016
0.0012
0.0008
0.0004
0.0000
0.01
0.03
0.05
0.07
0.09
39Ar/40Ar
Age = 10.70±0.29 Ma
Initial 40Ar/36Ar =299±11
MSWD = 2.1

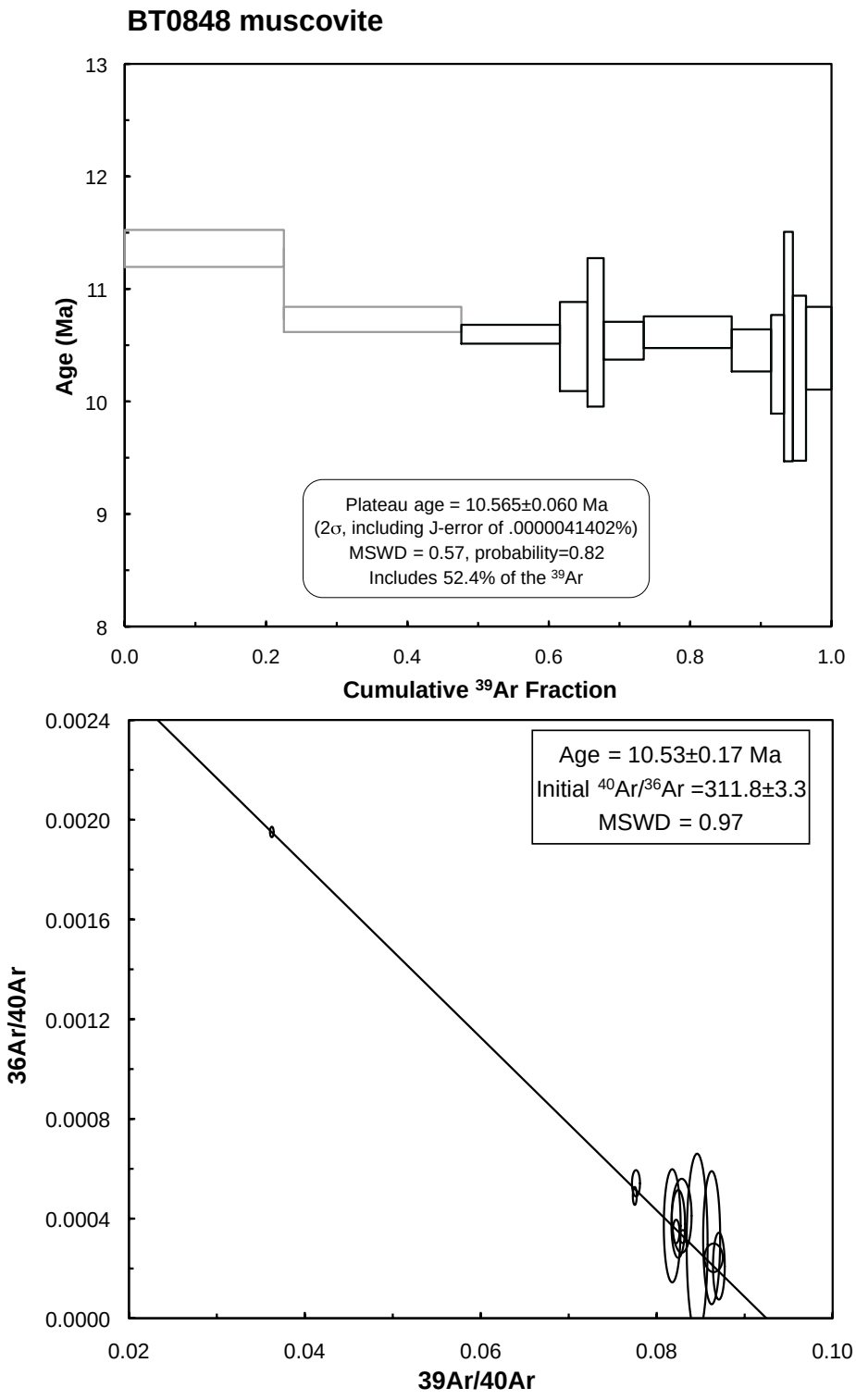
BT0848 muscovite
Age (Ma)
Cumulative 39Ar Fraction
Plateau age = 10.565±0.060 Ma
(2σ, including J-error of .0000041402%)
MSWD = 0.57, probability=0.82
Includes 52.4% of the 39Ar
36Ar/40Ar
39Ar/40Ar
Age = 10.53±0.17 Ma
Initial 40Ar/36Ar =311.8±3.3
MSWD = 0.97

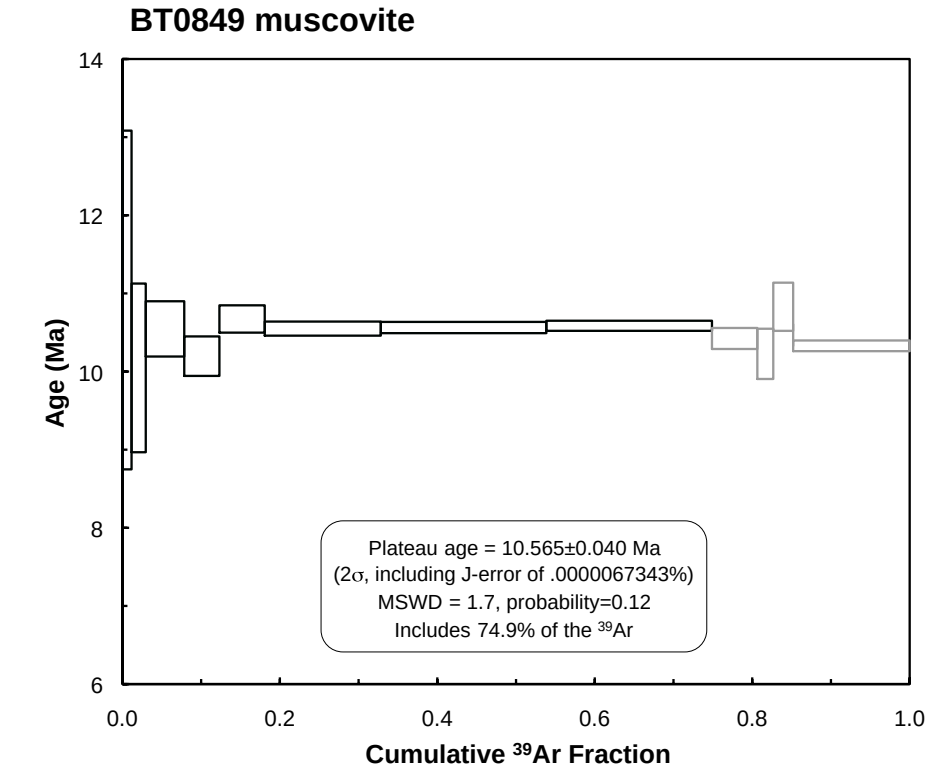
BT0849 muscovite
Age (Ma)
Cumulative 39Ar Fraction
Plateau age = 10.565±0.040 Ma
(2σ, including J-error of .0000067343%)
MSWD = 1.7, probability=0.12
Includes 74.9% of the 39Ar

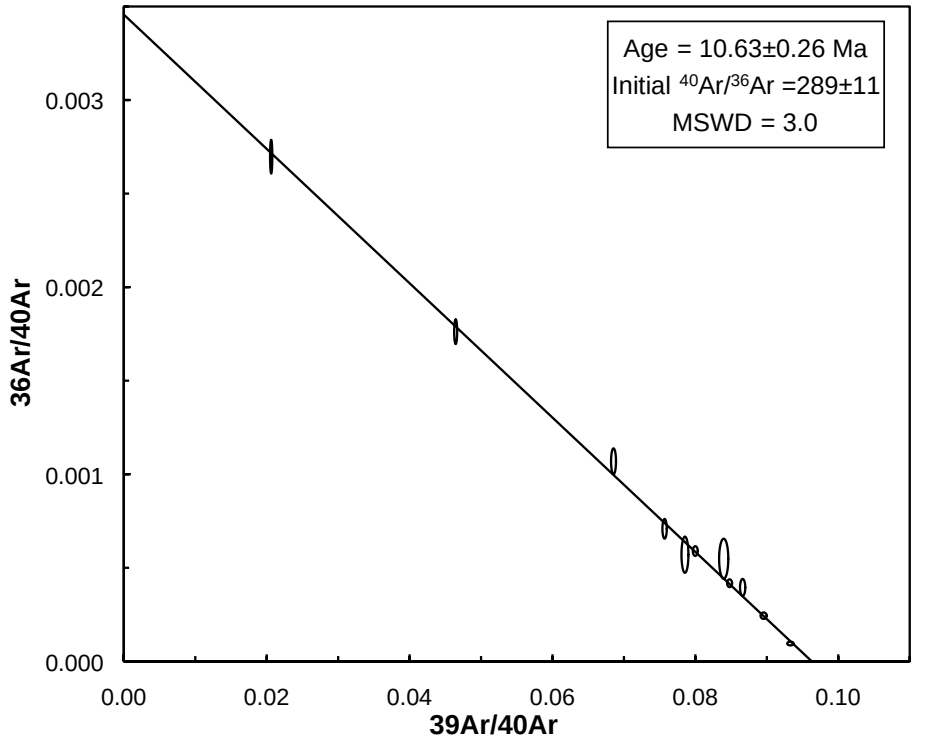
Age = 10.63±0.26 Ma
Initial 40Ar/36Ar =289±11
MSWD = 3.0
36Ar/40Ar
39Ar/40Ar

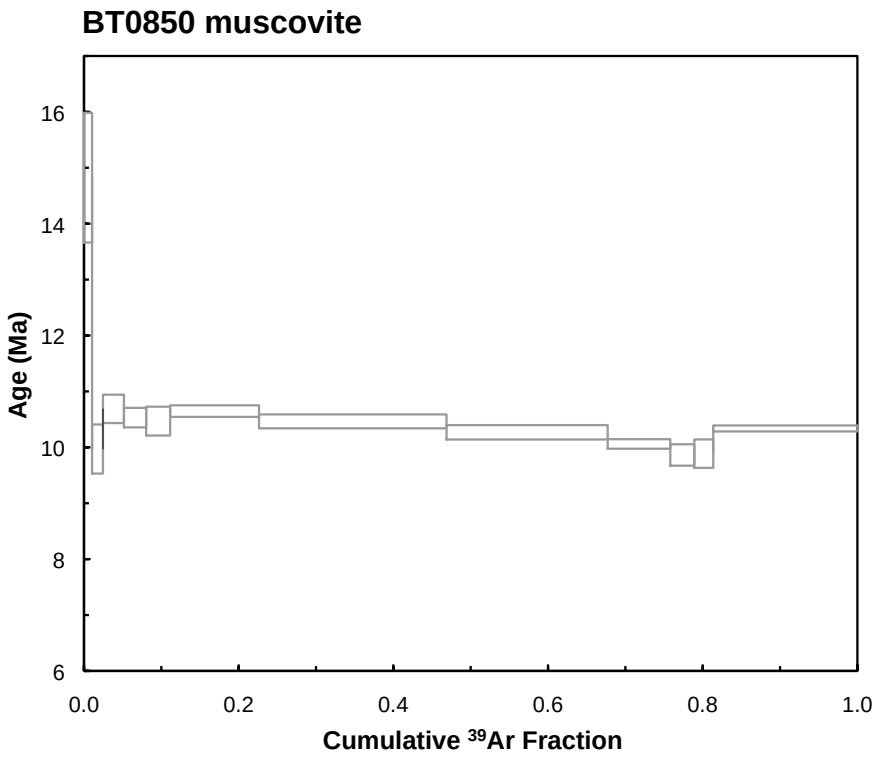
BT0850 muscovite
Age (Ma)
16
14
12
10
8
6
0.0
0.2
0.4
0.6
0.8
1.0
Cumulative 39Ar Fraction

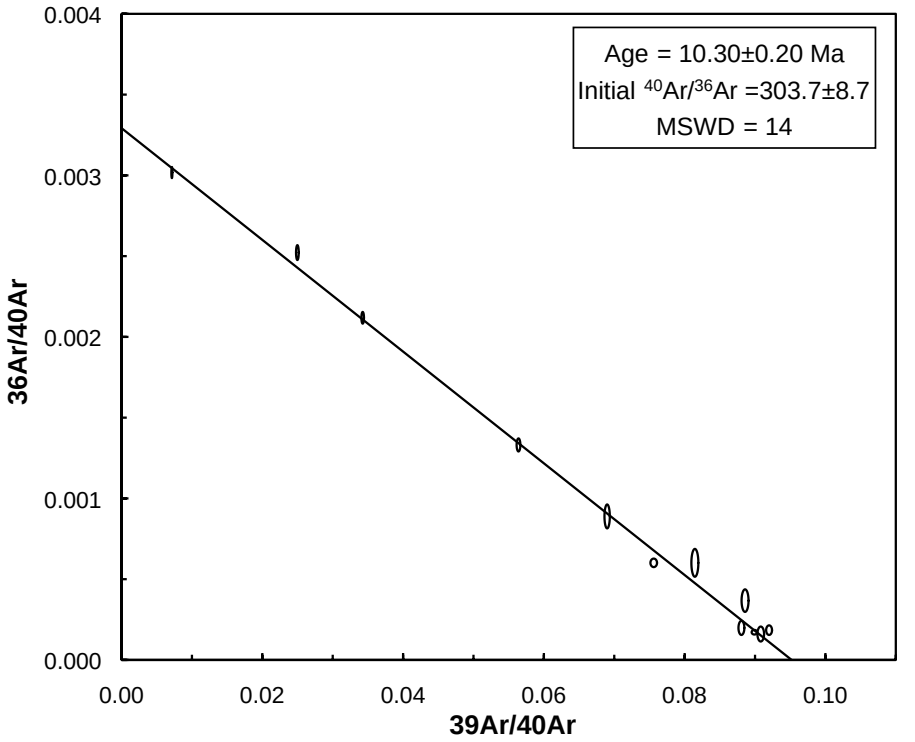
Age = 10.30±0.20 Ma
Initial 40Ar/36Ar =303.7±8.7
MSWD = 14
36Ar/40Ar
0.004
0.003
0.002
0.001
0.000
0.00
0.02
0.04
0.06
0.08
0.10
39Ar/40Ar

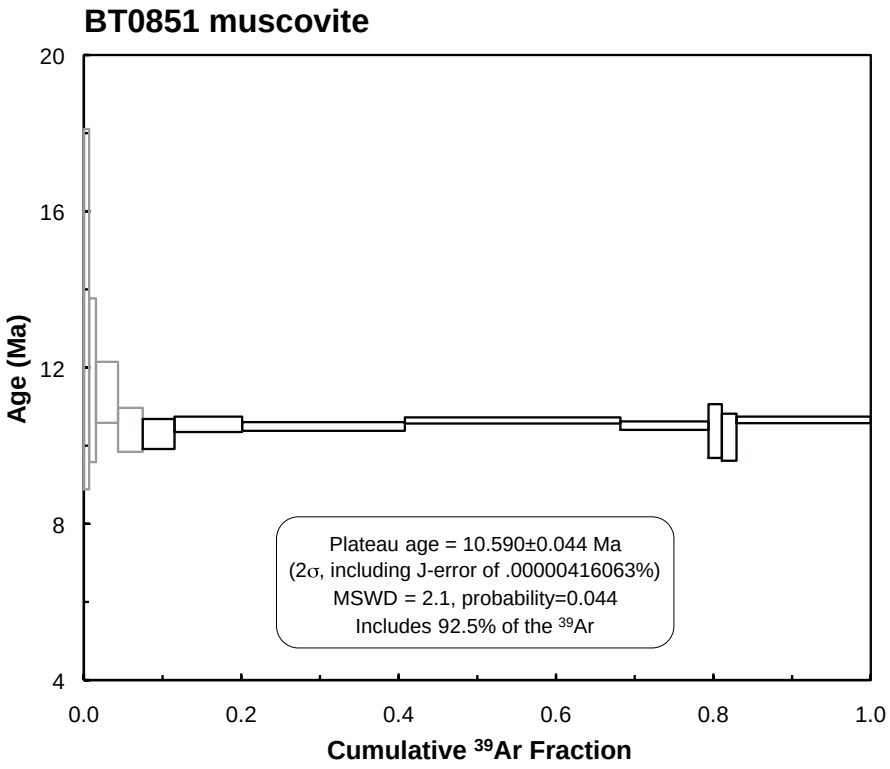
BT0851 muscovite
Age (Ma)
20
16
12
8
4
0.0
0.2
0.4
0.6
0.8
1.0
Cumulative 39Ar Fraction
Plateau age = 10.590±0.044 Ma
(2σ, including J-error of .00000416063%)
MSWD = 2.1, probability=0.044
Includes 92.5% of the 39Ar

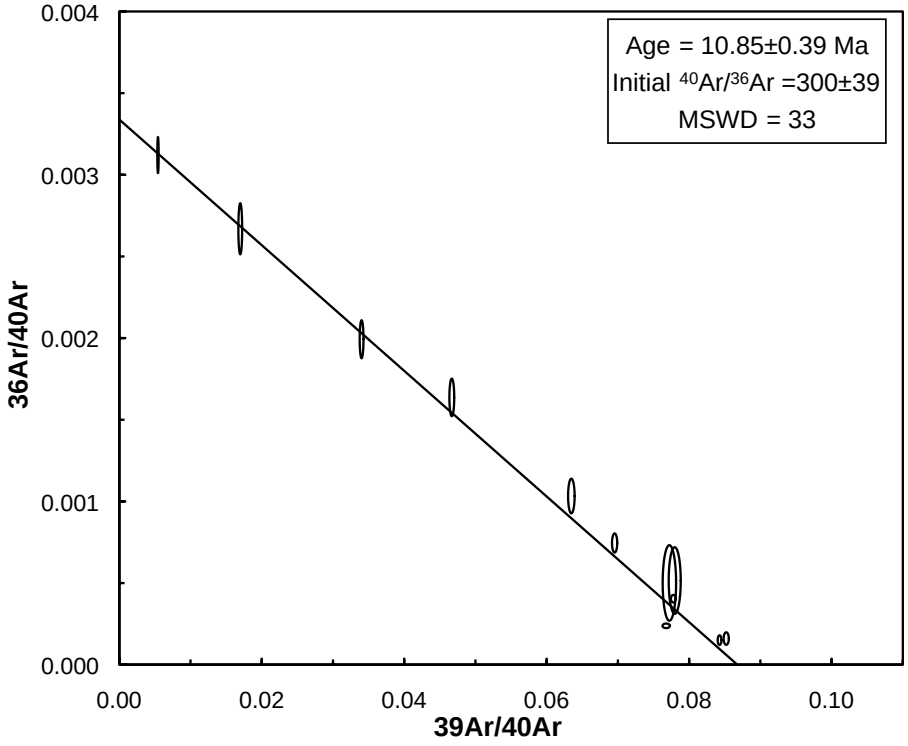
36Ar/40Ar
0.004
0.003
0.002
0.001
0.000
0.00
0.02
0.04
0.06
0.08
0.10
39Ar/40Ar
Age = 10.85±0.39 Ma
Initial 40Ar/36Ar =300±39
MSWD = 33

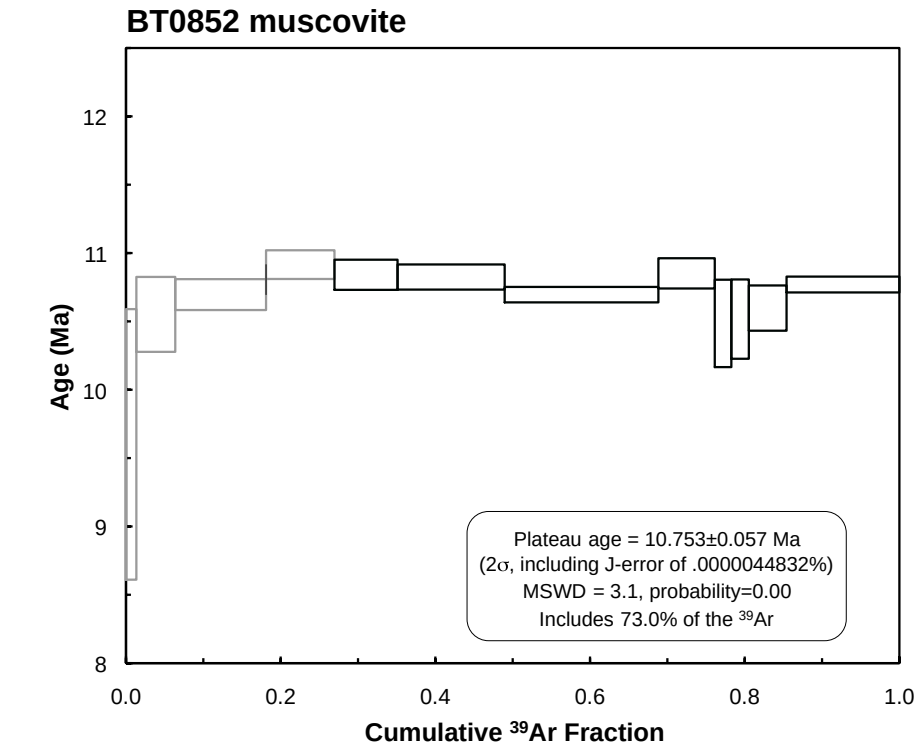
BT0852 muscovite
Age (Ma)
12
11
10
9
8
0.0
0.2
0.4
0.6
0.8
1.0
Cumulative 39Ar Fraction
Plateau age = 10.753±0.057 Ma
(2σ, including J-error of .0000044832%)
MSWD = 3.1, probability=0.00
Includes 73.0% of the 39Ar

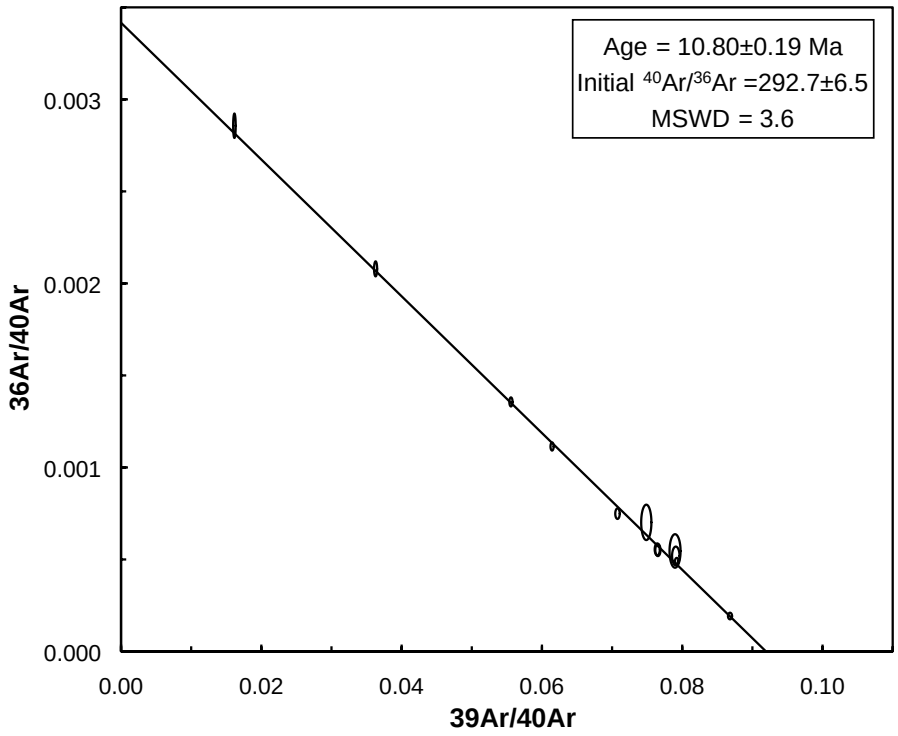
Age = 10.80±0.19 Ma
Initial 40Ar/36Ar =292.7±6.5
MSWD = 3.6
36Ar/40Ar
0.003
0.002
0.001
0.000
0.00
0.02
0.04
0.06
0.08
0.10
39Ar/40Ar

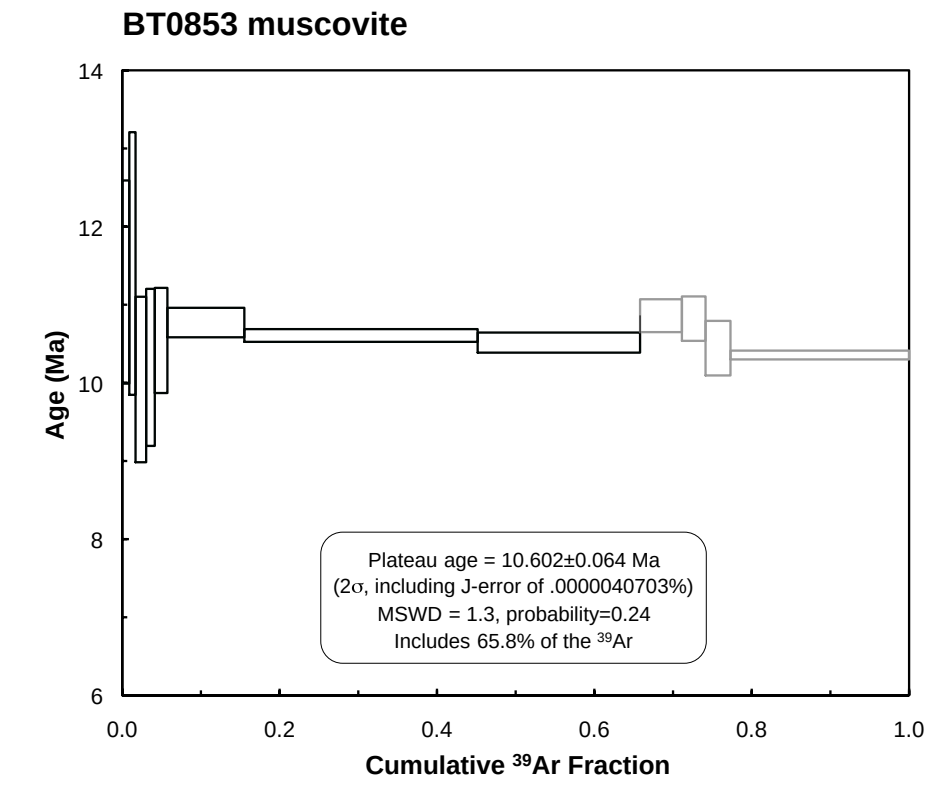
BT0853 muscovite
Age (Ma)
Cumulative 39Ar Fraction
Plateau age = 10.602±0.064 Ma
(2σ, including J-error of .0000040703%)
MSWD = 1.3, probability=0.24
Includes 65.8% of the 39Ar

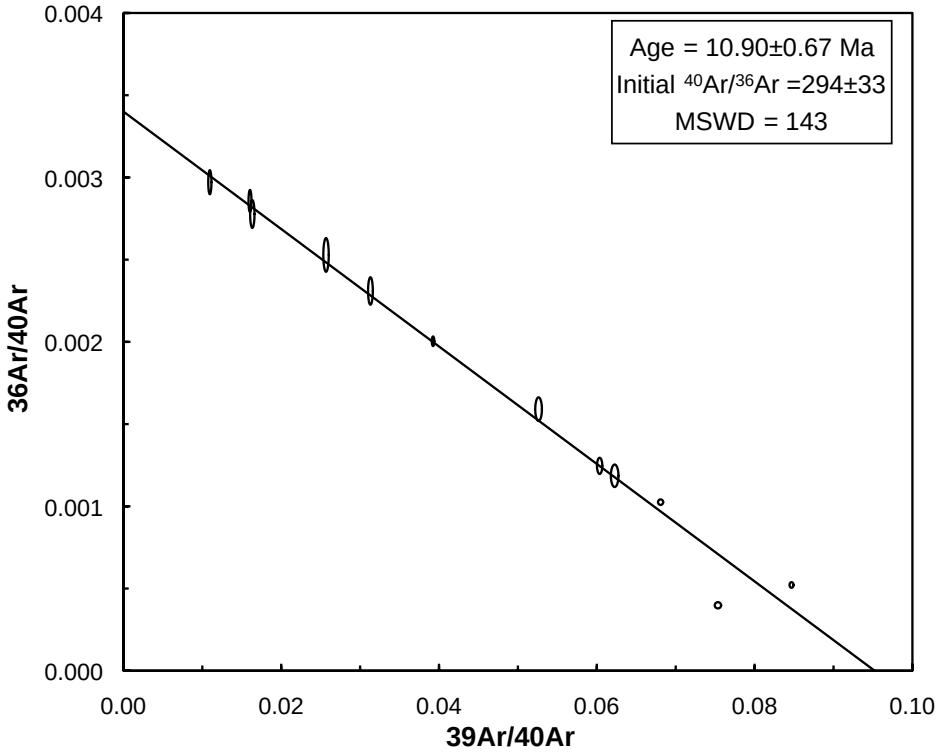
36Ar/40Ar
39Ar/40Ar
Age = 10.90±0.67 Ma
Initial 40Ar/36Ar =294±33
MSWD = 143

BT0914 muscovite

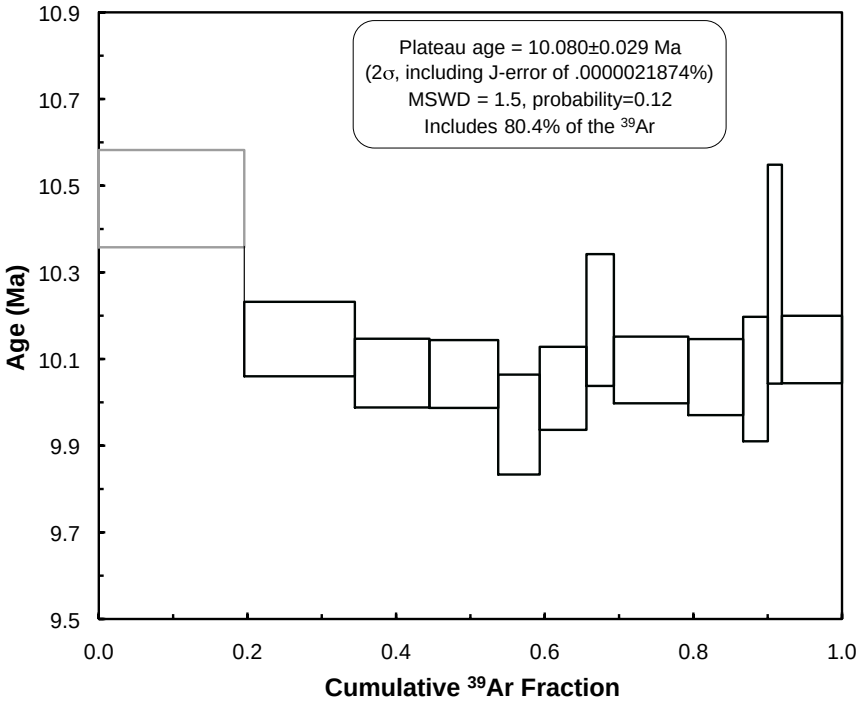

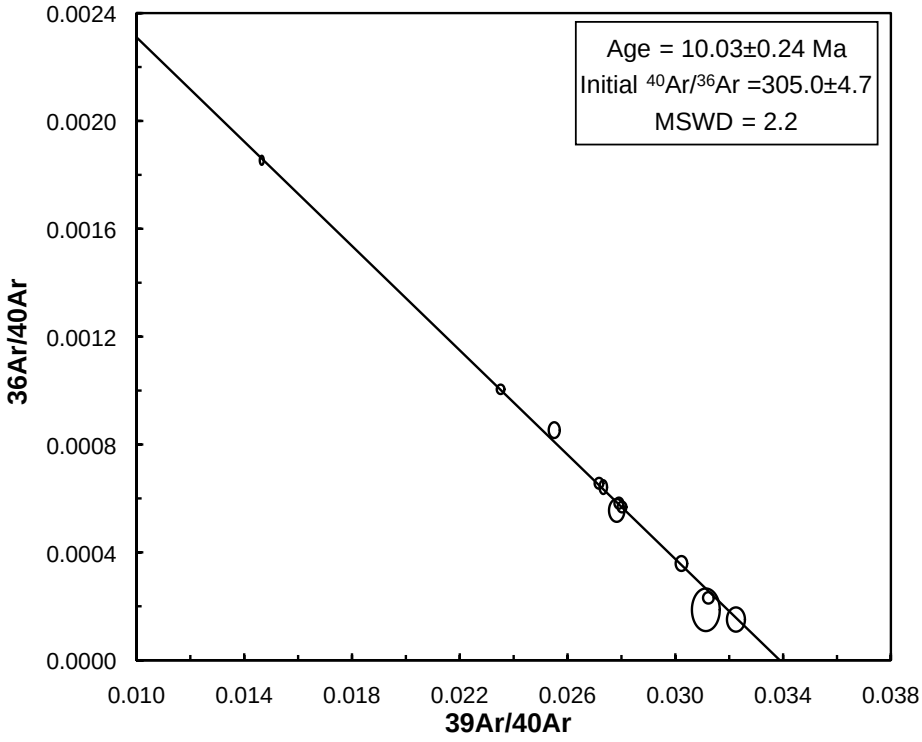

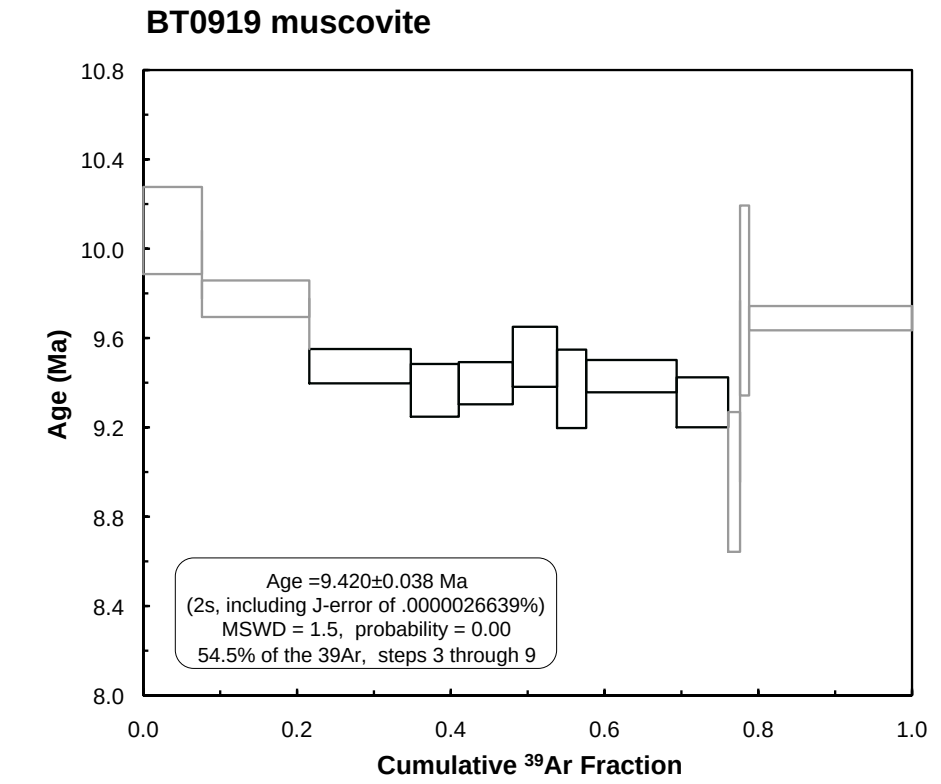
BT0919 muscovite
10.8
10.4
10.0
9.6
9.2
8.8
8.4
8.0
Age (Ma)
Age =9.420±0.038 Ma
(2s, including J-error of .0000026639%)
MSWD = 1.5, probability = 0.00
54.5% of the 39Ar, steps 3 through 9
0.0
0.2
0.4
0.6
0.8
1.0
Cumulative 39Ar Fraction

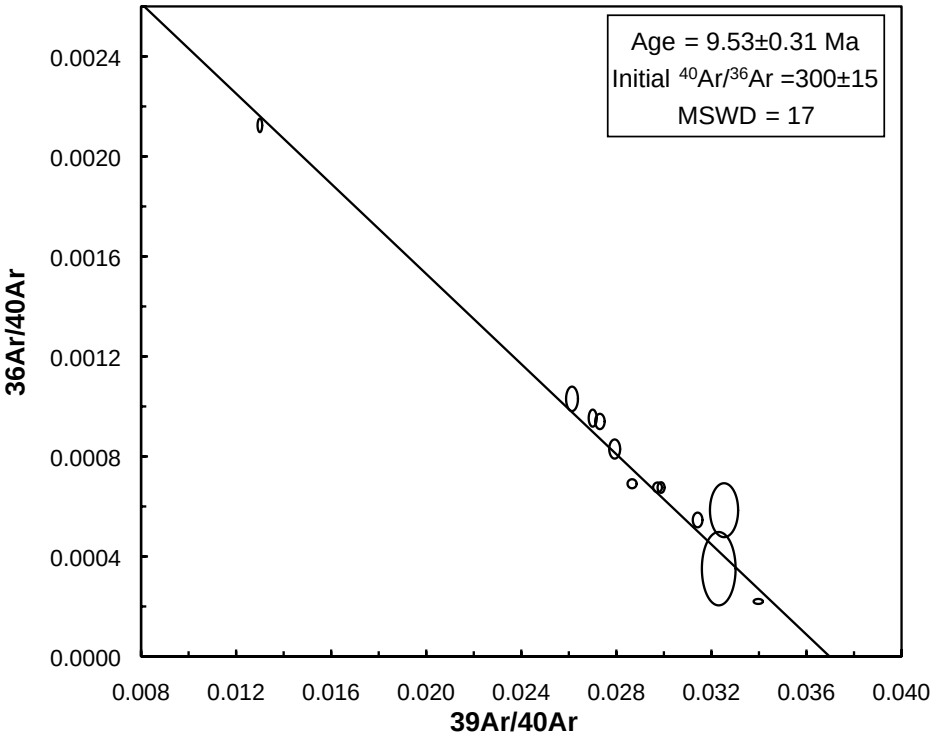
Age = 9.53±0.31 Ma
Initial 40Ar/36Ar =300±15
MSWD = 17
0.0024
0.0020
0.0016
0.0012
0.0008
0.0004
0.0000
36Ar/40Ar
0.008
0.012
0.016
0.020
0.024
0.028
0.032
0.036
0.040
39Ar/40Ar

BT0920 muscovite

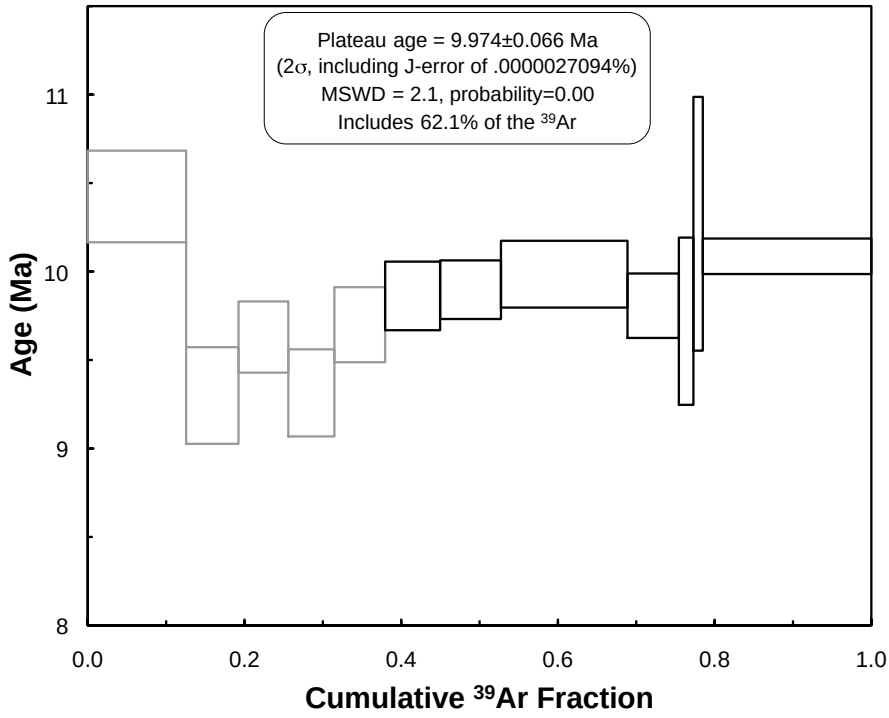

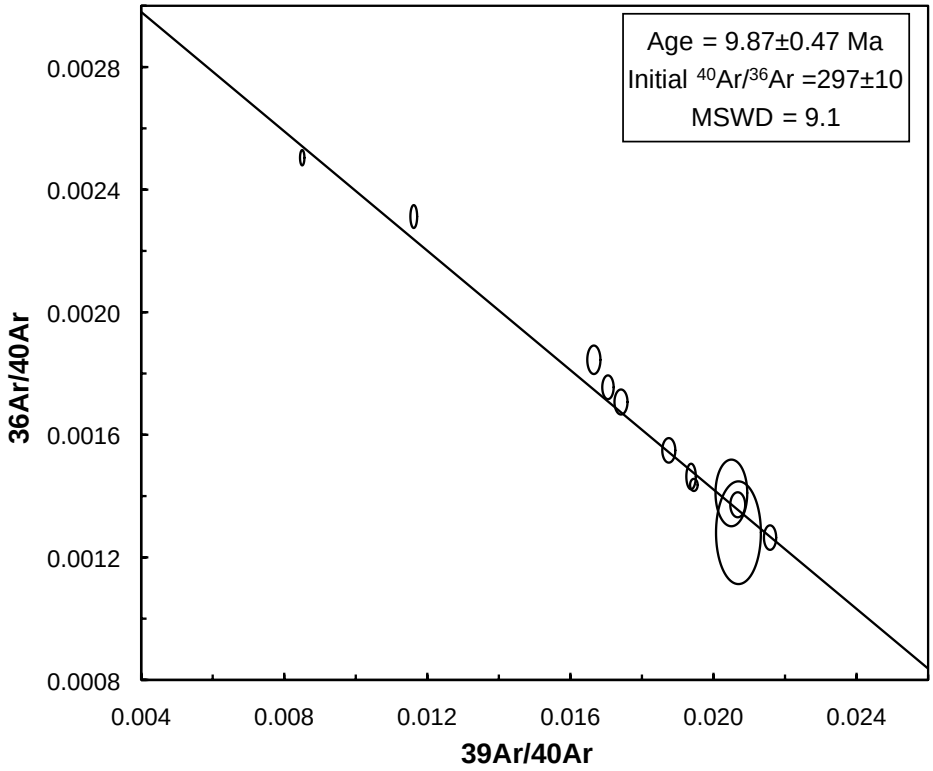

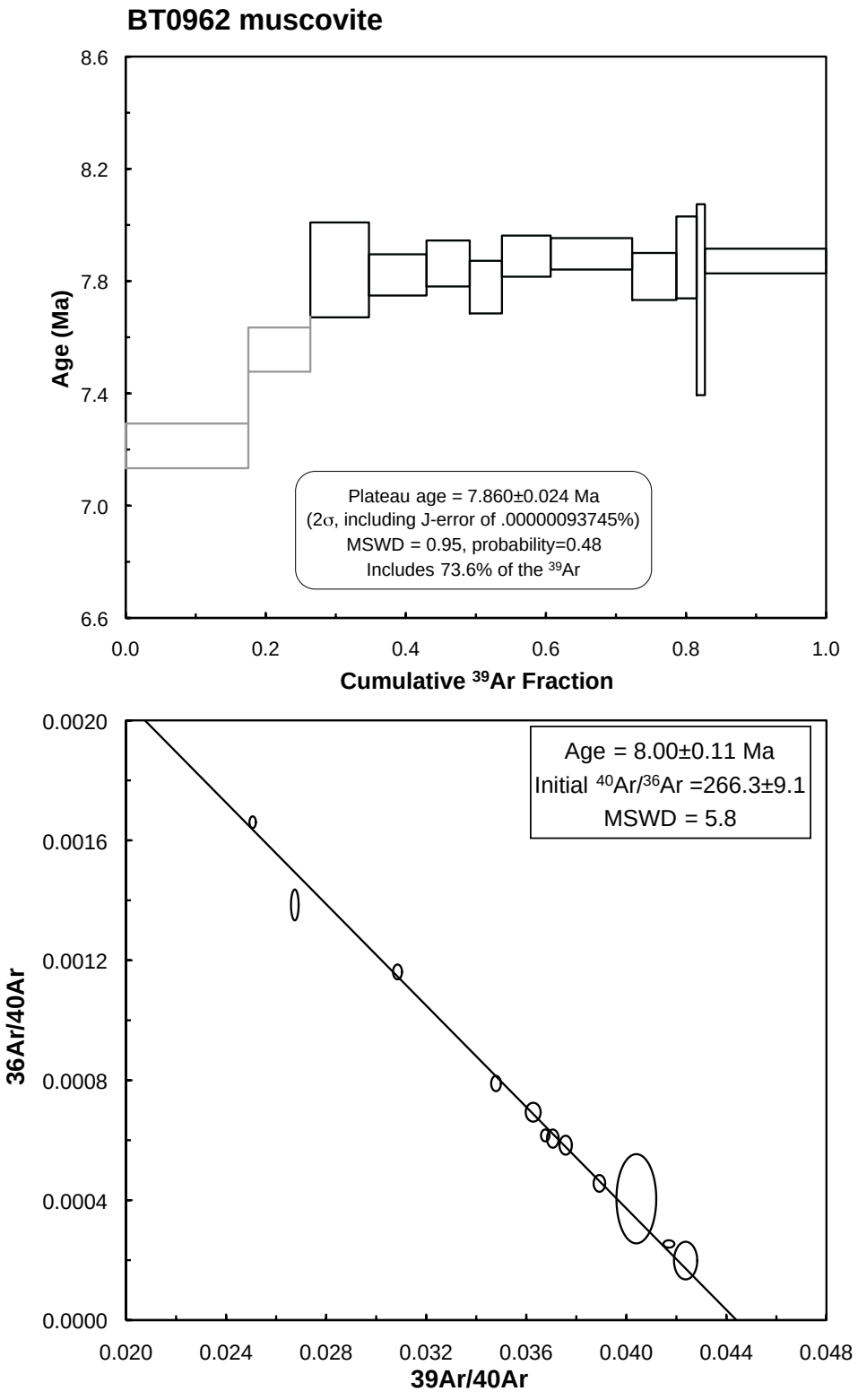
BT0962 muscovite
Age (Ma)
8.6
8.2
7.8
7.4
7.0
6.6
0.0
0.2
0.4
0.6
0.8
1.0
Cumulative 39Ar Fraction
Plateau age = 7.860±0.024 Ma
(2σ, including J-error of .00000093745%)
MSWD = 0.95, probability=0.48
Includes 73.6% of the 39Ar
36Ar/40Ar
0.0020
0.0016
0.0012
0.0008
0.0004
0.0000
0.020
0.024
0.028
0.032
0.036
0.040
0.044
0.048
39Ar/40Ar
Age = 8.00±0.11 Ma
Initial 40Ar/36Ar =266.3±9.1
MSWD = 5.8

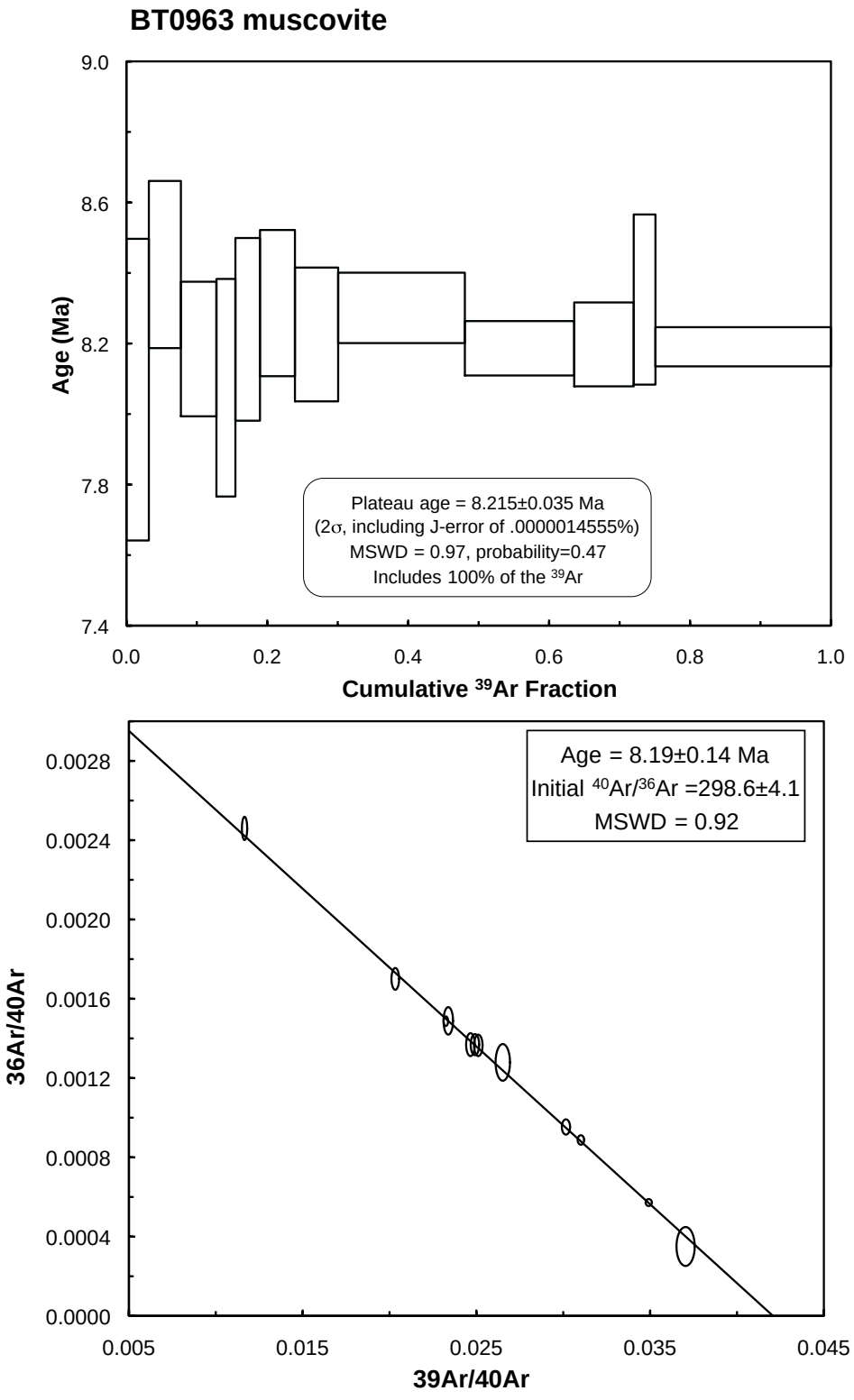
BT0963 muscovite
9.0
8.6
8.2
7.8
7.4
Age (Ma)
0.0
0.2
0.4
0.6
0.8
1.0
Cumulative 39Ar Fraction
Plateau age = 8.215±0.035 Ma
(2σ, including J-error of .0000014555%)
MSWD = 0.97, probability=0.47
Includes 100% of the 39Ar
Age = 8.19±0.14 Ma
Initial 40Ar/36Ar =298.6±4.1
MSWD = 0.92
0.0028
0.0024
0.0020
0.0016
0.0012
0.0008
0.0004
0.0000
36Ar/40Ar
0.005
0.015
0.025
0.035
0.045
39Ar/40Ar

BT0964 muscovite

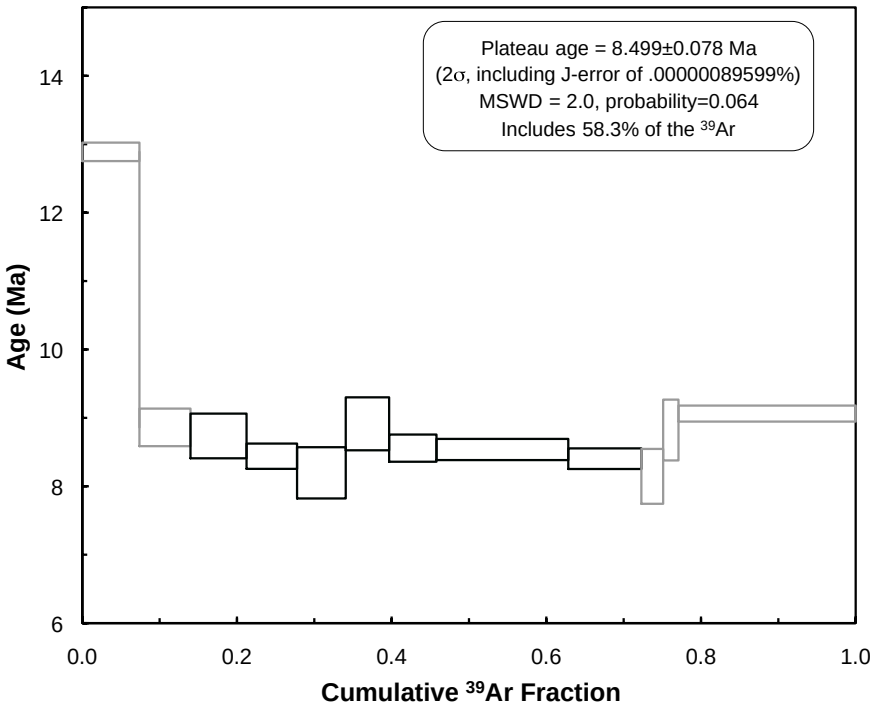

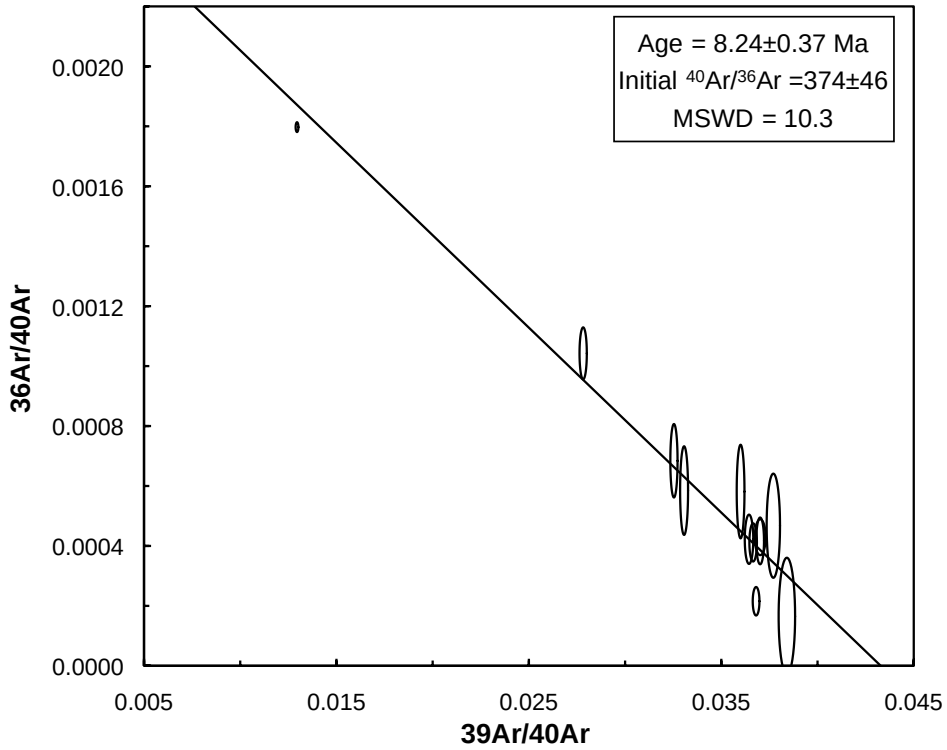

BT0987 muscovite

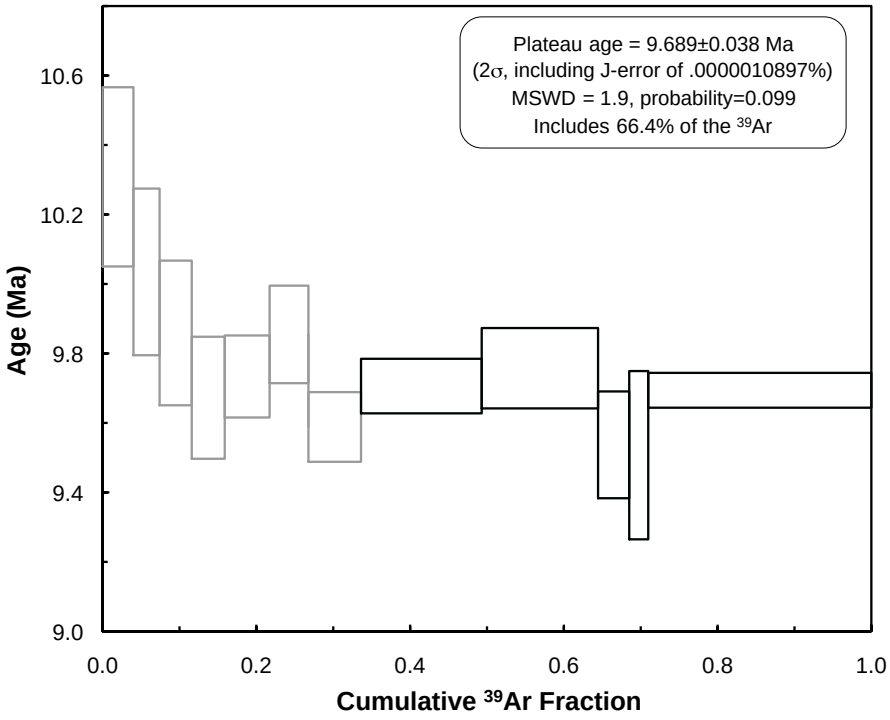

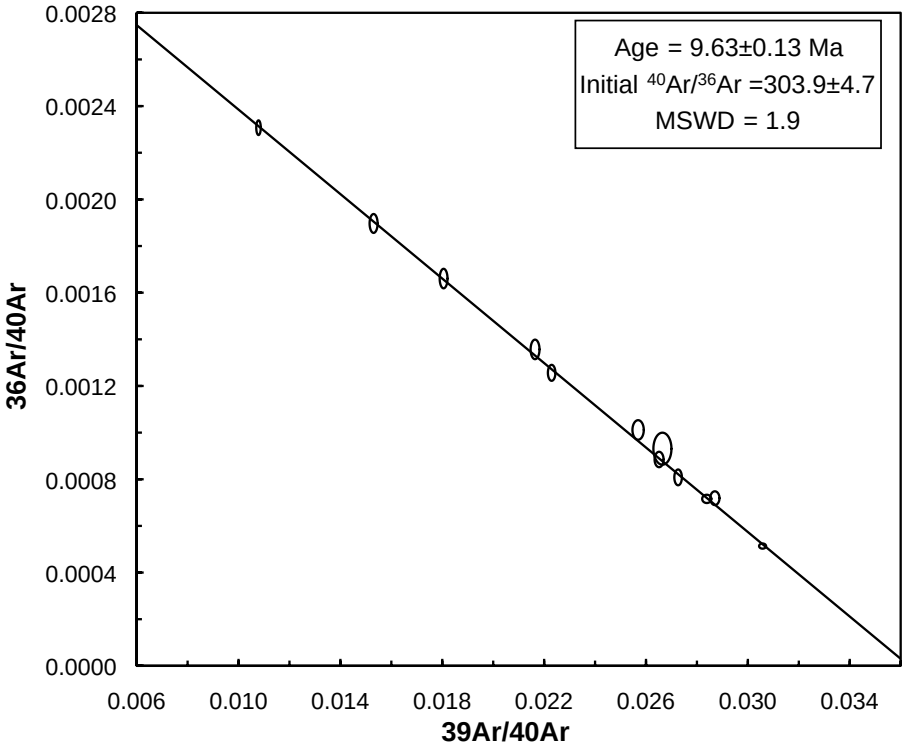

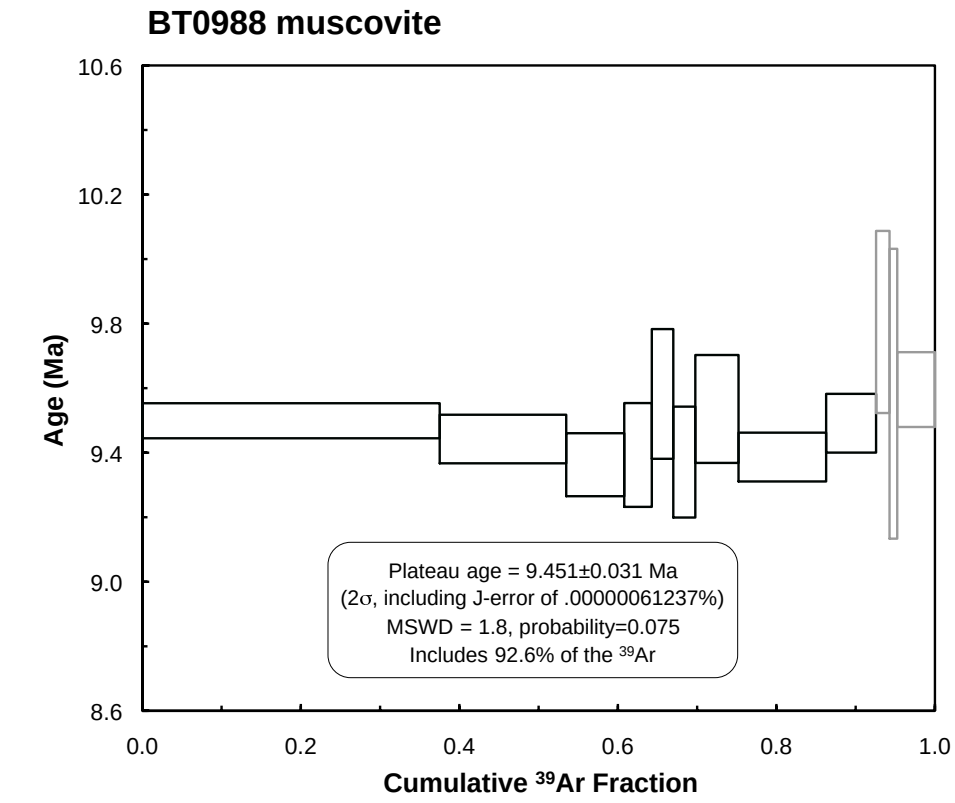
BT0988 muscovite
10.6
10.2
9.8
9.4
9.0
8.6
Age (Ma)
0.0
0.2
0.4
0.6
0.8
1.0
Cumulative 39Ar Fraction
Plateau age = 9.451±0.031 Ma
(2σ, including J-error of .00000061237%)
MSWD = 1.8, probability=0.075
Includes 92.6% of the 39Ar

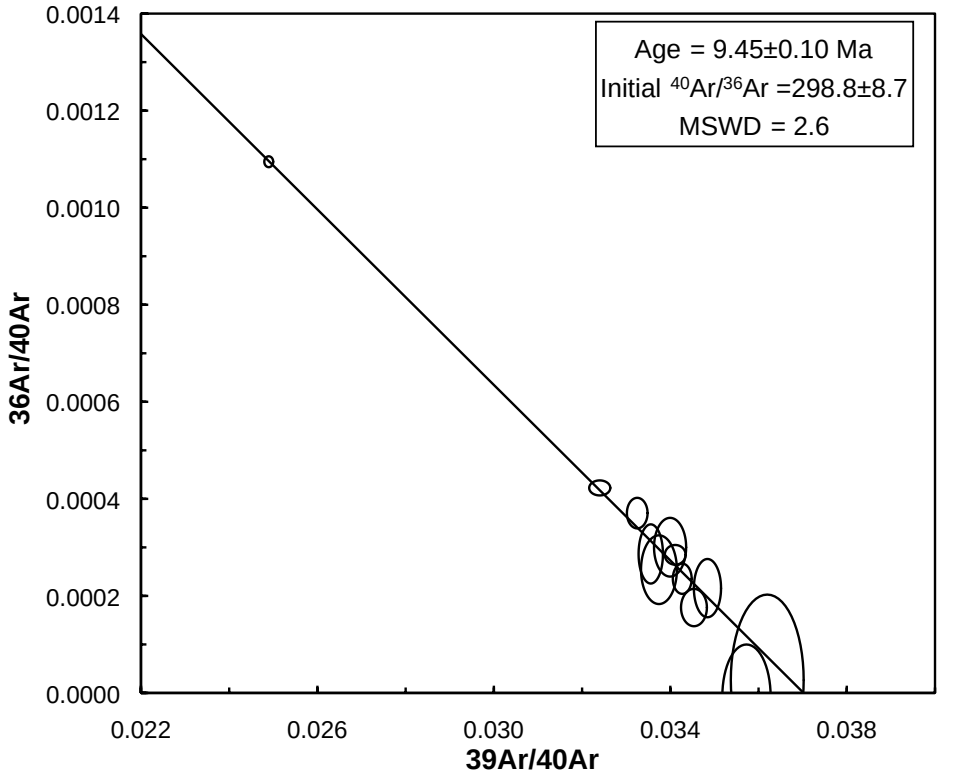
0.0014
0.0012
0.0010
0.0008
0.0006
0.0004
0.0002
0.0000
36Ar/40Ar
0.022
0.026
0.030
0.034
0.038
39Ar/40Ar
Age = 9.45±0.10 Ma
Initial 40Ar/36Ar =298.8±8.7
MSWD = 2.6

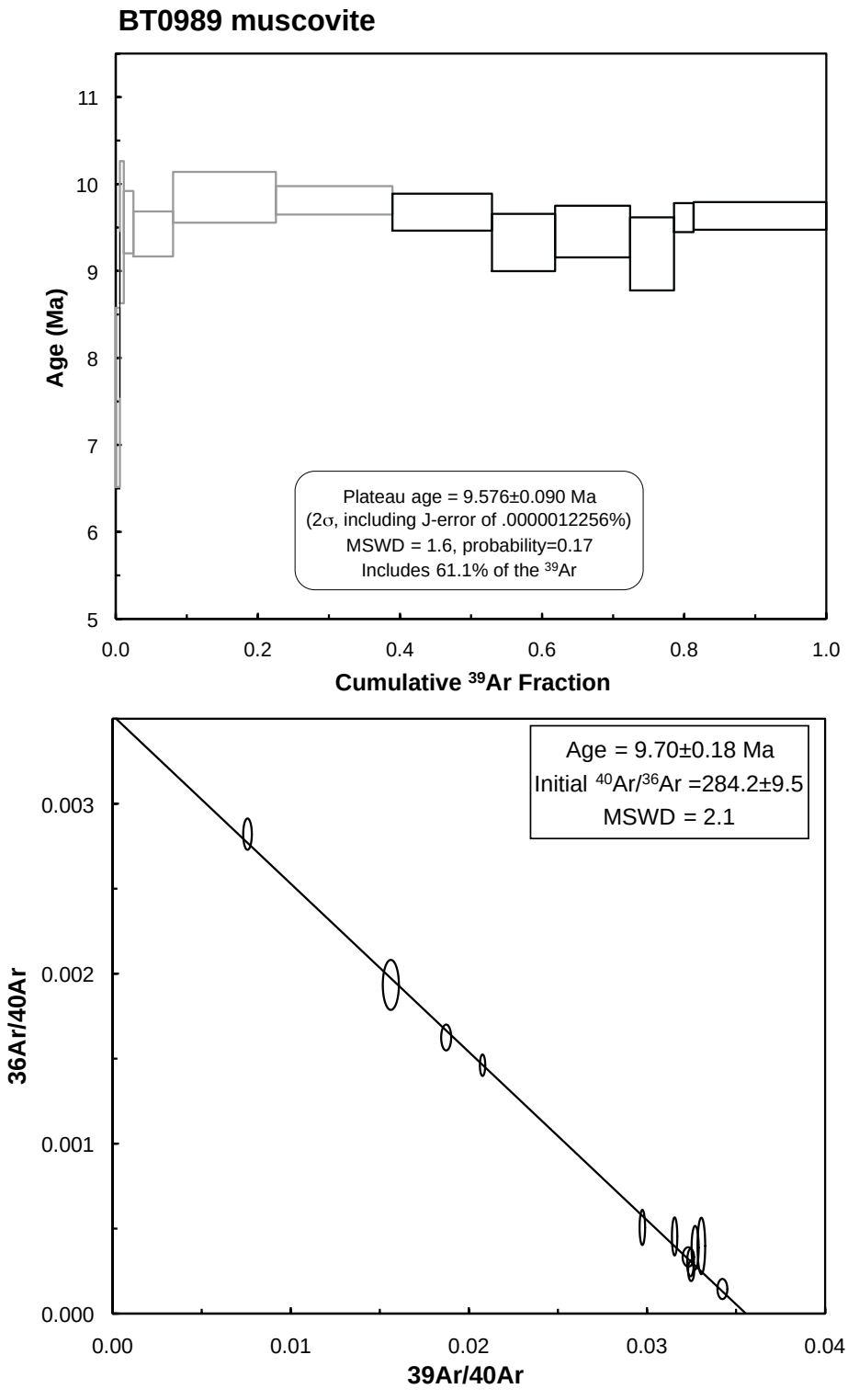
BT0989 muscovite
Age (Ma)
11
10
9
8
7
6
5
0.0
0.2
0.4
0.6
0.8
1.0
Cumulative 39Ar Fraction
Plateau age = 9.576±0.090 Ma
(2σ, including J-error of .0000012256%)
MSWD = 1.6, probability=0.17
Includes 61.1% of the 39Ar
36Ar/40Ar
0.003
0.002
0.001
0.000
0.00
0.01
0.02
0.03
0.04
39Ar/40Ar
Age = 9.70±0.18 Ma
Initial 40Ar/36Ar =284.2±9.5
MSWD = 2.1

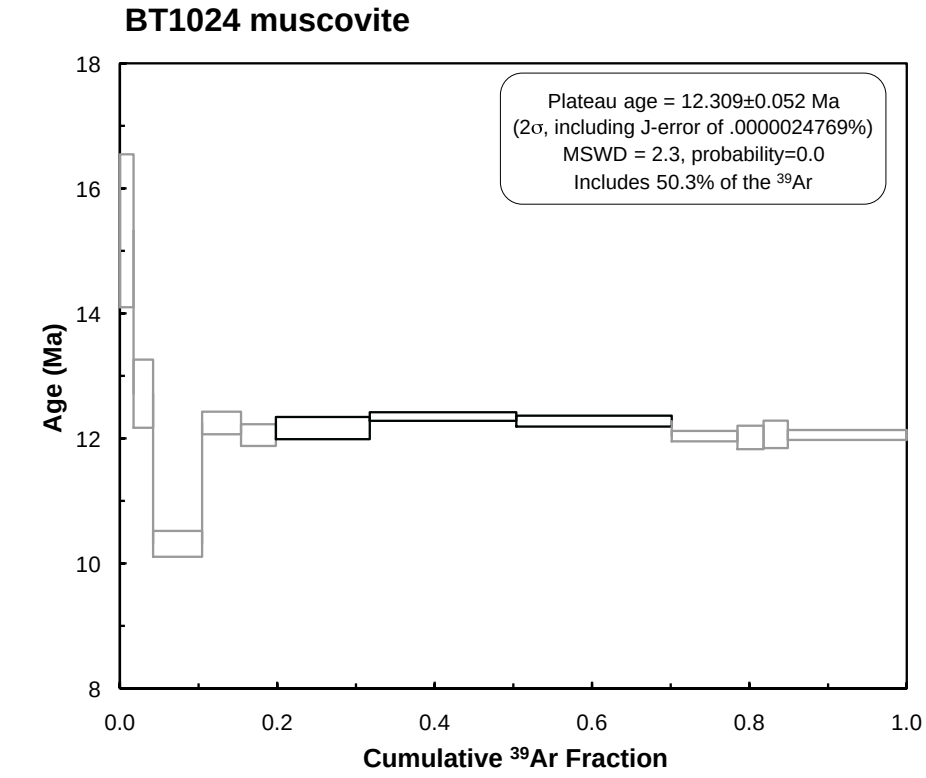
BT1024 muscovite
Plateau age = 12.309±0.052 Ma
(2σ, including J-error of .0000024769%)
MSWD = 2.3, probability=0.0
Includes 50.3% of the 39Ar
Age (Ma)
Cumulative 39Ar Fraction

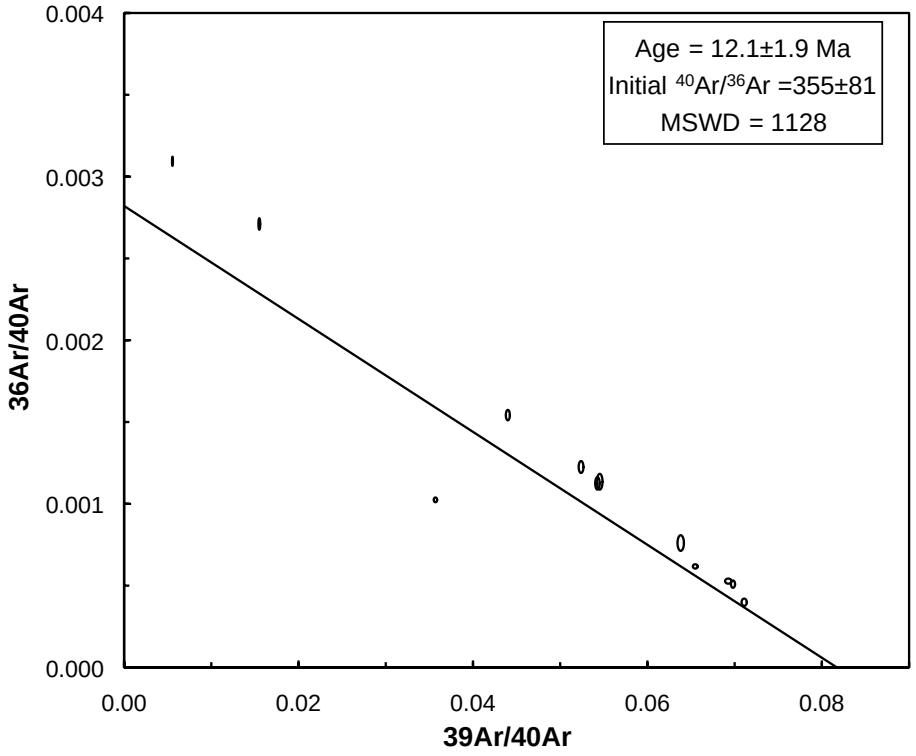
Age = 12.1±1.9 Ma
Initial 40Ar/36Ar =355±81
MSWD = 1128
36Ar/40Ar
39Ar/40Ar

BT0914 biotite

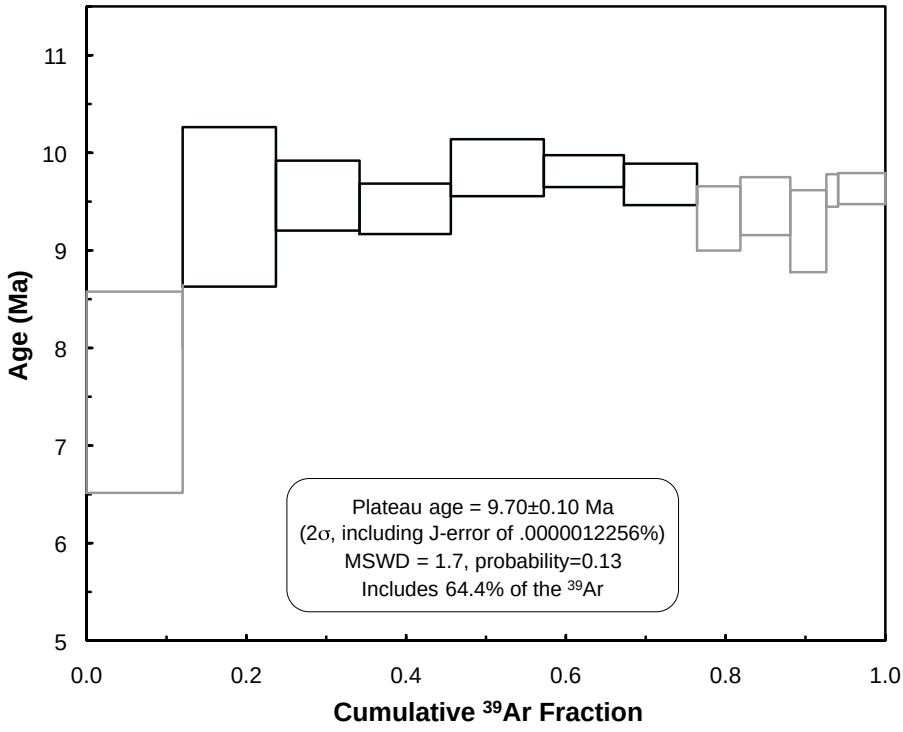

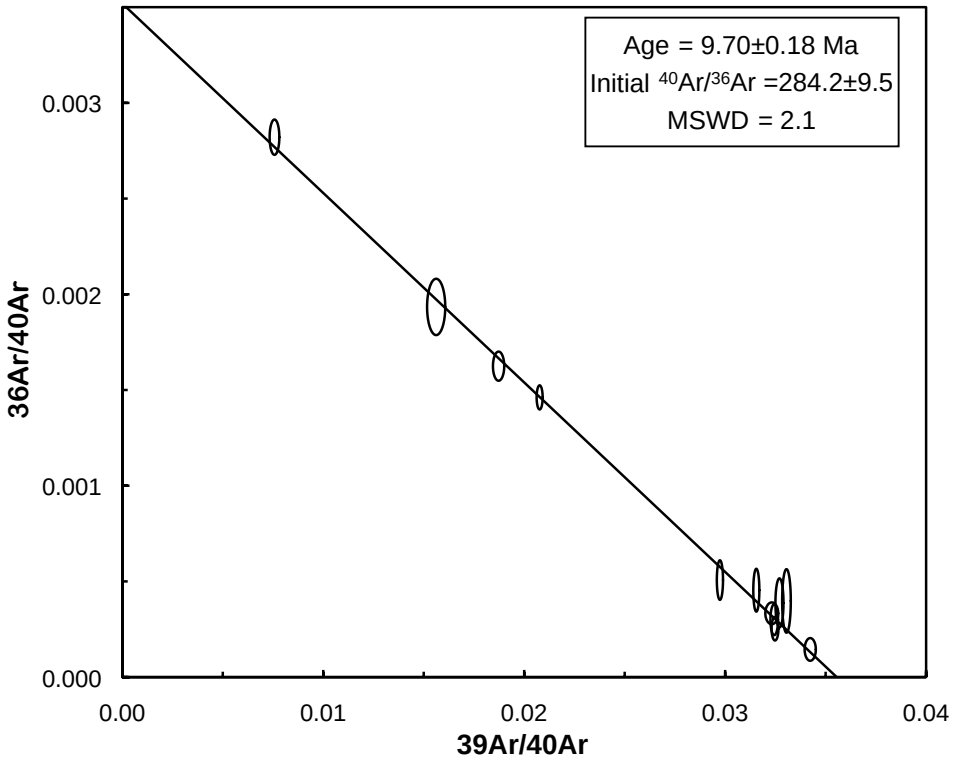

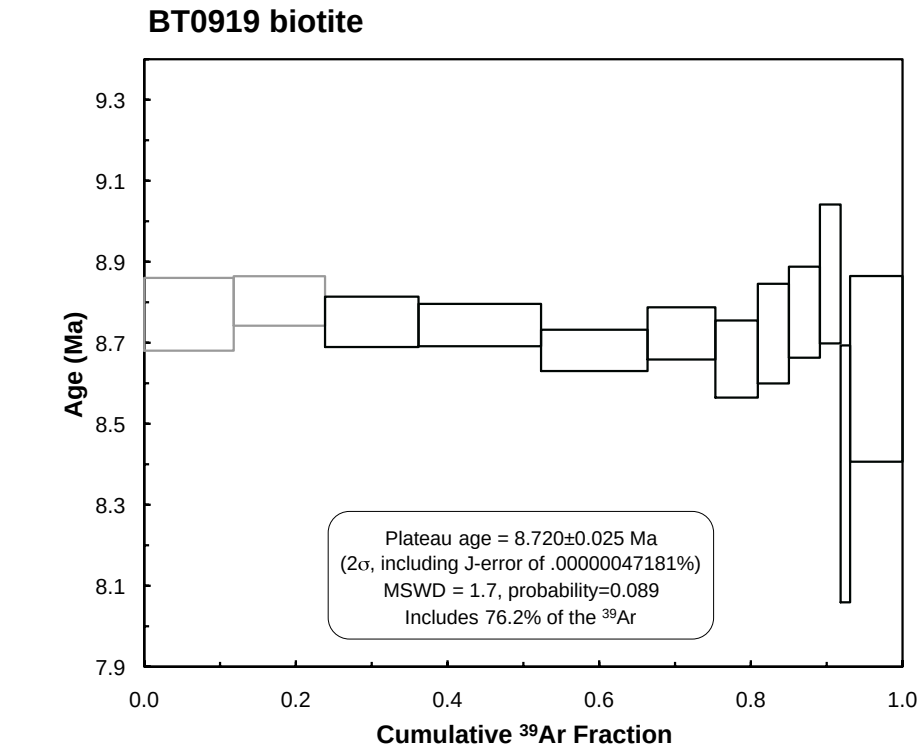
BT0919 biotite
Age (Ma)
9.3
9.1
8.9
8.7
8.5
8.3
8.1
7.9
0.0
0.2
0.4
0.6
0.8
1.0
Cumulative 39Ar Fraction
Plateau age = 8.720±0.025 Ma
(2σ, including J-error of .00000047181%)
MSWD = 1.7, probability=0.089
Includes 76.2% of the 39Ar

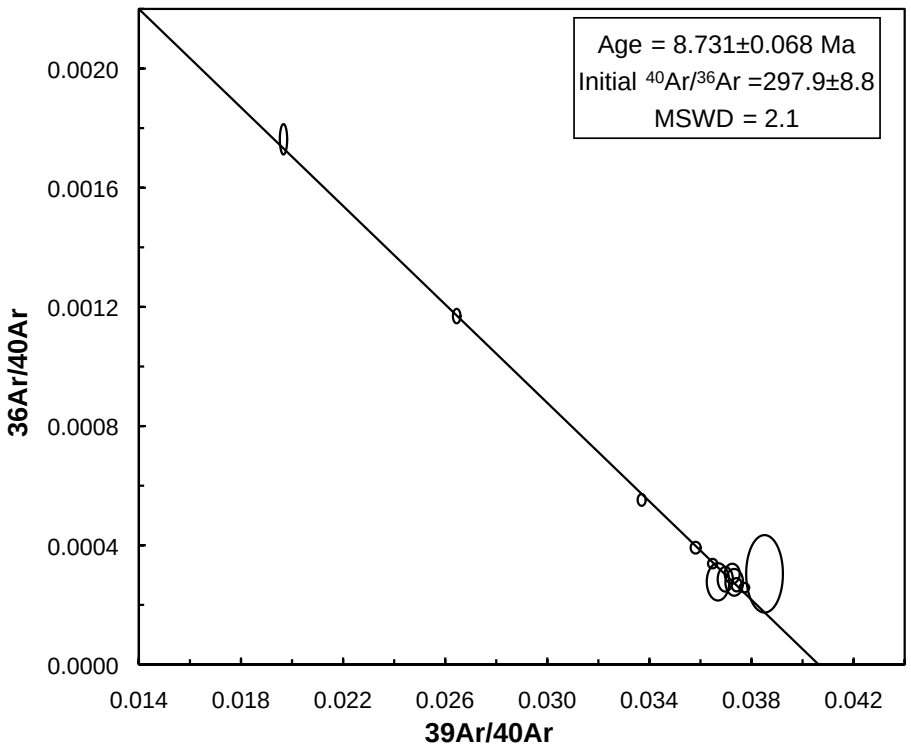
Age = 8.731±0.068 Ma
Initial 40Ar/36Ar =297.9±8.8
MSWD = 2.1
36Ar/40Ar
0.0020
0.0016
0.0012
0.0008
0.0004
0.0000
0.014
0.018
0.022
0.026
0.030
0.034
0.038
0.042
39Ar/40Ar

BT0920 biotite

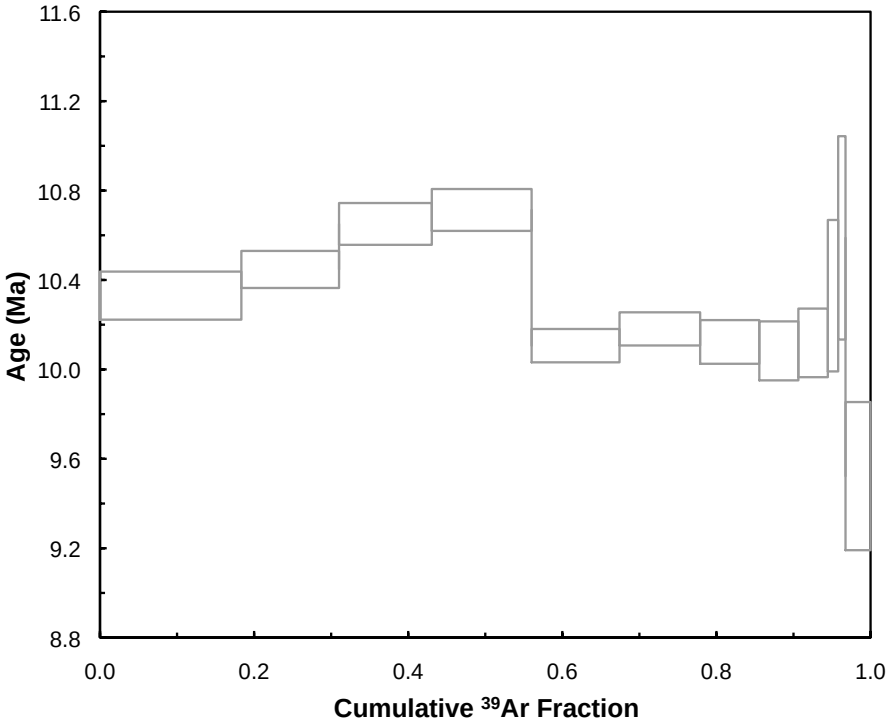

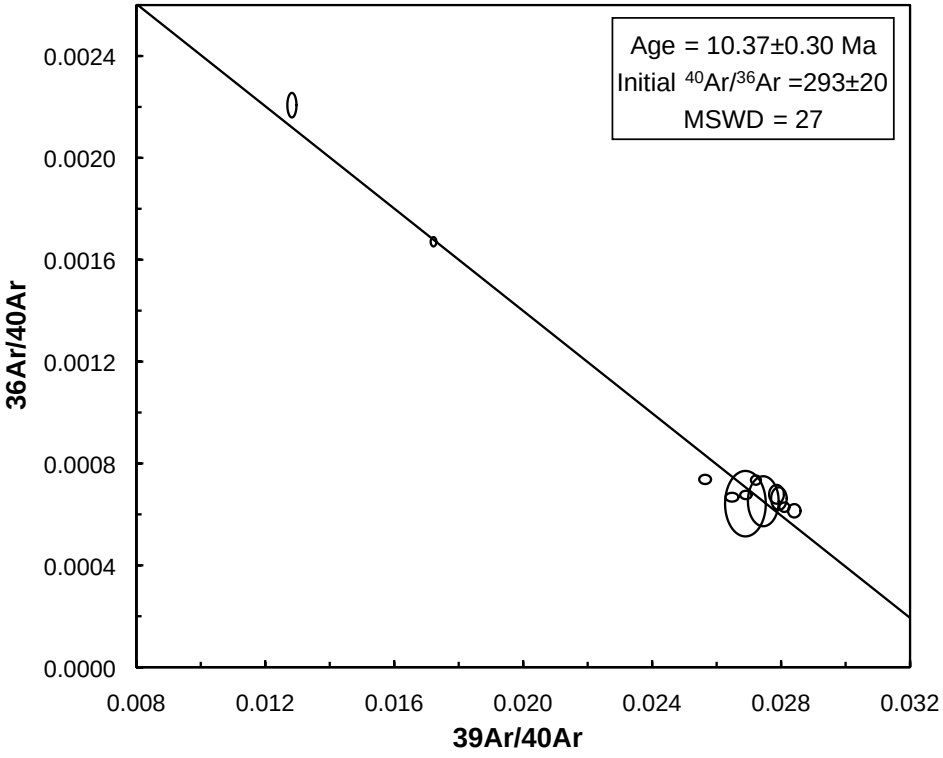

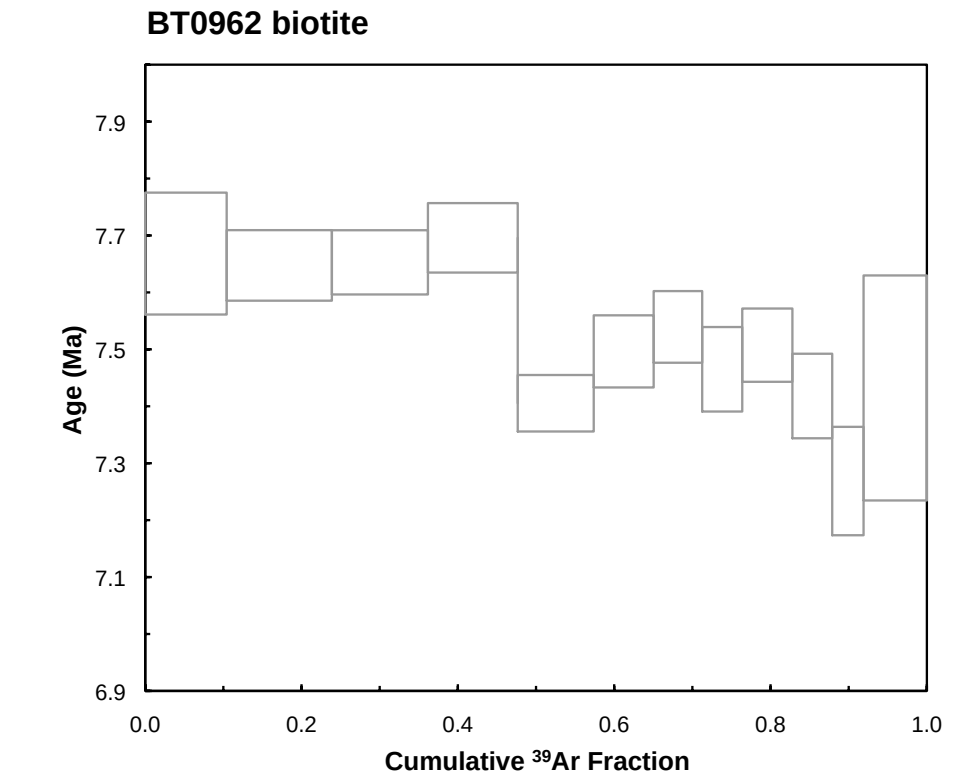
BT0962 biotite
7.9
7.7
7.5
7.3
7.1
6.9
Age (Ma)
0.0
0.2
0.4
0.6
0.8
1.0
Cumulative 39Ar Fraction

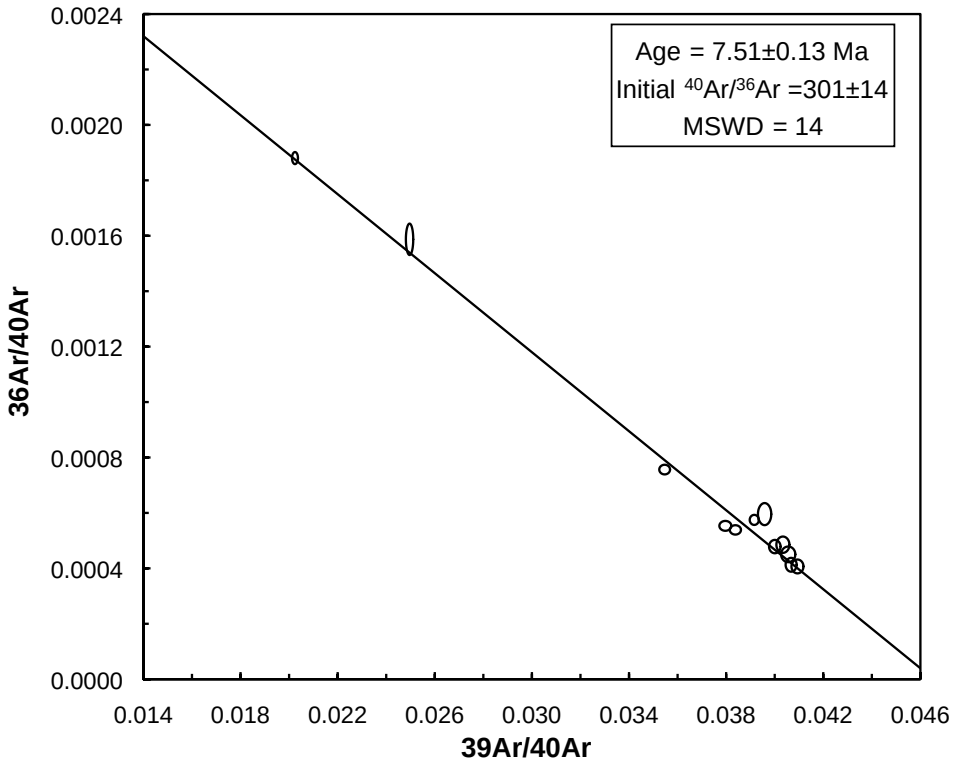
Age = 7.51±0.13 Ma
Initial 40Ar/36Ar =301±14
MSWD = 14
0.0024
0.0020
0.0016
0.0012
0.0008
0.0004
0.0000
36Ar/40Ar
0.014
0.018
0.022
0.026
0.030
0.034
0.038
0.042
0.046
39Ar/40Ar

BT0963 biotite

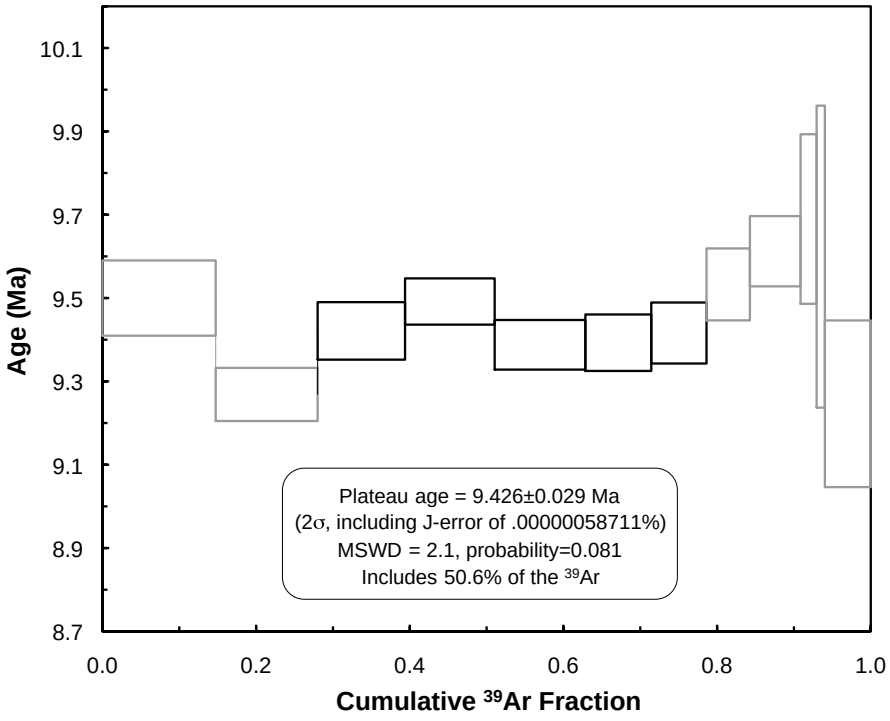

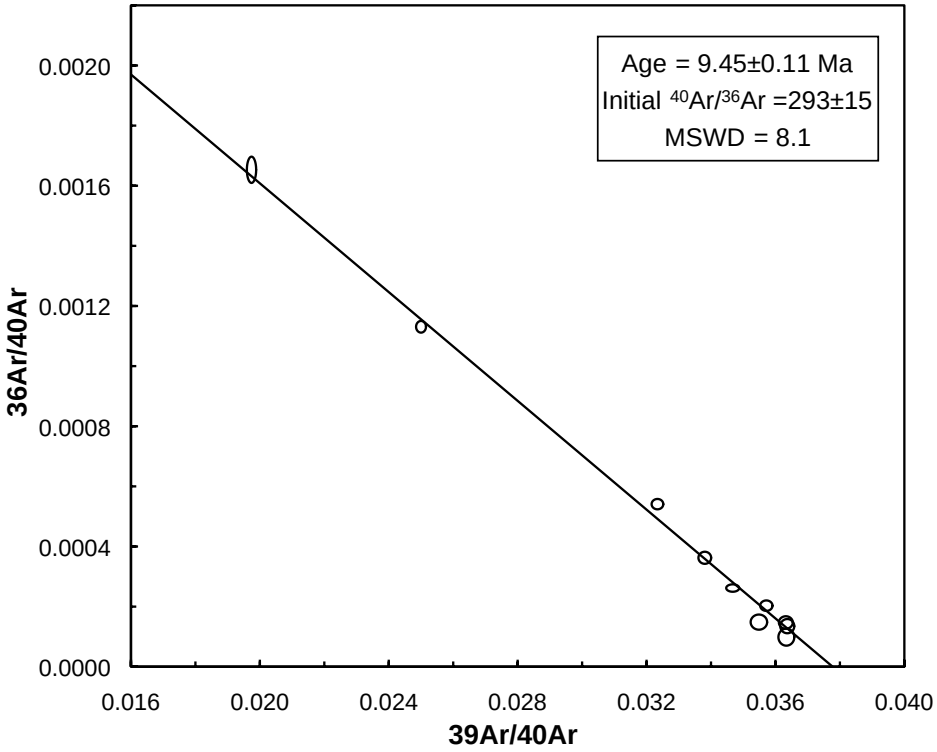

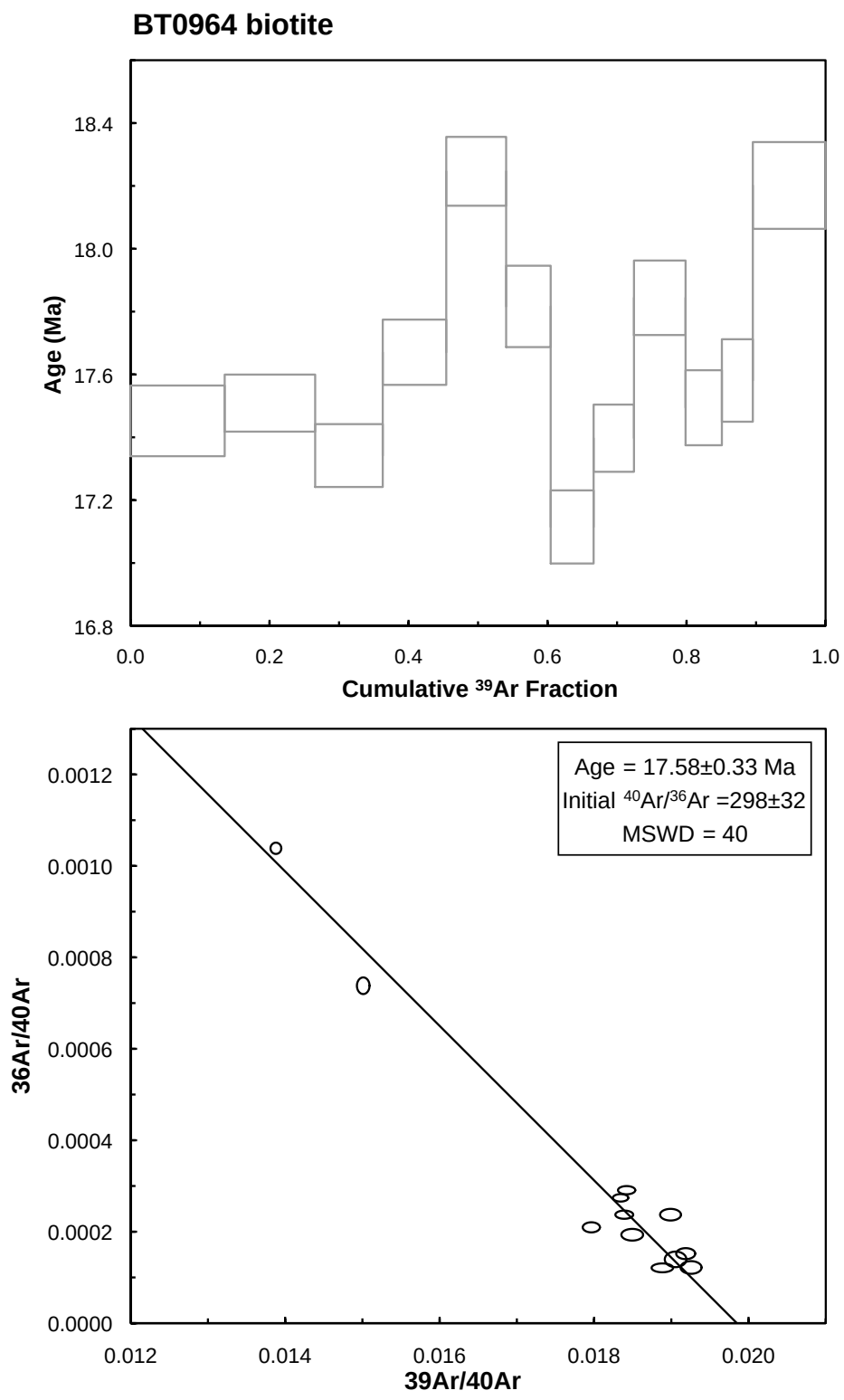
BT0964 biotite
Age (Ma)
18.4
18.0
17.6
17.2
16.8
0.0
0.2
0.4
0.6
0.8
1.0
Cumulative 39Ar Fraction
Age = 17.58±0.33 Ma
Initial 40Ar/36Ar =298±32
MSWD = 40
36Ar/40Ar
0.0012
0.0010
0.0008
0.0006
0.0004
0.0002
0.0000
0.012
0.014
0.016
0.018
0.020
39Ar/40Ar

BT0988 biotite

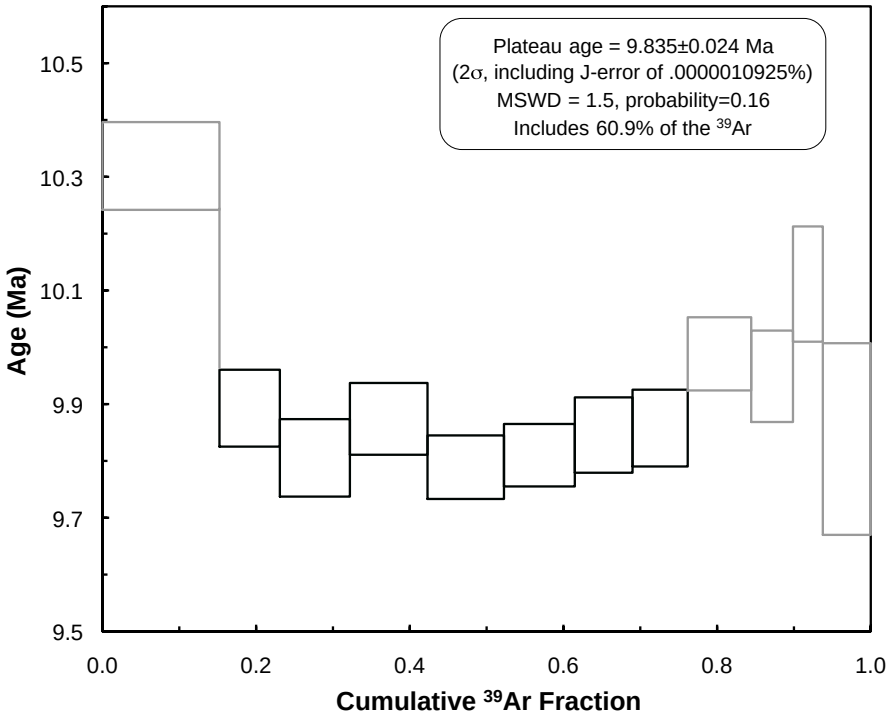

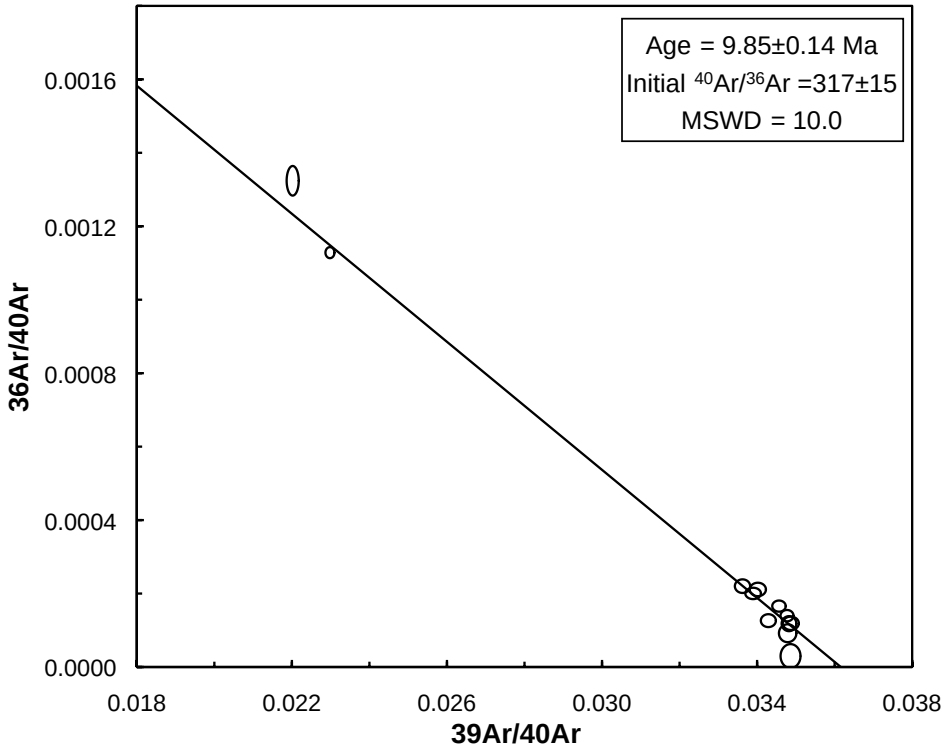

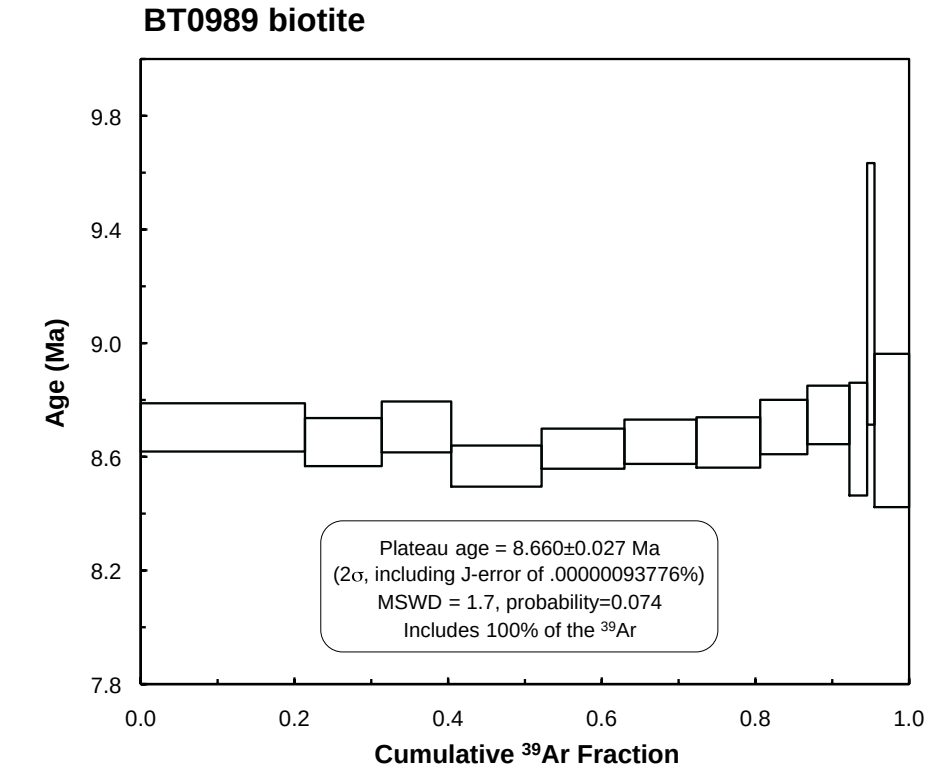
BT0989 biotite
Age (Ma)
9.8
9.4
9.0
8.6
8.2
7.8
0.0
0.2
0.4
0.6
0.8
1.0
Cumulative 39Ar Fraction
Plateau age = 8.660±0.027 Ma
(2σ, including J-error of .00000093776%)
MSWD = 1.7, probability=0.074
Includes 100% of the 39Ar

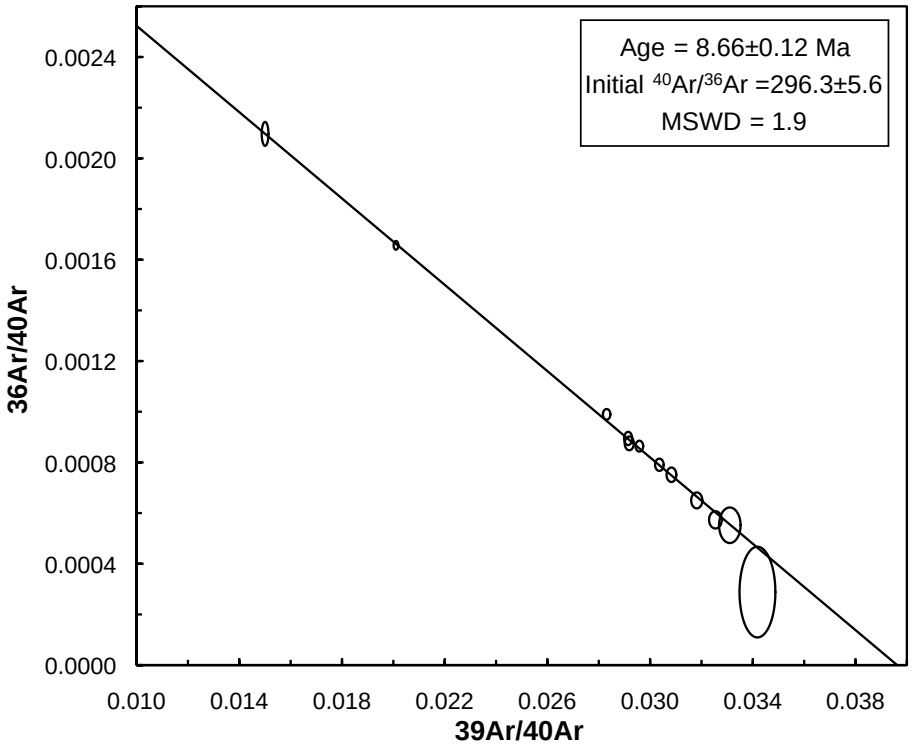
Age = 8.66±0.12 Ma
Initial 40Ar/36Ar =296.3±5.6
MSWD = 1.9
36Ar/40Ar
0.0024
0.0020
0.0016
0.0012
0.0008
0.0004
0.0000
0.010
0.014
0.018
0.022
0.026
0.030
0.034
0.038
39Ar/40Ar

APPENDIX C

CHAPTER 4 SUPPLEMENTARY MATERIALS

Table C1. CRONUS calculator input data sheet.

Sample Name	Effective Latitude* (N)	Centroid Longitude† (E)	Effective Elevation* (m)	Elevation Flag§	Thickness (cm)	Density (g/cm^3)	Shielding«	[^{10}Be] (atoms/g)	[^{10}Be] 1σ (atoms/g)	Be Standard¥	[^{26}Al] (atoms/g)	[^{26}Al] 1σ (atoms/g)	Al standard
bt0901	27.41537	90.60750	2948	std	1	2.7	1	44219	5683	07KNSTD	0	0	KNSTD
bt0902	27.31461	90.67056	2998	std	1	2.7	1	39267	3230	07KNSTD	0	0	KNSTD
bt0903	27.52611	90.55972	3116	std	1	2.7	1	94955	4890	07KNSTD	0	0	KNSTD
bt0904	27.53370	90.60333	3504	std	1	2.7	1	298794	11001	07KNSTD	0	0	KNSTD
bt0905	27.54657	90.64806	3431	std	1	2.7	1	475140	21725	07KNSTD	0	0	KNSTD
bt0906	27.47241	90.63167	3466	std	1	2.7	1	200487	16725	07KNSTD	0	0	KNSTD
bt0907	27.53796	90.62473	3451	std	1	2.7	1	261393	18222	07KNSTD	0	0	KNSTD
bt0909	27.66917	90.83083	3597	std	1	2.7	1	336625	26332	07KNSTD	0	0	KNSTD
bt0910	27.63185	90.95361	3629	std	1	2.7	1	351628	20649	07KNSTD	0	0	KNSTD
bt0912	27.67570	90.94778	3834	std	1	2.7	1	243388	11954	07KNSTD	0	0	KNSTD
bt0922	27.64382	90.60889	3611	std	1	2.7	1	311891	26495	07KNSTD	0	0	KNSTD
bt0926	27.48639	91.24667	2758	std	1	2.7	1	97598	5147	07KNSTD	0	0	KNSTD
bt0927	27.51685	91.22916	2619	std	1	2.7	1	170952	5250	07KNSTD	0	0	KNSTD
bt0928	27.54917	91.26972	2753	std	1	2.7	1	85463	2778	07KNSTD	0	0	KNSTD
bt0929	27.67083	91.13778	2258	std	1	2.7	1	95408	3569	07KNSTD	0	0	KNSTD
bt0931	27.66546	91.07333	2850	std	1	2.7	1	79985	3350	07KNSTD	0	0	KNSTD
bt0973	27.45509	90.98194	3773	std	1	2.7	1	642631	21388	07KNSTD	0	0	KNSTD
bt0974	27.46120	90.12361	3517	std	1	2.7	1	792250	38474	07KNSTD	0	0	KNSTD
bt0993	27.52567	89.78222	2455	std	1	2.7	1	165244	10102	07KNSTD	0	0	KNSTD
bt0994	27.67769	89.69195	3013	std	1	2.7	1	16682	1562	07KNSTD	0	0	KNSTD
bt0995	27.43315	89.81639	2544	std	1	2.7	1	109994	4843	07KNSTD	0	0	KNSTD
bt0996	27.29204	89.92167	2000	std	1	2.7	1	54706	3760	07KNSTD	0	0	KNSTD
bt0998	27.36148	90.05055	2190	std	1	2.7	1	26354	8401	07KNSTD	0	0	KNSTD
bt09108	27.40370	89.71944	3240	std	1	2.7	1	318378	14705	07KNSTD	0	0	KNSTD
bt1021	27.78435	91.18584	3220	std	1	2.7	1	170813	13217	07KNSTD	0	0	KNSTD
bt1036	27.32407	89.44444	3177	std	1	2.7	1	701376	30004	07KNSTD	0	0	KNSTD
bt1042	27.43542	90.10778	3407	std	1	2.7	1	548906	41782	07KNSTD	0	0	KNSTD
bt1043	27.42092	90.01472	3051	std	1	2.7	1	563798	63642	07KNSTD	0	0	KNSTD
bt1044	27.79750	89.64639	3795	std	1	2.7	1	68274	5037	07KNSTD	0	0	KNSTD

*Calculated using techniques described in Portegenga and Bierman (2011) and the constant production rate model of Stone (2000). †The longitude value at the centroid of the basin. §A flag that dictates how elevation are treated. We have used the standard elevation flag. «We assume on topographic shielding. ¥We use the standardization of Nishiizumi et al. (2007) as these measurements were made at PRIME Lab after November 14, 2007.

APPENDIX D

CHAPTER 5 SUPPLEMENTARY MATERIALS

METHODS

Cosmogenic analysis

All samples were processed at the Arizona State University, Surface Processes WOMBAT Laboratory. Quartz grains were separated and cleaned from the 250 – 1000 μm fraction of fluvial sands utilizing standard acid and gravimetric techniques. Sieved sediments were placed in aqua regia at room temperature for 12 hours. The samples were then leached in a 5% hydrofluoric and nitric acid solution and rolled on heat for 24 hours. Feldspars and micas were floated off using a wetting technique, and dense minerals were removed via heavy liquids. During the cleaning and separation process, quartz grains were leached at least five times with hydrofluoric and nitric acids. The quartz separates were then spiked with ^{9}Be, and digested with concentrated hydrofluoric and nitric acid. We removed interfering cations and anions using liquid chromatography techniques. Oxidized beryllium, was mixing with a matrix of niobium and loaded into cathodes for analysis on an accelerator mass spectrometer at PRIME Lab, Purdue University. Beryllium isotope ratios were referenced to the isotope ratio standards described in Nishiizumi et al. (2007).

In a recent publication Portenga and Bierman (2011) suggested a new method to make the calculation of basin average erosion rates more transparent and comparable between studies and other regions of Earth's surface. We utilized this theory to calculate a single elevation, latitude and longitude value that can be used in the CRONUS online calculator (Balco et al., 2008). Using the Advanced Spaceborne Thermal Emission Radiometer (ASTER) 30 m per pixel resolution digital elevation

dataset we calculated the scaled production rate based on the elevation and latitude of each pixel in a basin. To be internally consistent with the procedures of the CRONUS calculator, we calculated the production rate from spallation reactions using the scheme of Stone (2000), and the production rate from muon reactions using the equations of Heisinger et al. (2002a; 2002b). We calculated the mean of all total production rates (e.g. spallation and muon) within the basin and found the elevation and latitude values corresponding to this mean scaling factor, referred to here as the effective elevation and latitude of the basin. We then used the CRONUS calculator to calculate our erosion rates. Because we were not able to adjust the production rate of muons for the erosion rate at each pixel in the basin, it is not accurate to report any time-dependent erosion rate as calculated by the CRONUS calculator for this study. We, therefore, only report the constant production rate results as determined by the models of Lal (1991)/Stone (2000) from the CRONUS online calculator (Table DR1).

Topgraphic analysis

Mean hillslope gradient

This analysis was performed on a 90m Shuttle Radar Topography Mission (SRTM) digital elevation model. Hillslope gradients are defined as the maximum slope across a plane of 3 x 3 pixels within a DEM. This calculation was carried out with a moving window across the DEM, and then finding the mean of all pixels in a basin (Table DR1). Because of the number of pixels in each basin the standard error on the mean is several orders of magnitude smaller than the mean and therefore, we

have not plotted or reported these errors here.

Mean normalized channel steepness

As a means of comparison with other studies we used a 90 m DEM for this analysis. After channels are located within a DEM, relationships between the local channel gradient and the upstream drainage area calculated according the well known power-law given by Flint's law:

$$S = k_s A^{-\theta} \quad (1)$$

where S is the channel slope, k_s is the channel steepness, A is the upstream drainage area, and θ is the is the concavity. We use a reference value of $\theta = 0.45$, to normalize measures of S for the change in A along the length of the channel profile and calculate a normalized channel steepness, k_{sn} (Table DR1, Figure DR2). In this way we can compare channel gradients at all drainage areas (Wobus et al., 2006). To calculate a mean value for a basin, we calculate the mean normalized channel steepness for all portions of a basin, which are governed by fluvial processes. This generally occurs at drainage areas > 2 km^2. Because of this size limitation we are not able to calculate an accurate channel steepness value for one of our sampled basins in Bhutan (BT0974).

FIGURE CAPTIONS

Figure D1. Plot of mean hillslope gradient versus erosion rate. Erosion rate error bars are 1σ. Note the nearly linear trend from very low erosion rates to ca. 215 m m.y.$^{-1}$ in Bhutan. At rates beyond this point, mean hillslope gradients no longer track

increases in erosion rate. Data from the eastern margin of the Tibetan Plateau (Ouimet et al., 2009) and the Central Nepal Himalaya (Godard et al., 2014) have been added for comparison. In this plot variable relationships between topography and erosion rate can been seen, similar to Figure DR2.

Figure D2. Comparison of cosmogenic radionuclide erosion rates and mean normalized channel steepness values (k_{sn}) from the Himalayan-Tibetan orogenic system. Light grey triangles represent data from the eastern margin of the Tibetan Plateau (Ouimet et al., 2009). Dark squares represent data from the Central Nepal Himalaya (Godard et al., 2014). Envelopes show the results of 5000 Monte Carlo least squares regressions, dark curves show median best-fit curve (equation shown). Best-fit curves from the Tibetan Plateau and Nepal data are shown in blue and red, respectively. Data from Bhutan are colored by Tropical Rainfall Measuring Mission mean annual rainfall data (Bookhagen, in review). Error bars are 1σ.

REFERENCES

Balco, G., Stone, J.O., Lifton, N.A., Dunai, T.J., 2008, A complete and easily accessible means of calculating surface exposure ages or erosion rates from (10)Be and (26)Al measurements. Quaternary Geochronology, 3, 174-195.

Bookhagen, B., in review, High resolution spatiotemporal distribution of rainfall seasonality and extreme events based on a 12-year TRMM time series.

Godard, V., Bourlès, D. L., Spinabella, F., Burbank, D. W., Bookhagen, B., Fisher, G. B., Moulin, A., and Léanni, L., 2014, Dominance of tectonics over climate in

Himalayan denudation: Geology, p. G35342. 35341.

Heisinger, B., Lal, D., Jull, A.J.T., Kubik, P., Ivy-Ochs, S., Knie, K., Nolte, E., 2002a, Production of selected cosmogenic radionuclides by muons: 2. Capture of negative muons. Earth and Planetary Science Letters, 200, 357-369.

Heisinger, B., Lal, D., Jull, A.J.T., Kubik, P., Ivy-Ochs, S., Neumaier, S., Knie, K., Lazarev, V., Nolte, E., 2002b, Production of selected cosmogenic radionuclides by muons 1. Fast muons. Earth and Planetary Science Letters, 200, 345-355.

Lal, D., 1991, Cosmic-ray labeling of erosion surfaces – insitu nuclide production rates and erosion models. Earth and Planetary Science Letters, 104, 424-439.

Ouimet, W. B., Whipple, K. X., and Granger, D. E., 2009, Beyond threshold hillslopes: Channel adjustment to base-level fall in tectonically active mountain ranges: Geology, v. 37, no. 7, p. 579-582.

Portenga, E.W., Bierman, P.R., 2011, Understanding Earth's eroding surface with 10 Be. GSA Today, 21, 4-10.

Stone, J.O., 2000. Air pressure and cosmogenic isotope production. Journal of Geophysical Research: Solid Earth, 105, 23753-23759.

Wobus, C., Whipple, K. X., Kirby, E., Snyder, N., Johnson, J., Spyropolou, K., Crosby, B., and Sheehan, D., 2006, Tectonics from topography: Procedures, promise, and pitfalls: Special papers-Geological Society of America, v. 398, p. 55.

Table D1. Basin average erosion rate sample data.

Sample Name	Latitude (°N)[a]	Longitude (°E)[a]	Elevation (m)[a]	Basin Area (km^2)[b]	Mean basin slope (deg)[b]	Mean basin k_{sn}[b]	Mean basin k_{sn} 1SE[b]	Mean annual precipitation ($m\ y^{-1}$)[c]	[^{10}Be] (atoms/g)	[^{10}Be] 1σ (atoms/g)	Erosion Rate ($m\ m.y.^{-1}$)[d]	Erosion Rate 1σ ($m\ m.y.^{-1}$)[d]	Integration Time (k.y.)[e]
BT0901	27.41836	90.60650	1083	80	27	285	13	0.70	44219	5683	652	97	0.92
BT0902	27.35374	90.66857	1029	132	28	342	8	0.74	39267	3230	473	53	1.3
BT0903	27.50617	90.55857	2101	42	23	235	13	0.55	94955	4890	208	19	2.9
BT0904	**27.53484**	**90.60214**	**2864**	**48**	**15**	**115**	**4**	**0.42**	**298794**	**11001**	**79**	**7**	**7.6**
BT0905	**27.53888**	**90.64625**	**2899**	**27**	**17**	**113**	**6**	**0.45**	**475140**	**21725**	**47.8**	**4.4**	**13**
BT0906	**27.47286**	**90.62557**	**2875**	**30**	**19**	**107**	**6**	**0.45**	**200487**	**16725**	**117**	**13**	**5.1**
BT0907	**27.52203**	**90.62083**	**2871**	**110**	**17**	**108**	**3**	**0.43**	**261393**	**18222**	**89**	**9**	**6.8**
BT0909	**27.66006**	**90.82805**	**2785**	**65**	**22**	**157**	**7**	**0.63**	**336625**	**26332**	**74**	**8**	**8.1**
BT0910	**27.62422**	**90.95410**	**2777**	**56**	**17**	**180**	**7**	**0.62**	**351628**	**20649**	**72**	**7**	**8.4**
BT0912	**27.68652**	**90.94741**	**2865**	**50**	**23**	**198**	**14**	**0.61**	**243388**	**11954**	**115**	**11**	**5.2**
BT0922	**27.61863**	**90.60584**	**2735**	**114**	**18**	**172**	**6**	**0.46**	**311891**	**26495**	**80**	**9**	**7.5**
BT0926	27.47059	91.24598	930	59	27	362	18	0.58	97598	5147	168	15	3.6
BT0927	27.50980	91.23062	1045	21	26	352	33	0.58	170952	5250	88	7	6.8
BT0928	27.54972	91.27051	1071	53	29	322	11	0.60	85463	2778	191	16	3.1
BT0929	27.67441	91.13576	1240	13	29	218	11	1.20	95408	3569	131	11	4.6
BT0931	27.67680	91.07116	1278	91	30	250	5	1.10	79985	3350	215	19	2.8
BT0973	**27.46368**	**90.97917**	**3444**	**20**	**15**	**55**	**3**	**0.42**	**642631**	**21388**	**41.6**	**3.6**	**14**
BT0974	**27.46313**	**90.11234**	**3182**	**2**	***22***	**too small**	**too small**	***0.69***	**792250**	**38474**	**29.6**	**2.8**	**20**
BT0993	27.52631	89.77748	1440	114	23	204	4	0.85	165244	10102	134	13	4.5
BT0994	27.66848	89.77435	1372	108	27	269	6	0.97	16682	1562	1130	137	0.53
BT0995	27.45004	89.81466	1190	74	25	237	5	0.64	109994	4843	132	11	4.5
BT0996	27.28347	89.92412	750	41	27	237	11	0.83	54706	3760	318	31	1.9
BT0998	27.33546	90.05133	696	65	31	236	8	0.88	26354	8401	736	265	0.82
BT09103	26.87892	90.26807	309	137	24	164	4	3.40	22009	3252	342	28.5	1.75
BT09108	**27.40841**	**89.71839**	**2355**	**42**	**22**	**176**	**6**	**0.76**	**318378**	**14705**	**65**	**6**	**9.2**
BT1021	27.78506	91.18372	1283	72	27	349	18	0.72	170813	13217	193	21	3.1
BT1029	26.19193	89.45492	294	26	27	153	6	4.60	9439	2238	769	100	0.78
BT1036	**27.30971**	**89.44209**	**2203**	**37**	**22**	**200**	**6**	**0.64**	**701376**	**30004**	**45.0**	**4.0**	**13**
BT1042	**27.44001**	**90.10559**	**2918**	**38**	**19**	**101**	**5**	**0.70**	**548906**	**41782**	**65**	**7**	**9.2**
BT1043	**27.44946**	**90.00967**	**2595**	**57**	**17**	**117**	**4**	**0.76**	**563798**	**63642**	**53**	**7**	**11**
BT1044	27.77093	89.64485	1714	89	28	378	17	0.56	68274	5037	644	69	0.93

[a]Actual sample location data. [b]From 90 m resolution data. [c]From Tropical Rainfall Measuring Mission data (Bookhagen, in review) [d]Values calculated using the methods of Portenga and Biermann (2011) and the CRONUS calculator (Balco et al., 2008). Results were calculated using the constant prodution rate model of Lal (1991)/Stone (2000). [e]Time over which the erosion rate is integrated. This value is calculated by dividing the e-folding depth of the production of cosmic nuclides via spallation (0.6 m) by the erosion rate. Bold samples are located on low-relief landscapes.

FIGURE D1.

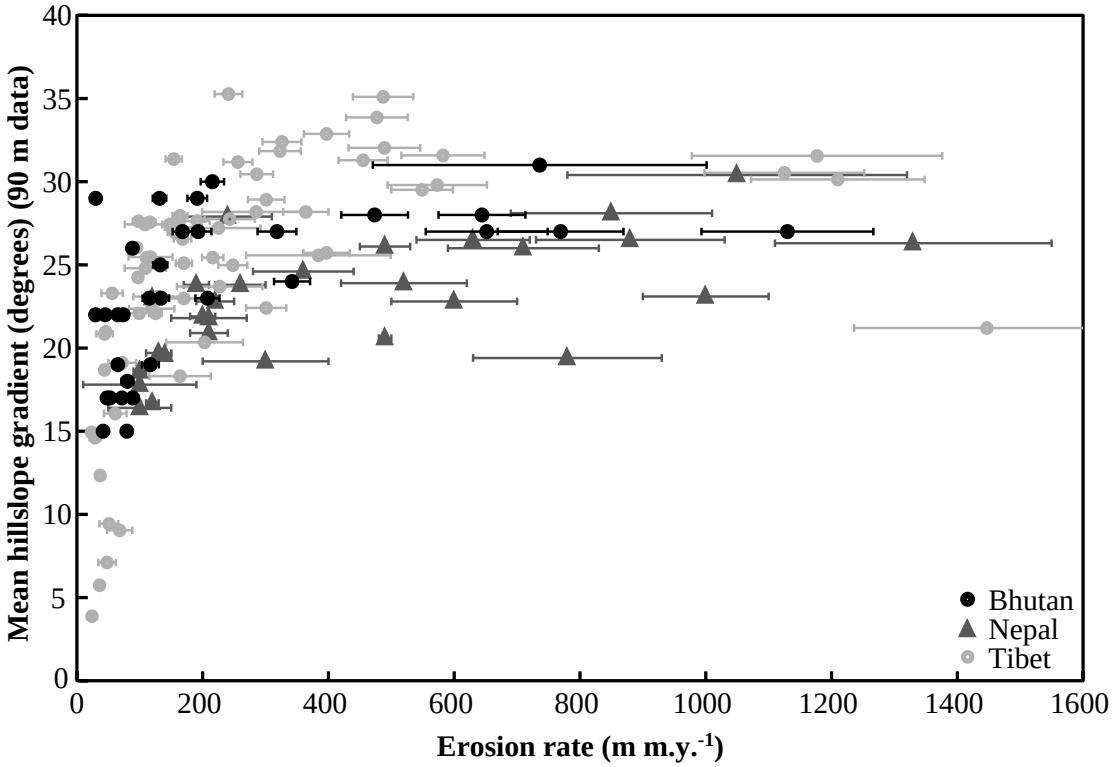
Mean hillslope gradient (degrees) (90 m data)
Erosion rate (m m.y.-1)
0
5
10
15
20
25
30
35
40
0
200
400
600
800
1000
1200
1400
1600
Bhutan
Nepal
Tibet

FIGURE D2.

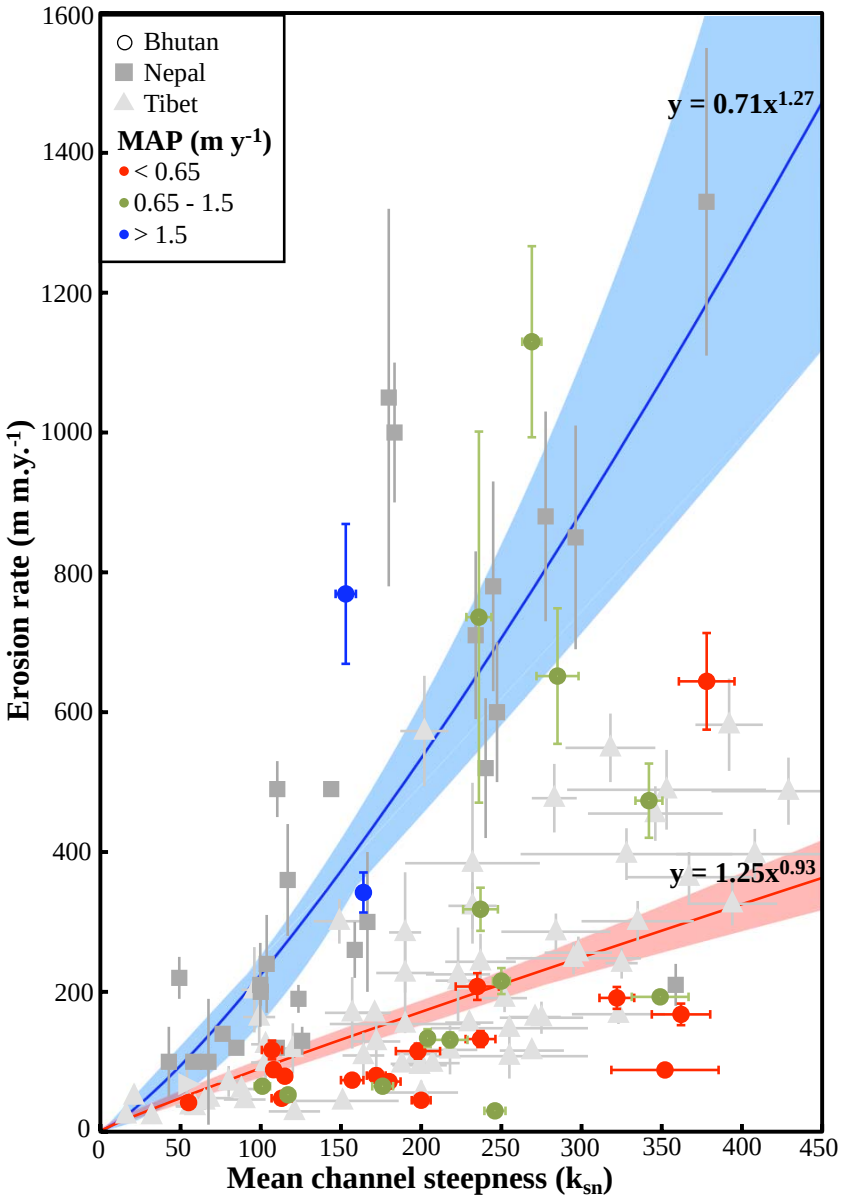
Bhutan
Nepal
Tibet
MAP (m y-1)
< 0.65
0.65 - 1.5
> 1.5
y = 0.71x1.27
y = 1.25x0.93
Erosion rate (m m.y.-1)
Mean channel steepness (ksn)
0
200
400
600
800
1000
1200
1400
1600
0
50
100
150
200
250
300
350
400
450

APPENDIX E

STATEMENT OF PERMISSION FROM CO-AUTHORS

Chapter 2 was prepared independently for publication with help from Kip v. Hodges, Kelin X Whipple, and Matthijs C. van Soest. These co-authors have acknowledged and granted permission for the use of this work in the context of this dissertation.

BIOGRAPHICAL SKETCH

I started in the Geological Sciences Ph.D. program within the School of Earth and Space Exploration at Arizona State University in 2007. I received a M.S. in Geology from the University of Cincinnati (McMicken College of Arts and Sciences 2007 Outstanding Master's Student). Before that I graduated from Ball State University with a B.S. in Geology (with honors) and a Minor in Chemistry.

My specific pursuits include developing and utilizing quantitative techniques (topographic analysis, thermochronometry, and cosmogenic nuclides) to better understand tectonic and surface processes and their interaction with climate. Most of this research has been focused on understanding the evolution of the Himalayan mountain belt.